Nanoparticle synthesis using the atmospheric pressure plasma source HelixJet

Dissertation

zur Erlangung des Doktorgrades an der
Mathematisch-Naturwissenschaftlichen Fakultät im Fachbereich
Physik

vorgelegt von
Maren Dworschak

Kiel
Mai 2025

Erster Gutachter:	Prof. Dr. Jan Benedikt
Zweiter Gutachter:	Prof. Dr. Lorenz Kienle
Tag der mündlichen Prüfung:	30.06.2025

Abstract

Nanoparticles hold unique properties such as high surface-to-volume ratios or quantum confinement effects, making them viable for countless applications in various scientific fields such as biomedicine, catalysis, detectors and sensing, opto-electronics or energy storage and harvesting. This work focuses on the synthesis and surface modification of silicon and metal nanoparticles, as well as multi-elemental core-shell or Janus particles using atmospheric plasma jets as a tool. Both a bottom-up approach in the form of gas phase synthesis using the reactive gas silane as well as a top-down approach using solid state source materials are demonstrated. As a first step, the HelixJet atmospheric plasma source is modified for a long term operation at high admixtures of reactive gases. The gas flow inside the jet is simulated using COMSOL® and the parameters of the jet are monitored closely. Particles synthesized in the gas phase are analyzed using a Scanning Mobility Particle Sizer (SMPS) and their crystallographic structure is made visible using Transmission Electron Microscopy (TEM). For a suitable set of parameters, silicon nanocrystals with diameters in the range of 3 to 7 nm are synthesized. Their crystallization is enabled by the admixture of hydrogen and the consequent selective heating. Measurements in collaboration with the Institute of Physics in Prague reveal a strong photoluminescence (PL) intensity in the visible red spectral region for these silicon nanocrystals. The position of the PL maximum can be shifted between 650 and 750 nanometers depending on the synthesis conditions. The combination of silicon particle synthesis and a fly-through annealing stage results in the formation of Janus particles with a special half-sphere structure containing a silicon-manganese alloy. This structure is analyzed in collaboration with the group of Synthesis and Real Structure of Prof. Kienle at the Faculty of Engineering in Kiel. With the design of a smaller version of the HelixJet, higher power densities of around $530\,\mathrm{Wcm^{-3}}$ are reached inside the plasma jet, diminishing the need for hydrogen admixture. Introducing a source metal wire into the middle axis of this jet, metal particles are produced even from high melting point metals such as tungsten. The influence of plasma parameters, such as power and gas flow, on the particle morphology and crystal structure is investigated using transmission electron microscopy, revealing that the average size of the tungsten nanocrystals can be tuned between 12 and 25 nm. Depending on the specific plasma parameters it is possible to synthesize monocrystalline tungsten particles with both α- and β-crystallographic phases as well as tungsten oxide nanoparticles. A short test combining both gas phase and source material synthesis results in the formation of copper particles with a silicon shell opening up a potential synthesis method for various silicon-metal-nanoparticles. Finally, two HelixJets are combined in a double jet setup for the subsequent synthesis and surface treatment of the particles. A reflective setup offers the employment of *in situ* Fourier-transform infrared spectroscopy (FTIR) allowing real time access to the chemical composition and surface modification, which are crucial to tailor nanoparticles for their intended applications. Using a pulsed methane plasma in the second jet, the formation of silicon carbon bonds is observed both in FTIR, as well as in XPS. This last experiment acts as a stepping stone for the possible multi-step synthesis and surface modification to tailor nanoparticles for their intended applications.

Kurzfassung

Nanopartikel verfügen über einzigartige Eigenschaften bedingt durch ihr hohes Verhältnis von Oberfläche zu Volumen oder duch sogenannte Quanteeinschlussseffekte im Fall von Halbleitermaterialien. Diese Eigenschaften machen sie nutzbar für unzählige Anwendungen in verschiedensten Bereichen wie zum Beispiel in der Biomedizin, Katalyse, für Detektoren und Sensorik, in der Optoelektronik oder für Energiespeicherung. Diese Arbeit konzentriert sich auf die Synthese und Oberflächenmodifikation von Silizium- und Metallnanopartikeln, sowie von Multielement- und insbesondere Janus-Partikeln unter der Verwendung von Atmosphärendruck Plasmajets. Zwei verschiedene Ansätze zur Synthese, einmal aus einem Festkörper und einmal aus der Gasphase, werden demonstriert. Dafür wird zunächst die Plasmaquelle HelixJet modifiziert, um den Langzeitbetrieb auch bei hohen Beimischungen reaktiver Gase zu gewährleisten. Der Gasfluss innerhalb des Jets wird mit Hilfe von COMSOL® simuliert und zeigt, dass die Modifikationen die Beschichtung verringern. Die Größe der in der Gasphase synthetisierten Partikel wird mit einem Scanning Mobility Particle Sizer (SMPS) analysiert und ihre kristallografische Struktur wird mit Transmissionselektronenmikroskopie (TEM) sichtbar gemacht. Bei geeigneter Wahl der Parameter können so Silizium-Nanokristalle mit Durchmessern im Bereich von 3 bis 7 nm synthetisiert werden. Durch die Beimischung von Wasserstoff und das sogenannte selektive Heizen wird das Erreichen der Kristallisationstemperatur ermöglicht. Messungen in Zusammenarbeit mit dem Institut für Physik in Prag (FZU) zeigen eine starke Photolumineszenz (PL) im roten Wellenlängenbereich für diese Nanokristalle. Die Position des PL-Maximums kann durch Anpassen der Syntheseparameter zwischen 650 und 750 Nanometern variiert werden. Die Kombination der Synthese von Siliziumpartikeln mit dem Durchlaufen einer Glühphase führt zur Bildung von Januspartikeln mit einer speziellen Halbkugelstruktur, die eine Silizium-Mangan-Legierung enthält. Die genaue Zusammensetzung dieser Partikel wird in Zusammenarbeit mit der Arbeitsgruppe von Prof. Kienle an der technischen Fakultät Kiel analysiert. Durch die Konstruktion einer kleineren Version des HelixJets können höhere Plasmadichten von bis zu 530 $\mathrm{Wcm^{-3}}$ erreicht werden, wodurch die Notwendigkeit der Wasserstoffbeimischung entfällt. Wird ein Metalldraht auf der Mittelachse eines solchen Jets eingebracht, können Metallpartikel selbst aus hochschmelzenden Metallen wie Wolfram erzeugt werden. Abhängig von den spezifischen Plasmaparametern lassen sich monokristalline Wolframpartikel mit sowohl α- als auch β-kristallographischen Phasen als auch Wolframoxid-Nanopartikel mit Durchmessern zwischen 12 und 25 Nanometern erzeugen. Ein kurzer Test der Kombination von Gasphasen- und Ausgangsmaterialsynthese führt zur Bildung von Kupferpartikeln mit einer Siliziumhülle. Für die kombinierte Synthese und Oberflächenbehandlung der Partikel werden zwei HelixJets miteinander verbunden. Ein reflektierendes Substrat ermöglicht den Einsatz von *in situ* Fourier-Transformations-Infrarotspektroskopie (FTIR), welche die chemische Zusammensetzung und die Oberflächenmodifizierung in Echtzeit misst. Durch den Einsatz eines gepulsten Methanplasmas im zweiten Jet kann die Bildung von Silizium-Kohlenstoff-Bindungen an der Partikeloberfläche sowohl im FTIR als auch mit XPS-Messungen beobachtet werden. Dieses letzte Experiment dient als Grundlage für die mehrstufige Synthese und Oberflächenmodifikation, um Nanopartikel für ihre beabsichtigten Anwendungen maßzuschneidern.

Contents

List of Abbreviations

AC	Alternating Current
APP	Atmospheric Pressure Plasma
APPJ	Atmospheric Pressure Plasma Jet
BF	Bright Field
CCD	Charge-Coupled Device
CCP	Capacitively Coupled Plasma
CPC	Condensation Particle Counter
CTEM	Conventional Transmission Electron Microscopy
CVD	Chemical Vapor Deposition
DBD	Dielectric Barrier Discharge
DC	Direct Current
DMA	Differential Mobility Analyzer
EDX	Energy-dispersive X-Ray Spectroscopy
EELS	Electron Energy Loss Spectroscopy
fcc	face centered cubic
FEG	Field Emission Gun
FTIR	Fourier-Transform Infrared Spectroscopy
FZU	Fyzikální ústav, Institue of Physics, Czech Academy of Science, Prague
GAS	Gas Aggregation Source
HAADF	High Angle Annular Dark Field
HF	High Frequency
HRTEM	High Resolution Transmission Electron Microscopy
LED	Light-Emitting Diode
LSP	Localized Surface Plasmon
LSPR	Localized Surface Plasmon Resonance
MRI	Magnetic Resonance Imaging
NC	Nanocrystal
NP	Nanoparticle
OES	Optical Emission Spectroscopy
OML	Orbital Motion Limited
PECVD	Plasma-Enhanced Chemical Vapor Deposition
PL	Photoluminescence
QD	Quantum Dot

RF	Radio Frequency
RNS	Reactive Nitrogen Species
ROS	Reactive Oxygen Species
SAED	Selected Area Electron Diffraction
SARS-CoV 2	Severe Acute Respiratory Syndrome Corona Virus Type 2
sccm	standard cubic centimeters per minute
SERS	Surface-Enhanced Raman Spectroscopy
SMPS	Scanning Mobility Particle Sizer
SPION	Super Paramagnetic Iron Oxide Nanoparticles
STEM	Scanning Transmission Electron Microscopy
TEM	Transmission Electron Microscopy
UV	Ultra Violet
XPS	X-ray Photoelectron Spectroscopy

1 | Introduction

Nanoparticles are an integral part of nanotechnology and therefore modern material science. Often overlooked by society, they already accompany us in many aspects of our daily life. For example, TiO_2 and ZnO nanoparticles can be found in sunscreens due to their UV absorbing and scattering properties, where they provide effective protection against UV radiation while maintaining transparency on the skin [1]. Silver nanoparticles are commonly used in toothpastes, shampoos and sanitizer sprays for their antimicrobial and antibacterial effects [2]. Beyond personal care, nanoparticles are also often hidden in thin coatings, improving, for example, the scratch resistance of exposed surfaces [3].

Many of these applications are not achievable with microparticles or the bulk material. The reason for this can be found in the increased surface-to-volume ratio of the nanoparticles that results in a drastic change of their properties. When taking a look at a silicon particle with a diameter of 1 µm, less then 1 % of the total number of atoms are located on its surface. This ratio changes drastically with a reduction in size. For a silicon nanoparticle with a diameter of 4 nm, 25 % of all atoms are surface atoms [4]. Going further down, a 2 nm silicon nanoparticle consists of 280 atoms, with 120 (43 %) of them being surface atoms [5]. Since many potential reactions, as well as catalytic and sensing properties, depend on the material's surface, the high surface area achieved in the form of nanoparticles is beneficial. Material in the form of nanoparticles not only enhances these properties but also reduces the total amount of material required.

Additionally, semiconductor nanoparticles with dimensions smaller than the exciton Bohr radius are subject to quantum confinement effects. These so-called quantum dots (QDs) are characterized by a change in the energy state structure from continuous to discrete.

In addition, an indirect band gap becomes direct, which increases their quantum efficiency and makes them suitable for opto-electrical applications in solar cells or light-emitting devices [6, 7].

Metal nanoparticles also possess unique optical, electronic and catalytic properties, which are highly dependent on their size, shape and surrounding environment [8, 9]. For example, localized surface plasmon resonance (LSPR) observed in noble metal nanoparticles, such as gold and silver, results in strong absorption and scattering of light at specific wavelengths, enabling their use in enhanced spectroscopy, sensing and bio-medical imaging [10, 11].

Traditional methods for synthesizing nanoparticles such as silicon and metal nanoparticles include chemical reduction, wet-chemical etching and thermal decomposition. These methods often require high temperatures, toxic chemicals and extensive post-processing [12–14]. Since the global nanomaterial market is rapidly growing, there is an ongoing search for more cost-efficient methods to meet the growing demand [15–17]. Plasma-based methods offer a promising alternative for the generation of nanoparticles, with advantages such as reduced environmental impact and room-temperature synthesis while maintaining precise control over particle size and composition [18, 19].

The growth of nanoparticles in low-pressure plasmas was first observed as a source of contamination in semiconductor processing in 1989 [20]. Since then, low-pressure plasma processes have been studied for the synthesis of semiconductor and other material nanoparticles through

gas phase synthesis [21], as well as sputtering methods [22]. The crystallization process is influenced by the local plasma temperature, selective heating and the availability of hydrogen, which acts as a surface passivant, preventing excessive coalescence and enabling the formation of well-defined nanocrystals [23]. More recent advances in this field have focused on improving the efficiency and scalability of low-pressure plasma systems. For example, researchers have explored innovative reactor designs, such as flow-through systems and rotating substrates, to enhance particle yield and uniformity while reducing energy consumption [24]. However, the reliance on vacuum systems in low-pressure plasma setups limits their advances in terms of cost reductions and scalability. The need for extensive pumping infrastructure and large-scale vacuum chambers increases operational expenses and limits throughput.

Atmospheric pressure plasmas can offer a cost-effective and scalable synthesis technique compared to conventional vacuum-based systems, where expensive pumping equipment is required [25]. Their setups are also space-efficient and modular, making them ideal for integration into existing industrial production lines without significant modifications [26]. Since they operate under room temperature, the advantages of the plasma environment can be combined into a treatment method that does not heat or alter the treated surface. Therefore, they have already made their way into scientific fields where the treatment of sensitive surfaces is needed. Today, atmospheric pressure plasmas are already assisting modern medicine with sterilization, wound healing and cancer treatment [27–29].

However, the synthesis of nanoparticles and especially nanocrystals using atmospheric pressure plasmas can be quite challenging, due to several factors. The absence of a vacuum pump inherently increases the concentrations of impurities such as oxygen or H_2O within the systems. Additionally, atmospheric pressure plasmas with high admixtures of reactive gases can be difficult to sustain. The high voltage needed for gas breakdown can often lead to arcing, a result of the current not being limited by the external circuit. Another phenomenon in high-pressure plasmas is filamentation. This instability is caused by a positive feedback loop with a locally high electron density leading to a higher gas temperature. The gas density decreases, leading to increased electron temperatures that increase electron densities even further.

As a result, there are not many publications on the successful synthesis of silicon nanocrystals in atmospheric pressure plasmas and most of them rely on the admixture of hydrogen [30–32], or only produce amorphous silicon oxide material [33]. Publications also report on the issue of material deposition within plasma sources with high deposition rates [30] that leads to unpredictable plasma environments or the clogging of utilized plasma sources.

If understood and utilized well, atmospheric pressure setups can be tailored to produce a wide variety of nanoparticles by adjusting parameters such as gas composition, power input and the combination of precursor gases or solid source materials.

Atmospheric pressure plasmas can also facilitate the much-needed option for *in situ* analysis of the nanoparticle synthesis process, since an atmospheric setup is more easily accessible and can be connected to several measurement techniques, such as the scanning mobility particle sizer for size distribution analysis. However, common measurement techniques for low-pressure plasmas, such as probes or mass spectrometry, are difficult to deploy in atmospheric pressure systems because of the limited spatial resolution.

A two-stage atmospheric pressure plasma system can facilitate subsequent nanoparticle synthesis and surface passivation.

The goal of this work is to demonstrate the potential of atmospheric pressure plasmas for

nanoparticle synthesis, with a focus on understanding the underlying mechanisms of nanoparticle formation, controlling particle properties and optimizing the plasma parameters to achieve certain material characteristics. In this thesis, first the different types of nanoparticles (semiconductor, metal and multielemental) with their specific properties, applications and common synthesis methods are introduced in chapter 2. Since the chosen synthesis method in this thesis involved the use of atmospheric plasma, this chapter will also give an overview of the plasma fundamentals. Additionally, the most common type of atmospheric plasma source, the atmospheric pressure plasma jet, will be explained in greater detail. Combining those fundamentals, the synthesis process by means of atmospheric plasma jets will be explained for both gas phase synthesis and the synthesis using a solid source material. Chapter 3 gives an overview of all diagnostics that were used in this thesis to investigate synthesized nanoparticles. This includes the scanning mobility particle sizer (SMPS) for information on the particle size, transmission electron microscopy methods (TEM) to investigate the particle morphology, chemical composition analysis using Fourier transform infrared spectroscopyant (FTIR) and finally photoluminescence spectroscopy. The design of the chosen plasma source as well as the specially designed setups that can be used in combination with the atmospheric plasma sources are highlighted in chapter 4. All findings and results, also in the form of peer-reviewed publications, are found in the chapters 5 to 8. Chapter 9 then summarizes the findings of this thesis and includes some prospects and ideas for future work.

2 | Fundamentals

Within the framework of this thesis, nanoparticles (NPs) of different elemental compositions have been synthesized using different synthesis methods. Synthesized NPs included semiconductor (silicon), metal (tungsten) and multielemental NPs, such as Janus NPs and core-shell NPs. This chapter will first present NP properties in general and then specific properties for each type of NP that was synthesized in this thesis. Common synthesis methods and possible applications are introduced. In addition, the importance of surface passivation and functionalization is highlighted.
In the next section, an introduction to plasma properties and plasma generation is given, since the scope of this thesis was to synthesize NPs using atmospheric pressure plasmas. This general overview on plasmas is followed by a more detailed description of atmospheric pressure plasma jets, the type of plasma source that was utilized in this thesis.
In the last section, plasma-assisted NP synthesis is highlighted for both the synthesis method from a source material in solid form and the gas phase synthesis using a precursor gas. Here, the important phenomenon of selective heating is explained in detail.

2.1 Nanoparticles

Nanoparticles are structures characterized by diameters of 1 to 100 nanometers [34, 35]. They can come in different shapes [36], but for this thesis the term will be used to describe mainly spherical NPs. The small size of NPs drives physical and chemical properties that are inherently different from those of the microparticles or the bulk material. Over the last decades, research into NPs has expanded and spread from material science to various other scientific fields. The research effort is driven by the extraordinary properties of NPs that stem from their high surface area-to-volume ratio, quantum confinement effects and surface/interface phenomena, which make them highly versatile and adaptable for many applications.
Quantum dots, for instance, are semiconductor NPs subjected to quantum confinement effects [37] which enable precise control over their optical and electrical properties, making them suitable for applications in technical environments such as displays [38], solar cells [39, 40], and biological imaging [41]. Similarly, metal NPs exhibit a phenomenon called localized surface plasmon resonance (LSPR), making them NP antennas, which drives applications in the areas of enhanced spectroscopy methods [42].
The NP properties have to be understood to be able to tailor them for their specific intended applications.

2.1.1 Properties

NP properties can differ based on their elemental composition and structure. One of the key properties that all NPs have in common is their increased surface-to-volume ratio compared to their bulk counterparts. To explain this characteristic in more detail, silicon NPs are taken as an example, but these considerations are similar for all NPs.

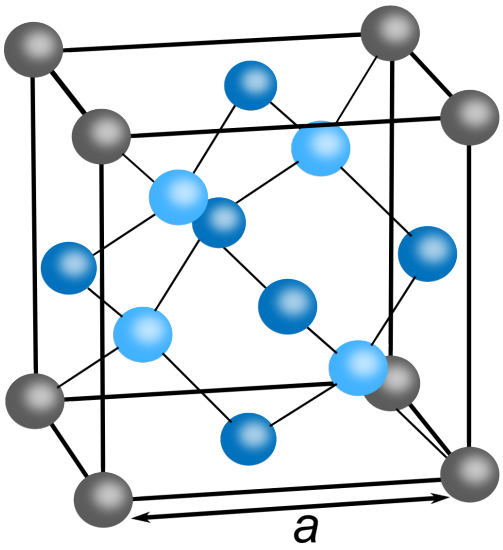

Figure 2.1: Crystallographic structure of silicon for a face centered cubic (fcc) structure. The inter-atomic distance is $a = 0.543\,\mathrm{nm}$.

Silicon most commonly appears in diamond cubic crystal structure. The diamond structure can be described as an fcc lattice with a basis containing two identical atoms positioned at each lattice point. In other words, the diamond cubic lattice can be thought of as two overlapping face-centered cubic (fcc) lattices displaced by one quarter of the body diagonal. The unit cell is shown in Figure 2.1. The lattice constant for silicon is $a = 5.43\,\text{Å}$, which represents the distance to the nearest neighbor corner atoms of the cube in Figure 2.1. The unit cell contains four atoms fully enclosed within the unit cell volume (light blue), eight atoms at the corners of the cube (gray), each contributing one eighth of an atom to the unit cell, and six atoms centered on the cube faces (blue), each contributing half of an atom to the cell. This adds up to a total number n_c of 8 atoms inside this cube.
To estimate the ratio of atoms located on the surface of an NP to the total number of atoms in the particle, the NP is assumed to be spherical with a diameter of r. The presence of facets is neglected. The NP can be visualized as being composed of small cubic cells with a side length of a. The total number of atoms N_v in the NP can then be estimated by calculating the total volume of the particle V_p and dividing it by the volume of one cubic cell, multiplied by the number n_c of atoms per cell:

$$N_\mathrm{v} = n_\mathrm{c} \cdot \frac{V_\mathrm{p}}{a^3} = n_\mathrm{c} \cdot \frac{4}{3}\pi \cdot \frac{r^3}{a^3}\,. \tag{2.1}$$

To estimate the number of atoms located on the NP's surface, a surface layer with a thickness of a is assumed. This implies that all atoms located within unit cells at the NP's surface are considered as surface atoms. Although some of these atoms may be located slightly below the geometrical surface (e.g. a few fractions of a nanometer inside the particle), this assumption is reasonable because of potential surface reconstructions and the fact that interactions with surface atoms often extend beyond the outermost atomic layer. For this calculation, the volume of the surface layer V_s is defined as

$$V_\mathrm{s} = V_\mathrm{p} - V_\mathrm{i}\,, \tag{2.2}$$

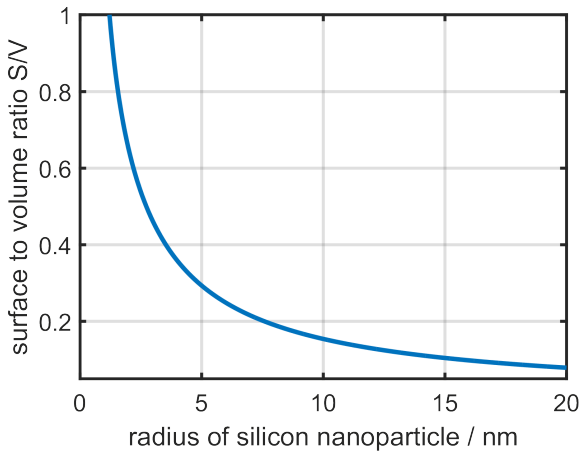

Figure 2.2: Surface to volume ratio S/V for a silicon NP based on calculations.

where V_i is the volume of the inner part of the NP. V_i corresponds to the volume of an NP with a reduced diameter $r_\mathrm{i} = r - a$. Then the number of surface atoms N_s in this surface layer is

$$\begin{aligned} N_\mathrm{s} &= n_\mathrm{c} \cdot \frac{V_\mathrm{p} - V_\mathrm{i}}{a^3} \\ &= n_\mathrm{c} \cdot \left[\frac{4}{3}\pi \cdot \frac{r^3}{a^3} - \frac{4}{3}\pi \cdot \frac{(r-a)^3}{a^3} \right] \\ &= n_\mathrm{c} \cdot \frac{4}{3}\pi \cdot \frac{3r^2a - 3ra^2 + a^3}{a^3} \,. \end{aligned} \tag{2.3}$$

The surface-to-volume ratio S/V can be thus calculated as a ratio of number of surface atoms N_s to all atoms in the NP N_v:

$$\begin{aligned} \frac{S}{V} = \frac{N_\mathrm{s}}{N_\mathrm{v}} &= \frac{3r^2a - 3ra^2 + a^3}{r^3} \\ &= \frac{3a}{r} - \frac{3a^2}{r^2} + \frac{3a^3}{r^3} \,. \end{aligned} \tag{2.4}$$

This equation is plotted in Figure 2.2 and shows the increasing number of surface atoms in relation to all atoms with decreasing NP size.

Properties of Semiconductor Nanoparticles

Apart from the high surface-to-volume ratio, which is characteristic for all NPs, semiconductor NPs such as silicon are recognized for a specific set of properties related to quantum confinement and the size dependence of the band gap.
The behavior of semiconductor nanostructures can be understood by looking at the energy band structure. In isolated single atoms, electrons occupy specific energy levels or orbitals around the nucleus. These energy levels are discrete, corresponding to quantized amounts of energy. However, when atoms approach one another, their atomic orbitals overlap and

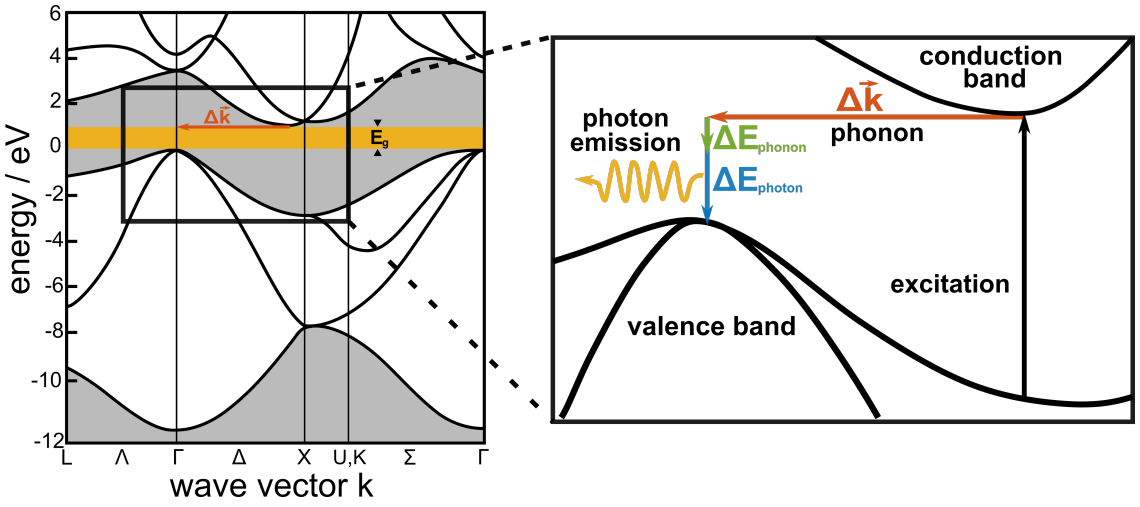

Figure 2.3: Band structure of bulk silicon determined using an energy-dependent nonlocal-pseudopotential calculation on the left. The band structure shows the presence of an indirect band gap with energy E_g. Schematic sketch of a radiative recombination process assisted by a phonon. Band structure adapted from [43].

the outer electron energy levels split due to interactions between the atoms. This splitting creates new, closely spaced energy levels, forming what are known as molecular orbitals or, in the case of solids, energy bands. In a solid, the large number of interacting atoms causes these energy levels to merge into broad, quasi-continuous bands, accommodating all electrons without violating the Pauli exclusion principle. The valence band is then the highest energy band fully occupied by electrons, while the conduction band is the next higher band, which may be partially filled or empty. The energy band gap between these bands is large for insulators and non-existing for metals. Semiconductors have a smaller band gap, allowing for limited electron flow at room temperature. At absolute zero ($T = 0\,°\mathrm{K}$) there is no thermal excitation and all electrons occupy the valence band. With increased temperature, electrons gain thermal energy, and statistic processes also allow electrons to be found in the conduction band. In bulk silicon, the position of the minimum of the conduction band is not found at the same wave vector position as the maximum of the valence band.
This is called an *indirect* band gap and can be found for group IV semiconductors (Si, Ge, α-Sn) [44] and also for some of the compound semiconductors such as GaP or AlSb [45]. Figure 2.3 shows the band structure of bulk silicon and its indirect band gap with the energy $E_g = 1.1\,\mathrm{eV}$.
The indirect band gap results in the fact that an optical transition of an electron from the conduction band to a hole in the valence band is only possible when a phonon participates in the process to satisfy the law of momentum conversation [46]. The emission or absorption of a phonon will shift the momentum in the direction of Δk, making the transition possible but much less likely, since this process has a very low collision rate. This makes the radiative recombination slower (e.g. with longer radiative lifetimes) and less probable in comparison with non-radiative processes in indirect band gap semiconductors that do not require a third particle (phonon). Therefore, bulk silicon shows only weak luminescence. In general, the luminescence is often the desired feature of NPs as it offers many applications in optics and opto-electronics.

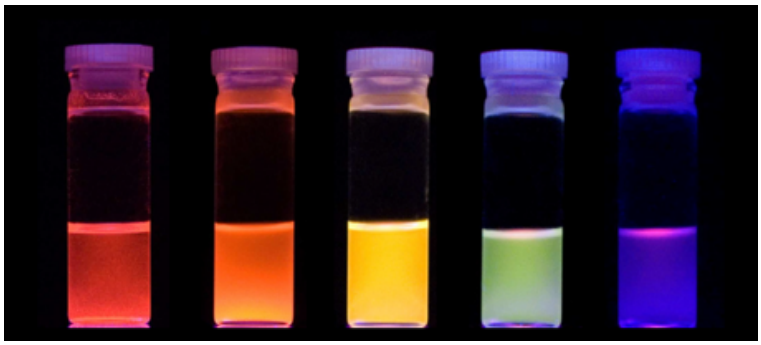

Figure 2.4: Photographs of deep red (740 nm), orange (675 nm), yellow (592 nm) and blue (441 nm) light emission from Si-NCs after excitation by a UV lamp (365 nm). Image adapted and reprinted with permission from [47].

When semiconductor NPs reach a radius close to or below the exciton Bohr radius, quantum confinement starts to play a role. Semiconductor NPs with diameters below the exciton Bohr radius are called *quantum dots* (QDs). The confinement of electrons in nanoscale semiconductor materials is similar to the confinement in the three-dimensional particle-in-a-box model, where the quantum mechanically allowed energy levels in the box are changing from a continuous distribution to a discrete one. As a result of the strong confinement in all three dimensions, QDs carry properties between bulk semiconductors and discrete atoms. Their properties change as functions of size and shape.
The most visible feature of silicon quantum dots that depends on their size is photoluminescence. When taking one more look at the band structure of silicon, electrons in the valence band can be exited by photons, electrons or ions, bringing them to higher electronic states. This process is possible if the energy transferred by the excitation source is sufficient to surpass the energy gap. If the source of the excitation was a photon, the relaxation process is called photoluminescence (PL). When the excited electron relaxes into the valence band, a photon is emitted, with a wavelength depending on the size of the energy gap $E_g = h\nu$. Since the size of the QD determines the size of the energy gap, the wavelength of the PL is strongly connected to the size of the quantum dots. This can lead to a very colorful variety in the emission spectrum of silicon nanocrystals, as shown in Figure 2.4. Larger silicon QDs ($5-6$ nm) emit longer wavelengths in orange or red, while smaller silicon QDs ($2-3$ nm) emit shorter wavelengths in the blue and green spectral region. The recombination process can be influenced not only by the band gap structure, quantum confinement and factors affecting the presence of phonons but also by material properties such as the quality of the material and the presence of defects. Impurities, unsaturated dangling bonds and adsorbed atoms on the surface, as well as crystallographic defects, grain boundaries and the presence of surfaces in general, introduce a wide variety of defects. Regardless of the choice of the synthesis process for silicon NPs, defects can be found inside the NPs, in the matrix that embeds them and/or at the interface between the NP and matrix. Defects often introduce energy levels within the energy band gap, leading to electron and hole trapping. This can result in non-radiative but also in different radiative recombinations localized at defect sites. Some defects can be passivated, for example by binding hydrogen to them, thereby preventing their influence on excited electrons. In other cases, the presence of defects may actually be desirable to achieve the desired luminescence.

Surface passivation, if applied, not only affects the defects on the surface but can also have a direct impact on the entire NP and its band structure. As it has already been stated, the band gap is 1.1 eV for bulk silicon, and can be found to increase up to 2.2 eV for H-terminated silicon NPs [48–50]. A closer look on the effect of surface passivation and functionalization for all types of NPs will be given later in this chapter, but this demonstrates again how strongly the properties of NPs are linked to their surface. Therefore, an optimal synthesis process also needs to be able to tailor the surface properties.

Properties of Metal NPs

The definition of metal differs between the different scientific fields. Using the physical definition, a metal is an element that is capable of conducting electricity at a temperature of absolute zero. Extending the story of energy band diagrams from the previous subchapter, in case of metal, the last occupied energy band is not completely filled with electrons, allowing electrons to flow freely. The highest occupied energy level at $T = 0\,\mathrm{K}$ is named *Fermi level*. There are many metal properties that are sought in their applications and which can be enhanced or altered when approaching nanometer dimensions. An important argument for the deployment of metal NPs is the same or increased effectiveness of surface-related properties while the amount of utilized material is drastically lowered. This reduces the cost, which is especially important for certain expensive or rare metals. The quantum confinement in the case of very small metal NPs alters the band structure in the same way as for semiconductor NPs and can also lead to tunable light emission.
Many applications are based on common properties of metals, such as plasmon resonance, chemical reactivity and catalytic activity, electrical conductivity, magnetic behavior and toxicity. Those properties are often strongly altered in case of NPs. The so-called localized surface plasmon resonance (LSPR) affects absorption, scattering and the color of metal NPs. LSPR arises from the excitation of electromagnetic surface modes, which are also called localized surface plasmons (LSPs) [51]. These modes represent the resonant oscillations of the surface charge density at the boundaries of the metal NP. In contrast to surface modes that can propagate along metal-dielectric interfaces, LSPs are stationary oscillations along the metal boundaries of the metal NP. When metal NPs are exposed to incident light, the free electrons on the surface oscillate coherently in response to the electric field of the light. This optical response of the localized oscillation can be described through the particle polarizability α that connects the strength of the incoming electric field $\vec{E}_0$ with the electric dipole moment:

$$\vec{p} = \alpha \vec{E}_0 \,. \tag{2.5}$$

It is a frequency dependent value that depends on the dielectric function of the metal, on the surrounding medium and most importantly on the particle geometry. For small NPs made from noble metals, the LSPR is typically in the visible range of the spectrum, making it responsible for the intense colors exhibited by metal NPs, such as the red color of gold NPs or the bright yellow of silver NPs [11]. The LSPR frequency can be tuned by varying the NP size and shape, making metal NP optical antennas that effectively convert electromagnetic radiation from the far field to the near field and vice versa [52]. A spherical metallic NP can be considered the simplest optical antenna. Scientific research in the dipolar surface plasmon of NPs is driven by two main interests. First, the electromagnetic near field of the plasmon excitation is strongly localized to the nanometer scale, allowing for an effective reduction

of the electromagnetic field oscillations to sub-wavelength dimensions. Second, the LSPR can increase the local fields around the particles ranging from 5-500 times enhancement in amplitude. This affect is used in many of the possible applications of NPs, such as field-enhanced spectroscopy or medical applications, which will be discussed later.
Some metal NPs, particularly iron, cobalt and nickel, exhibit magnetic properties and those magnetic properties are also strongly size-dependent. These NPs can be superparamagnetic, meaning that they are magnetically responsive in the presence of an external magnetic field but do not retain magnetization once the field is removed. The magnetization per atom and the magnetic anisotropy of NPs have been shown to be much greater than those of their bulk counterparts [53].

Properties of Janus particles

Janus particles are a special subgroup of multielemental NPs. Their name originates from the two-faced Greek god and was first mentioned in a scientific context by Casagrande *et al.* in 1989 [54]. Here, they presented spherical glass particles in the range of 50 to 90 micrometers, where one hemisphere was hydrophilic and the other was hydrophobic. Janus particles are distinguished from core-shell particles by the fact that two or more elements must be present on the surface of the particle. In other words, the surface has to have at least two or more distinct physical properties. This unique surface structure enables different types of chemistry to occur on the same particle. The properties of Janus particles are highly dependent on the materials they consist of. Janus particles can consist of two materials with opposing properties. In addition to the already mentioned amphiphilic properties [55, 56], the two surface materials can also exhibit different fluorescent [57, 58] or magnetic [59] properties. The most simple geometry for a Janus particle is a spherical particle combined of two different elements, where each hemisphere consists of a different element. More complex morphologies include the shapes of dumbbells [60, 61], snowmen [62–64] rods [65, 66] or disks [67, 68].

2.1.2 Common synthesis methods

Countless works have been published in regard to finding a stable way for the synthesis of well defined and monodisperse NPs with controllable size and optical properties. Here, the reproducibility of the synthesis process and the cost and efficiency are important factors. In general, synthesis methods for NPs can be categorized into two classes:

- bulk reduction methods (top-down)
- assembly methods (bottom-up)

One of the most popular reduction methods is the electrochemical etching of silicon wafers. Starting with a p-type silicon wafer, porous silicon (and later from this silicon nanowires or NPs) can be achieved using electro-chemical etching. This method was first presented in 1999 by Wolking *et al.*, where hydrofluoric acid was used [48]. The resulting porous silicon could then be scraped off and the product in the form of a powder contained nanocrystals with diameters as low as 3 nm. Silicon NPs produced with this method were also the first ones to have a reported room temperature PL. The degree of porosity and consequently the size of the silicon NPs can be tuned via changing the concentration of hydrofluoric acid and electric current. This method is also very time consuming and requires both a voltage generator

and a halogen lamp. Additionally, the production yield is limited and the photoluminescence of the produced samples was achieved only by strict avoidance of exposure to air, which is always a challenge in wet-chemical approaches.
Another top-down approach, which is commonly used for NP synthesis, is laser ablation. In the case of silicon, NPs are synthesized by removing material from a monocrystalline silicon wafer using short and intense laser pulses [69]. For this, the wafer is placed in a stylene solution or water and then exposed to the laser, causing miniature explosions of the material that expands into the solution. The created NPs remain solved within the solution after the ablation process [70]. They then have to be extracted from the dispersion using centrifugation, which is an inherent downside of this and other wet processes, as the particles are not directly available after the synthesis process. However, with synthesis rates approaching grams per hour [71], it is a competitive method, even though the purchase and maintenance of a laser is very cost-intensive. The method of laser ablation has also been used in the synthesis of metal particles as early as 1998 [72], where gold, silver and even permalloy particles could be synthesized using laser ablation. This method for NP production has been improved and is now considered ecological, since no stabilizing molecules or other chemicals are needed anymore [73]. Another method that does not require chemicals is ball milling, which is a very inexpensive top-down approach, where usually a high purity metal powder [74] or silicon oxide powders [75] are finely ground into NPs.
In contrast to those bulk reduction methods, the assembly methods (bottom-up) use mostly chemical routes. Using the rapid chemical expansion of supercritical fluids, the group around Korgel *et al.* used the decomposition of a silicon-containing precursor in solvents that were heated and pressurized above their critical points to create silicon NPs [76]. Although this method results in very monodisperse NPs, the chemical composition is difficult to control and the resulting NPs already obtained an alkoxy-termination during the growth process [77]. The synthesis method using supercritical fluids can also be used for other semiconductor materials and metal NPs [78, 79].
The so-called colloidal synthesis is a solution-based chemical bottom-up approach. In the case of silicon, it involves mixing of several precursors and stabilizers in a certain order. Subsequent heating of the mixture is required to result in the growth of nanocrystals [80]. In the case of colloidal synthesis of metal particles, metal ions are reduced to form small metal nuclei that can then grow into large NPs [81].
Multielemental NPs such as Janus particles are most often synthesized using such bottom-up approaches. The most simple method for Janus particle generation is surface modification. Here, a part of an initially homogeneous particle is protected using some form of mask, while the unprotected part is modified [82]. Other methods to synthesize Janus particles include microfluid synthesis, where two different heated liquid monomers are brought together, forming Janus droplets that later cool down into NPs [83].
Different synthesis methods come with their own set of advantages and disadvantages, but their overall requirements are the ability to synthesize NPs with a targeted size distribution with a certain overall reproducibility. An ideal method for the synthesis of NPs would address these requirements while also producing large amounts of pure elemental NPs in a short time, using low-cost, non-hazardous precursors and starting materials. A method that could possibly fulfill these requirements is the use of an atmospheric pressure plasma, as was done in this thesis. Therefore, a detailed explanation of the NP synthesis routes using atmospheric pressure plasmas will follow in section 2.3.

Surface termination, functionalization and passivation

Depending on the type of synthesis method and the chosen conditions, NPs always obtain a certain surface termination. Such a termination can influence the properties of NPs and/or passivate them, protecting them from the environment to which they are exposed. The terms "termination", "functionalization" and "passivation" are often used interchangeably in the literature, also because certain terminations can serve as both passivation and functionalization. Termination refers to chemical species or groups directly bonded to the surface atoms of a particle, typically replacing the dangling bonds of undercoordinated surface atoms. It defines the immediate chemical identity of the surface. The most common types of surface passivation upon silicon NPs are hydrogen termination and oxygen termination. In the case of porous silicon, a hydrogen termination is already established during the synthesis process using wet chemistry [84]. However, also low-pressure plasma systems that form silicon NPs have been shown to be capable of producing H-terminated silicon NPs [85]. Here, the possibility of the use of ultra-high vacuum systems can eliminate oxygen impurities. If silicon NPs are created in low-pressure plasmas, the coverage of the NP surfaces is often obtained from the dissociated atoms of the Si-containing precursor during synthesis. The use of the precursors SiH_4 [86] and $SiCl_4$ [87, 88] was reported to lead to the formation of NPs with hydrogen and chlorine termination, respectively. Both termination types are not very stable upon being exposed to air and especially water vapor. The hydrogen-terminated surface was fully oxidized after a time of ten minutes and the chlorine termination was even less stable [88]. Although Si-H bonds are stable in air, they do not protect strained Si-Si back bonds [89] from reaction with oxygen-containing species [90].
Liquid-phase functionalization describes methods that offer stable protection of NPs from both agglomeration and oxidation. In these methods, the NPs are either directly created or dissolved in a colloidal solution, where their surface can react with the species present in the system. For example, Mangolini *et al.* have presented a way to graft several organic ligands such as octadecene, dodecence and styrene on the surfaces of plasma-generated silicon nanocrystals, which improved their photoluminescent properties with quantum yields of up to 70 % [91, 92]. This method is ideal for improving the optical properties of silicon NPs and to prevent them from agglomeration. Even after long-term storage, when particles may aggregate and separate from the solution through sedimentation, they can always be redispersed by sonication. But in the sense of scalability, this is a rather unpractical approach. In addition, most of these methods require the handling of toxic chemicals.
Overall, termination can be short-lived. To sustainably prevent oxidation, ensure stability and to improve the NP properties for their intended purposes, *surface passivation* is often used. In the scope of nanomaterial science, surface passivation describes the coating of NPs, making them *passive*, meaning that they are less likely to interact with their environment or other materials. Additionally, certain passivation can also restrict agglomeration, which is often undesirable in NP production. Passivation can occur in the form of an outer layer that is formed purposely (coating) or through exposure to ambient air (oxidation).
In the case of silicon nanocrystals, a passivation with a thin layer of silicon oxide has been shown to increase the intensity of PL [93, 94]. Silicon NPs initially show no visible photoluminescence under UV illumination but develop it over hours to days as surface oxidation presumably passivates dangling bonds that act as non-radiative recombination centers. The same behavior has been observed in this thesis, where the prepared NPs originally did not

show any significant PL signal directly after deposition but the PL signal increased after surface oxidation occurred upon exposure to ambient air. Similarly, metal NPs are often coated with oxide shells either of their own metal or other metals, to enhance for example their suitability for catalytic applications [95, 96].
Plasmas can help facilitate the passivation process, usually by combining two reactors. One reactor will be responsible for the particle synthesis and the second one for the subsequent surface passivation. For low pressure systems, this has been already demonstrated by Mangolini and Kortshagen [97]. Here, they presented a two-step plasma process at low pressure (200 Pa) in which surface functionalization was performed immediately after synthesis by plasma-assisted in-flight grafting of organic molecules in a second plasma chamber. The first reactor consisted of a quartz tube with two ring electrodes operated at 13.56 MHz and with silane as a precursor. The NPs synthesized here were led by a gas flow to a second parallel plate plasma reactor, with a gas flow passing through a bubbly containing the liquid organic precursors. Reactive radicals of organic ligands such as 1-dodecene have been formed through electron impact dissociation in the plasma, which then enabled the reaction of these ligands with the surface of the silicon nanocrystals.
A setup for the subsequent synthesis and surface passivation of NPs using atmospheric pressure plasmas will be presented in this thesis in chapter 8.

2.1.3 Applications

Considering the large amount of finely tunable surface properties, it is not surprising that NPs find applications in various scientific fields. They can be roughly separated into five main categories, as shown below.

Medicine and biotechnology

In the scientific field of medicine and biotechnology, gold, silver and iron oxide particles are mostly studied. One of the most prominent applications, popularized by the spread of diseases such as SARS-CoV-2, are the antimicrobial properties of silver NPs. They are effective against a wide range of bacteria and are used in wound dressings, medical device coatings, and as components in antimicrobial textiles such as face masks [98, 99]. Mesoporous silicon NPs [100] and functionalized metal NPs [101] have been used as drug carriers to target specific cells or tissues. Similarly, NPs of gold, silver and iron oxide can be used in targeted drug delivery systems to improve the effectiveness of chemotherapy drugs while minimizing their side effects [102]. Both metal (gold and silver) as well as silicon NPs are used in diagnostic techniques such as biosensing and medical imaging. Gold NPs improve contrast in medical imaging techniques, allowing the detection of diseases in the early stages [103]. Superparamagnetic iron oxide NPs (SPIONs) are used as contrast agents in magnetic resonance imaging (MRI), improving image quality for better diagnosis of diseases such as tumors or cardiovascular problems [104]. Janus particles also find applications in biomedical environments. For example, polymer-polymer Janus particles have been tested for their ability to encapsulate two different drugs in each compartment of a spherical particle, where the different hemispheres exhibit different degradability for different pH values, enabling sequential drug release under varying conditions [105].

Catalysis

Various metals are widely used for their catalytic properties. In real applications, the stability and non-toxicity offered by noble metals, such as gold, are particularly important. Nevertheless, gold was long time considered a poor catalyst, with theoretical calculation even highlighting its noble behavior on the example of hydrogen dissociation at the surface of gold [106]. However, this changes when gold NPs are used [107, 108]. The high surface-to-volume ratios as well as the presence of steps, edges and corner sites on gold NPs [107] make them ideal for catalysis, since more surface atoms are available for the interaction with reactants. Gold NPs show, for example, high catalytic activity for CO oxidation at temperatures as low as 200 K [109] or enhanced photocatalytic degradation of various organic pollutants [110].
Apart from gold, mainly NPs of other noble metals such as platinum and palladium are used for heterogeneous catalysis [111]. Platinum NPs are commonly used in automotive catalytic converters to convert harmful gases such as carbon monoxide and nitrogen oxides [112, 113]. They can also function as catalysts in hydrogen membrane fuel cells, where they enhance the efficiency of oxygen reduction at the cathode [114, 115]. Metal oxide NPs such as TiO_2 and ZnO are effective photocatalysts that use sunlight to drive chemical reactions. They have been shown to increase the reactions of water splitting for hydrogen production [116] or the degradation of organic contaminants in water [117].

Energy Harvesting and Storage

NPs can enhance light absorption and charge separation in solar cells. Quantum dots [39, 40], perovskite NPs [118, 119] and plasmonic NPs [120, 121] have already been integrated into solar cells to increase their overall efficiency. They can absorb different parts of the solar spectrum and help reduce energy losses, making solar cells more efficient and cost-effective. Another research topic that is focused on sustainability is the development of thermoelectric materials that can directly and reversibly convert heat into electric energy. Here, the nanostructuring provided by NPs reduces the thermal conductivity while maintaining the electrical conductivity. Therefore, NPs have been proven to enhance this thermoelectric effect, reducing the losses in the waste heat of commercial energy consumption [122, 123]. In lithium-ion batteries, silicon or Fe_3O_4 NPs acting as anode materials can enhance parameters such as energy density, charging rates and lifespan [124, 125]. Nickel oxide NPs used as electrode material increase the performance of supercapacitors and electrochromic devices, enabling them to achieve higher energy densities than traditional capacitors while retaining fast charge and discharge capabilities [126, 127]. Metal hydride NPs can absorb and release hydrogen more efficiently, making them suitable for portable and renewable hydrogen-based energy storage systems [128, 129].

Optics and opto-electronics

As already discussed, metal NPs exhibit optical properties due to LSPR, which occurs when conduction electrons on the NP surface oscillate in response to incident light. An important application in this field of plasmonics is the development of substrates that can amplify the Raman scattering signal of molecules placed near their surface [130]. This effect is called surface-enhanced Raman scattering (SERS) and has been studied already since 1985 [131]. Surface-enhanced spectroscopy enables ultrasensitive detection of even single molecules [132].

Arrays of metallic NPs can enhance not only Raman scattering but also infrared absorption [133]. Metal NPs can also guide light by creating highly confined electromagnetic fields. In 2003, Maier *et al.* published on plasmonic waveguides based on a chain of NPs, which allow the transfer of optical signals in a lateral mode confinement below the diffraction limit of light [134, 135]. This can not be achieved using conventional waveguides or photonic crystals. In a similar manner, the so-called plasmonic lenses made from a curved chain of metal NPs can focus light below the diffraction limit of conventional optics [136].
When a small voltage is applied, the optical properties of a NP assembly can be modulated, effectively controlling the light transmission. This fast switching capability is essential for high-speed optical communication where data is transmitted by modulating light signals in the field of ultra-fast all-optical switching [137] which can be used in optical computing and in fiber-optic based communication networks. Here, mainly silver NPs [138] and ZnO NPs [139] can be used. Light-emitting diodes (LEDs) based on silicon nanocrystals [140] or silicon QDs [7] can be tailored for specific emission colors by using monodisperse, size-separated NPs.

Detection and Sensors

The surface plasmon resonance of metal NPs is often used to detect small changes in the local refractive index, enabling highly sensitive detection of biomolecules, toxins or environmental pollutants. The aggregation of NPs leads to a visible color change, which can indicate the presence of specific molecules. Gold NPs, for example, are used in biosensors to detect specific biomolecules. In the context of environmental monitoring, Wang *et al.* have shown that gold NP-based sensors can be used to detect toxins, inorganic and organic pollutants and heavy metals in water with high sensitivity [141]. Glucose sensors equipped with different metal NPs can be used to non-invasively monitor blood sugar levels in diabetes patients [142, 143]. Since hydrogen-based storage systems as sustainable energy carriers are becoming more and more common, sensors are needed that detect leaks in hydrogen fuel lines. Here, palladium NPs are often used due to their high affinity for hydrogen molecules [144–146].

2.2 Plasmas

The term plasma was first introduced by Irving Langmuir in 1928 [147]. Plasmas are often referred to as the *fourth state of matter*. Taking the phase transitions of water as an example, phase transitions from ice to water and from water to vapor occur when energy is transferred into the system. When a gas is supplied with energy, the gas atoms can become ionized. If the degree of ionization is high enough, a plasma state is reached. There are different examples of plasmas in nature; in fact, more than 99% of the visible matter in the universe is in the plasma state [148]. This includes stars but also less dense interstellar matter. Prominent examples on Earth range from simple fires such as the flame of a candle, over the lightning striking between clouds and Earth during thunderstorms to more colorful phenomena such as the *aurora borealis*, also known as northern lights [149, 150]. This section will give an overview of the basic properties necessary to describe a plasma and how to generate it. For a deeper insight, the reader is referred to text books such as [151–153].

2.2.1 Plasma properties

A plasma is an ionized gas composed of free electrons, ions and often also neutral particles, depending on its degree of ionization. The most important parameters to describe a plasma are the densities n and temperatures T of both electrons (n_e, T_e) and ions (n_i, T_i), which determine their dynamics and interactions.
Unlike in a neutral gas, where temperature is a measure of the average kinetic energy of particles, electron and ion temperatures can differ significantly in a plasma due to their different masses and energy exchange rates. Under the same conditions, electrons can reach higher energies and, therefore, higher temperatures than the heavier ions. The disparity in temperatures between electrons and ions serves as a basis for distinguishing between *thermal* and *non-thermal* plasmas.
Thermal plasmas are typically *high-temperature* plasmas in which electrons and ions are in thermal equilibrium ($T_\mathrm{e} \approx T_\mathrm{i}$), or close to it. An example are fusion plasmas, where temperatures of the species can reach over 100 million Kelvin ($T_\mathrm{e/i} \sim 10\,\mathrm{keV}$) [154].
Non-thermal plasmas, on the other hand, are often *low-temperature* plasmas, where the electron temperature is increased, while ions and bulk gas remain relatively cool $T_\mathrm{e} \gg T_\mathrm{i} \simeq T_\mathrm{gas}$. These plasmas are often used in industrial applications such as semiconductor processing and surface treatment, where typical electron temperatures range from 1 to 10 eV [155], while the ion and gas temperatures stay close to room temperature. Despite the low degree of ionization, these plasmas still carry enough energy in the electrons to initiate chemical reactions.
An important characteristic of a plasma is often referred to as the *collective behavior*. The collective behavior is a result of the Coulomb forces for electrostatic interaction between particles which scale with $\propto r^{-2}$ compared to $\propto r^{-6}$ for the Van der Waals forces in neutral gases. If, for example, a point-like negative space charge Q_s is introduced into the plasma, a positive space charge zone of the same magnitude is formed around it, shielding the charge from its surroundings. This shielding is known as Debye shielding. The space charge problem can be solved using the Poisson equation:

$$\Delta\Phi = -\frac{1}{\varepsilon_0}\left[Q_\mathrm{s}\delta(\vec{r}) - en_\mathrm{e}(\vec{r}) + en_\mathrm{i}(\vec{r})\right] , \tag{2.6}$$

where Φ describes the electrostatic potential, ε_0 the electric field constant in vacuum, δ the delta function and $n_\mathrm{i}(\vec{r})$ and $n_\mathrm{e}(\vec{r})$ describe the local electron and ion densities around the charge Q_s. For a small perturbation ($e|\Phi| \ll k_\mathrm{B}T$) the approach from Debye and Hückel [156] results in the potential:

$$\Phi(r) = \frac{Q_\mathrm{S}}{4\pi\varepsilon_0 r}\exp(-r^2/\lambda_\mathrm{D})\,, \tag{2.7}$$

with the electric field constant ε_0 and the distance to the space charge r. The so-called *Debye length* λ_D describes the combined shielding action of electrons and ions. It consists of the individual electron Debye length λ_De and ion Debye length λ_Di:

$$\lambda_\mathrm{D} = (\lambda_\mathrm{De}^{-2} + \lambda_\mathrm{Di}^{-2})^{-1/2}\,, \tag{2.8}$$

which can be expressed using the temperatures and densities of those species:

$$\lambda_\mathrm{De} = \left(\frac{\varepsilon_0 k_\mathrm{B} T_\mathrm{e}}{n_\mathrm{e0} e^2}\right)^{\frac{1}{2}} \quad , \quad \lambda_\mathrm{Di} = \left(\frac{\varepsilon_0 k_\mathrm{B} T_\mathrm{i}}{n_\mathrm{i0} e^2}\right)^{\frac{1}{2}}\,. \tag{2.9}$$

For an increased density of the shielding particles, the shielding is more efficient and the disturbed volume will be smaller. At the same time, with an increase in temperature, the shielding becomes less efficient. Using the Debye length, a sphere with radius λ_D can be defined, outside of which only $1/e$ of the initial space charge potential is present. Debye shielding can only be effective, if the number of charged particles N_D inside the sphere is sufficient:

$$N_\mathrm{D} = n_\mathrm{e}\frac{4}{3}\pi\lambda_\mathrm{D} \gg 1\,. \tag{2.10}$$

Outside of this sphere, the plasma is considered to be quasi-neutral, meaning that the overall number of q_k times positively charged ions of density $n_{\mathrm{i}k}$ is similar to the charges e on electrons with density n_e:

$$-en_\mathrm{e} + \sum_k q_k n_{\mathrm{i}k} \approx 0\,. \tag{2.11}$$

The sum contains all variously charged ions of both positive and negative charge.
A second important aspect of the collective behavior that a plasma exhibits, is the time scale on which information, such as the presence of a point charge, is propagated. Assuming again a small perturbation, the average velocity of an electron is not significantly affected by the potential and can be still considered to be its thermal velocity:

$$v_\mathrm{th,e} = \sqrt{k_\mathrm{B}T_\mathrm{e}/m_\mathrm{e}}\,. \tag{2.12}$$

The typical response time τ is given by the time needed for an electron to travel the corresponding Debye lengths $\tau = \lambda_\mathrm{De}/v_\mathrm{th,e}$. A similar consideration can be applied for ions analogously. In the field of plasma physics, the reciprocal of these responses are more commonly used, which are the *plasma frequencies*:

$$\omega_\mathrm{p,e} = \frac{v_\mathrm{th,e}}{\lambda_\mathrm{De}} = \sqrt{\frac{n_\mathrm{e}e^2}{\varepsilon_0 m_\mathrm{e}}} \quad \text{and} \quad \omega_\mathrm{p,i} = \frac{v_\mathrm{th,i}}{\lambda_\mathrm{Di}} = \sqrt{\frac{n_\mathrm{i}e^2}{\varepsilon_0 m_\mathrm{i}}}\,. \tag{2.13}$$

Those plasma frequencies differ greatly for ions and electrons. To fulfill the criterion of collective behavior, the motion of both electrons and ions has to be dominated by electromagnetic forces, rather than by collisions:

$$\omega_{\mathrm{p}} \Delta t > 1 \,, \tag{2.14}$$

with Δt describing the average time between collisions.
While the atmospheric pressure plasmas utilized in this thesis fulfill the criteria of *quasi-neutrality* (eq. 2.11) and *collective behavior* (eq. 2.10) in regard to Debye-shielding, it has to be noted that the collision rate in atmospheric plasmas is significantly increased, due to high particle densities. Electron-neutral collision frequencies in atmospheric pressure plasmas are typically in the order of THz ($10^{12}\mathrm{s}^{-1}$) [157]. Atmospheric plasmas are driven by DC to microwave frequency, which is many orders of magnitude below the collision frequency. Under such conditions, electrons collide with neutral gas atoms or molecules during every oscillation of their motion. These collisions cause the electrons to lose energy while exciting and ionizing the gas atoms, creating more plasma species. In radio-frequency (RF) driven plasmas, typically operated at 13.56 MHz, electrons are able to follow the external excitation and, through frequent collisions with neutrals, sustain the ionization processes. In contrast, ions, being much heavier than electrons, do not follow the oscillations of the electromagnetic field and mainly drift under the influence of time-averaged electric fields. Together, these mechanisms support successful plasma generation.

2.2.2 Plasma generation

In a laboratory environment, there are several ways how to generate a plasma. All of them transfer energy into a gas. To understand the physics behind the plasma generation, a textbook example of a DC discharge can demonstrate the processes that happen in an RF plasma. For this model, a parallel plate reactor consisting of cathode and electrode separated by a distance d is assumed. The inter-electrode volume is filled with the noble gas argon. There are typically few low-energy electrons already present inside the volume that are generated due to cosmic radiation. These electrons can be accelerated by an electric field E_0, their velocity v obtained after a certain time t can be described using the equation:

$$v(t) = \frac{eE_0}{m_{\mathrm{e}}} t \,, \tag{2.15}$$

and subsequently, their kinetic energy will be:

$$E_{\mathrm{kin,e}} = \frac{1}{2} m_{\mathrm{e}} v^2 = \frac{(eE_0)^2}{2m_{\mathrm{e}}} t^2 \,. \tag{2.16}$$

Using this, the time t_{ion} that is required until an electron reaches a kinetic energy high enough to ionize an argon atom is given by:

$$t_{\mathrm{ion}} = \frac{\sqrt{2 m_{\mathrm{e}} E_{\mathrm{ion}}}}{eE_0} \,, \tag{2.17}$$

using the ionization energy of the gas atom E_{ion}, which can be for example 15.76 eV for the first ionization energy of argon. This time t_{ion} is connected to the distance λ_{ion} an electron needs to travel until it reaches E_{ion}:

$$\lambda_{\mathrm{ion}} = \frac{E_{\mathrm{ion}}}{eE_0} \,. \tag{2.18}$$

If the mean free path λ_{mfp} is smaller than λ_{ion}, the electron will most probably collide with another atom before reaching the energy that is sufficient for ionization to take place. For a given neutral gas density n_{n} and the cross section of elastic collisions of electrons with neutral argon atoms σ_0, the mean free path can be calculated using:

$$\lambda_{\mathrm{mfp}} = \frac{1}{n_{\mathrm{n}}\sigma_0}\,. \tag{2.19}$$

At room temperature and atmospheric pressure, this results in a mean free path in the range of $\lambda_{\mathrm{mfp}} = 75\,\mathrm{nm}$ for argon [158]. If an electron reaches the energy needed after passing through the mean free path for ionization λ_{ion} and hits another atom, the ionization process generates an ion and a new electron that is now also following the electric field, creating an electron avalanche. Some of the electrons in excited atoms will fall back into the ground state, emitting a photon of the corresponding wavelength, resulting in the typical violet argon plasma light. The process of this electron avalanche can be described statistically. The number $\mathrm{d}n_{\mathrm{e}}$ of newly generated electrons in an interval $\mathrm{d}z$ is

$$\mathrm{d}n_{\mathrm{e}} = \alpha n_{\mathrm{e}}\mathrm{d}z\,, \tag{2.20}$$

with the gas multiplication factor $\alpha = \lambda_{\mathrm{ion}}^{-1}$ introduced by Townsend [159]. This leads to exponential growth of the number of electrons $n_{\mathrm{e}}(z) = n_{\mathrm{e}}(0)\mathrm{e}^{\alpha z}$. In a coordinate system where $z = 0$ marks the cathode and $z = d$ marks the anode, the electron flux at the anode can be described using

$$\Gamma_{\mathrm{e}}(d) = n_{\mathrm{e}}(d)\mu_{\mathrm{e}}E\,, \tag{2.21}$$

with the electron mobility μ_{e}. Since an equal amount of electrons and ions is generated in the avalanche process, the ion flux at the cathode is given by $\Gamma_{\mathrm{i}} = -\Gamma_{\mathrm{e}}(d) + \Gamma_{\mathrm{e}}(0)$. Therefore,

$$\Gamma_{\mathrm{i}}(0) = \Gamma_{\mathrm{e}}(0)\left(\mathrm{e}^{\alpha d} - 1\right)\,. \tag{2.22}$$

Given by the ratio of emitted electron flux to incoming ion flux, a coefficient γ can be used to describe the probability to release a secondary electron from the cathode during ion impact:

$$\gamma = \left|\frac{\Gamma_{\mathrm{e}}(0)}{\Gamma_{\mathrm{i}}(0)}\right|\,. \tag{2.23}$$

A gas breakdown occurs, when the number of newly generated electrons is higher than the losses from processes such as recombination and collisions with the chamber walls and the avalanche process can maintain itself. This state is described by the balance equation:

$$\gamma\left(\mathrm{e}^{\alpha d} - 1\right) = 1\,. \tag{2.24}$$

An empirical law to describe α depending on the electric field E was derived by Townsend

$$\frac{\alpha}{p} = A \cdot \exp\left(-\frac{B}{E/p}\right)\,, \tag{2.25}$$

where A and B are gas-specific constants [159]. Combining equations 2.24 and 2.25 and defining the breakdown voltage $U_{\mathrm{bd}} = E_{\mathrm{bd}}d$ yields the Paschen's law

$$U = pd\frac{B}{\ln(pd \cdot A) - \ln(1 + \gamma^{-1})}\,, \tag{2.26}$$

which was derived by Friedrich Paschen in 1889 [160]. Figure 2.5 shows the Paschen curves for different gases for a value of $\gamma = 10^{-1}$. All of these curves exhibit a pronounced minimum. Left of this minimum, there are not enough atoms for the ionization of the gas used. On the right side of the minimum, the energy gained over the mean free path is not enough to maintain the electron energy that is needed for ionization. Both effects would need to be compensated for by using a higher electric field, leading to a higher breakdown voltage. It has to be noted that these curves are describing the gas breakdown in DC discharges. For RF discharges, the Paschen curves look slightly different, but show the same pronounced minimum [161–164]. Using this Paschen law, it can be seen that in order to ignite a plasma at atmospheric pressure, the interelectrode distance d needs to be decreased to reach a sufficient breakdown voltage. One subtype of plasmas fulfilling these conditions are atmospheric pressure plasma jets (APPJs).

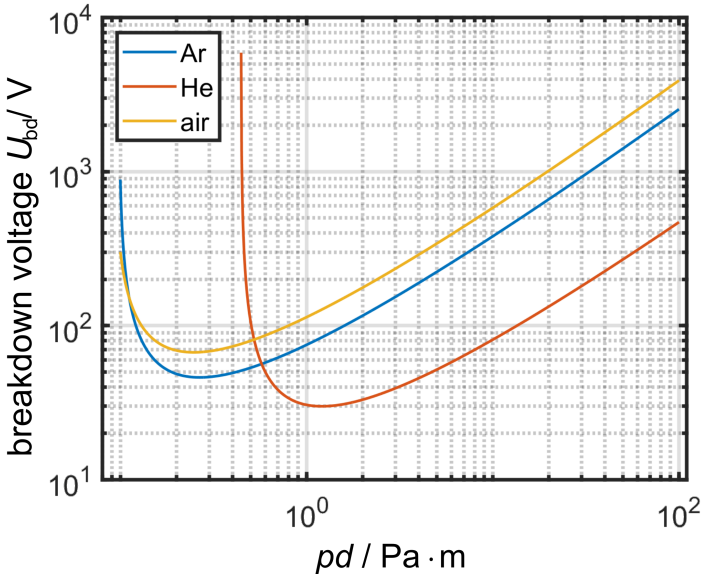

Figure 2.5: Paschen curves showing the breakdown voltage U_{bd} for $\gamma = 10^{-1}$ as a function of the product of pressure p and electrode distance d for different gases.

2.2.3 Atmospheric pressure plasma jets

Atmospheric pressure plasma jets are a subgroup of cold atmospheric non-equilibrium plasmas. Unlike traditional plasma systems that operate under conditions of reduced pressure achieved by using vacuum pumps, APPJs operate at or near atmospheric pressure, making them a cost-efficient alternative for practical applications that require small and modular setups. There are several different types of atmospheric pressure plasma jets used in various research groups and described in literature. A good overview can be found in [26]. This section will focus on the most common types of plasma jets that show the greatest potential in medical and industrial applications.
All APPJs are a form of gas discharge, where the plasma is generated between two electrodes, often also including a dielectric material in between [165]. One of the key advantages is their ability to generated a localized controllable plasma environment at room temperature.

This makes them suitable for surface treatments such as sterilization, cleaning or surface modification, without causing damage to sensitive materials [27]. Due to this characteristic, plasma jets have also shown promising results in medical applications like wound healing and cancer treatment [28, 29]. Here, the reactive species generated by the plasma, such as reactive oxygen species (ROS) and reactive nitrogen species (RNS), have been found to exhibit antimicrobial properties and can be beneficial for tissue regeneration [166]. In materials science, APPJs are utilized for the surface modification of polymers, textiles or metals to improve adhesion, wettability and biocompatibility [167–169]. In manufacturing applications, APPJs are used for the cleaning and activation of surfaces before bonding or coating processes, ensuring strong adhesion [170]. They can also be used in the fabrication of thin films with deposition rates higher than most other atmospheric and low-pressure thin film deposition processes such as spray pyrolysis and physical sputtering [171]. In addition, they are compatible with combined deposition processes such as plasma-enhanced chemical vapor deposition (PECVD) [172]. APPJs offer flexibility in the choice of gases often mixing noble with reactive or precursor gases. The setups of atmospheric plasma jets can be divided into various subcategories depending on the specifics of the discharge. One important group of atmospheric plasma jets are **Capacitively Coupled Plasma Jets (CCPJs)**. They utilize an electric field generated between two electrodes. The discharge can be either generated using a direct current (DC) or an alternating current (AC). DC-Jets are comparatively simple in design and operation, making them ideal for surface treatment applications such as cleaning of surfaces and polymer or water activation [173–175]. On the other hand, a DC current is not desirable in the medical field, due to a higher risk of injury for patients. This has two reasons: For a DC current, the effective cross-sectional area through which a DC-current flows is equal to the overall conductor cross-section. If a person comes in contact with a DC electrode, the current would pass through the whole body, prioritizing areas with the lowest resistance such as veins and the heart. For a high frequency AC current, the skin effect [176] is beneficial since it mitigates current-related injuries. Here, the magnetic field produced by the current inside the conductor directs the current to flow towards the outer surface of the conductor causing the current density to exponentially increase from the conductor core to its surface. As a result, the electric current flows mainly at the *skin* of the conductor between the outer surface and a level called the *skin depth* δ. With increasing frequency, the skin depth decreases. If a subject were to touch an AC-powered electrode, the current would mostly run through the most outer layer of the body, leaving vital organs unaffected. Therefore, high frequency plasma jets are more suitable for medical applications due to this inherent safety feature.

The frequency in AC-Jets can be chosen to be in the area of radio frequency (RF) that is in the range of kHz to MHz, or microwaves (GHz). Microwave plasmas can reach high plasma densities, uniformity and straight forward scalability making them suitable for large-scale industrial processes like plasma-assisted combustion, chemical synthesis and materials processing [177–179] but their operation requires high powers. One of the more cost-effective choices, and thus often utilized in research and industrial applications, are radio frequency plasma jets operating in the kHz to MHz range. A very common choice of the driving frequency of the electric field generated between two electrodes is 13.56 MHz and its harmonics, since they are part of the ISM-bands (Industrial, Scientific and Medical), which are approved for license-free usage in these fields. Typically, one of the electrodes is powered by the chosen frequency, while the other one is grounded. In some cases, the second electrode can also

be floating, decreasing the voltage needed for plasma ignition [180]. Often the electrodes are separated by a dielectric barrier (DBD) such as glass, quartz, a ceramic or a polymer [181]. The subgroup of radio frequency discharges can be further specified by the geometry of the electrodes as well as the orientation of the electric field between them in relation to the gas flow. Assuming a standard parallel plate reactor setup for the electrodes, a so-called *cross-field jet* has an electric field perpendicular to the gas flow opposing to a *parallel-field jet* [32]. This terminology is also applicable to other electrode geometries. The geometry of the electrode can be chosen from a wide variety, ranging from a parallel plate reactor [31] to ring electrodes [182] to more complicated geometries like the HelixJet [183]. This HelixJet is the atmospheric plasma jet that was used for the majority of this thesis. It is a capacitively coupled discharge that is operating at an RF of 13.56 MHz and will be described in detail in section 4.1.

2.3 Plasma-assisted nanoparticle synthesis

The investigation of nanoparticle growth in plasmas started in the middle of 1980, but picked up speed and interest after findings from Selwyn *et al.* in 1988, where the formation of particles was observed as unwanted contamination in the processing of semiconductor wafers [20]. Therefore, the investigation of nanoparticle formation in plasmas was mainly driven by the goal to avoid particle formation in plasmas overall. With more research and time, both low-pressure and atmospheric pressure plasmas have proven to be a tool to facilitate the synthesis of various NPs. This chapter will demonstrate the synthesis processes for two different approaches. The first way generates particles in an approach that resembles a top-down method starting with a source material in a solid form. However, that material is evaporated or sputtered, depending on the method, and then individual atoms or clusters grow into NPs. The second method synthesizes particles through a bottom-up approach from the gas phase, utilizing reactive gases like silane for silicon NPs or acetylene for carbon NPs.

2.3.1 Synthesis from a source material in solid form

Since Pfund's discovery in 1930 [184], it has been known that the thermal evaporation of metals under higher pressure leads to the deposition of porous layers. Such porous structures can reach sizes below 100 nanometers [185]. Magnetron plasma sputtering provides a more controllable transfer of material from the solid to the gas phase. One plasma-based method for the synthesis of NPs, in which a source material is used, is called the gas aggregation source (GAS). The idea dates back to work done by Haberland *et al.* in 1992, where they presented a procedure to generate thin films from the deposition of charged clusters as the result of a sputtering process [186]. Today, it is often used for the synthesis of metal and metal oxide NPs [187]. The GAS involves the condensation of vaporized material into NPs within a chamber filled with inert gas. It is a bottom-up approach, in which the source material to be synthesized into NPs is vaporized through magnetron sputtering, where atoms or molecules from a solid target are ejected by bombarding the target with gas ions. The vaporized atoms enter a condensation zone at a specific pressure usually in the range of 10 to 100 Pa. The elevated pressure is necessary to promote frequent collisions between the sputtered atoms and the gas molecules, enabling effective cooling, nucleation and aggregation of NPs. Depending on the residence time, the size of the resulting NPs can be finely tuned [188]. The method even allows the production of multielemental particles or metal alloy NPs, as has already been shown by Vahl *et al.* in 2017 for the example of AgAu alloy NPs [189].
An interesting approach combining atmospheric pressure plasmas with a source material for the synthesis of NPs was presented in 2006 by Shimizu *et al.* [190]. Using a consumable metal wire and etching it inside an O_2/Ar microplasma, tungsten oxide nanoparticle material could be produced and deposited on a localized surface area below the microplasma jet. For this "wire spray technique", a tungsten wire with a diameter of 100 µm was placed in the nozzle of an atmospheric microplasma generator consisting of a quartz capillary with a copper coil electrode. The microplasma was operated at ultra high frequencies and with a power of 20 W. The tungsten reacts with oxygen and is etched by oxygen species in the plasma. For lower flow rates (5 to 10 sccm), most NPs were observed to nucleate and grow on the wire surface and then were later transported downstream. The authors hypothesized that slight evaporation and recondensation at the plasma-wire interface results in the growth of particles here. The

particles were heated and fully oxidized in the plasma, leading to the downstream deposition of WO_3 NPs. At higher flow rates (20 to 40 sccm), the dominant process mechanism was the condensation from the vapor phase on both the inner wall of the capillary and the substrate. In a repeating process, the surface of the wire was oxidized by the oxygen in the plasma, the oxide layer was then volatilized and scaled off, revealing a new tungsten layer for the oxidation process. Due to the nature of the experiment, this approach could not be used to produce oxygen-free metal particles.

2.3.2 Synthesis from a gaseous precursor

This section describes a method for producing NPs or materials from a gaseous precursor material using chemical reactions and physical processes in the gas phase. Initial application oriented works on the synthesis of silicon from silane as a precursor was focused mainly on the deposition of amorphous silicon films, which were needed for photovoltaic applications. One of the first to report on the formation of silicon NPs from a low pressure argon-silane plasma was the group around Roth *et al.* in 1985 [191]. Here, light scattering on silicon NPs synthesized from silane in a low-pressure plasma RF discharge was published. Since then, several other research groups/researchers studied the generation of NPs from silane as a precursor and helped identifying important steps in the particle growth process [21, 192–194].

The current understanding of nanoparticle fabrication is shown in Figure 2.6, which shows the growth process of silicon NPs inside the gas phase using silane as a precursor. The growth process can be separated into four steps. In the beginning, the precursor silane is decomposed. This can happen either thermally or via plasma decomposition, where silane is dissociated by electron impact [195]. The thermal decomposition of mono-silane starts already at 400 °C [46] and highly reactive monomers such as SiH_2 are formed. As a next step, nucleation occurs, where the monomers can come together to form clusters. The initial nucleation is followed by a third step, coagulation into small particles, which then grow in size due to the surface deposition of radicals (4th step). To keep the nucleation process running, a constant supply of precursor material is needed into the reaction volume and its continuous dissociation. The synthesized particles can further coagulate and the synthesized material leaves the reaction volume in the form of single NPs and/or agglomerates. The details of the clustering process have been investigated by several research groups, where the question of the dominant pathway for silicon hydride clustering in silane plasmas has always been the center of discussion. Watanabe *et al.* concluded in their studies that the species dominantly contributing to the nucleation are short lifetime neutral radicals such as SiH_x ($x = 0..3$), especially SiH_2, which was found to have the highest generation rate among all and the fastest insertion reactions [196]. In their experiments, they observed the SiH_2 and particle density profiles for different radio frequencies and concluded that short-lived neutral radicals are involved in many steps of the polymerization chain, suggesting that clustering is driven by SiH_2 insertion reactions.

Hollenstein *et al.* conducted mass spectroscopy measurements and partial depth modulation experiments on capacitive coupled plasmas synthesizing silicon NPs. Here, they observed that particle formation was progressing as long as the negative ions remained trapped inside the plasma. Therefore, they suggested a pathway dominated by anion-neutral reactions [193, 194].

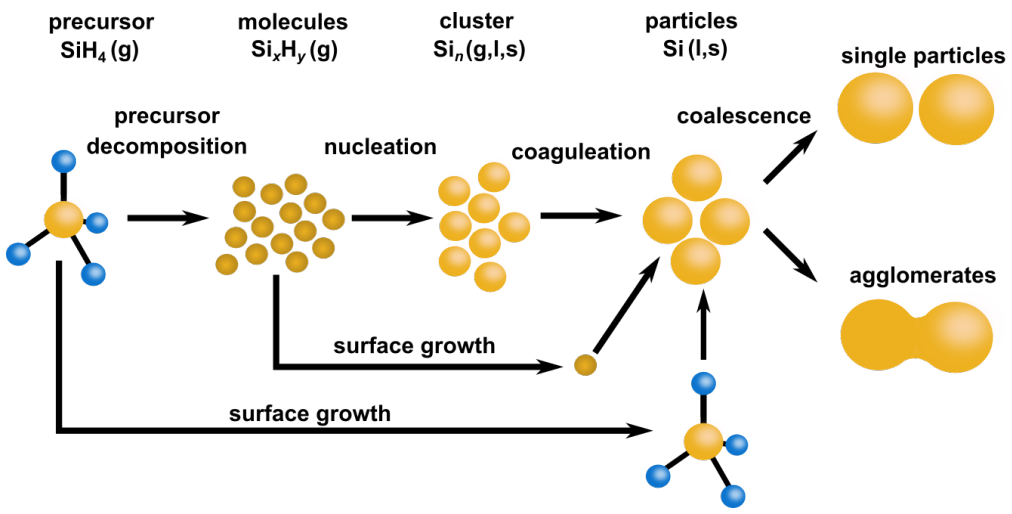

Figure 2.6: Growth process of silicon NPs in a plasma. The gaseous precursor is decomposed. Initial nucleation is followed by coagulation into small particles. The aggregate state of reactants and products is noted as either gaseous (g), liquid (l) or solid (s). Figure adapted from [46].

Bhandarkar *et al.* published a study in 2000 that modeled the formation of NPs from silane as a precursor in more detail [197]. The zero-dimensional chemical kinetic nucleation simulation was done for a low-pressure plasma with a pressure of 100 mTorr (≈ 13 Pa), even though the model itself was based on the mechanism for the clustering of neutral species in atmospheric pressure thermal CVD of silicon from silane. Important reactions in this plasma model were the electron dissociation and attachment reactions, anion-neutral reactions, and all reactions involving silyl and H radicals. The anionic pathway was found to be the main pathway for silicon hydride clustering. SiH_2 insertion in neutral clusters was found to be important only among the small silicon hydrides with up to three or four silicon atoms.
The currently most favored investigations done by De Bleecker *et al.* in 2004 [198] are based on one-dimensional fluid model simulations of a parallel-plate capacitively coupled RF discharge for a pressure of 40 Pa at a power of 5 W. The model contained 68 different species and the formation of silicon hydrides containing up to 12 silicon atoms. They found that the early stages of particle formation start primarily from the anions silyl (SiH_3^-) and silylene (SiH_2^-), which are formed through the dissociative attachment of SiH_4:

$$SiH_4 + e^- \rightarrow SiH_3^- + H\,, \tag{2.27}$$

$$SiH_4 + e^- \rightarrow SiH_2^- + 2H\,. \tag{2.28}$$

The dominant negative ions SiH_2^- and SiH_3^- are the first species of particle formation and can undergo the following anion-molecule chain reactions which then start the clustering:

$$SiH_2^- + SiH_4 \rightarrow Si_2H_4^- + H_2\,, \tag{2.29a}$$

$$Si_2H_4^- + SiH_4 \rightarrow Si_3H_6^- + H_2\,, \tag{2.29b}$$

$$\vdots \tag{2.29c}$$

$$Si_nH_{2n}^- + SiH_4 \rightarrow Si_{n+1}H_{2n+2}^- + H_2\,. \tag{2.29d}$$

A similar reaction sequence can also start from SiH_3^-:

$$SiH_3^- + SiH_4 \rightarrow Si_2H_5^- + H_2\,, \tag{2.30a}$$
$$Si_2H_5^- + SiH_4 \rightarrow Si_3H_7^- + H_2\,, \tag{2.30b}$$
$$\vdots \tag{2.30c}$$
$$Si_nH_{2n+1}^- + SiH_4 \rightarrow Si_{n+1}H_{2n+3}^- + H_2\,. \tag{2.30d}$$

The enthalpies of reactions of the first four steps in the clustering process are are -0.07, $+0.07$, $+0,07$ and $0,00\,\mathrm{eV}$, respectively. According to Friedman *et al.*, this thermoneutral and even slightly endothermic nature of some reactions from the chain would result in an energy barrier or even a kinetic bottle neck [199]. De Bleecker *et al.* considered in their simulations also vibrationally excited molecules, which bring the necessary internal energy to overcome this energy barrier. The vibrationally excited molecules $SiH_4^{(2-4)}$ and $SiH_4^{(1-3)}$ enhance the anion-neutral reactions. It was found from these simulations that the anion SiH_3^- is the most dominant primary precursor in the formation of particles. Over 90 % of the gas phase synthesis process undergoes the silyl anion ($Si_nH_{2n+1}^-$) pathway, starting at SiH_3^-, while only 10 % proceeds through the silylene anion ($Si_nH_{2n}^-$) pathway, starting from SiH_2^-. The involvement of vibrationally excited silane molecules $SiH_4^{(2-4)}$ and $SiH_4^{(1-3)}$, as well as the role of SiH_3 radicals in the particle formation process depends on the exact rate constant of anion-groundstate SiH_4 reactions, which is so far unknown [198]. Simulations for different reaction rate constants show that the pathway distribution can vary. For a rate constant of $10^{-18}\,\mathrm{m^3s^{-1}}$, about 38 % of the anions would react with SiH_4 groundstate molecules, 36 % of anions would proceed through the $SiH_4^{(2-4)}$ pathway and over 25 % would react with SiH_3 radicals. The authors favor an increased reaction rate closer to $10^{-16}\mathrm{m^3s^{-1}}$, at which the contribution of radicals and vibrationally excited species drop radically below 1 % and leave the anion-groundstate SiH_4 reactions as the most dominant pathway.
Although most of these simulations have been done for low-pressure plasma systems, it is assumed that the general reactions and pathways are the same for atmospheric pressure plasmas.
Experimentally, gas phase synthesis using low pressure plasmas dates back to 2005, where Mangolini and Kortshagen demonstrated a quartz tube plasma reactor filled with an argon-silane gas mixture operated at 200 W and at a frequency of 27.12 MHz over two copper ring electrodes [200]. Silicon NPs with diameters of 3 nm a photoluminescence maximum in the red spectral region could be produced using this system. Subsequent publications include changes to lower powers (50 W) and frequencies (13.56 MHz), while increasing the mass yield of luminescent silicon powder to up to 50 mg/h [24, 91, 97]. A good review on the topic of low-pressure non-thermal plasma synthesis of semiconductor nanocrystals can be found in [23].
In comparison, the silicon nanoparticle synthesis using atmospheric pressure plasmas has been much less frequently investigated. Moreover, the synthesis of silicon nanocrystals with optical properties in atmospheric pressure plasmas is more complex. Due to the high affinity of silicon for oxygen and the overall susceptibility of atmospheric pressure systems for oxygen impurities, the production of optical-quality material is challenging. Sankaran *et al.* reported in 2005 on the synthesis of silicon NPs with diameters of up to 3 nm using a continuous flow atmospheric pressure micro-discharge reactor [33]. Supplementary TEM images of this study

show that the particles were amorphous. Therefore, the blue PL that was reported here can most likely be traced to silicon oxide [201–203]. In 2007, Nozaki *et al.* published a study on an atmospheric pressure microplasma reactor operated at a very high frequency of 144 MHz for the synthesis of silicon nanocrystals with sizes below 3 nm [30]. Here, the admixture of hydrogen was necessary to turn the particles crystalline, possibly due to the reductive nature of hydrogen. It was also demonstrated that the increased admixture of hydrogen etches the particles smaller and has therefore a strong influence on the position of the PL maximum. Other works focused on atmospheric plasma synthesis include the studies from Barwe *et al.* who presented the synthesis of silicon nanocrystals in a DC atmospheric microplasma jet [31, 32]. Sakari *et al.* demonstrated that the synthesis of crystalline silicon NPs is also possible in atmospheric pressure low-temperature microplasmas without hydrogen admixtures [204]. Combining theoretical and experimental approaches, the authors concluded that gas temperatures well below the crystallization threshold of silicon are sufficient for the formation of silicon nanocrystals due to a phenomenon called *selective heating*.

Selective Heating

The most important factor in the synthesis of silicon nanocrystals is the temperature. Theoretical calculations [205] and subsequent experiments showed that small amorphous silicon structures with diameters below 10 nm can be turned into nanocrystals at temperatures below the melting point of bulk silicon. For instance, particles with diameters of 4 and 8 nm crystallize when their temperatures rise over 770 and 1200 K, respectively [206]. With the reported gas temperatures of low-pressure plasmas reaching only as high as 500 K, it was surprising that the requirements for the synthesis of nanocrystals had still been reached. An explanation for this phenomenon was reported by Mangolini *et al.* under the term *selective heating* [24]. NPs in plasmas are preferentially heated through mechanisms such as collisions, ion recombinations and chemical reactions of plasma species on the particle surfaces. These reactions release energy that can be transferred to the particle, where it contributes to an increase in temperature.
The process of selective heating was described as follows: A stochastic Monte Carlo simulation was used to study the particle temperature inside a plasma. The model uses a non-steady description of the energy balance of a spherical particle with radius r_p and temperature T_p:

$$\frac{4}{3}\pi r_\mathrm{p}^3 \rho C \frac{dT_\mathrm{p}}{dt} = G - L\,, \tag{2.31}$$

where ρ and C are the density and specific heat of silicon, which are assumed to be equal to those of the bulk material. G describes a heat generation and L a heat sink term. For the simulation, it was further assumed that the particle temperature equilibrates instantaneously through a particle. The term L is calculated as:

$$L = \frac{1}{4} n_\mathrm{gas} S \sqrt{\frac{8 k_\mathrm{B} T_\mathrm{gas}}{\pi m_\mathrm{gas}}} \cdot \frac{3}{2} k_\mathrm{B} \left(T_\mathrm{p} - T_\mathrm{gas}\right) \tag{2.32}$$

and describes the heat conduction losses to a background gas with density n_gas and temperature T_gas, which was assumed to be argon in this publication. S describes the surface area of the particle. For this term, only heat conduction via neutral collision with the background

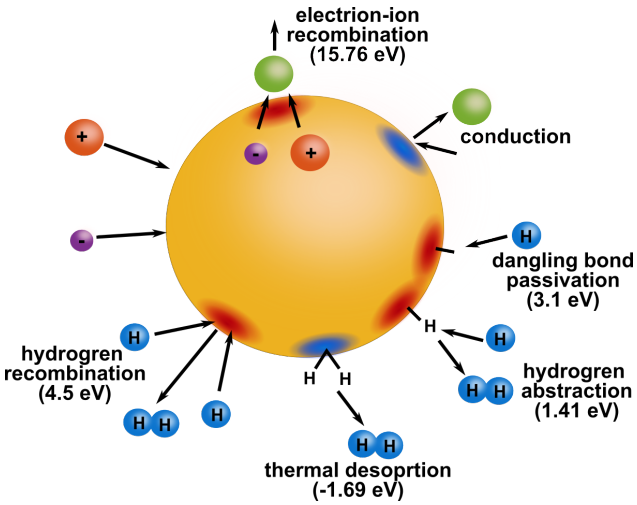

Figure 2.7: Heating and cooling events occurring on the surface of a silicon nanoparticle. Heating events are indicated in red, cooling events in blue. The electron–ion recombination energy is equal to the argon ionization potential of 15.76 eV. Dangling bond passivation, hydrogen abstraction and hydrogen recombination deliver energies of 3.1 eV, 1.41 eV and 4.51 eV, respectively. Cooling events mainly are usually induced from collisions with colder gas atoms, with the exception of thermal desorption of hydrogen with an energy loss of 1.69 eV for each desorbed hydrogen molecule. Figure adapted from [207].

gas is considered, since they occur more frequently than collisions with ions or radicals. Furthermore, radiation was neglected, since the time scale for radiative cooling is longer than the timescale of heat transfer processes considered for this simulation.
The heat generation G is caused by recombinations and chemical reactions on the surface of the particle. Figure 2.7 shows the possible events that occur on the surface of a silicon nanoparticle that contribute to its heating or cooling. The following section explains these events in more detail. Possible recombinations and chemical reactions include ion-electron recombinations, which release an energy corresponding to the ionization energy or the reaction of two atoms/radicals forming a molecule and releasing the corresponding binding energy. Silicon NPs are typically generated in an atmosphere of inert gas (Helium, Argon) combined with silane (SiH_4) as a precursor. With silane in the plasma, a surplus of hydrogen is to be expected. Therefore, exothermic and endothermic reactions of hydrogen with the particle surface need to be also considered. Collisions of electrons and ions with the surface of a particle in a plasma can be estimated via the respective collision frequencies, as given by the orbital-motion-limited (OML) theory [208], which is suitable for particles smaller than 10 nm [209]. The collision with an argon ion will lead to an electron-ion recombination on the particle surface atom, releasing the equivalent of the ionization potential of argon at 15.76 eV. Collisions with atomic hydrogen can result in different energy transfer mechanisms depending on the fractional hydrogen surface coverage f_S, which is the number of already present hydrogen surface atoms divided by the number of available hydrogen surface sites. If a hydrogen atom collides with a dangling bond (an unterminated surface site), the sticking coefficient is 1, which always results in the release of 3.1 eV, equal to the binding energy of the Si−H bond. If a hydrogen radical collides with a fraction of the surface that is already hydrogen-terminated, it has a probability of 11 % of abstracting another hydrogen

atom from the surface as described by the Eley-Rideal mechanism [210]. This releases an energy of 1.41 eV, which is equal to the binding energy of the hydrogen molecule (4.51 eV) minus the energy of the broken Si−H bond (3.1 eV). In the other 89 % of cases, hydrogen will be physisorbed and diffuse along the particle surface. The diffusion coefficient D of atomic hydrogen on a hydrogen-terminated silicon surface is given by

$$D = D_0 \cdot \exp\left(-E_\mathrm{D}/k_\mathrm{B}T_\mathrm{p}\right) , \tag{2.33}$$

following an Arrhenius expression. The activation energy E_D and prefactor D_0 can be estimated via simulations to be $\mathrm{E_D} = 0.1\,\mathrm{eV}$ and $D_0 = 2.27 \times 10^{-4}\,\mathrm{cm^2/s}$ [211]. If the lifetime τ_D of the physisorbed atomic hydrogen is small compared to the time until the next hydrogen hits the surface (Δt_H), the hydrogen is able to diffuse along the surface until it reaches a surface dangling bond and release an energy of 3.1 eV there. If $\tau_\mathrm{D} > \Delta t_\mathrm{H}$, the physisorbed hydrogen atom can recombine with the new incoming radical instead, releasing 4.51 eV. For high particle temperatures above 900 K, thermal desorption of hydrogen can occur via the Langmuir-Hinshelwood mechanism [212]. Here, a H−H bond is formed, while two Si−H bonds are broken, resulting in a total energy loss of 1.69 eV for this process.
Overall, the results of the simulation of Mangolini *et al.* for silicon NPs synthesized in $\mathrm{Ar/SiH_4}$ plasmas show that the average temperature of NPs in a plasma environment is roughly 100 K higher than the gas temperature. This effect is independent of the particle size, because both cooling and heating effects scale in the same manner with the particles surface area. However, the energy coming from an interaction with species in the plasma (e.g. ion recombination, reaction with hydrogen atoms) has a bigger influence on smaller particles. Here, the model shows a rapid short-term increase in the particle temperature. These spikes in temperature are greater for smaller particles. While 10 nm particles remain almost at a constant value of around 400 K, smaller particles can temporarily reach temperatures of up to 700 K for a 3 nm particle and up to 1100 K for a 2 nm particle. These results show that the particle temperature inside a plasma can easily exceed the crystallization temperature needed for the synthesis of silicon nanocrystals.

3 | Diagnostics for nanoparticle characterization

The following chapter summarizes the material diagnostics that were used in this thesis for the analysis of NPs synthesized by various experimental methods. These methods result in information about the nanoparticle size (SMPS, TEM), morphology (TEM), chemical composition (FTIR, TEM) and their optical properties (PL).

3.1 Scanning Mobility Particle Sizer (SMPS)

The Scanning Mobility Particle Sizer (SMPS) is a device that is used to measure submicrometer particles in aerosols. It is commercially used to measure particulate matter in car exhausts [213, 214] or to detect NPs in cigarette smoke [215]. The device exploits the fact that the differential electric mobility of a spherical particle is dependent on its diameter. The great advantage of differential mobility analysis is the fact that the particles remain airborne without any manipulation in the form of sample preparation. A typical SMPS consists of a neutralizer to establish a known charge distribution, a differential mobility analyzer to carry out the sorting and a particle counter for the subsequent counting of the sorted particles. In order to sort particles by their differential mobility, their charge distribution has to be known. Aerosol particles are charged as a result of collisions between ions and particles, i.e. through bipolar diffusion charging. If the particles in the aerosol are exposed long enough to positive and negative ions, the bipolar charged particles will achieve stationary charging as a function of their size [216]. The equilibrium charge distribution can be calculated using the Boltzmann formula in the continuum regime and the Fuchs charging theory [217] in the transition and free molecular regimes. Several methods for the unipolar and bipolar charging of particles have been reported, such as corona discharges, ionization chargers [218] or the use of radioactive sources such as ^{241}Am or ^{85}Kr [219]. Corona discharges can generate a high concentration of unipolar ions, but have the downside of generating ozone, as well as other unwanted material through erosion and gas-phase reactions that occur in the strong electric field on the discharge electrodes [220]. Radioactive sources require expensive safety measures and often underlie severe legal restrictions. Moreover, their limited ion concentrations inhibit their charging efficiency as the particle concentration increases. The alternative to these methods is using a source of soft X-rays. It can be handled more safely and, unlike a radioactive source, can be turned on and off on demand. Because of these safety reasons and the ability to produce a large amount of bipolar ions, soft X-ray ionization is the most common method for establishing a known charge distribution in aerosols for particle size measurements.

3.1.1 Aerosol X-ray Neutralizer

In this thesis, an Advanced Aerosol Neutralizer (Model 3088) was used. It contains an X-ray source, which produces soft X-rays with an energy between 3 and 9.5 keV, with a

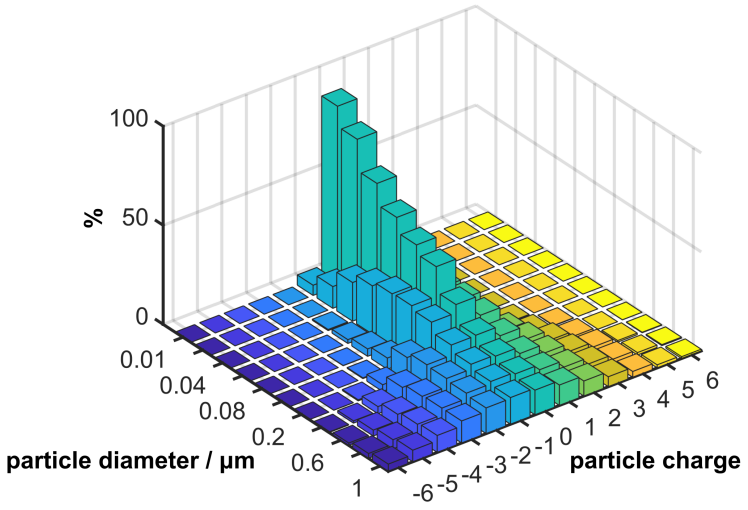

Figure 3.1: Equilibrium charge distribution applied to the aerosol by the neutralizer as calculated from [221]. Most particles receive a neutral charge while only some bigger particles can obtain up to six positive or negative charges.

maximum at the tungsten L_α-line (8.4 keV). These X-rays create both positive and negative ions from the inherent air. Those ions are then attracted to particles of the opposite charge. Such a neutralizer can neutralize particle concentrations of up to $10^7\,\mathrm{cm}^{-3}$. The particles achieve a known charge distribution. The charge distribution is shown in Figure 3.1 and was calculated from the expanded theoretical model published by Wiedensohler *et al.* [221]. For small particle diameters, the charges are mostly neutral, with only a small percentage on single positive or single negative charges. When the particle size increases, the charge distribution function broadens and particles with up to six elementary charges can be found.

3.1.2 Differential Mobility Analyzer (DMA)

Particles with a known charge distribution function then enter the core part of each scanning mobility particle sizer, the so-called *differential mobility analyzer* (DMA). As the name indicates, particles are sorted here in regard to their electric mobility. Figure 3.2 shows a cross section of the DMA. It consists of two cylindrical electrodes with radii r_i and r_o and length L. The inner cylinder can be charged positively in a wide voltage range. For a certain voltage U, only particles of electric mobility μ have a fitting trajectory and can pass through the device. The ratio between voltage and mobility is

$$U = \frac{Q \cdot \ln\left(\frac{r_i}{r_o}\right)}{2\pi L \mu}\,, \tag{3.1}$$

where Q describes the gas volume flow. If spherical particles are assumed, their diameter d and electric mobility μ are correlated by the Stokes' Law:

$$\mu = \frac{neC}{3\pi\eta d}\,, \tag{3.2}$$

with the number n of elementary charges e on a particle, as well as the dynamic gas viscosity η. C describes the *Cunning slip correction* which can be found in [222].

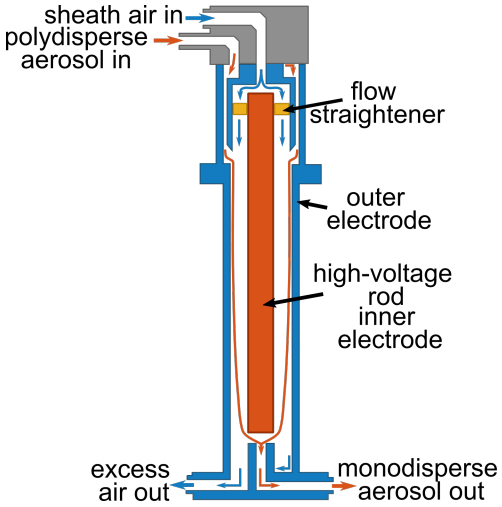

Figure 3.2: Sketch of the differential mobility analyzer (DMA). A polydisperse aerosol enters at the top together with sheath air. The NPs inside the aerosol are sorted by differential electric mobility via a high voltage. A monodisperse aerosol exits the device and can be counted.

In this thesis, two different DMAs have been used. The long DMA can resolve particles in the size range of 10 nm to 1 µm. The second mobility analyzer is the 1nm-nano-DMA. As the name indicates, it can resolve particles down to 1 nm with an upper limit at 150 nm. Here, the high inlet flow and short inlet passage reduce residence time and therefore lower particle diffusion losses [223]. After passing the DMA, the aerosol is now considered to be monodisperse and ready to be detected.

3.1.3 Condensation Particle Counter (CPC)

There are various options to detect particles optically. When trying to detect particles below a size of 50 nm, conventional optical techniques fail. Condensation Particle Counters (CPCs) are one of the most common particle counters used in combination with DMAs inside a Scanning Mobility Particle Sizer [224]. They are using a detection principle, where the particles inside an aerosol are first enlarged (using them as nucleation centers for the creation of droplets in a supersaturated gas) and then counted. The CPC used in this thesis was the Model 3750 from TSI. It uses *n*-butanol as a working fluid. The aerosol to be sampled is drawn continuously through a heated saturator, in which the butanol evaporates into little droplets and diffuses into the sample stream. The butanol vapor and aerosol sample then enter a cooled condenser, in which the vapor becomes supersaturated and ready to condense. The supersaturation in the condenser is usually between 100 and 200 %, because the vapor pressure over a convex surface is less than over a plane, requiring a greater content of vapor in air for supersaturation criteria. The needed supersaturation level increases for smaller particles. The critical diameter for which condensation can occur at a certain level of saturation is called *Kelvin diameter* [225]. However, if the supersaturation level is increased to a level of around 300 %, homogeneous nucleation can cause liquid molecules to form clusters when they collide [226, 227]. This can result in false counts. Particles in the aerosol serve as condensation nuclei. Particles larger than a certain threshold diameter will grow quickly

into larger droplets. After this growth process, particles are measured via optical detection using an opaque meter. This optical sensor consists of a laser diode, several lenses and a photodiode detector. A second photodiode is used as a reference to keep the laser power output at a constant level. The temperature of the housing is kept at a higher level than the saturator itself, to avoid condensation on all lens surfaces. In single count mode, the detection limit for the CPC is 10^5 particles per cm^3. For higher concentrations, the CPC uses a live-time coincidence correction to maintain accuracy. Coincidence occurs, when one particle obscures another one, resulting in an undercounting error. Using this, the CPC is able to detect airborne particles with a concentration up to 10^7 particles per cm^3 and down to a diameter of 7 nm. If smaller particles should be detected, this device needs to be combined with a Nano Enhancer. The Nano Enhancer (Model 3757) is a pre-stage that can be inserted into the scanning mobility particle sizer in front of the CPC. Its working principle is similar to the one described for the CPC. It uses diethylene glycol instead of butanol to activate particles as small as 1 nm and make them grow to a size around 100 nm, which makes them easy to be detected with the traditional condensation particle counter.

3.1.4 Statistic description of the charge distribution

Standard statistics based on normal Gaussian distribution functions are not suitable for most airborne particles (aerosols). Even though there is no theoretical reasoning for it, log-normal distributions have proven empirically to be the best fit for single source aerosols [228, 229]. Therefore, when statistical analysis is applied to the size distributions as measured by a scanning mobility particle sizer, log-normal distributions are used. They are most useful, when the data range (the difference between the smallest to biggest measured diameter) is greater than 10 in ratio. If the data range is narrow, the log normal distribution will approximate a normal (Gaussian) distribution. The SMPS measures a continuous size distribution by m discrete size intervals yielding m numbers for N_k ($1 \leq k \leq m$) with the total concentration

$$N_{\text{tot}} = \sum_{k=0}^{m} N_K \,. \tag{3.3}$$

The log normal distribution for discrete size channels $D_{P,k}$ is defined by:

$$\frac{dN}{dD_P} = \frac{N_{\text{tot}}}{\sqrt{2\pi} D_{P,k} \ln\sigma_g} \exp\left(-\frac{(\log D_{P,k} - \log D_g)^2}{2(\log\sigma_g)^2}\right) . \tag{3.4}$$

In many cases, the size distribution given by an average size D_g and a spread σ_g is more practical to work with. For log-normal distributed aerosols with the geometric mean size D_g is used as defined by:

$$\log D_g = \frac{\sum_{k=0}^{m} N_k \log D_{P,k}}{N_{\text{tot}}} \,. \tag{3.5}$$

In aerosol log-normal distributions, the logarithm of the particle diameter is normally distributed. The well known linear based standard deviation σ is replaced with the standard deviation of logarithms, the *geometric standard deviation* σ_{g}:

$$\log\sigma_{\text{g}} = \left[\frac{\sum N_k (\log D_{P,k} - \log D_g)^2}{N_{\text{tot}}}\right]^{1/2} . \tag{3.6}$$

An aerosol can be considered monodisperse for $\sigma_{\text{g}} \leq 1.25$ and polydisperse otherwise.

3.1.5 Limitations of the SMPS

The scanning mobility particle sizer is an optimal tool to measure size distribution functions of particles in atmospheric pressure plasmas, since the outflow of the jet can be directly connected to the inlet of this measuring device. Nevertheless, there are certain limitations connected to its deployment. One limitation is related to the particle concentration. As discussed in the previous section the SMPS can reliable measure particles to concentrations up to 10^7 particles per cm^3, limited by capacity of the X-ray neutralizer. For high concentration of reactive gases in the plasma jet, particles in the center of the size distribution are often synthesized with a concentration that exceeds this limit. As a result, the measured size distribution will be saturated, leading to a cut-off in the center of the log normal distribution with only the left and right flank being measured correctly. During this thesis several attempts have been made to reduce the particle concentration for example by separating the flow into two parts and discarding one half via a pumping system. Measuring of the reaming half showed that these attempts do not reduce the concentration homogeneously, but selectively. The measured size distributions were shifted to greater or smaller particles depending on the type of modification done to the aerosol stream.
The second limitation of the SMPS is correlated with the term of size. In mobility analysis, the particle size is representative for single spherical particles, but that is not always the case. In aerosol technology, several equivalent diameters are used to describe irregular shaped particles or particle agglomerates. The *equivalent circle diameter*, typically used in TEM image analysis, is the diameter of a sphere, of which the projected area equals the one of the measured particle. The *Stokes diameter* is the diameter of a sphere with the same settling velocity and the same density as the respective particle. In contrast, the *aerodynamic diameter* is the diameter of a sphere which has the same settling velocity as the particle and a density of $1\,g/cm^3$, which is used when the material and therefore the density are unknown [230].
In mobility analysis, such as used by the differential mobility analyzer, the particle size is represented by the size of a sphere with the same differential mobility [231]. This equivalent diameter is called the *mobility diameter*. It is determined via the relation between the magnitude of an electrical field and the velocity of the particles, which is constant, when the drag force and the Coulomb force are of the same magnitude. If agglomerates enter the SMPS, a mobility diameter for the agglomerate will be measured and presented as the diameter of a single spherical particle. Therefore, it is crucial to always combine SMPS measurements with microscopy methods such as Transmission Electron Microscopy.

3.2 Transmission Electron Microscopy (TEM)

Microscopic methods can be used to access more detailed information on the composition of NPs. This includes the size and morphology of the nanoparticles and information concerning their chemical composition, the spatial distribution of elements (e.g. interesting for core-shell or Janus-type morphologies) and crystallographic information (e.g., crystalline phase, orientation and structure) on nanoparticles agglomerates or even single particles with down to atomic resolution. With various detectors fit to the products of the interaction of electrons with the sample, the TEM presents a full-featured analytic tool revealing valuable information about synthesized NPs. The spatial resolution of an optical system can be calculated by the Rayleigh criterion [232]. Two point-sized objects in distance a can still be resolved if

$$a = \frac{0.61\lambda}{n \cdot \sin(\theta)}\,, \tag{3.7}$$

where λ is the wavelength of illumination, θ the angle of incident and n the refractive index of the medium between lens and picture. By decreasing the wavelength, the resolution can be increased. For visible light at a wavelength of 500 nm and a refractive index $n = 1$ for air, this results in a resolution of around 0.2 µm. Therefore, it is impossible to access the information of nanostructures by optical microscopy. In 1925 the wave-like characteristics of electrons were postulated by Louis de Broglie:

$$\lambda = \frac{h}{p}\,, \tag{3.8}$$

with the Planck constant h and momentum p, meaning that the wavelength of electrons can be calculated from their kinetic energy. An electron passing the electric potential difference of 1 V gains an energy of 1 eV. Assuming electrons with an energy of 50 keV, their wavelength is around 0.05 Å, which is 10^5 times smaller than the wavelength of visible light. In 1926 it was found by H. Bush that an electromagnetic field can be used to focus and manipulate the beam of electrons. Together, these findings led to the development of the first electron microscope in 1932 by Ernst Ruska and Max Knoll [233]. Since then, technology has improved rapidly. Today's TEMs are capable of resolving single atoms. The theoretical resolution offered by the electron light source is now only limited by effects such as lens aberrations described in section 3.2.1. For this thesis, a Tecnai F30 G^2 from FEI as well as a JEM-2100 and a JEM-ARM200F "NeoARM" from JEOL were used to analyze the samples.

3.2.1 Setup of a TEM

Although the different transmission electron microscopes differ from each other in design, arrangement of individual elements and control, they are very similar in principle. A TEM consists of an electron source, a tube with electromagnetic lenses and apertures, a sample holder and various detectors. All of this is placed in a high vacuum environment, which ensures undisturbed electron movement and reduces contamination of the sample and detectors. Figure 3.3 a shows a schematic sketch of a typical transmission electron microscope. The electron source (electron gun) inside a TEM consists of an electron emitting cathode and an anode that accelerates them by a voltage U. For an electron to be emitted from the

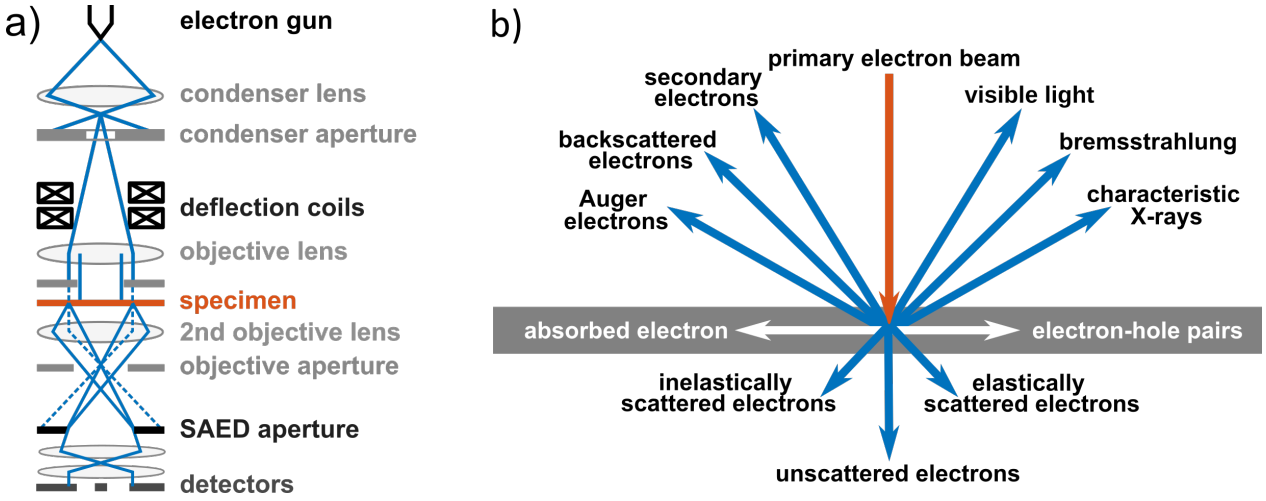

Figure 3.3: a) Schematic sketch of the basic setup of a transmission electron microscope. b) The primary electron beam interacts with the specimen resulting in several scattering processes, emitting detectable signals such as characteristic X-rays or secondary electrons. Figures adapted from [234].

cathode, it needs to overcome an energy barrier of the work function Φ_W. The electrons are extracted from the cathode using thermionic emission or field emission. During thermoionic emission, the source material, for example a Tungsten or LaB_6 filament, is heated to temperatures high enough to overcome the work function. However, field emission works either at room temperature (cold FEG) or with a slightly heated tip (Schottky emitter). Here, a sharp tip results in an increased electric field. If a potential is applied to the tip, Φ_W is lowered and electrons can tunnel out of the material through field emission. In comparison with thermionic emission, FEG emits electrons from a very small area with a very low energy dispersion. After emission, electrons are attracted towards the positively charged anode by a high acceleration voltage. The acceleration voltage determines the energy and velocity of the electron beam, affecting the resolution and penetration depth. Typical electron energies range from 30 to 300 keV, although lower and higher acceleration voltages are also possible and used for their own applications.
The electron beam can be manipulated using different apertures and lenses. Electromagnetic lenses in a transmission electron microscope have a function similar to glass lenses in optical microscopes, and the electron beam is focused along the desired axis. Inside an electron microscope, electromagnetic coils generate a field that can focus or manipulate the electron beam with the Lorentz force. Apertures can be inserted and removed from the electron beam depending on the desired operation mode. Electron lenses have three different kinds of aberration that are impossible to eliminate completely. These lens aberrations are spherical and chromatic aberration, as well as axial astigmatism.

3.2.2 Sample beam interaction

The primary electron beam emitted from the electron source can interact with the sample in numerous ways. Figure 3.3 b shows an overview of the possible interactions. A part of the beam passes through the specimen without almost any interaction, while the rest undergoes

a set of different scattering processes. Some of the scattered electrons leave the specimen in a forward direction (scattering angle $< 90°$). Electrons found under a scattering angle $> 90°$ are called back scattered electrons, which are defined by energies $> 50\,\text{eV}$, compared to the less energetic secondary electrons ($< 50\,\text{eV}$), which are generated by inelastic scattering of the primary electrons in the specimen. TEM imaging methods are using unscattered and both inelastically and elastically scattered electrons. When electrons are deflected, bremsstrahlung is emitted. Characteristic X-rays are generated in the relaxation process, after a beam electron excited inner-shell electrons. Instead of X-rays, the relaxation process can also occur without any emitted radiation, where an Auger electron of the corresponding energy will leave the sample instead. These characteristic photons and electrons can be used to access the chemical composition of the sample using energy-dispersive X-ray spectroscopy (see section 3.2.4).

3.2.3 Imaging Modes

Imaging modes in a conventional TEM (C-TEM) can be generally divided into *bright field mode* and *dark field mode*. They are achieved by inserting different apertures into the beam path. For bright field mode, a contrast aperture is inserted into the beam path allowing only unscattered electrons and small angle electrons to contribute to the image. In dark field mode, the primary beam is filtered out by tilting the specimen to a certain angle, allowing only a selected diffracted beam to pass through the aperture. Thus, additional information will be obtained using this mode only for crystalline specimens, where certain diffraction patterns can be highlighted with increased contrast. To obtain a high resolution TEM (HRTEM) image, several diffraction beams are used to create the image and interference effects become more pronounced in the resulting image [234].
Similarly to a scanning electron microscope, the beam can also be converged and used to systematically scan the sample. The image is constructed by the detection of scattered electrons. This mode is called Scanning TEM (STEM). Depending on the detector used, subcategories in this imaging mode open up: Inelastically electrons, or elastically scattered electrons with a small scattering angle below 10 mrad are detected using a bright field detector (BF-STEM). For scattering angles between 10 and 50 mrad, an annular dark-field detector (ADF-STEM) is used. At angles above 50 mrad a special high angle dark field detector (HAADF) is used. In ADF- and HAADF-STEM images, heavy elements and thicker areas of a specimen generate a bright image, whereas it is the opposite for bright field CTEM and STEM. For this reason, HAADF-STEM was mainly used for the analysis of metal NPs in this thesis.

3.2.4 Energy-dispersive X-ray spectroscopy (EDX)

As described in section 3.2.2, an inelastic scattering event induced by the electron beam will stimulate the X-ray emission of the sample. In the Bohr model, electrons move on discrete energy levels (shells). These shells are named either by their main quantum numbers ($n = 1, 2, 3...$) or often referred to as K-shell ($n = 1$), L-shell ($n = 2$) and so on. An electron from the ground state can be excited and jump into a higher shell. After this, an electron from the outer shell will then fall back to the ground state, releasing energy in the form of an X-ray. The energies of these X-ray photons are well defined and are characteristic for

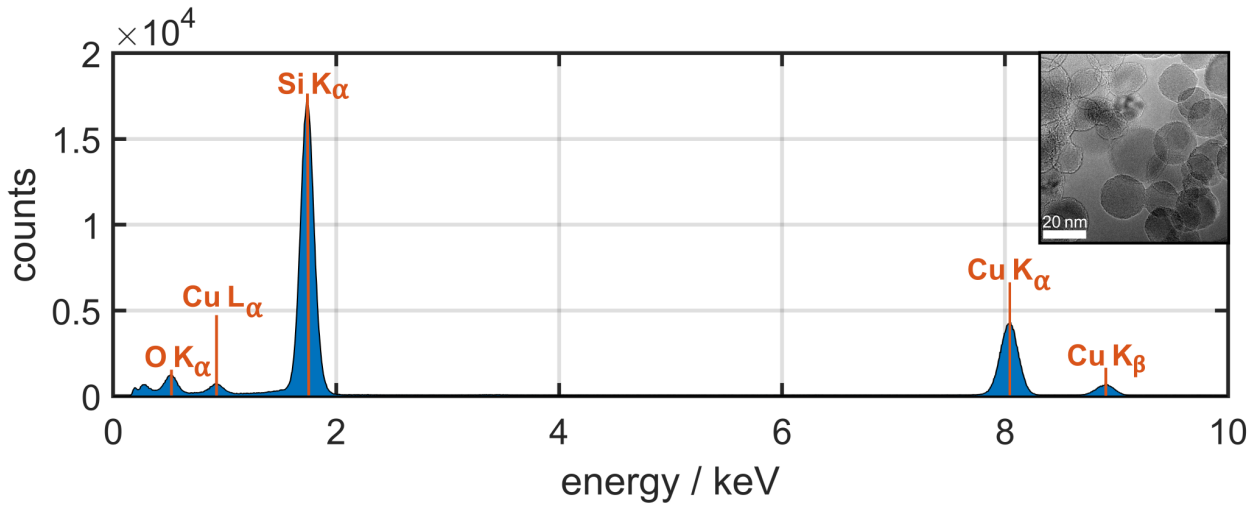

Figure 3.4: EDX spectrum of silicon NPs on a copper TEM grid and the related STEM HAADF image. The silicon particles are big in diameter and as a result only very slightly oxidized. The measured copper lines are measured from the grid.

every element. These X-ray photons can be detected by inserting an energy-sensitive photon detector into the TEM column above the specimen.
A typical EDX spectrum of silicon NPs synthesized in atmospheric plasma and measured after transfer through air is shown in Figure 3.4. Several peaks are visible which correspond to the elements O, Cu and Si. The nomenclature is as follows: Transitions are named after the shell in which the electron ends. Greek letters are used to denote the shell where the electron originated, in approximate order of intensity (α-transitions are more intense than β-transitions). The highest peak belongs to K_α-silicon, as the particles are very large, fully crystalline silicon NPs. EDX measurements allow also for quantitative analyses. The weight ratio of two elements in a sample can be obtained using the Cliff-Lorimer equation [235]. In the case of this sample, the oxygen content in this sample is very low with 94 atm% silicon versus only 6 atm% oxygen. The reason for this is the large diameter of the particles. Since oxygen is located at the surface and the surface-to-volume ratio for large particles is smaller, the oxygen content will also decrease.
Some of the primary electrons are scattered and can then hit the TEM grid. This is called stray radiation. Stray radiation also causes an X-ray signal that is generated by the material of the TEM grid, in this case Cu. Since the collimator on the EDX detector is pointing at the measured sample, the X-ray signal coming from the stray radiation should be minimized, however it can not be avoided completely. X-ray photons with higher energy (Cu K-line) can reach the detector better than ones with lower energy (L-line), therefore, the Cu-L peak will be smaller in case of stray radiation and larger, if Cu is a component of the sample. Typical sample depths of EDX range from 10 to 100 nm, which means that, in the case of NP, the full particle volume will be included in the results of the analysis of this technique.

3.2.5 Selected Area Electron Diffraction (SAED)

Crystalline samples can be analyzed inside a TEM using Selected Area Electron diffraction (SAED), where the user can select an area of the sample. This method uses the fact that

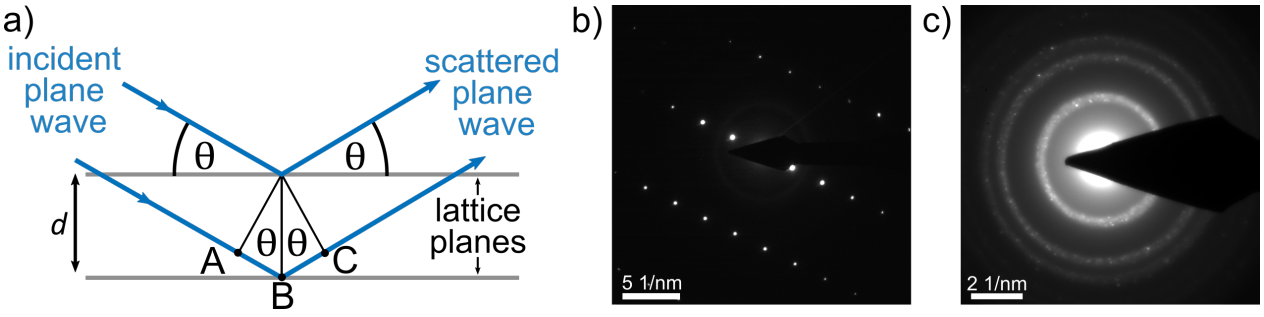

Figure 3.5: a) Diffraction of wave between the lattice planes of a crystal. Adapted from [234]. b) SAED spot pattern for monocrystalline silicon. c) SAED ring pattern for randomly oriented silicon nanocrystals. The diffraction patterns were taken by Martin Müller.

electron waves are diffracted on the crystal lattice due to their small wavelength. The diffraction is similar to light diffraction on a grid. Figure 3.5a shows the path difference $\overline{AB} + \overline{BC}$ of two waves with wavelength λ that are diffracted at adjacent lattice planes in distance d. Constructive interference of the order n and will be observed under angles θ_n following the Bragg condition:

$$2d \sin \theta_n = n\lambda \tag{3.9}$$

This equation allows to access information about the distance between lattice planes d, since λ is known from the electron energy and the angle θ can be measured. The diffraction pattern recorded by the TEM is strongly correlated to the topology of the sample. If the beam has been reflected by a single crystal or a small number of single crystals, a spot diffraction pattern will be observed (Figure 3.5b). This pattern can be used to determine lattice constants and the distances and angles between crystallographic planes. These are often distinctive for materials, allowing the user to distinguish between materials using this technique. If the illuminated area selected by the user contains many differently oriented crystals, the diffraction patterns of all these crystals superimpose and form an image of concentric rings, as shown in Figure 3.5c. This is the case for nanocrystals, since they are always present on the sample in a random orientation. The diameter of each ring then corresponds to the interplanar distance of a plane system present in the sample.

3.3 Fourier Transformed Infrared Spectroscopy (FTIR)

Fourier Transformed Infrared Spectroscopy (FTIR) is an analytical method that provides information about the chemical composition of a sample by using the characteristic frequencies of molecular vibrations. The basic principle uses a black body radiation source, which emits a beam of photons in the spectral region, typically ranging from 4000 to 400 cm^{-1}. This light can then be absorbed by the molecules present in the sample and induce vibrational and rotational transitions here. The following section introduces the basic principles of molecular vibrations as well as the experimental setup of a commercial FTIR spectrometer.

3.3.1 Molecular vibrations

The theoretical aspects of molecular vibrations can be explained using classical Newtonian mechanics as well as quantum mechanics. Considering the ideal case of harmonic oscillations, the potential V can be estimated from the solution of Hooke's law as a parabola. A molecule absorbs electromagnetic radiation of a certain energy $E = h\nu$, which then excites the molecular vibrations from the ground state ($n = 0$) to the first excited state ($n = 1$). The necessary energy E can be calculated from solving Schrödinger's equation:

$$-\frac{\hbar}{2\mu}\frac{\mathrm{d}^2\Psi}{\mathrm{d}x^2} + V\Psi = E\Psi\,, \tag{3.10}$$

using the reduced Planck constant $\hbar = \frac{h}{2\pi}$. For a diatomic molecule with atomic masses m_1 and m_2, the reduced mass is calculated as

$$\mu = \frac{m_1 m_2}{m_1 + m_2}\,. \tag{3.11}$$

Assuming a harmonic oscillator with force constant k, the potential can be written as $V{=}\frac{k}{2}x^2$. The solution of the Schrödinger's equation delivers energy states with quantum number $n = 0, 1, 2...$:

$$E_n = \left(n + \frac{1}{2}\right) h\nu = \left(n + \frac{1}{2}\right) \hbar\sqrt{\frac{k}{\mu}}\,. \tag{3.12}$$

A system will be excited by a photon of energy $E = h\nu$, if this energy is equal to the energy difference of two neighbored states with $\Delta n = 1$. In this case, the frequency of the incoming photon will be equal to the vibrational frequency ν of the molecule. An N-atomic molecule has $3N$ degrees of freedom, since each atom contributes 3 degrees of freedom with its movement in x-, y- or z-direction. From these $3N$ degrees of freedom, three correspond to the translation of the whole molecule in the direction of the three Cartesian axes. For non-linear molecules, three more degrees are reserved for the rotational movements. The linear molecule is invariant under rotation around the molecule's axis, therefore only two rotational degrees of freedom are accounted. This leaves $3N - 5$ for linear and $3N - 6$ for non-linear molecules as the degrees of freedom for vibration. Vibrational modes are classified in two main classes: valence vibrations (ν) which are characterized by a change in the binding lengths and deforming vibrations (δ, γ, θ), indicated by a change of binding angle [236]. The valance vibration (or stretching modes) can be further classified by their symmetry as symmetric (s) and asymmetric (as).

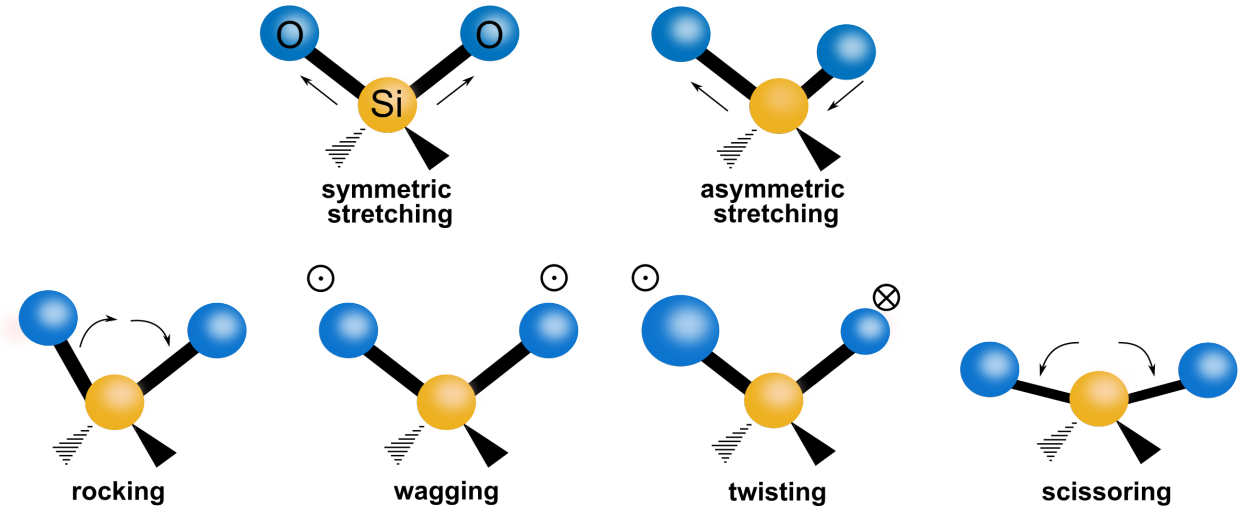

Figure 3.6: Different types of stretching and bending modes on the example of a SiO_2 molecule. The oxygen atoms are bound by double bonds, shown as a thick black line here. Valence vibrations are shown at the top, deforming vibrations at the bottom.

Figure 3.6 shows the different types of vibrational modes for the example of a SiO_2-molecule. The two double bonds to the oxygen atoms are indicated by a thick black line. Valence vibrations are shown at the top, deforming vibrations at the bottom. For symmetric stretching (top left), the change in dipole moment is zero ($\Delta\vec{p} = 0$), while for asymmetric stretching (top right) it is greater than zero ($\Delta\vec{p} > 0$). This figure also distinguishes the possible deformation modes, namely scissoring (δ), rocking (γ), wagging (κ) and twisting (τ).
Although FTIR spectroscopy is a commonly used and wide spread analytic method, it is not applicable without limitations. Depending on the type of the induced vibrations, they can be classified as either IR-active or IR-inactive. A vibrational mode is classified as 'IR-active' if it changes the dipole moment of the molecule [237]. For this reason, symmetric molecules such as nitrogen (N_2) and oxygen (O_2) cannot be observed using this technique.
For all other molecules, the frequencies of these vibrations are characteristic. Valence vibrations need more energy to be excited than deforming vibrations. Therefore, they are found mainly at wavenumbers above $1500\,\mathrm{cm}^{-1}$, while deforming vibrations are found at smaller wavenumbers.
Each molecule has a characteristic fingerprint pattern in the infrared spectrum, which is why FTIR is such an excellent tool to determine the chemical composition of a sample. Reference values in the literature (e.g. Socrates *et al.* [238]) can help identify molecules present in the sample, as they list the positions of the strongest absorption peaks.

3.3.2 FTIR spectrometer principle of operation

The operation principle of most interferometers that are used for today's infrared spectrometry is based on the two-beam interferometer designed in 1891 by Albert A. Michelson [239]. The *Michelson-Interferometer* divides a beam of radiation into two paths, which recombine after a path difference Δ has been introduced. As shown in Figure 3.7 the IR beam generated by an IR-source is focused onto a beam splitter. Half of the beam is directed onto a fixed mir-

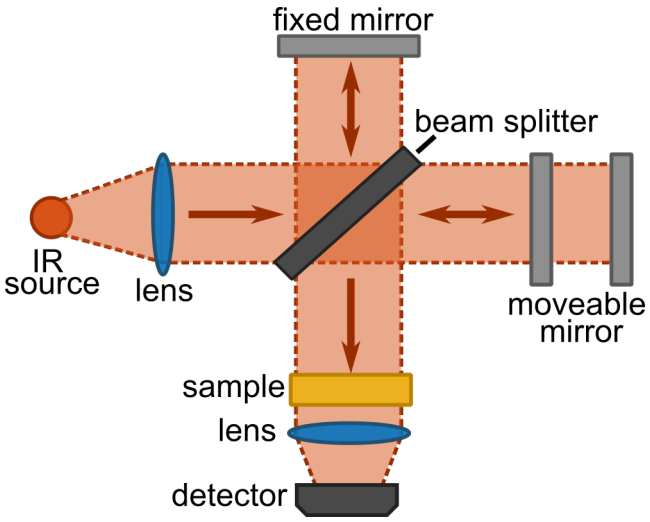

Figure 3.7: Schematic setup and functional principle of an FTIR spectrometer.

ror and then reflected, while the other half is directed onto a movable mirror and is reflected there. The distance between the moving mirror and the beam splitter can be varied. Depending on the distance of the beam splitter and the movable mirror, constructive or destructive interference takes place when the split paths are reunited. The resulting interferogram is the sum of all frequencies. This reunited beam now passes through the sample, where it is absorbed by the molecules and induces vibrations. A liquid-nitrogen-cooled MCT detector detects the remaining IR radiation by transferring optical signals to electrical signals. Using Fourier transformation, the summed up frequency information from the interferogram can be divided into single frequencies and then be displayed as an IR-spectrum. This process will be explained now in greater detail.

3.3.3 Generating a spectrum

To understand the process of spectrum generation, an idealized situation should be considered, where a source of monochromatic radiation produces a perfectly collimated, narrow beam of wavelength λ_0, with wavenumber

$$\nu_0 = \frac{1}{\lambda_0}\,. \tag{3.13}$$

The intensity corresponding to this wavenumber is denoted as $I(\nu_0)$. Furthermore, the beam splitter is considered ideal, which means that the reflectance and transmittance are exactly 50 %. A typical interferogram displays the signal intensity $I'(\Delta)$ measured at the detector as a function of the beam path difference Δ and is shown in Figure 3.8a. If both fixed and movable mirrors are equidistant from the beam splitter, the two beams are perfectly in phase upon recombination. At this point, the beams interfere constructively, meaning that the intensity of the beam passing to the detector is the sum of intensities. This leads to the so-called *center burst* observed in the interferogram. If the movable mirror is operated at a constant velocity, the signal at the detector will vary sinusoidally. A maximum in the detector will be registered every time that the path difference Δ is an integral multiple of

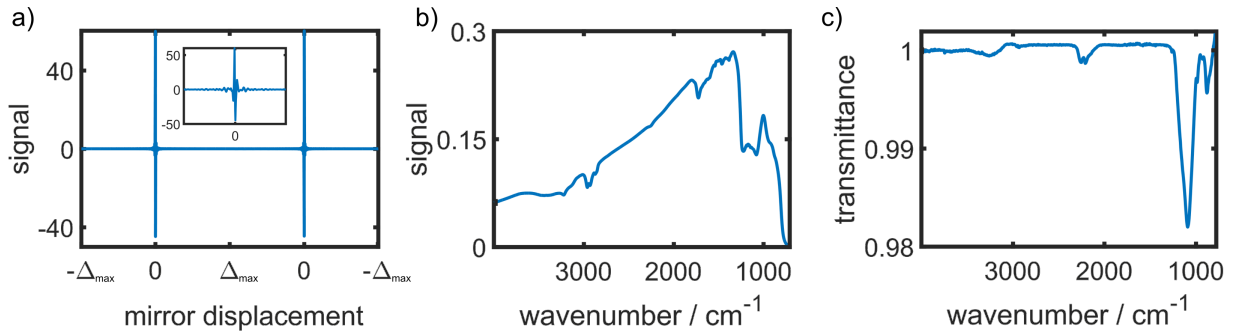

Figure 3.8: Steps in the generation of an FTIR spectrum. a) Interferogram displaying the mirror displacement and the corresponding measured signal with two center burst (inset) at zero path difference $\Delta = 0$. b) Source emission spectrum as a result of the Fourier transform of the interferogram. c) Transmission spectrum showing the absorption lines after division of two measurements.

the wavelength λ_0. Therefore, the intensity $I'(\Delta)$ measured in the detector will be equal to $I(\nu_0)$ when $\Delta = n\lambda$ $(n = 1, 2, 3...)$. At all other values of Δ, the intensity of the beam at the detector can be calculated by:

$$I'(\Delta) = \frac{1}{2} I(\nu_0) \left[1 + \cos\left(2\pi \frac{\Delta}{\lambda_0} \right) \right] . \tag{3.14}$$

It can be seen that this equation is composed of a constant component and a modulated component. The term interferogram specifically corresponds only to the modulated cosine term. Applying a *Fourier transform* $\mathcal{F}$ to this equation brings:

$$S(\Delta) = B(\nu_0) \cos\left(2\pi\nu_0\Delta\right) , \tag{3.15}$$

where the parameter $B(\nu_0)$ provides the intensity of the source at wavenumber ν_0, modified by the instrumental characteristics. The spectrum $S(\Delta)$ is therefore calculated from the interferogram using the cosine Fourier transform, giving this spectroscopy method its name. The Fourier transform of a single cosine wave interferogram is a single wavelength, or wavenumber of radiation. Mathematically, the entire spectrum from 0 to $+\infty$ (in cm^{-1}) could be measured at infinitely high resolution. But to achieve this in reality, the moving mirror would need to travel an infinitely long distance. Since only a limited value of Δ is experimentally possible, the resulting spectrum also has a finite resolution. Typical spectra measured in this thesis were collected in a wavenumber range of $700 - 4000\,\mathrm{cm}^{-1}$ with a resolution of $4\,\mathrm{cm}^{-1}$. The resulting source emission spectrum after a Fourier transform has been applied to the interferogram can be seen in Figure 3.8b. This spectrum is considered to be the "raw" source emission spectrum. Since the NPs are most often collected on a wafer, a comparison with a background reference spectrum is needed. Therefore, an FTIR measurement always includes the measurement of a background reference as a first step. The measured background spectrum is stored and as a last step of spectrum processing, the measured spectrum (Figure 3.8b) is divided by the background spectrum. Figure 3.8c displays the result as the final transmission spectrum calculated from the ratio of measured spectrum and background T/T_{BG} for silicon NPs measured on a silicon waver background. Here, the strongest line of absorption at $1100\,\mathrm{cm}^{-1}$ corresponds to the stretching vibrations in Si-O-Si.

Additional post-processing of the spectrum for display can typically include the subtraction of a baseline if needed and the calculation of the absorption spectrum.

3.4 Photoluminescence spectroscopy

The photoluminescent properties of silicon nanocrystals can be analyzed using photoluminescence (PL) spectroscopy. There are two different methods. In steady-state PL spectroscopy, the particles are continuously excited with a light source, and the emitted light is analyzed to determine the wavelength-dependent intensity. This technique offers information about the energy levels and the band gap of the SiNCs. A broad emission spectrum can be related to their size distribution and surface passivation [240]. Time-resolved PL spectroscopy extends the capabilities of steady-state analysis by providing temporal resolution of the luminescence decay after excitation. This method reveals the dynamics of exciton recombination and non-radiative processes. For SiNCs, time-resolved PL spectroscopy is particularly useful for distinguishing between surface-related recombination and quantum confinement-induced radiative lifetimes.

3.4.1 Steady-state photoluminescence spectroscopy

Steady-state PL spectroscopy uses a photon source to excite electrons in the sample material. After radiative recombination processes, a photon is generated and emitted as it has been already described in section 2.1.1. In this thesis, a Helium-Cadmium UV laser with a wavelength of 325 nm and $P_{\max} = 2.3\,\mathrm{mW}$ or 442 nm and $P_{\max} = 17\,\mathrm{mW}$ was used as the photon source. The light emitted by the sample material after excitation by the laser was collected via an optical fiber at a 45° angle and detected with an imaging spectrograph Shamrock 300i (Oxford Instruments) coupled with a CCD camera (Newton 971, Oxford Instruments). A low-pass filter was used to suppress wavelengths below 488 nm, leading to a sampled wavelength ranging from 500 to 1050 nm. For one spectrum, 200 accumulations at an acquisition time of 0.2 s were used. Using this setup, dry powder samples on a substrate and also wet samples, where the NPs are dispersed in a liquid, can be measured. For this thesis, only dry samples were used. Therefore, the resulting PL spectra have to be corrected for the substrate material. These corrections then allow for the direct comparison between different samples, even though the measurement of PL intensity gives only relative information about PL efficiency.

3.4.2 Time-resolved photoluminescence spectroscopy

Compared to steady-state PL spectroscopy, the time-resolved measurement allows access to information about the timescales of the recombination process with a resolution of hundreds of picoseconds. Because the lifetime of photoluminescence that originated from a NP's crystalline core is typically several orders of magnitude longer than that of the PL decay from defects, this method can be used to identify the origin of the PL signal. Several experimental techniques can be utilized to characterize the PL decay [241]. In this thesis a direct characterization method was used that requires only an optical excitation source and an optical detector. The excitation source was a pulsed femtosecond laser (Pharos SP) with a pulse

width of 150 fs. The pulse duration of the laser can be adjusted in accordance to the characteristic lifetime of the decay process. The signal was excited by pulses at 343 nm with a 1 kHz repetition rate and an intensity of 65 μJ/cm^2 which corresponds to approximately $1.2 \cdot 10^{14}$ photons per cm^2. The angle between the detection and excitation paths was 90°. The PL decay was detected using streak camera and the decay of the PL intensity signal can be fitted with a stretched-exponential function:

$$I = I_0 \cdot e^{-\left(\frac{t}{\tau}\right)^{\beta}}, \tag{3.16}$$

where I_0 is the initial intensity, t is the time, τ is the life time of the decay [242]. The average decay time as a function of emitted wavelength can be obtained using the following equation:

$$\tau_{\mathrm{av}}(\lambda) = \frac{\Gamma\left(-\frac{2}{\beta(\lambda)}\right)}{\Gamma\left(\frac{1}{\beta(\lambda)}\right)}\tau(\lambda), \tag{3.17}$$

where τ is the lifetime of a state at emission wavelength λ, $\Gamma(x)$ is the Gamma function and β is the dispersion parameter.

4 | Experimental setup

Several plasma sources with different electrode geometries have been tested during the course of this thesis. The most promising ones have been utilized and improved continuously. The publications related to this thesis use mainly one type of atmospheric pressure plasma jet, the so-called HelixJet, in two different size variants. The following chapter will first give an overview of the utilized plasma sources, with their specifications and intended purposes. A simulation of the gas flow using COMSOL Multiphysics is presented. After that, the *in situ* FTIR setup and the annealing stage are explained in detail. The chapter concludes with a demonstration on how two of these plasma sources can be connected to realize, for example, the combined synthesis and surface modification of NPs.

4.1 Atmospheric Plasma Source: HelixJet

The initial design of this plasma source was developed by Jan Schäfer *et al.* in 2019 [183]. In this publication, the HelixJet is a capacitively coupled atmospheric plasma source operated at radio frequency, which is applied to two helix electrodes forming a double-helix. The helix-shaped electrodes are placed around a quartz glass tube with an inner diameter of 0.7 cm and a total length of 12 cm. The gas, in this case argon, can be fed into the jet from the top with a varying gas flow between 100 and 2000 sccm. The electrodes are made from a flat copper wire (5 mm) with the helix consisting of nine total turns at an inclination of 57° and a distance of 5 mm. The special geometry of the electrodes was constructed to address a known problem of atmospheric pressure plasma jets, namely filamentation. Filaments are discharge channels inside the plasma that cause a steep gradient of all plasma parameters involved, such as electron density, temperature, or electric field [243]. Since the applications of these plasma jets include medical applications, a controlled homogeneous discharge is essential. Several studies of atmospheric plasma jets report on the formation of filaments inside the discharge. Several studies have also been devoted to understanding the formation and subsequent movement of these filaments experimentally [244] and through fluid modeling [245, 246]. For most atmospheric plasma sources, the formation of the filament is often chaotic and unstable in nature. For a plasma jet that is driven in the so-called "locked mode" [247, 248], they usually form equidistantly around the inner walls of the capillary and rotate around the symmetry axis. This phenomenon was observed in argon, krypton and neon, but not in helium [249]. For a cylindrical capillary with two ring electrodes, a stable solution could be found which contains three plasma filaments that incline inside the jet in a helix shape and rotate around the symmetry axis. The rotation frequency and the angle of inclination of the filaments are correlated. Small variations of the utilized gas flow and/or RF power were proven to result in instabilities of the filament's movement [244]. The electrodes of the HelixJet were constructed perpendicular to these inclined filaments. Although this helical structure complicates the structure of the resulting electric field, the resulting discharge was filament-free and mostly homogeneous [183].
An additional advantage of helix-shaped electrodes is the possibility to easily scale-up this setup. By simply adding more revolutions to the helix and therefore covering a longer part

of the capillary, the plasma volume can be easily increased. The resulting plasma will still be homogeneous along the middle axis of the capillary. In contrast to the case of ring electrodes, where the plasma will always be stronger around the rings and an increased distance between them requires much higher power to ignite or sometimes cannot be ignited at all. Other geometries involving more than two ring electrodes or parallel plate reactor setups offer scalability options, but at the cost of homogeneity.
This HelixJet design from Schäfer *et al.* was initially used for plasma-assisted additive manufacturing [183]. For this, the running jet was fed from the top with a polyamide powder. Particles introduced into the jet this way were melted and deposited below the jet. An analysis of the resulting samples revealed that the plasma-assisted process combined the features of laser sintering and heat treatment. The initial design of the jet was kindly made available for this thesis by Jan Schäfer. As a first step, two modifications have been carried out to improve the jet's ability to synthesize NPs from reactive gases.

4.1.1 Modifications to the jet

The HelixJet has been modified to optimize its operation for the synthesis of silicon NPs from the reactive silane gas. Since silane is a very electronegative gas, it depletes the plasma of electrons [250]. When high admixtures of silane are used, this effect weakens and ultimately extinguishes the plasma discharge. Additionally, high admixtures of silane into the general gas feed of the HelixJet will lead to increased deposition of silicon on the jet walls. Deposition is an unwanted effect in atmospheric plasma jets, as a thin layer of material can influence the plasma properties negatively. For smaller capillary dimensions, increased deposition can even clog the capillary, although this effect has been reported to be the strongest for powder deposition [251] or small-dimensional plasma jet nozzles [252]. A combination of two modifications is introduced to combat these two problems: First, the admixture of noble and reactive gases is split. In the original version of the HelixJet, noble and reactive gases had to be premixed and fed into the jet.

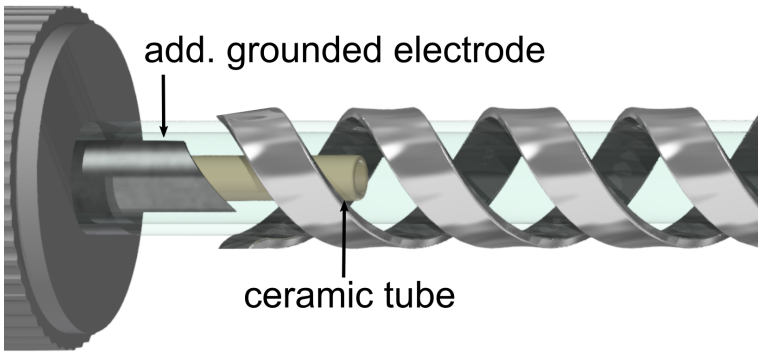

Figure 4.1: CAD drawing highlighting the two modifications in the form of an additional grounded electrode and a ceramic tube for the on-axis injection of reactive gases. The additional electrode is placed inside the glass tube and cut to the same angle as the neighboring driven Helix electrode.

As it can be seen in Figure 4.1, a ceramic tube with a diameter of 4 mm and a wall thickness of 0.7 mm has been placed on the middle axis of the jet. Noble gases such as argon or helium

are now fed on the outer part close to the jet walls and the reactive gas silane is now only introduced to the jet on the middle axis.
For a certain combination of flows for each inner and outer capillary, a laminar flow without vortexes can be established, which consequently reduces the diffusion of reactive gas and particles towards the jet walls. As a result, wall deposition is reduced. The flow inside the modified HelixJet has been simulated using COMSOL Multiphysics® in the following section.
The placement of the ceramic tube has an additional advantage which is in relation to the second modification: An additional grounded electrode in the form of a thin metal sheet is placed inside the quartz glass capillary in close proximity to the first driven helix electrode. The metal sheet was cut at the same angle as the helix electrodes. This placement should ignite a first strong plasma between the additional electrode and the first helix revolution, since only noble gases are present here. Radiation and electrons from this plasma help to maintain the plasma downstream of the jet, which then also contains the reactive gas.

4.1.2 Simulations of the gas flow

The modification of the on-axis gas injection of the reactive gases is only able to efficiently reduce the deposition on the jet walls for a configuration, in which the flow established inside the capillary is laminar. For a laminar flow, the inner flow of the reactive gas is shielded by the outer flow and, therefore, cannot reach the walls. The chosen values for the flow in the inner Φ_i and outer Φ_o capillaries will depend on the diameters of the capillaries. To estimate flow values that result in laminar flow, a fluid flow simulation was performed. This was realized by a 2D axis-symmetric model in COMSOL Multiphysics® 5.1. The model geometry depicts the gas channel formed by the outer and inner capillaries. Two domains for the carrier gas flow (helium) and for the reactive gas flow (0.01 % silane in argon) were established. The fluid equations are solved using the finite element method. Therefore, the model geometry is discretized to a mesh on which the equations are solved. The mesh used for the model is a so-called physics-controlled mesh with 223914 elements. The model parameters are the flows in both the inner Φ_i and outer Φ_o capillaries.
To calculate the fluid velocity field, the so-called "low Reynolds k-ε" flow model [253] is used, which can depict flow oscillations. However, in case of a vortex free and laminar behavior of the flow, the model is also suited to describe this fluid velocity field. To validate the use of a low Reynolds number model, the Reynolds number Re can be calculated using the following equation:

$$\mathrm{Re} = \frac{uL}{\nu} = \frac{\rho u L}{\mu}\,, \tag{4.1}$$

where u is the flow speed, ρ the density and μ the dynamic viscosity of the fluid. L describes a characteristic length. Since the Reynolds number is different for the different parts of the jet, it will be calculated for the most critical part, which is the ceramic tube that has the smallest diameter. Therefore, L will be the inner diameter of the ceramic tube. Using the density ($\rho = 1.6617\,\mathrm{kg/m^3}$) and dynamic viscosity ($\mu = 2.2294 \cdot 10^{-5}\,\mathrm{kg/ms}$) for argon and the highest possible fluid velocity for a flow of 800 sccm (2.5 m/s) this equals a Reynolds number of 486 which can be still considered as low, since the transition between laminar and turbulent occurs at a Reynolds number between 2000 and 13000 [254].
The study of the fluid velocity field is based on several boundary and initial conditions as well as physics-based equations. The initial conditions are defined based on a stable state

with a predefined stable flow into the jet. The problem is solved using the time-independent incompressible Navier-Stokes equations for conservation of mass and momentum:

$$\rho \nabla \cdot \boldsymbol{u} = 0\,, \tag{4.2}$$

$$\rho(\boldsymbol{u} \cdot \nabla) = \nabla \cdot \left[-p\boldsymbol{I} + \mu(\nabla \boldsymbol{u} + (\nabla \boldsymbol{u})^T)\right]\,. \tag{4.3}$$

With ρ and μ again being the density and dynamic viscosity of the respective gas (argon or helium), p is the pressure and $\boldsymbol{I}$ represents a unit diagonal matrix.

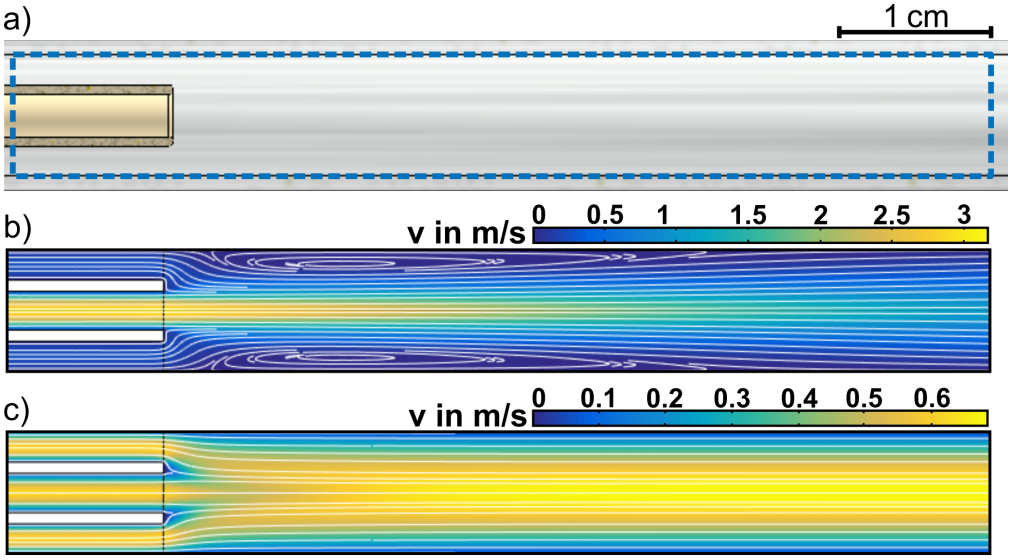

Figure 4.2: a) CAD cross-section view of both capillaries of the jet. The area in which flows are simulated is highlighted with a dashed blue line. b) Simulation results for the velocity field with input flows of inner and outer capillary being the same ($\Phi_\mathrm{o} = \Phi_\mathrm{i} = 400\,\mathrm{sccm}$). A flow field with vortexes can be observed. c) Simulation results with an optimized ratio of inner and outer flows ($\Phi_\mathrm{i} = 100\,\mathrm{sccm}$; $\Phi_\mathrm{o} = 700\,\mathrm{sccm}$).

The simulated velocity fields are shown in Figure 4.2. Figure 4.2b shows the velocity field for both inner and outer flows at 400 sccm. The established velocity field shows a vortex as can be seen on the white stream lines, which form clear vortexes directly after the exit of the ceramic capillary. Additionally, the overall peak flow with 3 m/s is high compared to the flow profile shown in Figure 4.2c. Here, the outer flow was chosen to be 700 sccm compared to the inner flow of 100 sccm. Under optimized flow conditions, the resulting velocity field is vortex-free and the overall peak velocity never crosses a value of 0.7 m/s. Based on this first simulation step, the resulting velocity field can be used for a time-dependent simulation of the transport of admixed species by convection and diffusion. The conversation of mass of a species i can be described using

$$\frac{\delta}{\delta t}(\rho\omega_i) + \nabla \cdot (\rho\omega_i \vec{u}) = -\nabla \cdot \vec{j_i} R_i\,, \tag{4.4}$$

with ω_i describing the number density, $\vec{j_i}$ the corresponding diffusive flux and R_i the reaction rate expression of each species. The simulation was performed using a mixture-averaged

diffusion model, where the diffusive flux is formulated in terms of a mixture-averaged diffusion coefficient representing the diffusion of each species into the resulting mixture [253].

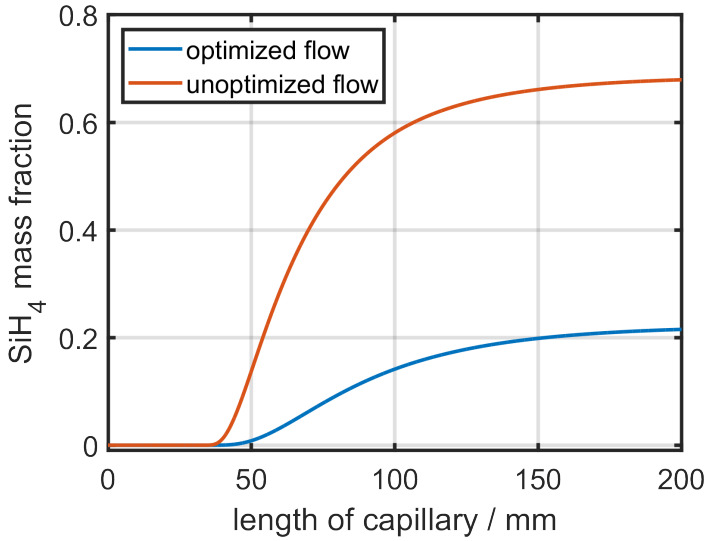

Figure 4.3: Mass fraction of silane compared to the feed gas along the wall of the capillary. If the flow is not optimized (red), the mass fraction of silane at the capillary wall is up to 70 % close to gas feed. This can possibly result in a high deposition. For an optimized, vortex-free flow (blue) the mass fraction of silane drops to around 20 %.

Figure 4.3 shows the mass fractions of silane compared to the feed gas along the capillary wall of the jet. If the flow is not optimized, the mass fraction of silane at the wall is almost 70 %, indicating that an increased amount of silane is reaching the wall and can induce deposition there. This decreases strongly to only 20 %, when an optimized flow ratio is used.

4.1.3 Smaller version of the jet

A smaller version of the HelixJet was developed to increase the power density inside the jet with the initial aim to achieve the crystallization temperature for silicon NPs without the need for an additional annealing stage or the selective heating using hydrogen. Figure 4.4 highlights the size comparison between the original sized modified HelixJet version (bottom) and the downsized version (top). The smaller version also uses a quartz glass capillary, but the dimensions here are smaller, with an inner diameter of only 3 mm and a wall thickness of 1 mm. For a better comparison, the power density and residence time in the plasma have been calculated for both small (S) and large (L) HelixJet. The power density ρ is calculated using the RF power of the generator P and the plasma volume V that is enclosed by the capillary with inner diameter d_i below the electrodes covering a section with length l:

$$\rho = \frac{P}{V} = \frac{4P}{l \cdot \pi d_\mathrm{i}^2} \,. \tag{4.5}$$

Using the same power of 150 W set on the generator for both jets, the power densities are $\rho_\mathrm{S} = 530\,\mathrm{W cm^{-3}}$ for the smaller version compared to only $\rho_\mathrm{L} = 30\,\mathrm{W cm^{-3}}$ for the larger jet.

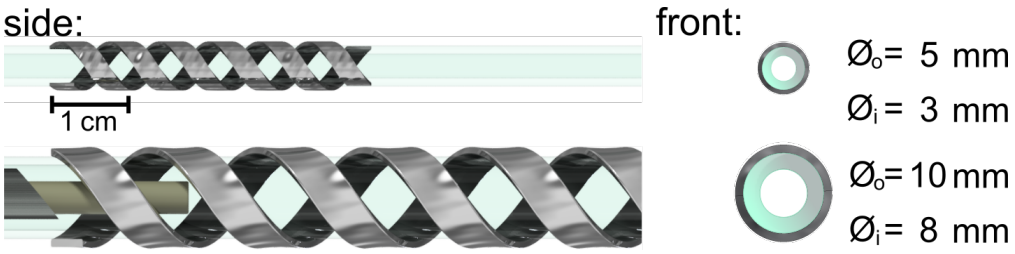

Figure 4.4: Comparison of the side and front view of the two different sized HelixJet versions.

The residence times of particles inside those plasmas can be calculated as a function of the overall gas flow Φ in sccm and the inner tube diameter d_i and plasma length l:

$$t(\Phi) = \frac{15\pi l d_\mathrm{i}^2}{\Phi}\,. \tag{4.6}$$

Taking the average flows utilized for those jets, the residence times can be estimated to be $t_\mathrm{S} \approx 84\,\mathrm{ms}$ for the small jet and $t_\mathrm{L} \approx 380\,\mathrm{ms}$ for the big jet. Even though the residence time for the particle is much longer in the bigger jet, the plasma density is significantly lower. It was still possible to synthesize nanocrystals using the bigger jet with the addition of hydrogen (enhanced selective heating due to hydrogen recombination), or using a subsequent annealing stage after the particle synthesis. Both options will be discussed in chapter 5. Attention should also be drawn to the fact that for the smaller jet, the helix inclination is chosen in a way that does not prevent the filamentation but instead favors it. This filamentation and higher power densities were beneficial for the nanocrystal synthesis and it was possible to produce monocrystalline NPs with sizes ranging from 3 nm to 80 nm. This will be discussed in Chapter 8. Modifications in the form of an additional electrode and on-axis gas injection were waived. Instead, this jet was used for the plasma-assisted synthesis of metal NPs, where a consumable metal wire was inserted on the jet axis (see Chapter 7).

4.2 *In situ* FTIR setup

FTIR spectroscopy is an excellent tool to gather information about the chemical structure of a sample. For NPs, the most common analysis technique is *ex situ* FTIR, where the particles are usually deposited onto a substrate that is transparent in the infrared. After deposition, the particles are transported to and placed inside the FTIR spectrometer. Then the spectrometer is evacuated and the measurement is done under vacuum conditions. An *in situ* setup, on the other hand, is able to study the NPs under the operating conditions in real time, ensuring that the measured data represent the nanoparticle state upon deposition. For NPs, many of their key processes occur on the surface, where functional groups and ligands react. *In situ* FTIR is ideal for monitoring these surface-specific processes as it is able to capture changes in the surface chemistry directly when they take place. Realizing an experimental setup for *in situ* FTIR measurements is more complex than using the commercial *ex situ* method. Figure 4.5 shows the core part of the reflective *in situ* setup that was utilized in this thesis. It consists of a metal part that has been laser sintered in an additive manufacturing process to accommodate all requirements. It consists of three separate chambers. The IR beam is coupled out of the FTIR device and enters the first chamber. Here, it is reflected by a mirror

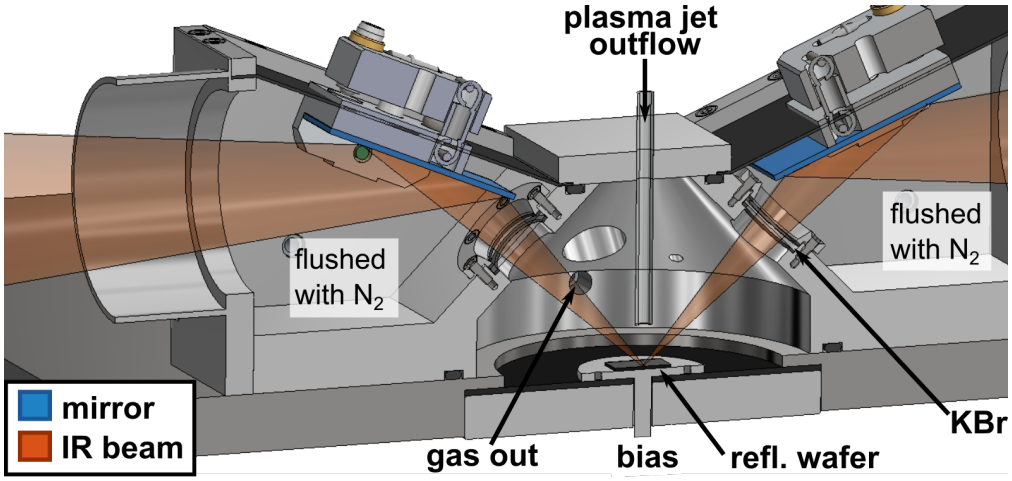

Figure 4.5: Sketch of the *in situ* FTIR setup. The IR-beam is directed out of the FTIR device onto a mirror. The beam path is flushed with nitrogen.

(blue) and passes through an infrared transparent potassium bromide (KBr) window into the middle chamber. The middle chamber is filled with gases from the outflow of the plasma jet, which is positioned above the setup. Particles exiting the jet are carried downwards and through the IR beam onto a silicon wafer or a polished stainless steel substrate. The substrate can be positively biased (up to +10 kV) to increase the particle yield. The IR beam is focused on the spot directly below the plasma jet outflow. A part of it is absorbed here by the sample but also by gases that are present in the atmosphere above the sample. This can be used as an indicator for the amount of reactive gases that were not consumed in the jet. After being reflected from the wafer, the IR beam passes through a second KBr window into the third chamber, where it is reflected by a second mirror into the detector. Both outer chambers are constantly flushed with dry nitrogen to ensure that the IR-beam is not disturbed by CO_2 and H_2O present in the air.

4.3 Annealing stage

The annealing of NPs has been used not only for the transformation of amorphous into crystalline material [255, 256], but also for the reduction of surface defects [257, 258]. Annealing can be carried out at various pressures reaching from vacuum conditions to atmospheric pressure. For this thesis, the annealing stage is operated at atmospheric pressure and can be connected directly to the atmospheric plasma jet output. It consists of a stainless-steel tube spiral inside a muffle furnace that can be heated to up to 1300° C. The stainless-steel tube has an inner diameter of $d = 4\,\text{mm}$ and the total length of the spiral is $l = 2\,\text{m}$. The tube material is chosen to be stainless steel (No. 1.4571) which, in addition to iron (Fe), contains 16.5 % chromium (Cr), 10.5 % nickel (Ni) and up to 2 % of each manganese (Mn) and molybdenum (Mo), as well as possible traces of carbon, silicon, titan, phosphor and sulfur. NPs exiting the jet enter this stainless-steel tube. The time-of-flight t inside the annealing stage can be calculated using equation 4.6. For gas flows between 200 and 800 sccm they have times of flight between 2 and 8 s inside the oven. After passing this annealing stage, they can be analyzed using either the scanning mobility particle sizer or the FTIR. They can also

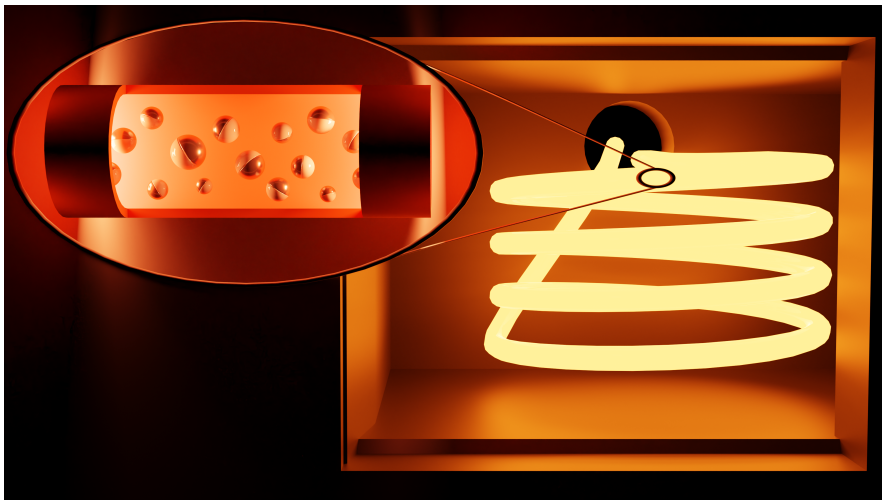

Figure 4.6: Three-dimensional model of the heated muffle furnace containing the glowing stainless steel drift tube. The inset shows the formation of Janus particles.

be collected on a TEM grid for microscopy analysis. The temperature inside the furnace is monitored using a Type K thermocouple. Figure 4.6 depicts the situation inside the annealing stage using a three-dimensional rendered model. The stainless steel coil is depicted in the glowing state, which was reached at high temperatures inside the furnace. The stainless steel tube enters and leaves the oven through a hole in the back. The inset on the left-hand side shows the situation inside the tube, where in this case Janus particles are passing through. This annealing stage was used for the synthesis of large monocrystalline particles in chapter 5, but it also played a crucial role in the synthesis process of Janus particles, as will be discussed in chapter 6.

4.4 Double jet setup

A double jet setup involving two or more of the presented atmospheric pressure plasma jets placed sequentially offers several advantages. As already mentioned, the surface of an NP is the key for tailoring its properties. In such a double jet setup, one jet can be used for the NP synthesis and the second one can serve to passivate or modify the surface of those NPs, creating a flexible and highly tunable process. By separating the functions of NP generation and surface modification, a double jet setup allows for fine-tuning of each process independently. The first jet can focus on particle formation, optimizing parameters such as particle size and morphology, while the second jet can be adjusted to precisely control surface passivation without interfering with the particle synthesis.
Using silane in the first jet, silicon NPs can be produced. As these particles move downstream, they enter the second jet, where a passivating gas is introduced. The plasma in this second jet can functionalize the NP surfaces by forming a stable layer, protecting the core material and/or enhancing its properties for specific applications.
For this thesis, a symmetrical gas connector has been designed in four versions to realize a double jet setup. A CAD sketch of one version of the connector in both a full (left) and a half-section view (right) is shown in Figure 4.7. The different versions of the connector

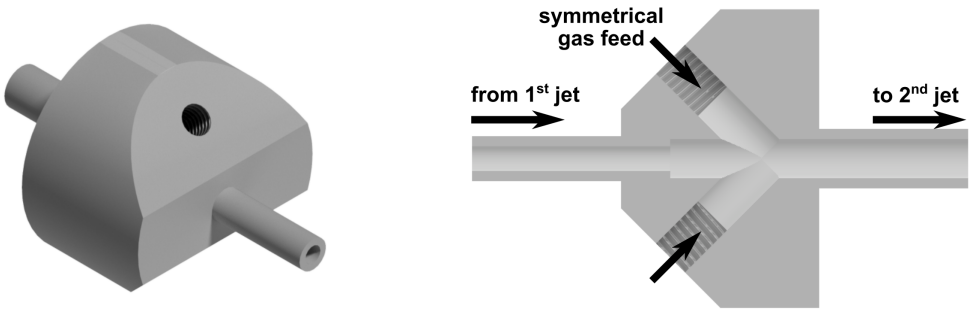

Figure 4.7: CAD sketch of the full connector on the left and a half section view on the right indicating the gas flows.

allow to connect either two small or two large HelixJets with each other, or to allow a combination of both sizes, where either size can be the first jet. The connector is designed to feed additional gases for the second jet at an angle of 45°, to avoid the formation of vortexes and the consequent loss of particles. In chapter 8, the gas connector for two small HelixJets is utilized for the combined synthesis and methane passivation of silicon NPs, but there are several other applications for such a double jet setup, for example, the synthesis of core-shell NPs.

5 | Synthesis of photoluminescent silicon nanocrystals

Publication I: Silicon nanocrystal synthesis with the atmospheric plasma source HelixJet

Authors	M. Dworschak, N. Kohlmann, F. Matějka, P. Galář, L. Kienle, J. Schäfer, J. Benedikt
Journal	Plasma Processes and Polymers [259]
Utilized Diagnostics	Power measurements, SMPS, SEM, TEM, steady-state and time-resolved PL spectroscopy
Own Contribution	Approx. 75%

Motivation:

The advantages of the modifications to the HelixJet that were introduced in section 4.1.1 should be tested on their ability to enable a long-term operation with higher reactive gas admixtures and less deposition. Using silane and hydrogen as reactive gases, plasma parameters should be found that result in the synthesis of photoluminescent silicon nanocrystals. Additionally, the validity of the SMPS size selection was tested by comparing a sample of 50 nm-particles as given by the SMPS, to the SEM images.

Main results:

The modifications to the HelixJet resulted in the possibility of long-term operation with high amounts of reactive gases, thus increasing nanoparticle yield. Various varieties of nanomaterials could be produced in the range 3 to 100 nm, depending on the operating parameters of the jets. The admixture of hydrogen alongside the high RF powers led to the formation of nanocrystals with a strong photoluminescence intensity. Post-synthesis in-flight annealing allowed the formation of large crystalline NPs. Additionally, the discrepancy between SMPS measurements and reality due to agglomeration (see section 3.1.5) was highlighted.

Received: 15 July 2022 | Revised: 15 September 2022 | Accepted: 4 October 2022

DOI: 10.1002/ppap.202200129

RESEARCH ARTICLE

PLASMA PROCESSES AND POLYMERS

Silicon nanocrystal synthesis with the atmospheric plasma source HelixJet

Maren Dworschak[1] | **Niklas Kohlmann**[2] | **Filip Matějka**[3] | **Pavel Galář**[3] | **Lorenz Kienle**[2] | **Jan Schäfer**[4] | **Jan Benedikt**[5]

[1]Group of Experimental Plasma Physics, Institute of Experimental and Applied Physics, Kiel University, Kiel, Germany

[2]Group of Synthesis and Real Structure, Institute of Material Science, Kiel University, Kiel, Germany

[3]Department of Thin Films and Nanostructures, Institute of Physics, Czech Academy of Sciences, Prague, Czech Republic

[4]Division Materials and Surfaces, Leibniz Institute for Plasma Science and Technology, Greifswald, Germany

[5]Kiel Nano, Surface and Interface Science KiNSIS, Kiel University, Kiel, Germany

Correspondence
Jan Benedikt, Institute of Experimental and Applied Physics, Experimental Plasma Physics, Kiel University, Leibnizstr. 19, Kiel 24098, Germany.
Email: benedikt@physik.uni-kiel.de

Funding information
Deutsche Forschungsgemeinschaft, Grant/Award Numbers: 426208229, KI 1263/17-1

Abstract

The HelixJet, a plasma source operating under atmospheric pressure with RF power, was used for the synthesis of silicon nanoparticles (Si-NPs) in the context of relevance in nanomedicine, sensor technology, and nanotechnology. The HelixJet was operated with a variety of He/Ar/H_2/SiH_4 gas mixtures to characterize the Si-NPs in regard to their size, crystallinity, structure, and photoluminescence. Distinct varieties of nanomaterials in the size range from 3 nm to over 100 nm were synthesized depending on the operation parameters of the HelixJet. Admixture of H_2 alongside high RF powers led to the formation of crystalline nanoparticles with a strong photoluminescence intensity, where the photoluminescence properties as well as the nanocrystal synthesis yield were tunable by adjustment of the synthesis parameters. Post-synthesis in-flight annealing allowed the formation of large crystalline nanoparticles. In addition, the experiments conducted in this study resulted in a design improvement of the HelixJet plasma source that extends the stability of the operating range. Furthermore, the added spatial separation of the He/H_2 and He/Ar/SiH_4 streams (SiH_4 injection on-axis) minimizes material deposition within the HelixJet and enables continuous long-term operation.

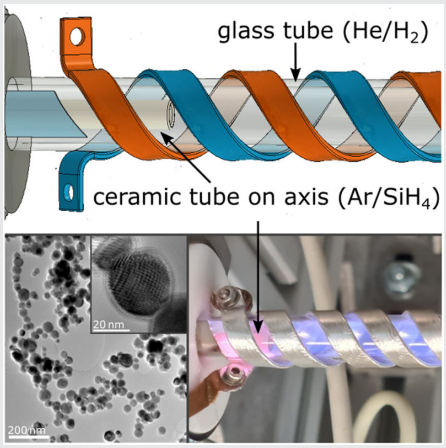

KEYWORDS
atmospheric pressure plasmas, photoluminescence, silane, silicon nanocrystals

1 | INTRODUCTION

Silicon nanoparticles (Si-NPs) represent a class of nanomaterials that are currently being studied very intensively since their application in nanotechnology and in the field of life science opens up surprising possibilities. For example, Fu et al. published the unique optical characteristics of spherical Si-NPs.[1] Depending on the size of the Si-NPs and the wavelength of the incoming light, the Si-NPs exhibit a direction-dependent light scattering. This feature is crucial for the production of new metamaterials and nano-antenna devices. For light-on-chip technology, the production of defined Si-NPs with the required shape and size is absolutely essential. The current technology uses complex vacuum reactors for this.[2] Precise and efficient production of Si-NPs at atmospheric pressure would thus be a breakthrough.

Another use of optically active nanomaterials is their in vivo application for diagnostic and therapeutic purposes. These nanomaterials have to meet many important requirements such as being nontoxic and not triggering undesirable metabolic reactions. They should be broken down systematically in a short time and not accumulate in the body. In this context, Park et al. 2009 published a study that points to the relevance of porous silicon nanoparticles as a drug carrier, which has not yet been explored sufficiently.[3] Their fundamental diagnostic properties are near-IR photoluminescence, which allows monitoring of both their accumulation and degradation in vivo.

Moreover, a special subclass of Si-NPs is silicon nanocrystals (Si-NCs) with diameters below 10 nm. The quantum confinement effects result in a changed band structure and direct band-gap behavior with the band gap being controlled by the nanoparticle size and its passivation. Si-NCs are investigated since the 1990s with increasing interest due to their potential exciting applications in the microelectronic, photonic, photovoltaic, and nanobiotech industries.[4] Low-pressure plasmas have been used as the method of choice for nanocrystal generation due to a very good size control with narrow size distributions and the ability of surface passivation.[5] This is maintained by the nonequilibrium nature of the low-pressure plasmas, where a negative nanoparticle charge prevents their agglomeration and where selective heating due to surface recombination processes promotes particle crystallization even under conditions with low gas temperature.[6]

Atmospheric pressure nonequilibrium plasmas have been investigated as alternative sources for the synthesis of Si-NCs as well.[7–11] The advantages of this technology are the operation without vacuum equipment which opens up modular configuration options in situ or the combination with other systems. In particular, the particle extraction and connection to a scanning mobility particle sizer (SMPS) are very easy and allow for qualitative improvements in technology regarding the control of particle size distribution. However, the disadvantages include low particle yields, low efficiency, clogging of plasma nozzles, and thus limited stability and reproducibility of the process.

The above examples show the urgency of the Si-NP studies with regard to their controlled efficient production resulting in a defined shape, size, and optical activity. For this study, we decided to investigate the synthesis of Si-NPs and Si-NCs by means of a plasma jet introduced by Schäfer et al. in 2020 as the HelixJet, which is operated at atmospheric pressure by RF power.[12] The HelixJet has demonstrated surprising versatility in recent applications due to its unusual properties compared to other plasma nozzles. This is mainly based on the radial homogeneity of its plasma across and along the discharge space, where other sources of atmospheric plasma contract into a filamentary structure. In HelixJet, filaments are not formed, even in a tube with a diameter of 1 cm. In addition, it is a source that is economical in terms of gas consumption. These properties have been advantageously used for the defined treatment of plastic microparticles used for 3D printing or for the synthesis of stoichiometrically pure silica as corrosion protection.[12,13]

2 | EXPERIMENTAL SETUP AND DIAGNOSTICS

2.1 | HelixJet

The so-called HelixJet is a plasma jet with a double-helix electrode configuration (see Figure 1a). The design of the HelixJet was inspired by the investigations on self-organization phenomena in the plasma jet named ntAPPJ.[14] It could be shown previously that filaments tend to self-assemble. They form equidistant groups and, under certain conditions, are able to rotate at high speeds.[15] During filament rotation (locked mode), filaments are twisted spirally while the inclination correlates with the radial velocity. The HelixJet was designed in a way that the electric field lines match the tilt of filaments in the original self-organized jet. Hence, the stable and uniform conditions of the plasma generated by the HelixJet can be explained by the synergy between self-organization mechanisms and the optimal spiral arrangement of the double-helix electrodes. The electrodes are placed around a 22 cm long quartz

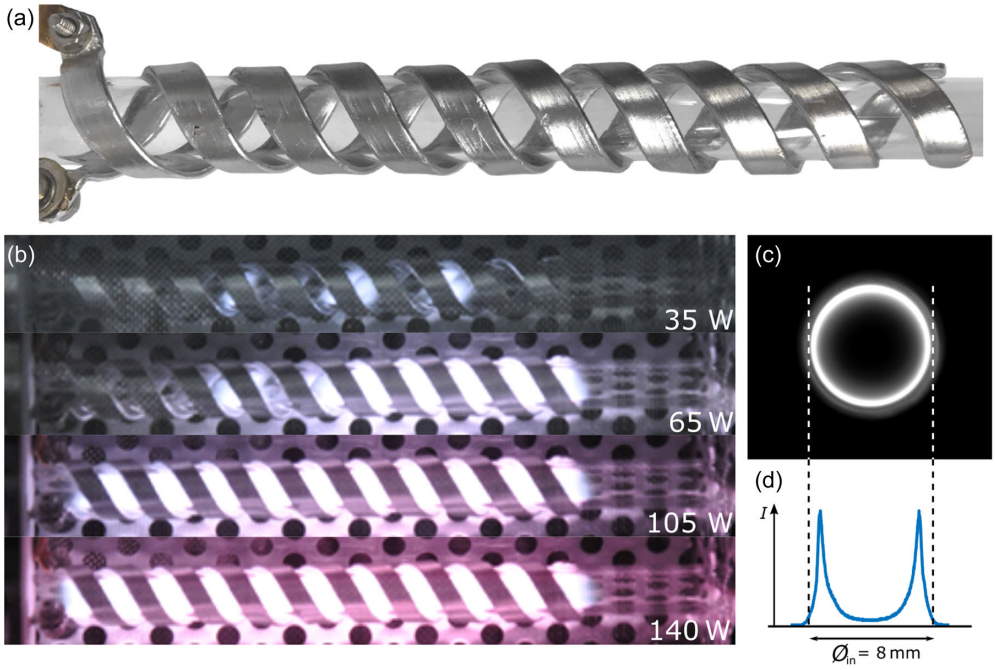

FIGURE 1 Side-view images of the HelixJet without plasma (a) and with a pure helium plasma at various powers (b). Increasing the applied power enables the jet to be operated at its full length. The front view taken with a telecentric lens (c) and the corresponding intensity profile (d) of a plasma emission with 5 ppm silane concentration.

glass tube with an inner diameter of 8mm and a wall thickness of 1 mm. One of the helix electrodes is grounded, while the other one is driven by a 13.56 MHz generator with impedance matching. Powers entering the matchbox are measured with a Z-Scan RF measurement probe (advanced energy). Measured powers range from 20 to 230 W with corresponding peak-to-peak-voltages between 400 and 700 V_{pp}.

In general, the HelixJet can be operated in noble gases with admixtures of molecular gases or particles. Here, the plasma has been generated in helium at flows as low as 100 standard cubic centimeters per minute (sccm) and with small admixtures of SiH_4 as a precursor. During its operation, the jet is always cooled with a constant flow of compressed air to ensure uniform and reproducible behavior. An example of the HelixJet's discharge is shown in Figure 1b. This side view shows how the discharge is able to fill the whole volume in between the electrodes when the power is increased. Figure 1c,d shows a front image taken with a telecentric lens and a Basler acA1440 camera and the corresponding light emission intensity profile at an admixture of 5 ppm, respectively. The radial profile of the emitted radiation shows increased intensity towards the walls of the jet, which is the typical behavior of an atmospheric plasma operated in γ-mode as described in Yang et al.[16] Apart from this, the intensity profile shows spatial homogeneity, which has a significant effect on the efficiency of the process in the tube. The resulting plasma density is expected to be homogeneous across the tube as presented for example in Shi et al.[17] Based on a comparison with the published results in an argon discharge at a time resolution of ns,[12] it can be assumed that even at the conditions here, the discharge is quasi-stationary without any visible modulations.

2.1.1 | HelixJet modifications

The particle yield at atmospheric pressure is low when working with small reactive gas admixtures. For most analytical methods and applications it is crucial to have a sufficient amount of nanoparticles collected in a short time. To achieve this, the admixture of silane has to be increased. However, when the HelixJet is operated with a large admixture of strongly electronegative silane, the discharge becomes unstable. This can be observed over the extension of the discharge which is not filling the whole interelectrode volume anymore and gets shorter (as it is seen for the helium case and low power operation

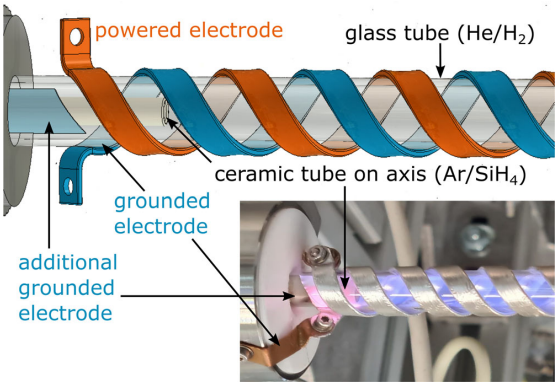

FIGURE 2 CAD-sketch of the modified HelixJet (top) and depiction of the actual experiment (bottom). Additionally to the helix-shaped electrodes, a grounded tantalum electrode (blue) has been inserted into the quartz glass tube. It is placed in close proximity to the driven electrode (red). The gas inlet has been altered to a configuration, where the silane is injected on-axis to reduce deposition on the tube's inner wall.

in Figure 1) or extinguishes completely. This effect can be counteracted by increasing the applied power until the discharge is filling the whole volume again, but this power is limited in our case. Additionally, powers exceeding 230 W have been causing overheating of the electrodes. The original HelixJet setup has been, therefore, modified with an additional electrode inserted into the glass tube and with the on-axis injection of the reactive gas as shown in Figure 2.

The additional grounded electrode is cut at the same angle as the helices and is positioned in close proximity to the driven RF-helix-electrode. With these modifications, a plasma is easily ignited in the large electric field at this additional grounded electrode. The absence of silane in this region (see later) prevents any deposition here. This additional plasma provides ions, electrons, and high-energy photons that facilitate the ignition and operation of the regular plasma inside the HelixJet. Tantalum was chosen as a material for this second electrode due to its lower vapor pressure at elevated temperatures.[18] The second modification is concerning gas injection. With the previous model, all gases (reactive and noble) were premixed and then fed into the plasma. The on-axis gas injection approach splits the gas injection into an outer and inner flow. Noble gases and hydrogen can be fed through the outer flow whereas the silane diluted in noble gas is fed through the ceramic tube on the jet's axis. The ceramic tube has a diameter of 4 mm and a wall thickness of 0.7 mm. This approach limits the contact of the high-density plasma at the quartz glass tube inner wall with silane and thus reduces thin film deposition there. The position of the inner capillary is adjusted in a way that injects the silane downstream of the additional grounded electrode to prevent particle formation or material deposition there. The evidence of the spatially separated gas injections can be seen at the bottom right of Figure 2. The first plasma consisting of only the carrier gas helium is emitting in orange, while the following plasma contains the additional admixture of 0.01% silane diluted in argon and is therefore glowing in the typical violet argon color. These measures result in an even longer lifetime of the HelixJet (half a year and counting) compared to a premixed gas injection (deposition visible after a day) due to further elimination of material deposition inside the jet.

2.2 | SMPS

SMPS can be used to measure size distribution functions from a polydisperse stream of submicrometer particles down to diameters approaching 1 nm. The SMPS used in this paper was a TSI Universal-SMPS (Model 3938). Particles exiting the HelixJet pass through an aerosol neutralizer, where a known charge distribution is established according to Wiedensohler et al.[19] The particles are then fed into the differential mobility analyzer (DMA). In this paper, two different DMAs were used. The 1-nm-DMA (Model 3086) was used for well-resolved classification of particles between 1 and 50 nm. The Long DMA (Model 3081A) was used for particle sizes up to 1000 nm. Both models consist of two aligned cylindrical electrodes with respective radii r_i and r_a and length L. The inner cylinder is charged positively. Only particles of a certain electric mobility μ can pass the DMA and reach its outlet for a set voltage U_{DMA}.

$$U_{\mathrm{DMA}} = \frac{Q \times \ln\left(\frac{r_i}{r_a}\right)}{2\pi L \mu}, \tag{1}$$

where Q describes the gas volume flow. Under the assumption of spherical particles, the particle diameter d and electric mobility μ are correlated by Stokes' Law.

$$\mu = \frac{neC}{3\pi\eta d}, \tag{2}$$

where n is the number of elementary charges on the particle, e the elementary charge, η the dynamic gas viscosity, and C the Cunningham slip correction, which can be found in Kim et al.[20] A condensation particle counter (CPC) can be positioned downstream of the DMA. Particles leaving the DMA pass through a chamber saturated with n-butyl alcohol. The vapor condensates on each particle making them increase in size until they can

be detected by an opacity meter. When working with the SMPS, a transfer function for diffusion losses of particles in the flow path within the SMPS was used, which is especially important when particles below 100 nm are sized. With the setup described, the SMPS is not only limited to measuring particle size distribution functions but it can also be used to select the particle size on demand. By applying a certain voltage U_{DMA}, only particles with a certain diameter (certain mobility) can pass the device and can then be collected behind it. We stress here that this selection of particle size "on demand" can currently be realized with high flexibility and accuracy only with atmospheric plasma sources providing an additional argument for their further development and characterization.

2.3 | Electron microscopy

Direct investigation of particle sizes, crystal structure, and chemical composition was performed by transmission electron microscopy (TEM) as well as scanning electron microscopy (SEM). The TEM used in this paper was an FEI Tecnai F30 G^2 STwin operated at 300 kV. Scanning electron microscopy measurements were conducted on a ZEISS Sigma 300 Field emission SEM operated at 30 kV. TEM samples were either obtained by placing TEM Cu grids with a lacey carbon carrier film (Plano GmbH) below the output of the jet or by gentle pressing of the grid onto a particle-coated Si wafer in the case of fluorescent nanoparticles. The crystallographic phase of the synthesizes material is investigated both by high-resolution TEM (HRTEM) as well as selected area electron diffraction (SAED). TEM energy dispersive X-ray spectroscopy (EDXS) is used to analyze the chemical composition. The Z-contrast of high-angle annular dark field (HAADF) scanning TEM (STEM) is used to identify whether single particles or clusters of particles were synthesized for a given set of parameters.

2.4 | Steady-state and time-resolved photoluminescence spectroscopy

A thorough description of the system for steady-state photoluminescence (PL) spectroscopy as well as the one for time-resolved measurements can be found in Galář et al.[21] In brief, the spectra of the silicon nanocrystals were collected using a Shamrock 300i (Andor, Oxford Instruments) spectrograph coupled with an EMCCD camera (Newton 970, Andor, Oxford Instruments). The nanoparticles were collected on silicon wafers and those samples were excited using a continuous laser beam at 325 nm generated by a HeCd laser. The initial laser intensity (≈2.8 mW) was reduced to ≈0.5 mW by ND filters to eliminate potential surface modification of the nanocrystals. The measurements were realized at ambient conditions and the resulting spectra were corrected to the spectral sensitivity of the whole system. The laser pulses exciting the samples in the time-resolved setup were generated using a laser cascade composed of a femtosecond Pharos SP (light conversion) laser and a HiRo (light conversion) harmonic generator. The original IR pulses (1030 nm, 1 kHz repetition rate) were converted by HiRo into ones of 343 nm. The output pulse intensity was decreased to about 60 μJcm^{-2} which corresponds to about 10^{14} photons per square centimeter. The resulting PL signal was collected using a streak camera (Hamamatsu) coupled with an imaging spectrometer. As a proof of minimal modification of the samples during measurements, the spectra of each sample were collected two times and the data were accepted only in case that both measurements were matching. The data were processed and analyzed using a procedure published in Kůsová and Popelář.[22] Here the influence of a finite pulse duration on the PL decays was eliminated using deconvoluted data. The signal-to-noise ratio was increased by integration over four spectral neighboring decays. The onset was determined using a single exponential fit. Afterward, the decays were fitted precisely by a stretched-exponential function.

$$I = I_0 \cdot \exp\left[-\left(\frac{t}{\tau}\right)^{\beta}\right], \tag{3}$$

where τ is the time constant and β is the stretching exponent. This function describes the superposition of exponential functions which, because of the size distribution of nanocrystals, commonly describes exciton-related PL decays of silicon nanocrystals well.

The final average decay time at a specific wavelength was obtained using:

$$\tau_{av}(\lambda) = \frac{\Gamma\left(\frac{2}{\beta(\lambda)}\right)}{\Gamma\left(\frac{1}{\beta(\lambda)}\right)}\tau(\lambda). \tag{4}$$

3 | RESULTS AND DISCUSSION

3.1 | Standard helix jet

This section covers the results obtained with the unmodified standard HelixJet. It has been operated at an overall flow of 800 to 2000 sccm, which results in a residence time of the particles in the plasma between 200 and 600 ms. The noble carrier gas is helium, and the

reactive gas for particle production is 0.01% silane diluted in argon, meaning that the amount of argon in the gas mixture is changing with the silane admixture. Silane concentrations are given in ppm and hydrogen concentrations in %.

The particle production and particle properties have been studied through various analytical methods. The SMPS has been used to analyze the mean particle diameter of the nanoparticles that are synthesized with the HelixJet at different concentrations of silane (see Figure 3). For a constant overall flow of 1000 sccm, the silane concentration has been adjusted between 1 and 36 ppm for a constant power of 125 W. This has led to the synthesis of nanoparticles in the range of 10 nm up to 100 nm. To synthesize nanoparticles below 10 nm, the gas flow of the carrier gas helium was increased at a constant flow of silane. This reduced the particle diameter as seen in the inset in Figure 3.

The nanoparticles synthesized in the HelixJet have been analyzed with SEM measurements. To decrease the amount of collected particles for microscopy methods, one particle diameter is selected from the distribution function using the DMA voltage. The particles have been collected on a holey carbon TEM grid. It is found, that for increased silane concentrations, smaller nanoparticles agglomerate to bigger ones and are detected by the SMPS as such. Here, only an effective aerodynamic diameter of the agglomerate is measured by the SMPS based on the drift properties of the agglomerate. This is demonstrated in Figure 4, where preselecting nanoparticles with a diameter of 50 nm in the SMPS (remember they are assumed to be spherical particles to calculate

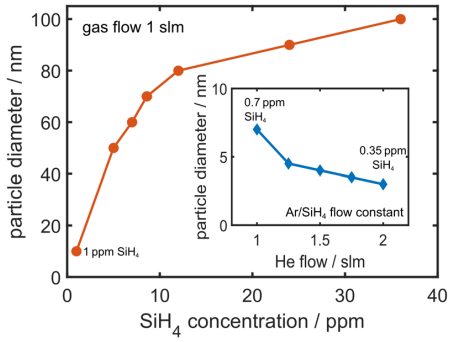

FIGURE 3 Dependence of mean particle diameter on silane concentration as measured with SMPS for the total gas flow of 1000 sccm and a power of 125 W. Inset: Dependence of mean particle diameter on helium flow. Increasing the helium flow decreases the SiH_4 concentration while the Ar/SiH_4 flow is constant during the measurements.

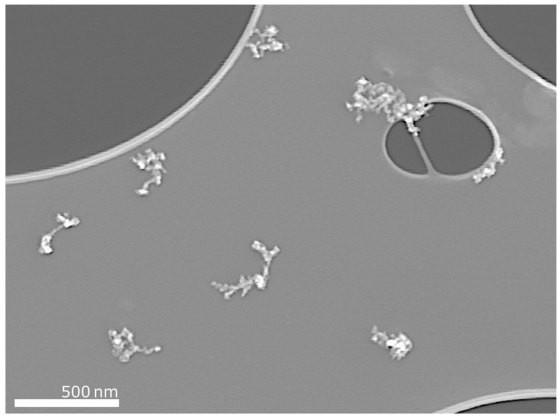

FIGURE 4 SEM image of amorphous silicon nanoparticle agglomerates generated at 33 ppm silane admixture and 125 W collected on a holey carbon TEM grid. The particle diameter was pre-selected by the SMPS to be 50 nm. SEM, scanning electron microscopy.

their mobility) resulted in agglomerates composed of several tens of roughly 10 nm large particles.

3.1.1 | Annealing stage results

By introducing an annealing stage in the form of a muffle furnace, the initially synthesized agglomerates (as shown in Figure 4) could be fused into smaller crystalline particles with the measured mean diameters corresponding to the real diameter. To achieve this, the particles are led through the furnace (1100°C) in stainless steel tubing. The path through the oven is 2 m long which results in a "time of flight" of around 9 s in the oven. Figure 5 shows four different size distribution functions that have been measured with the SMPS. The dashed lines belong to a SiH_4 concentration of 13 ppm. At room temperature (blue) this concentration produces particles with an effective measured mean diameter 10 nm. After being treated in the annealing stage, the mean diameter reduces to 6 nm as it can be seen in the red curve. An even more significant change in diameters through the introduction of the annealing stage is observed for an increased concentration of 36 ppm (solid lines). Here the mean particle diameter decreases from 90 nm mean diameter at room temperature (blue) to 40 nm mean diameter (red) after passing the annealing stage. The resulting particles of this adapted synthesis process have the real size corresponding to their aerodynamic size as seen in Figure 6a and are fully crystalline with a thin amorphous shell as seen from HRTEM in the inset of the same figure.

These annealed nanoparticles are fully crystalline, yet often consist of multiple crystallites as seen from the moiré pattern in Figure 6a. The nanoparticles synthesized in this manner have relatively wide size distributions up to 100 nm in diameter and even monocrystalline particles with diameters up to 200 nm could be found. Elemental analysis via EDXS revealed a stoichiometry of 41 atm% Si, 29 atm% Mn, and 26 atm% O. Traces of Cr could be detected as well. Due to the close proximity of the Mn-L and O-K lines, it is likely, that the amount of oxygen is overestimated in the EDXS quantification. A non-negligible amount of manganese alongside traces of chromium is a consequence of the manganese and chromium in the stainless steel alloy of the tubing in the annealing stage. Manganese has a relatively high vapor pressure compared to other metals, so it is released from the metal earlier than other components of the alloy. Together with the high annealing temperatures exceeding 1000°C it is present in the annealing stage and gets incorporated into the particles. Using another alloy can lead to the formation of different silicides or ceramic/glass tubing could be used to avoid silicide formation at all.

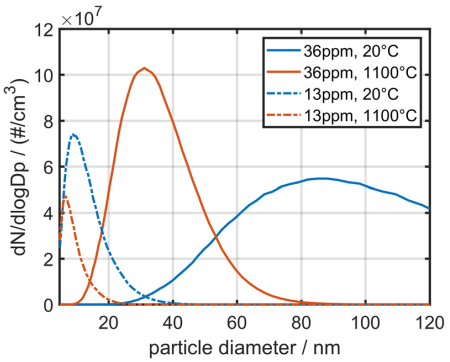

FIGURE 5 Size distribution functions for two different silane concentrations. Each measured after the annealing stage first at room temperature 20°C and second at 1100°C. Total gas flow 800 sccm.

Analysis of the crystallographic phase of the particles via electron diffraction reveals that Mn_4Si_7, as well as MnSi, are the dominant phases, (see Figure 6b). Distinct reflections originating from each phase only show that particles of both phases are synthesized simultaneously. A small amount of crystalline Si material is present as well, as indicated by the weak 111 reflection of Si. Particles of both phases have been identified from HRTEM and fast Fourier transform (FFT) analysis. Looking at the overall stoichiometry determined via EDXS a phase mixture of Mn_4Si_7 and MnSi is in good agreement with the ratio of Mn to Si obtained from EDXS quantification. The particles are stable in air and no effects of oxidation have been observed when investigating samples again several weeks after their synthesis even after having been stored in ambient conditions for a prolonged time. HRTEM shows an amorphous layer around the particles (Figure 6a). It is likely that this layer is made up of silicon and/or manganese oxide and it prevents further oxidation of the particle cores. The short time of flight of roughly 9 s (see Section 3.1.1) is highly likely not sufficient for the crystallites in the particles to

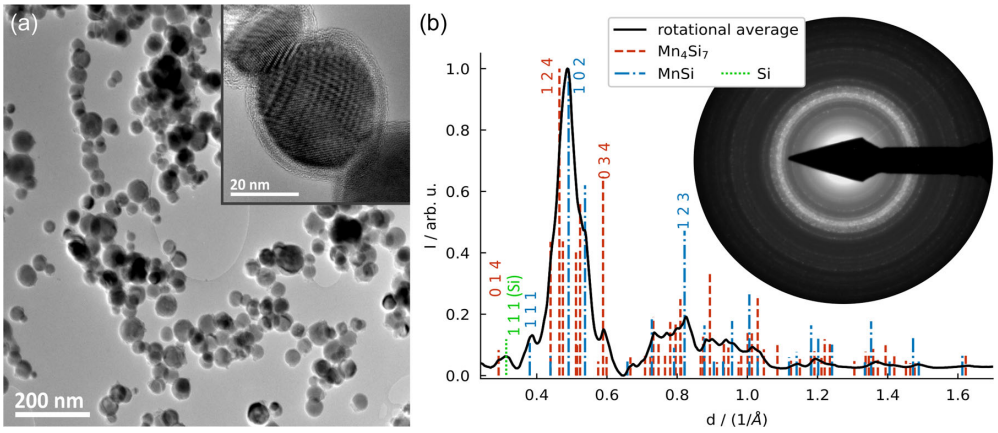

FIGURE 6 TEM micrograph (a) of crystalline nanoparticles of various sizes synthesized with identical plasma parameters as in Figure 4 with the addition of an annealing stage at 1100°C with the inset showing an HRTEM micrograph of a 20 nm particle. (b) SAED pattern and the corresponding rotational average of a large number of the particles shown in (a). Rotational average shows that MnSi alloys are dominant. SAED, selected area electron diffraction; TEM, transmission electron microscopy.

fully merge. Introducing a longer tubing, and thus a longer annealing time could enable the synthesis of single-crystalline particles in the future.

Higher manganese silicides (HMS) such as Mn_4Si_7, Mn_7Si_{12}, $Mn_{11}Si_{19}$, and so on have a direct band gap of about 0.7 eV and show ferromagnetic behavior, which makes them ideal ferromagnetic semiconductors for optoelectronic applications. Mn_4Si_7 and other HMS compounds have been studied for example in Liu et al.[23] Possible other applications for crystalline silicon particles on the larger end of the size scale include all-dielectric nanophotonics.[24] Also, quantum emitters could be coupled to these silicon nanospheres instead of being coupled to plasmonic (metallic) nanoparticles. This would result in various advantages, since metals can normally lead to nonradiative resonances and eventually quenching, in contrast to dielectric nanoparticles that could enhance the (spontaneous) emission.[25] Additionally, arrays of these nanoparticles can have photo-crystal or wave-guiding functionalities.[26,27]

3.1.2 | Stability diagram

If the particles are not annealed in an oven, crystallinity can also be achieved by introducing H_2 to the gas mixture. Admixing hydrogen enhances the particle temperature due to selective heating and suppresses oxidation due to the presence of a small amount of gas impurities (mainly H_2O) in the used gas mixture.[6] Additionally, hydrogen-related radicals and ions result in nanoparticle etching, reducing their size. But an increased hydrogen concentration brings the operation of the HelixJet to its limits: Due to the higher ionization energy of hydrogen and much larger concentration of molecular gas in the mixture, a larger power is needed to ignite and sustain the discharge. Figure 7 displays the power P_f that is needed to sustain the discharge at the whole interelectrode volume inside the HelixJet (called the full discharge further on) at different concentrations of reactive gases. It can be seen for the unmodified HelixJet that the power needed for a stable full discharge operation increases with increasing silane concentration. Without hydrogen admixture, up to 160 W is needed to generate the full discharge at the highest silane concentration used. Adding hydrogen, P_f further increases to values of up to 200 W even for small concentrations of silane. The jet can not be safely operated with hydrogen at silane concentrations above 15 ppm. These instabilities result in limited flexibility since small changes in gas composition or other plasma parameters can lead to unstable plasma. Running the jet at these high powers would also result in the heating of all jet components including the generator and matchbox. When collecting particles, the jet has to be operated for a prolonged time and an elevated temperature of those components (which can not be compensated by simple air cooling anymore) can potentially reduce their reliability.

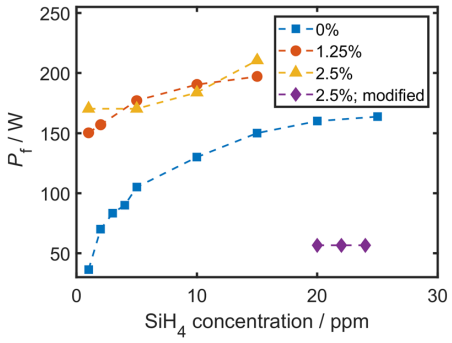

FIGURE 7 Stability diagram showing the minimal power P_f that is needed to ignite the full discharge dependent on the different concentrations of silane. This is shown for different H_2 concentrations and for the modified version of the HelixJet.

3.2 | Modified HelixJet

Modifications of the original HelixJet have been, therefore, introduced to improve the stability and range of its operation. The purple rhombus symbols in Figure 7 demonstrate, that the jet can now be operated stably at high hydrogen and silane concentrations while only using one-fourth of the power (55 W). The particle production with the modified version of the jet and their properties can be discussed now.

3.3 | SMPS results

3.3.1 | H_2 Admixture

Figure 8 shows the dependency of the effective mean particle diameter as determined with SMPS for different concentrations of hydrogen and silane at a fixed power of 145 W. When using no hydrogen (blue triangles) the particle size increases steeply until a concentration of 5 ppm followed up by a slower linear increase with increasing silane concentration. With this, a particle size of 80 nm can be achieved for a concentration of 25 ppm. Again, it is not expected to be the size of a single particle, but rather an effective diameter of an agglomerate of smaller particles as discussed above for the case of the

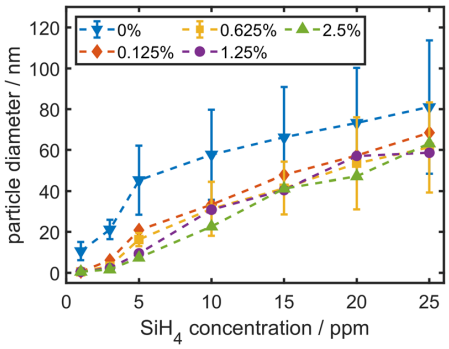

FIGURE 8 Particle mean diameter as measured with SMPS for different concentrations of silane and hydrogen at a fixed power of 145 W and an overall flow of 800 sccm.

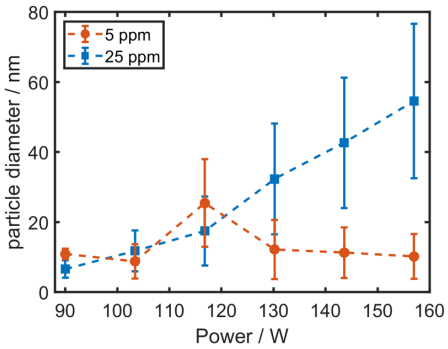

FIGURE 9 Particle or particle agglomerate effective diameter for different applied powers at an overall flow of 800 sccm. Two concentrations of silane were used (5 and 25 ppm). The hydrogen concentration was 1.25% for both.

standard HelixJet. Error bars have been determined from the FWHM of the fitted lognormal distribution of the size distribution function. For a better overview, only error bars for 0% and 1.25% hydrogen admixture are shown. The error bars of all curves with hydrogen are similar.

When adding hydrogen to the gas mixture, the effective mean particle size decreases. This is due to the interaction of atomic and molecular hydrogen with the particles leading to their partial etching as has been observed for silicon films in Nguyen et al.[28,29] Additionally, the presence of hydrogen will contribute to the reduction of oxygen from the surface and hence compensate for the effect of impurities (O_2, H_2O) in the gas mixture. The enhanced selective heating, oxygen removal and hydrogen passivation of defects will improve the nanoparticle properties with respect to crystallinity and stability against post-oxidation. Overall the reduction of the effective diameter of the particle agglomerates is only weakly dependent on the H_2 concentration within the used range of 0.125%–2.5%.

3.3.2 | Effect of power

Figure 9 shows the dependency of the particle diameter for different applied powers P. The experiment was done for two different silane concentrations of 5 and 25 ppm and a hydrogen concentration of 1.25%. The particle size for the smaller silane concentration (red circles) does not change with power, except for one outlier. For a higher concentration, the particle size increases steadily with increasing applied power. Samples synthesized at 90 and 160 W have been investigated via HAADF-STEM to calibrate the particle sizes obtained via SMPS to a direct measurement of the Feret diameter (90 W case) as well as to corroborate our assumption about the formation of particle agglomerates (160W case). Single particles with a diameter of roughly 10nm as well as agglomerates of a few 10 nm particles are observed (see Figure 10a) at an applied power of 90 W. When the power is increased to 160 W larger agglomerates with encircling diameters of 50–100 nm are clearly evident (Figure 10b). HRTEM, as given in Figure 10c), shows that in the case of agglomeration at 160 W individual particles have diameters of less than 10 nm and are amorphous. SAED patterns of the same particles confirm their amorphous nature. At lower silane concentrations, agglomeration of the 10-nm particles does not seem to be happening. At a concentration of 25 ppm single particles still possess diameters of 10 nm or less, yet form increasingly bigger agglomerates when a higher power is applied. The changed value of the available power per silane molecule ratio can provide a plausible explanation for this behavior. All silane molecules are most likely consumed in the particle formation under conditions with 5 ppm of silane. Increasing the plasma density by increasing the applied power does not increase the available amount of precursors, therefore, the amount of generated particles. This seems not to be the case for large silane concentrations of 25 ppm, where an increase of the applied power results in generation of more particles and, consequently, their faster agglomeration. It remains an open question, whether the agglomeration takes place in the plasma or during the transport (≈17 s) from the plasma to the SMPS device. The particles were deposited directly onto carbon film TEM grids, thus, additional agglomeration from sample transfer is minimized. However, it is still likely that some of the larger agglomerates with encircling diameters exceeding the SMPS measurement range have formed during the deposition process. The TEM measurements show, that SMPS analysis provides precise, well-tailored particle diameters in the range of 10 nm and below. When measuring larger nanoparticles under our conditions, it is

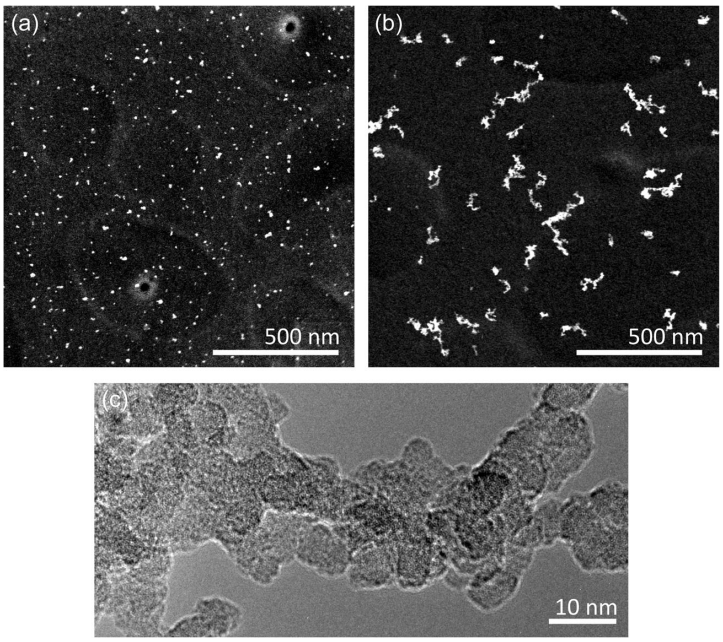

FIGURE 10 HAADF-STEM micrographs of samples created with 25ppm silane concentration at 90W (a) and 160W (b). At higher powers, particles form larger agglomerates as evidenced by HRTEM given in (c). HAADF, high-angle annular dark field; HRTEM, high-resolution TEM; STEM, scanning TEM.

necessary to crosscheck for agglomeration with suitable microscopy methods, whether single spherical particles or particle agglomerates are being measured.

3.4 | Generation of photoluminescent nanocrystals

To test the ability of the modified HelixJet to synthesize silicon nanocrystals, we have produced samples at various experimental conditions. Synthesis conditions varied in the concentration of reactive gases as well as the power of the HelixJet. The samples have been collected on silicon wafers and were analyzed with photoluminescence measurements.

Our studies showed that a strong photoluminescence signal could be achieved for low silane admixtures (5 ppm) and high powers (above 140 W). Hydrogen had to be admixed.

As an example, we present a sample in Figure 11 that has been synthesized with 5 ppm of silane and 0.625% of hydrogen admixture at a power of 145 W.

To elucidate the origin of the photoluminescence of nanocrystals, this sample was further investigated with time-resolved photoluminescence spectroscopy using a streak camera system. In the case of Si-NCs, the photoluminescence can either occur on the surface (charge recombination on traps/functionalization) or in the core of a particle (exciton radiative recombination).[30,31] While surface-related

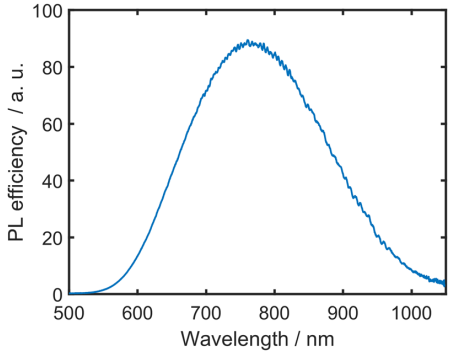

FIGURE 11 Spectral dependence of photoluminescence of a sample created at with admixtures of 5 ppm silane and 0.625% hydrogen at a power of 145 W.

recombination can be manifested in many various ways, the latter results in a multi-exponential/stretch-exponential PL decay at a microsecond timescale.[32] The PL temporal decay of this sample at 700 nm is shown in Figure 12. The PL was excited using laser pulses at 325 nm and an excitation intensity of 80 μJcm^{-2}. Clearly, the decay was multi-exponential showing the average temporal constant of 84 μs. This temporal constant and decay behavior is a sign of well-ordered silicon nanocrystals and corresponds to silicon nanocrystals with homogeneous surface oxygen termination.[33,34]

Particle diameters of this sample can be estimated according to Wen et al.[35] and Mazzaro et al.[32] to be between 3 and 6 nm. To investigate the validity of the size estimations, the nanocrystal sizes, their crystallinity as well as the overall morphology, TEM measurements have been carried out (Figure 13). Figure 13a shows an HRTEM micrograph of our exemplary sample, which was generated with 5 ppm silane and 0.625% H_2. Nanocrystals (identified by visible lattice fringes) alongside amorphous material can be seen. The nanocrystals are clustered together and often embedded in an amorphous phase. Depending on the synthesis parameters, either clustered, single particles or particles completely embedded in an amorphous phase are observed for photoluminescent active samples. For all synthesis parameters, if nanocrystals are formed, they have individual diameters between 5 and 10 nm. To investigate the crystallographic phase of the nanocrystals SAED is utilized. By using SAED a large number of particles is evaluated, and thus, more representative results are obtained.

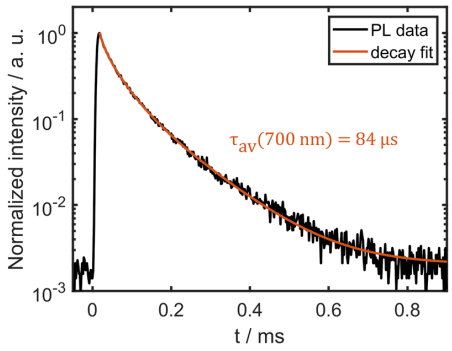

FIGURE 12 Temporal decay of photoluminescence of the exemplary sample (5 ppm silane and 0.625% hydrogen admixture at 145 W) measured at 700 nm. The decay was fitted using a multi-exponential curve, the final average time of the decay was calculated using Equation (3).

The SAED pattern shown in Figure 13b is characteristic of nanocrystalline samples. Due to the presence of larger quantities of amorphous material a strong background intensity is present. For an evaluation, the rotational average is taken and a background subtraction using a fifth-order polynomial background model is applied. The results are in very good agreement with a cubic silicon reference (Figure 13b) clearly proofing the synthesis of Si nanocrystals. EDXS measurements show a stoichiometry of 58 atm% silicon to 42 atm% oxygen. This is consistent with nanocrystals embedded in amorphous SiO_x. Synthesis parameters of 5 ppm silane and 0.625% H_2 thus lead to a large volume fraction of crystalline Si nanoparticles passivated by SiO_x material. The high PL intensity found for these synthesis parameters again confirms the hypothesis that PL intensity scales both with the total amount of active material as well as the volume fraction of nanocrystals to amorphous material. The synthesized nanocrystal-amorphous material system is invariant to oxidation due to storage at ambient conditions. Both the PL intensity as well as the structure as investigated by TEM did not change several months after the initial synthesis. This again is in support of the proposed structure of nanocrystals passivated by SiO_x layers which protects them from further oxidation and provides the surface termination.

Several additional tested conditions typically with high silane concentrations of 25 ppm and low applied

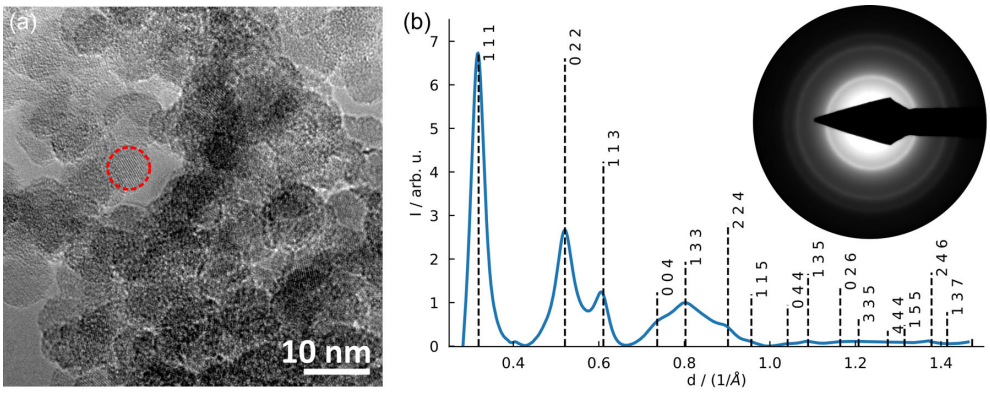

FIGURE 13 (a) HRTEM micrograph of Si nanoparticles synthesized with 5 ppm silane and 0.625% H_2 at 145 W. A crystalline particle with a radius of 7 nm is highlighted. (b) SAED pattern and corresponding rotational average, with calculated reflections from cubic silicon as a reference. HRTEM, high-resolution TEM; SAED, selected area electron diffraction.

powers below 110 W have led to the synthesis of amorphous particles or particle agglomerates without a measurable PL. For these silane admixtures, the maximum particle generation rate can be estimated for an overall flow of 800 sccm to be around 0.3 mg/h. While this exceeds the deposition rate of comparable atmospheric plasma sources, it can still not compete with the generation rates of low-pressure systems that can exceed 100 mg/h.[36]

4 | CONCLUSIONS

The HelixJet has been used successfully to generate a wide range of nanoparticles depending on the synthesis parameters and the use of an annealing stage. Distinct species of nanoparticles could be created: amorphous SiO_x particles, crystalline MnSi nanoparticles, and Si nanocrystals embedded in SiO_x. The stability of the discharge has been increased with modifications in form of an additional electrode and on-axis injection of the SiH_4 molecules allowing the HelixJet to be operated at large admixtures of reactive gases for prolonged times (weeks of continuous operation). The measurements with SMPS, TEM, and the nanoparticle PL have revealed that hydrogen admixture and high applied power lead to the generation of crystalline particles. The combination of silane and hydrogen concentrations can be used to tune the particle size between 3 and 10 nm, where even smaller particles can be probably generated with a further reduction of the silane concentration. The crystalline particles are covered by an amorphous SiO_x layer and show strong photoluminescence nonetheless with a decay time in the range of tens of microseconds. Up to 50 µg/h of SiNCs can be synthesized under the conditions leading to material with a high PL yield (5 ppm silane, hydrogen admixture, powers above 140 W).

High SiH_4 concentrations lead to the formation of larger agglomerates of amorphous ~10 nm diameter nanoparticles. An additional annealing stage can be used to transform these agglomerates into crystalline alloy nanoparticles with broad size distributions and diameters up to 200 nm. SMPS can be used as a filter to collect only particles with the desired size at the differential mobility analyzer with fixed settings. Manganese atoms, originating in the stainless steel tubing used in the annealing stage, have been detected in large amounts in the annealed crystalline particles with MnSi and Mn_4Si_7 being the dominant phases. Using ceramic tubing would avoid metal silicide formation. On the other hand, it suggests a possible synthesis method for these crystals for example for optoelectronic applications.

Overall, this article has demonstrated that the large plasma cross-section, large stability at high admixtures of precursor gases, long operation time, and the ability to tune the nanoparticle properties make the HelixJet a promising atmospheric plasma source for the generation of silicon and other material nanoparticles or nanocrystals.

ACKNOWLEDGMENTS

We gratefully acknowledge funding of this project by the German Research Foundation (DFG, project number 426208229 & KI 1263/17-1) and the Meta-ZIK project "PlasMark" sponsored by the German Federal Ministry of Education and Research (BMBF), grant number 03Z22D511. The German Academic Exchange Service (DAAD) is also acknowledged for the support of researcher exchange between the research groups in Kiel and Prague (project number 57449433). We thank Paul Bittorf for conducting the SEM measurement and Robert Petersen for the photos of the HelixJet. Open Access funding enabled and organized by Projekt DEAL.

DATA AVAILABILITY STATEMENT

The data that support the findings of this study are available from the corresponding author upon reasonable request.

ORCID

Maren Dworschak http://orcid.org/0000-0001-9787-502X
Jan Schäfer http://orcid.org/0000-0002-0652-5057
Jan Benedikt http://orcid.org/0000-0002-8954-1908

REFERENCES

[1] Y. H. Fu, A. I. Kuznetsov, A. E. Miroshnichenko, Y. F. Yu, *Nat. Commun.* **2013**, *4*, 2041. https://doi.org/10.1038/ncomms2538
[2] A. Bapat, C. R. Perrey, S. A. Campbell, C. BarryCarter, U. Kortshagen, *J. Appl. Phys.* **2003**, *94*, 1969. https://doi.org/10.1063/1.1586957
[3] J. H. Park, L. Gu, G. vonMaltzahn, E. Ruoslahti, S. N. Bhatia, M. J. Sailor, *Nat. Mater.* **2009**, *8*, 476. https://doi.org/10.1038/nmat2398
[4] L. Pavesi, R. Turan, *Silicon Nanocrystals Fundamentals, Synthesis and Applications*, Wiley-VCH Verlag, GmbH & Co. KGaA, Weinheim, Germany **2010**.
[5] L. Mangolini, D. Jurbergs, E Rogojina, U. Kortshagen, *J. Lumin.* **2006**, *121*, 327. https://doi.org/10.1016/j.jlumin.2006.08.068
[6] L. Mangolini, U. Kortshagen, *Phys. Rev. E* **2009**, *79*, 1. https://doi.org/10.1103/PhysRevE.79.026405
[7] S. Askari, I. Levchenko, K. Ostrikov, P. Maguire, D. Mariotti, *Appl. Phys. Lett.* **2014**, *104*. https://doi.org/10.1063/1.4872254

[8] T. Nozaki, K. Sasaki, T. Ogino, D. Asahi, K. Okazaki, *Nanotechnology* **2007**, *18*, 235603. https://doi.org/10.1088/0957-4484/18/23/235603

[9] R. M. Sankaran, D. Holunga, R. C. Flagan, K. P. Giapis, *Nano Lett.* **2005**, *5*, 537. https://doi.org/10.1021/nl0480060

[10] B. Barwe, F. Riedel, O. E. Cibulka, I. Pelant, J. Benedikt, *J. Phys. D: Appl. Phys.* **2015**, *48*, 314001. https://doi.org/10.1088/0022-3727/48/31/314001

[11] B. Barwe, A. Stein, O. E. Cibulka, I. Pelant, J. Ghanbaja, T. Belmonte, J. Benedikt, *Plasma Process. Polym.* **2015**, *12*, 132. https://doi.org/10.1002/ppap.201400047

[12] J. Schäfer, A. Quade, K. J. Abrams, F. Sigeneger, M. M. Becker, C. Majewski, C. Rodenburg, *Plasma Process. Polym.* **2020**, *17*, 1900099. https://doi.org/10.1002/ppap.201900099

[13] L. Rebohle, A. Quade, T. Schumann, D. Blaschke, R. Hübner, R. Heller, R. Foest, J. Schäfer, W. Skorupa, *Thin Solid Films* **2022**, *753*, 139257. https://doi.org/10.1016/j.tsf.2022.139257

[14] J. Schäfer, F. Sigeneger, J. Šperka, C. Rodenburg, R. Foest, *Plasma Phys. Control. Fusion* **2018**, *60*, 014038. https://doi.org/10.1088/1361-6587/aa8f14

[15] J. Schäfer, R. Foest, A. Ohl, K. D. Weltmann, *Plasma Phys. Control. Fusion* **2009**, *51*, 124045. https://doi.org/10.1088/0741-3335/51/12/124045

[16] X. Yang, M. Moravej, G. R. Nowling, S. E. Babayan, J. Panelon, J. P. Chang, R. F. Hicks, *Plasma Sources Sci. Technol.* **2005**, *14*, 314. https://doi.org/10.1088/0963-0252/14/2/013

[17] J. J. Shi, M. G. Kong, *J. Appl. Phys.* **2005**, *97*, 023306. https://doi.org/10.1063/1.1834978

[18] R. Honig, David Sarnoff Research Center, *Vapor Pressure Data for the More Common Elements*, R. C. of America RCA Laboratories Division **1957**.

[19] A. Wiedensohler, H. Fissan, *J. Aerosol Sci.* **1988**, *19*, 867. https://doi.org/10.1016/0021-8502(88)90054-7

[20] J. Kim, G. Mulholland, S. Kukuck, D. Pui, *J. Res. Natl. Inst. Stand. Technol.* **2005**, *110*, 31. https://doi.org/10.6028/jres.110.005

[21] P. Galář, J. Khun, A. Fučíková, K. Dohnalová, T. Popelář, I. Matulková, J. Valenta, V. Scholtz, K. Kůsová, *Green Chem.* **2021**, *23*(2), 898. https://doi.org/10.1039/D0GC02619K

[22] K. Kůsová, T. Popelář, *J. Appl. Phys.* **2019**, *125*, 193103. https://doi.org/10.1063/1.5097065

[23] H. Liu, G. She, X. Huang, X. Qi, L. Mu, X. Meng, W. Shi, *J. Phys. Chem. C* **2013**, *117*, 2377. https://doi.org/10.1021/jp310700r

[24] K. V. Baryshnikova, D. A. Smirnova, B. S. Luk'yanchuk, Y. S. Kivshar, *Advanced Optical Materials* **2019**, *7*(14), 1801350. https://doi.org/10.1002/adom.201801350

[25] Q. Zhao, Z. J. Yang, J. He, *Photon. Res.* **2019**, *7*, 1142. https://doi.org/10.1364/PRJ.7.001142

[26] G. W. Castellanos, S. Murai, T. Raziman, S. Wang, M. Ramezani, A. G. Curto, J. GómezRivas, *ACS Photonics* **2020**, *7*(5), 1226.

[27] S. Murai, G. W. Castellanos, T. V. Raziman, A. G. Curto, J. G. Rivas, *Adv. Opt. Mater.* **2020**, *8*, 1902024. https://doi.org/10.1002/adom.201902024

[28] H. V. Nguyen, I. An, R. W. Collins, Y. Lu, M. Wakagi, C. R. Wronski, *Appl. Phys. Lett.* **1994**, *65*, 3335. https://doi.org/10.1063/1.113024

[29] C. Tsai, G. Anderson, R. Thompson, *J. Non-Crystalline Solids* **1991**, *137-138*, 673. https://doi.org/10.1016/S0022-3093(05)80210-8

[30] D. C. Hannah, J. Yang, P. Podsiadlo, M. K. Chan, A. Demortière, D. J. Gosztola, V. B. Prakapenka, G. C. Schatz, G. C. Kortshagen, R. D. Schaller, *Nano Lett.* **2012**, *12*, 4200. https://doi.org/10.1021/nl301787g

[31] K. Kůsová, L. Ondič, E. Klimešová, K. Herynková, I. Pelant, S. Daniš, J. Valenta, M. Gallart, M. Ziegler, B. Hönerlage, P. Gilliot, *Appl. Phys. Lett.* **2012**, *101*, 143101. https://doi.org/10.1063/1.4756696

[32] R. Mazzaro, F. Romano, P. Ceroni, *Phys. Chem. Chem. Phys.* **2017**, *19*(39), 26507. https://doi.org/10.1039/C7CP05208A

[33] K. Kůsová, *Phys. Status Solidi (A)* **2018**, *215*, 1700718. https://doi.org/10.1002/pssa.201700718

[34] S. Miura, T. Nakamura, M. Fujii, M. Inui, S. Hayashi, *Phys. Rev. B* **2006**, *73*(24), 245333. https://doi.org/10.1103/PhysRevB.73.245333

[35] X. Wen, P. Zhang, T. Smith, R. Anthony, U. Kortshagen, *Sci. Rep.* **2015**, *5*, 22. https://doi.org/10.1038/srep12469

[36] O. Yasar-Inceoglu, T. Lopez, E. Farshihagro, L. Mangolini, *Nanotechnology* **2012**, *23*, 255604. https://doi.org/10.1088/0957-4484/23/25/255604

How to cite this article: M. Dworschak, N. Kohlmann, F. Matějka, P. Galář, L. Kienle, J. Schäfer, J. Benedikt, *Plasma. Process. Polym.* **2022**, e2200129. https://doi.org/10.1002/ppap.202200129

5.1 A closer look into the photoluminescence

The modified version of the large HelixJet setup has been used to synthesize silicon NPs under various experimental conditions. The resulting particles have then been analyzed using steady-state photoluminescence spectroscopy. Table 5.1 summarizes the synthesis conditions (applied plasma settings) together with the measured position of the photoluminescence maxima.

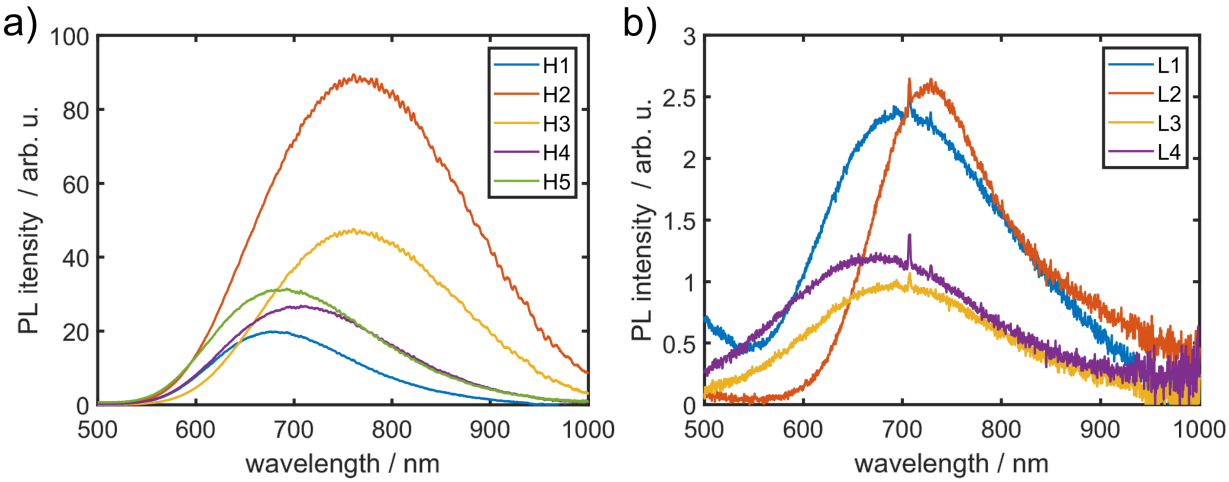

Figure 5.1: Spectral dependence of photoluminescence of samples showing a high (a) or low (b) photoluminescence response. Two sharp peaks observed in the second image originate from the aluminum substrate.

Samples are grouped by their photoluminescence into three groups: two groups are sorted by intensity, where H (high) stands for samples showing a significant PL intensity in the red-to-orange spectral interval, which can also be observed with the naked eye, and L (low) shows only a mild PL response. A third group of samples has been observed to show a blue (B) photoluminescence response. Figure 5.1a shows the results of the photoluminescence response measurements of the H samples. The positions of their PL intensity maxima vary from 670 nm

Sample	SiH_4	H_2	U	PL_{max}
H1	5 ppm	0.25 %	700 V	680 nm
H2	5 ppm	0.625 %	700 V	764 nm
H3	5 ppm	1.25 %	650 V	762 nm
H4	5 ppm	1.25%	700 V	711 nm
H5	5 ppm	1.25%	720 V	678 nm
L1	3 ppm	1.25%	700 V	699 nm
L2	5 ppm	0%	700 V	730 nm
L3	15 ppm	1.25%	700 V	702 nm
L4	25 ppm	1.25%	720 V	677 nm

Table 5.1: Settings for the samples created with the modified HelixJet. Samples are classified by their photoluminescence intensity as high (H) or low (L). The total gas flow was 800 sccm.

to 760 nm depending on the synthesis conditions and are related to the particle size and their surface chemistry. It is difficult to evaluate the influence of the synthesis conditions on the PL intensity of these samples in detail, since the PL signal intensity is also dependent on the amount of collected material, which changes with silane admixture even at the same collection time. According to the position of the PL spectra, there is an evident dependence on plasma generation voltage. For higher applied voltages, the PL maximum shifts towards lower wavelengths (H3 – H5). However, a clear trend between the hydrogen concentration and the PL maximum is not evident (samples H1,H2,H4), which confirms the complex behavior of nanocrystal formation in a non-thermal plasma. However, the concentration of 5 ppm silane as well as the presence of hydrogen in the gas mixtures used are essential for the synthesis of nanocrystals with strong PL signals. Other synthesis conditions as seen in Table 5.1 resulted in nanocrystals of weak PL intensity spectrally located at approximately 700 nm (see Figure 5.1b). This effect can be interpreted as insufficient conditions for the formation of high-quality nanocrystals or low nanoparticle yield, meaning the ratio of PL-active nanocrystals versus non-active material. The parameters that lead to high PL intensity show the same overall morphology with nanocrystal cores covered with a SiO_x layer. Although the volume fraction of nanocrystals to amorphous material differs, no significant differences in nanocrystal diameter are found. Due to the decreased contrast introduced by the amorphous matrix, particle diameters can only be determined as an upper limit. It is likely that smaller nanocrystals exist that do not exhibit sufficient contrast to be identified in HRTEM. Several additional tested conditions typically with high silane concentrations of 25 ppm and low applied voltages below 650 V have led to the synthesis of amorphous particles or particle agglomerates without a measurable PL. Considering the conditions that create crystalline particles with a strong optical response (i.e. a silane concentration of 5 ppm), the particle generation rate can be estimated for an overall flow of 800 sccm to be around 0.3 mg per hour. While this exceeds the deposition rate of comparable atmospheric plasma sources, it can still not compete with the generation rates of low-pressure systems. For comparable rates, the silane concentration would have to be 20 ppm, which did not allow the synthesis of crystalline NPs using this particular experimental setup.

5.1.1 Aging behavior

The aging behavior of photoluminescent silicon nanocrystals or silicon quantum dots has already been published in several publications. For example, Ledoux *et al.* have shown in the early 2000s that a thin oxide shell on top of a silicon nanocrystal can increase the observed photoluminescence and induce a blue shift of the PL maximum [93, 94]. They already stated that the surface oxidation as a result of exposure to ambient air is a self-limiting process for this type of nanocrystals. To test the aging behavior of the NPs synthesized in this thesis, a larger amount of NPs was collected over the course of 6 hours. NPs were synthesized in the small version of the HelixJet with an overall flow of 800 sccm and a silane admixture of 5 ppm. The applied plasma power was 150 W. After collection on a silicon wafer, the sample was placed in the setup for PL measurements and left to oxidize under ambient air. The photoluminescence spectra were measured over the course of a month using a blue LED (365 nm) for the excitation and the PL signal was detected using an Ocean Optics HR4000 spectrometer. Figure 5.2a show the development of the photoluminescence intensity as measured over the course of one month. It can be seen that the intensity of the signal

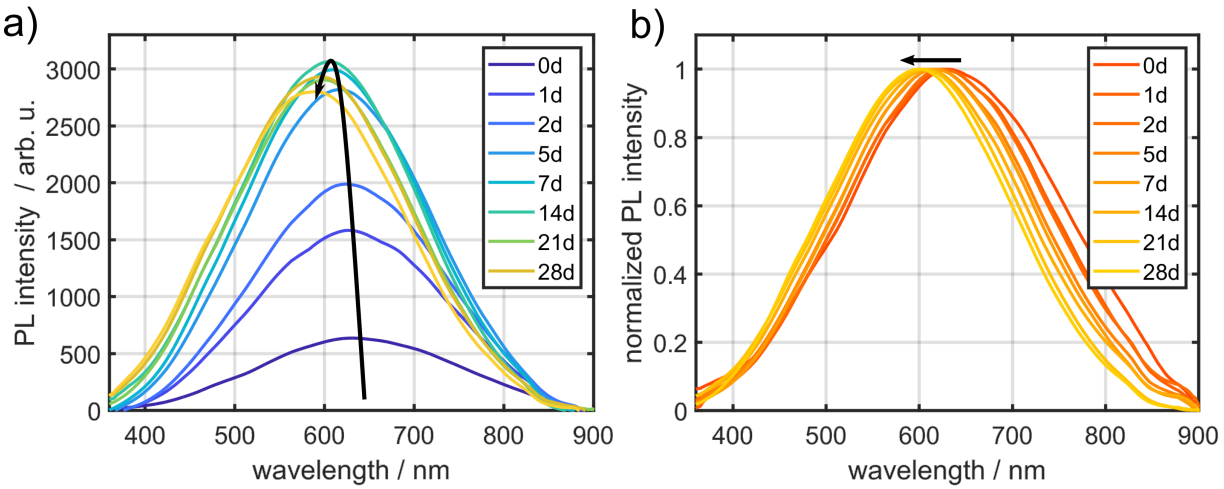

Figure 5.2: a) Aging of the photoluminescence intensity for particles synthesized with the HelixJet measured over a month. b) Normalized PL signal color coded by the wavelength in the visible spectrum indicating a blue shift of the photoluminescence maximum. Black arrows help indicate the time development.

increases rapidly over the first two weeks, before it slightly decreases and stabilizes. When taking a look at the normalized PL spectra in Figure 5.2b, the aging process is also combined with a blue shift. The emitted PL maximum starts of dark red and then shifts to a more orange color and stabilizes there. Ledoux *et al.* used this blue shift to deduce a change in the size of the crystalline core. As the oxide layer increases, the size of the core decreases, leading to a blue shift in the PL maximum. The same behavior is observed for the silicon nanocrystals in this thesis. It is important to keep in mind the time scale of this aging behavior when planning the measurements of photoluminescent silicon nanocrystals. For this thesis, most of the photoluminescence measurements were conducted in the Institute of Physics of the Czech Academy of Sciences in Prague. Therefore, it can be expected that the particles underwent the majority of oxidization already and were at or close to the stabilized state at the end of this self-limiting aging process.

6 | Janus particle synthesis using an annealing stage

Publication II: Transmission Electron Microscopy Investigation of self-assembled 'Si/Mn_4Si_7-alloy' Janus nanosphere architectures produced by a HelixJet atmospheric plasma source

Authors	N. Wolff, M.Dworschak, J. Benedikt, L. Kienle
Journal	Particle and Particle Systems Characterization [260]
Utilized Diagnostics	TEM, STEM, EDX, EELS
Own Contribution	Approx. 25%

Motivation:

Multielemental particles with two or more elements present on the surface of the particle are an interesting research field due to their different applications in different scientific fields. The state-of-the-art synthesis methods are mostly chemical routes, which are time consuming and prone to errors. The HelixJet and other atmospheric plasma jets can possibly facilitate the targeted and tailored synthesis of such complex nanoparticle structures.

Main results:

The HelixJet as the source of silicon NPs combined with an in-flight annealing stage in the form of a stainless steel drift tube at 1000 °C formed Si-based Janus particles. Thorough analysis with TEM revealed the formation of a Si/Mn_xSi_y nanoparticle, where the alloyed side was covered by a semi-spherical shell containing Cr and Fe.

RESEARCH ARTICLE

Particle & Particle Systems Characterization
www.particle-journal.com

Transmission Electron Microscopy Investigation of Self-assembled 'Si/Mn_4Si_7-Alloy' Janus Nanosphere Architectures Produced by a HelixJet Atmospheric Plasma Source

Niklas Wolff, Maren Dworschak, Jan Benedikt, and Lorenz Kienle*

The HelixJet atmospheric plasma-assisted synthesis can be a new toolbox to realize dedicated nanoparticle architectures such as Janus-type morphologies. Silicon nanoparticles produced by the decomposition of Silane molecules are directed into an in-flight annealing stage. The applied high-temperature supplies a metal vapor rich atmosphere containing Manganese, Chromium, Iron, and Tin outgassing from the used steel tube. The metal atoms alloy into the Silicon nanoparticles and form a self-assembled 'Si/Mn_xSi_y-alloy' Janus nanosphere architecture. The Janus particles nanochemistry is thoroughly examined in detail by the analytic capabilities of transmission electron microscopy. The combined approach of electron diffraction, EDS, and EELS identifies the Janus particle composition consisting of a pure Si hemisphere interfaced to an alloyed Mn_4Si_7 hemisphere covered by a thin $(Mn_aFe_bCr_c)Si_y$ surface shell.

1. Introduction

Binary or multinary nanoparticle compounds offer great flexibility in composition, morphology, and structure. A subgroup of these compounds are inorganic Janus particles, where the bulk or surface of the particle consists of two faces with different physical and chemical properties. In this wide definition, a plethora of nanostructures with Janus-like shapes have been reported in literature described as, e.g., dumbbell, snowman, mushroom, or rod-like designer nanoparticles.[1–4] They are heavily sought after because of their diverse composition and surface chemistry that enables application in numerous scientific fields. For example, their anisotropic behavior makes them applicable in biomedicine as multidrug carriers[5] or as bioimaging markers,[6] where one half-sphere surface is commonly functionalized by polymer or drug-containing molecules. Their possibility to create active sides offers up potential use in catalytic processes.[7] If nanocrystals are generated, the resulting bandgap is associated with enhanced optical properties and tunable luminescence ranging from the UV to the near-infrared region, which opens up applications in the fields of energy conversion and storage.[8] Nevertheless, the synthesis and design of such poly-elemental compounds on the nanometer scale is still challenging due to the complexity to control the kinetic and thermodynamic conditions of the synthesis process.[9] In general, inorganic Janus-type nanoparticles are mostly synthesized by wet chemical methods such as seeded growth, cation exchange, and galvanic replacement reactions to name just a few.[4,10] These methods require a proper choice of the participating reactants and their concentrations, as well as the reaction conditions such as temperature, atmosphere, reactor volume, and injection rates. Overall, these methods are time consuming and prone to errors. Further multi-step approaches to create a Janus-type morphology contains masking strategies of single element spheres, where parts of the nanoparticle surface are protected and the free surface is subsequently coated by designed materials. However, for an in-depth overview of the recent developments and prospects in preparation and application of Janus nanoparticles, the reader is referred to review studies, e.g., by Li and Duan.[11,12]

In this paper, we report on a single-step synthesis approach that could facilitate the generation of multinary nanoparticles, e.g., Janus-particles while using atmospheric pressure plasmas as a tool. In earlier work, we described the synthesis of crystalline Si nanospheres using an atmospheric pressure plasma HelixJet, which can be operated stable and safely for a long time at low

N. Wolff, L. Kienle
Synthesis and Real Structure, Department of Material Science
Kiel University
Kaiserstraße 2, D-24143 Kiel, Germany
E-mail: niwo@tf.uni-kiel.de
N. Wolff, J. Benedikt, L. Kienle
Kiel Nano, Surface and Interface Science (KiNSIS)
Kiel University
Christian-Albrechts-Platz 4, D-24118 Kiel, Germany
M. Dworschak, J. Benedikt
Experimental Plasma Physics
Institute of Experimental and Applied Physics
Kiel University
Leibnizstr. 19, D-24118 Kiel, Germany

DOI: 10.1002/ppsc.202300094

ADVANCED SCIENCE NEWS
www.advancedsciencenews.com

Particle & Particle Systems Characterization
www.particle-journal.com

power.[13] The HelixJet produces crystalline Si nanospheres with a broad size distribution ranging from 3 to over 100 nm and offers the possibility to precisely select particles from this range with a differential mobility analyzer. In combination with an in-flight annealing stage steel tube placed inside an oven, the formation of Mn_xSi_y-alloy nanoparticles was initially observed by transmission electron microscopy (TEM) and electron diffraction experiments. The formation of Mn_xSi_y-alloy nanoparticles was reasoned by the higher vapor pressure of Mn promoting its preferential release from the stainless-steel coil tubing used to guide the Si particle stream within the oven at 1100 °C.

Choosing slightly lower annealing conditions of 1000 °C increased the synthesis kinetics and the formation of Si-Mn-Cr-Fe Janus nanospheres was observed. The generated Janus nanospheres show a complex compositional architecture, which has been investigated by analytical scanning transmission electron microscopy (STEM) techniques showing the separation into crystalline Si/Mn_4Si_7-alloy hemispheres partially covered by a thin $(Mn_aFe_bCr_c)Si_y$ surface layer, which opens up possibilities for functionalization with regards to biomedical application approaches.The approximated Janus-particle yield for idealized 30 nm large particles using the described setup was 4.4 mg h^{-1} with estimated costs of ≈1 Euro mg^{-1}.

2. Results and Discussion

2.1. Structure Characterization

The sub-nanometer spatial resolution of advanced analytical methods of scanning transmission electron microscopy such as energy-dispersive X-ray spectroscopy (EDS) and electron energy-loss spectroscopy (EELS) are very suitable to examine the local elemental distribution and composition as well as the chemical and crystalline structures of complex low-dimensional nanoscale architectures such as Janus nanospheres.[14–16] An overview on the collected nanoparticle species is provided in **Figure 1**a showing elliptical to spherical shaped Janus nanosphere morphologies with a particle size distribution symmetrically centered at 25–30 nm (Figure 1b) estimated over 270 nanoparticles. The high-angle annular darkfield (HAADF) STEM mode gives rise to a typical atomic number (Z)-dependent contrast, which provides direct evidence of the Janus nature of the nanoparticles. A solid Si-hemisphere (dark contrast) is clearly differentiated from a bright intensity surface layer that is covering the second hemisphere. The chemical nature of both the pure Si and alloyed hemispheres is identified in this work. For enhanced visibility, a color filter is superimposed on the original Z-contrast image. Two distinct types of the thin surface layer covering the alloyed hemisphere are observed. The first morphology is described by a bulged shell (compare Figure 1c-i) exhibiting a pronounced tail feature and the second morphology (compare Figure 1c-ii) shows a homogeneous surface layer thickness with sharp terminated edges having only slight tail features. As EDS mappings will show later on, this shell is spatially surrounded by a thin oxide layer of the elements contained in the surface layer. In addition, the complete particle is wrapped in a thicker layer containing carbon and oxygen species as illustrated in Figure 1c-iii. This model of the Mn_xSi_y-alloy filled hemispherical shell-like morphology is further supported by the image series presented in Figure 1d showing the stepwise tilt of one nanoparticle by 15 °. Due to the low atomic number of Si, the pure solid Si hemisphere looks highly transparent allowing an edge-on-view onto the alloyed hemisphere cross-section. Tail features reaching from the thin outer shell are differentiated against the more solid hemisphere. Those features are indicated by white arrows for more clarity in Figure 1d. The assessment of the crystalline phases is performed by electron diffraction experiments collecting reflected intensities from multiple nanoparticles as shown in Figure 1e. The obtained speckle diffraction pattern is evaluated by subtracting the Rutherford scattering background intensity and comparing the reciprocal *q*-distance of the radially integrated intensity with crystallographic reference data of Si and possible Mn_xSi_y-alloy phases (compare Figure S1, Supporting Information). The comparison gives the best matches to the cubic Si and the tetragonal Mn_4Si_7 phases, but slight variation of lattice parameters exist, which can be reasoned by the non-equilibrium synthesis process and associated non-stoichiometric alloying with Mn.

The special Janus nanosphere architecture is further examined by STEM-EDS analysis mapping out the spatial elemental distribution and correlating the chemical composition of single nanoparticles with their measured particle diameter as presented in **Figure 2**. The elemental distribution maps (see Figure 2a) are recorded across a large ≈60 nm nanoparticle visible in the center of the HAADF micrograph and a small ≈10 nm nanoparticle located in the top left corner, hence covering both tails of the determined particle size distribution. The spatial distribution of the collected Si–K signal intensity displays the separation of the large particle into a pure Si hemisphere and a Mn_xSi_y-alloyed hemisphere very well. On the alloyed hemisphere, the Si and Mn concentrations were quantified to 61 and 39 at.%, which is close to the atomic ratio for the Mn_4Si_7 phase determined by electron diffraction. Further, two kinds of oxide layers are evidenced. The first oxide layer is spatially restricted to the alloyed hemisphere, whereas the second carbon containing oxide layer wraps the complete particle. For the alloyed hemisphere X-ray signals of the elements Mn (86.3 at.%), Cr (6.8 at.%), Fe (4.9 at.%), and Sn (2.0 at.%) are recorded and displayed by decreasing order of their atomic fraction. Due to the low atomic percentage of Sn, this element is neglected in the following discussions. Further, an EDS line-scan profile (Figure 2b) across the nanoparticle demonstrates the Janus nature of the particle. To rationalize the presented EDS maps, the complete sum spectrum is provided in the Figure S2 (Supporting Information). Notably, the elemental X-ray contributions recorded on the very small particle show high intensity for Cr–K and Fe–K signals, but almost no intensity of Mn–K was recorded. This suggest a significant size dependency on the composition, which is examined further by EDS measurements on single nanoparticles. The overall composition of the main alloying metal elements Mn, Cr, and Fe were determined by EDS measurements over a larger number of nanoparticles for each of six measurements, averaging out any variations in composition between the particles. The results of these measurements showed a 2/3 : 1/6 : 1/6 ratio of Mn to Cr to Fe as displayed in Figure 2c. Next, EDS measurements were conducted on single particles and their elemental content was plotted against the particle diameter in Figure 2d,e. As already suggested by the EDS maps, there is strong variation of the nanoparticle composition within the alloyed shell/hemisphere architecture. For small

ADVANCED SCIENCE NEWS
www.advancedsciencenews.com

Particle & Particle Systems Characterization
www.particle-journal.com

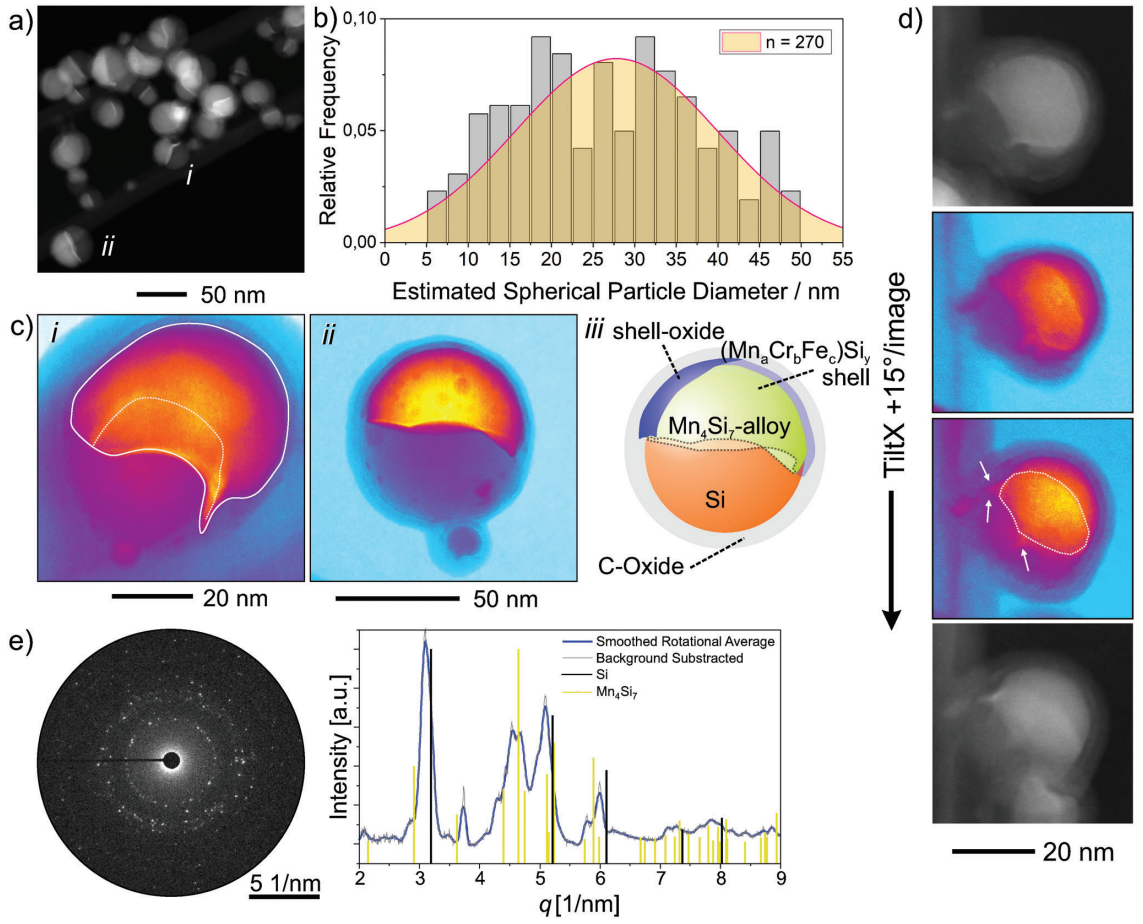

Figure 1. Assessment of the Janus nanosphere particle morphology and crystalline structure. a) STEM micrograph showing nanoparticles on a carbon support. b) Estimated particle size distribution. c) Janus nanosphere particle morphologies with i) bulged shells showing prominent tail features and ii) conformal shell geometries covering the alloyed hemisphere. The dashed line indicates the opening of the shell toward the Si hemisphere. iii) Sketch of the proposed nanoparticle architecture composed of a Si/Mn$_x$Si$_y$-alloy Janus nanosphere covered by an oxidized (MnFeCr)$_x$Si$_y$ hemispherical shell and a carbon oxide layer. d) STEM tilt series showing the shape of the Mn$_x$Si$_y$-alloy filled semispherical (Mn$_a$Fe$_b$Cr$_c$)Si$_y$ shell. e) Electron diffraction pattern recorded on nanoparticle clusters and according phase analysis of the diffracted intensities.

particles with a diameter less than 20 nm, the concentration of Cr and Fe is fairly larger than that of Mn, a tendency that is reversed above this threshold value. Considering the composition of the complete nanoparticles by adding the total amount of Si to the analysis, as shown in Figure 2e, the observed trend gets more pronounced, indicating the formation of the Mn$_4$Si$_7$-alloy. As visible from Figure 2d, the atomic fractions of Cr and Fe follow an approximate declining reciprocal $\approx 1/r$-dependence over particle diameter (compare Figure S3, Supporting Information). Considering the scaling behavior of the surface area to volume ratio of a hemisphere, the observed $\approx 1/r$-fit is expected and strongly supports the suggested (Mn$_a$Fe$_b$Cr$_c$)Si$_y$ shell/Mn$_4$Si$_7$ hemisphere model describing a homogeneous thickness of this shell layer.

The discussed EDS data is strongly supported by complementary EELS investigations. **Figure 3** summarizes the conducted experiments on both hemispheres of a ≈40 nm large single Janus spheres displayed in Figure 3a. The respective core-loss spectra presented in Figure 3b show the ionization edges of non-oxidized Si on the Si hemisphere (as well as on the alloyed hemisphere, not shown) and the edges of O–K, Cr–L, Mn–L, and Fe–L recorded on the alloyed hemisphere. Further, the spatial signal intensity of the core-loss edges is mapped as displayed in Figure 3c matching to the discussed interpretation of the EDS data. The depicted particles show a brighter contrast at the half-shell interface due to the bulged morphology of the ridge. The enhanced contrast could also be related to subtle chemical differences of a locally decreased Si content coupled with a higher content of Mn (Z = 25) and Fe (Z = 26) over Cr (Z = 24) at this ridge (compare Figure 3c; Figure S4, Supporting Information). Considering the energy-loss near edge structures (ELNES) of the transition metals Mn, Fe,

ADVANCED SCIENCE NEWS
www.advancedsciencenews.com

Particle & Particle Systems Characterization
www.particle-journal.com

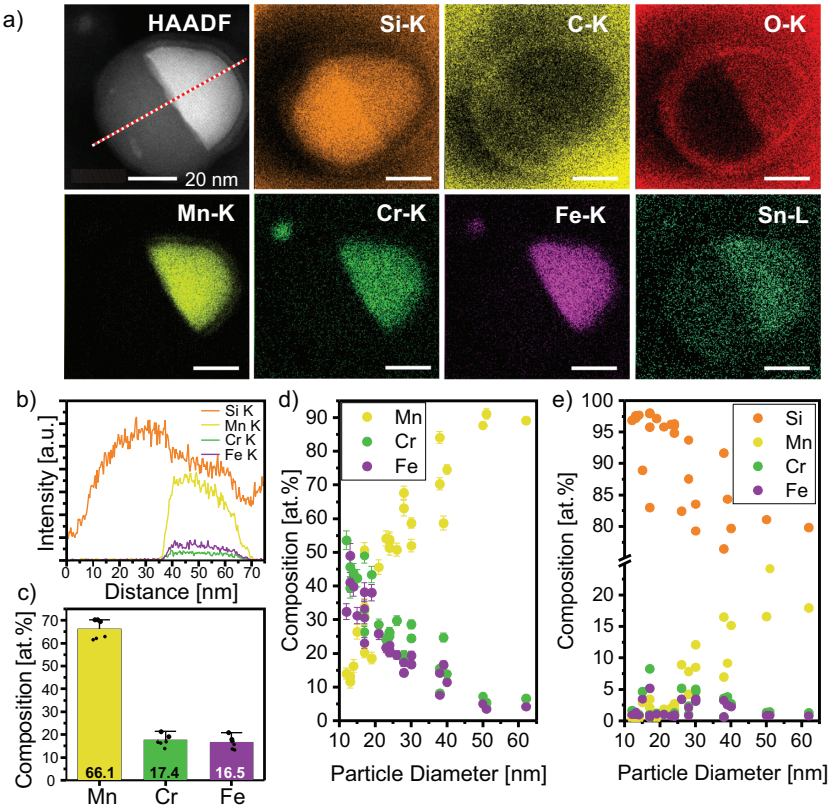

Figure 2. Chemical composition analysis of the Janus nanospheres by STEM-EDS. a) STEM-EDS maps recorded on a ≈60 nm large Janus nanosphere and ≈10 nm small particle located in the left corner of the image. b) Extracted EDS line-scan profile across the Janus sphere particle. c) Nanoparticle composition of main alloy elements Mn, Cr, and Fe averaged over multiple particle clusters. d) Chemical composition of the hemisphere main alloy elements Mn, Cr, and Fe plotted versus the particle diameter. e) Chemical composition of the complete Si-rich Janus nanosphere particle including the main alloy elements Mn, Cr, and Fe plotted versus the particle diameter.

and Cr, information can be drawn from the prominent L_3, L_2 doublets shown in Figure 3b. The intensity ratio of these white-line doublet is an indicator for the metal oxidation state in an oxide phase.[17] However, no significant intensity differences between the L_3, L_2 doublets are observed suggesting the presence of Cr and Fe atoms in an alloy. The same statement is made for the Mn_xSi_y-alloy where no energy shift of the Si-L edge (not shown) is observed. This would be a sign for Si oxidation, hence experimental evidence by SAED of Si forming an alloy is supported.

To further elucidate the individual elemental contributions within the Janus spheres, EELS analysis of the low-energy transitions coupling to bulk plasmon resonances was conducted on a larger particle. The measurement demonstrates distinguishable changes of the plasmon energy states from the Si-hemisphere across the interface to the capped and alloyed hemisphere as presented in **Figure 4**. Three individual plasmon peak maxima centered at 17.0 eV, 18.5 eV, and 20.3 eV were identified from the recorded low-loss EELS data after deconvolution. They are separated by ≈1.5 eV in energy, peak intensity, as well as peak width (c.f. Figure 4a). Figure 4b displays the STEM image of the Janus sphere and the local regions of the selected plasmon peak references. The sharp plasmon peak centered at 17.0 eV is referenced to crystalline Si.[18,19] The evaluation of the plasmon peak generated from the oxide layer covering the particle is omitted in this discussion. The selected reference spectra were fitted to the spectrum imaging low-loss data using the MLLS fitting routine with a high coincidence represented by the map of the χ^2 parameter (c.f. Figure 4c). The resulting maps correspond to the regions that exhibit the selected plasmon peak (maps showing the fit coefficient) and are displayed in Figure 4d. The maps show a clear separation between the bulk plasmon resonances located at the two hemispheres and a sharp localized interface plasmonic state. Furthermore, the superimposed intensity profiles demonstrate the asymmetry of the interface plasmon's spatial distribution being broadened towards the Si-hemisphere. An explanation of this interface plasmon is reasoned in combination with information gained from extracted intensity profiles across the EELS core-loss maps presented in Figure 3c (c.f. Figure S4, Supporting Information). The intensity profiles indicate the distinct onset of the Mn–L edge spatially overlapping with the Si–K edge

ADVANCED SCIENCE NEWS
www.advancedsciencenews.com

Particle & Particle Systems Characterization
www.particle-journal.com

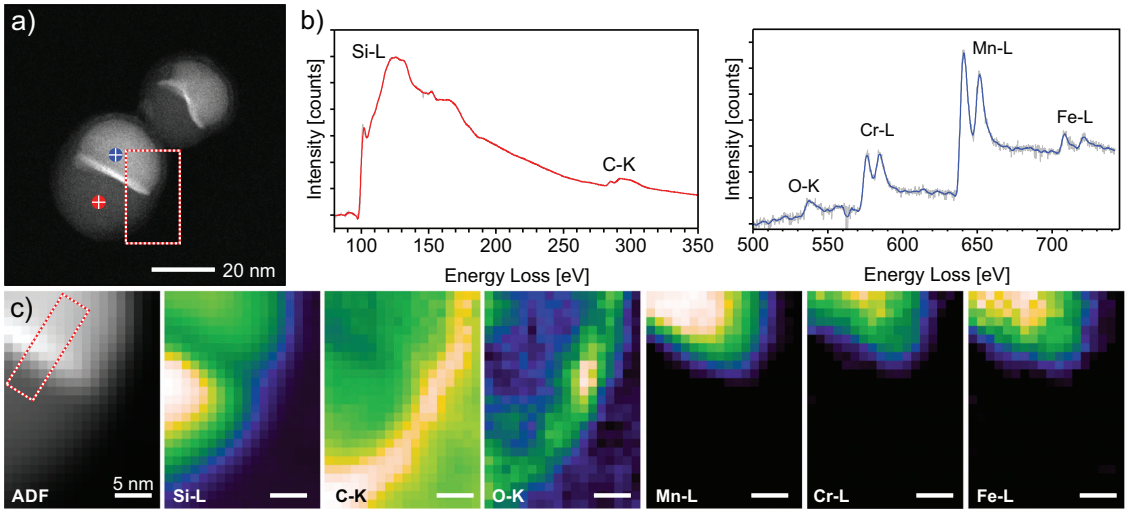

Figure 3. Electron energy-loss spectroscopy investigation. a) STEM-ADF image showing the region of interest for mapping core-loss signals of the elements (red-dotted frame). b) Deconvolved core-loss EEL spectra recorded on single points on the Si hemisphere (red spot) and the shell-covered Mn_xSi_y-alloy hemisphere (blue spot). c) Spectrum imaging maps showing the spatial distribution of the elements core-loss features complementary to EDS results. An intensity profile of the Si, Mn, Cr, and Fe core-loss edges across the two hemispheres (red-dotted frame) is shown in Figure S4 (Supporting Information).

at the interface. Hence, it seems likely that chemical changes at the interface region, e.g., Mn diffusion across the hemisphere interface into the Si-hemisphere (MnSi-alloy interface layer) is causing the observed asymmetry of the interface plasmon. A highly localized MnSi-alloy interface layer could be in line with the observation of a reduced Si–L intensity at this interface (compare Figure 3c, frame: Si–L). On the Mn_xSi_y-alloyed-hemisphere side, the observed plasmon contribution is likely a superposition from the Mn_xSi_y-alloy and the thin $(Mn_aFe_bCr_c)Si_y$ surface shell.

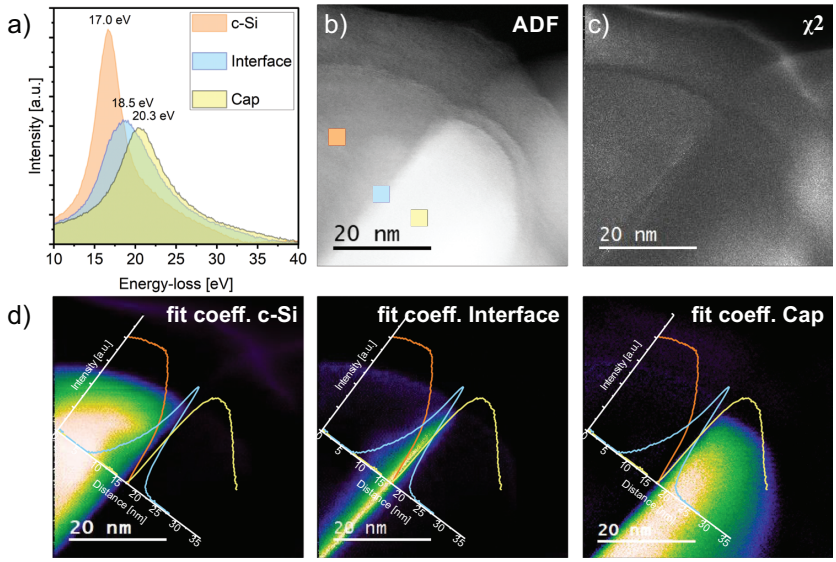

Figure 4. Electron energy-loss spectroscopy investigation of the low-loss region. a) Energy shift of the plasmon peaks from the Si hemisphere, the interface and the alloyed hemisphere used for MLLS fitting. b) ADF-STEM image and c) map of the fit deviation parameter χ^2. d) Plasmon peak maps showing the spatial distribution of the local energy landscape fitted to the selected references. Data of the oxide layer is omitted for clarity.

ADVANCED SCIENCE NEWS
www.advancedsciencenews.com

Particle & Particle Systems Characterization
www.particle-journal.com

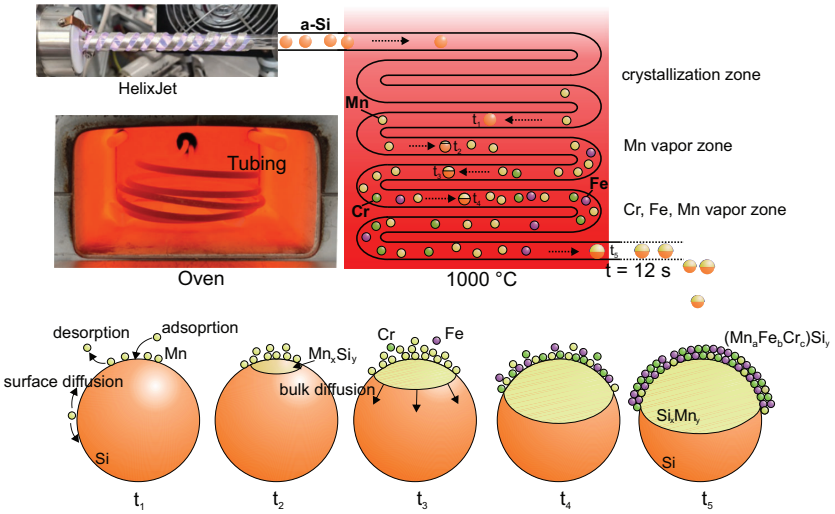

Figure 5. Sketch of the Janus nanosphere formation process showing images of the HelixJet and the steel tubing within the heated oven. A schematic of the steel coil and the metal species within demonstrates the particle formation mechanism resulting in Janus nanospheres. The C–O shell is omitted for simplification.

2.2. Discussion of the Proposed Grwoth Mechanism

When the precursor gas silane is added to the plasma it gets dissociated into radicals and ions.[20] The following particle generation in plasma is a multi-setup process.[21] The first step is started off with the rapid formation of small nuclei from silane radicals and ions. Both ions and neutral radicals participate in this nucleation process. Subsequently, clusters and small particles grow from nuclei and they can hold either a positive or a negative electric charge. This charging endorses the agglomeration of clusters and triggers a coagulation phase where clusters merge together. When the particle density is in the range of the plasma ion density, the agglomeration rate decreases. Due to the higher mobility of electrons in the plasma environment, the negatively charged particles prevail, which suppress further agglomeration.[22] The following interaction of the generated particles with the plasma species can facilitate the crystallization of these particles. This effect of selective plasma heating due to collisions of particles with ions and recombination of ions on particle surfaces leads to the increase in particle temperature. This temperature is now significantly greater than the temperature of the background gas and thus able to crystallize small Si nanoparticles.[23,24] The mechanisms behind are described by the reduction of the activation energy for crystallization of Si nanoparticles compared to a closed thin film[25] and a strong size-dependence of the crystallization temperature below 10 nm.[26] As a result, a mixture of amorphous and crystalline Si nanoparticles exit the jet and is forwarded into the in-flight annealing stage as visualized in the sketch shown in **Figure 5**. In the first part of the stainless steel tube, the increase in temperature causes the amorphous Si particles to crystallize, as the crystallization temperature and melting point for amorphous nano-Si is surpassed.[27,28] Regarding larger particles sizes, previous studies have shown almost complete crystallization of up to 18 nm particles within 120 ms and 830 °C within an in-flight annealing stage.[23] Hence, considering the higher temperatures reached within our in-flight annealing setup, the complete crystallization of all Si nanoparticle sizes is expected within the few first seconds of the 12 s annealing time. After or during crystallization, the nanoparticles pass through the metal vapor zone. Due to its high vapor pressure, Mn is the first to be evaporated from the stainless steel alloy already at lower temperatures[29] causing it to be present already in the cooler first section of the oven. Other metals such as Fe and Cr or Sn evaporate at higher temperatures (compare Figure S5, Supporting Information for a discussion of the vapor pressure of the various metals with temperature). Hence, the middle section of the stainless steel coil that is located in the hottest part of the oven holds an atmosphere enriched with all three metal species in vapor form (we neglect Sn in the further discussion). The individual steps of the Janus particle formation within this metal vapor zone are illustrated in Figure 5. From the binary Si–Mn phase diagram,[30] the formation of intermetallic phases rather solid solution mixing after diffusion is expected. A miscibility gap between the elements is an often-observed feature in Janus particle formation under equilibrium-like conditions.[31] At a time t_1, the first Mn atoms attach to the Si surface and randomly accumulate at a starting site after the establishment of an adsorption/desorption equilibrium forming an initial subsurface Mn layer.[32] The nucleation of Mn on the Si(100) and Si(111) surfaces has been extensively studied both theoretically and experimentally concluding that Mn is energetically most likely to form thin 2D islands of Mn monosilicide (MnSi) with B20 structure on the Si(111) surface rather than pure Mn layers.[32–34] These initial sites act as centers for Mn diffusion into the Si nanocrystal bulk since Mn is known to exhibit a high mobility in Si via interstitial site motion and forming Mn-silicide phases of MnSi and the Nowotny Chimney Ladder compound Mn_4Si_7 at temperatures exceeding 800 °C.[35–37] Large gradients in metal vapor densities across the tube diameter could be

ADVANCED SCIENCE NEWS
www.advancedsciencenews.com

Particle & Particle Systems Characterization
www.particle-journal.com

responsible for the preferential deposition of Mn on just one side of the particles. An alternative explanation could be based on a short contact of the nanoparticle with the tube wall, resulting in the deposition only on the one particle side, independent of its size. Further research will be dedicated to a more intense study of this mechanism. At the time t_3 where the nanoparticles enter the Cr and Fe containing atmosphere, a Mn_xSi_y-alloy has already been formed and Mn adatoms occupy the alloyed surface. Hence, the addition of the minor species of Fe and Cr metals and their good solubility in the MnSi surface structure renders possible the formation of a thin and doped $(Mn_aFe_bCr_c)Si_y$ silicide surface shell (t_4, t_5).[38] In the end, the combustion processes taking place under normal atmosphere conditions oxidize the surface of the $(Mn_aFe_bCr_c)Si_y$ shell and covers the Janus nanosphere with a layer of carbon-oxide.

3. Conclusion

The atmospheric plasma source is a promising tool for the targeted synthesis of new Janus-type nanoparticle morphologies. In this work, the generation of Si-based Janus-type nanoparticle architectures is reported after crystallization at 1000 °C using a stainless steel drift tube. Nanoscopic structure investigation of the Janus-type particles via analytical transmission electron microscopy suggests the formation of Si/Mn_xSi_y-alloy nanoparticles with the alloyed side being covered by a semispherical shell containing close to equiatomic amounts of Cr and Fe and traces of Sn. Further, the Mn_xSi_y-alloy capped half of the particle features a strictly terminated oxide layer, whereas the entire particle is embedded by a thin layer of carbon-oxide species. The chemical analysis by energy-dispersive X-ray spectroscopy shows a strong correlation between the Mn and Si concentration in the nanoparticle and the particle diameter indicating the formation of Mn_xSi_y-alloy under the metallic cap, which is supposed to be Mn_4Si_7 suggested by electron diffraction data. The formation of this special nanoparticle morphology is explained by the release of the transition metals during annealing the Si nanoparticles within the stainless steel tubing and the high miscibility of Mn in Si to promote the tendency to form silicides rather than metallic alloys with Cr and Fe. Hence the formation of a thin $(Mn_aFe_bCr_c)Si_y$ shell is supposed to form on top of the Mn_4Si_7 silicide surface.

In perspective, the presented synthesis approach could enable the design of new Si-based Janus-type particles by choosing the right experimental conditions regarding annealing temperature and tubing material.

4. Experimental Section

Nanoparticle Synthesis by a Helical Plasma-Jet: The Janus particles studied in this publication were prepared in two step process. First, small silicon particles were synthesized in an atmospheric plasma HelixJet, then they passed through an annealing stage. The HelixJet was a dielectric barrier discharge (DBD) with a quartz glass capillary. The capillary had a diameter of 10 mm and a wall thickness of 1 mm. Two helical electrodes were placed around the capillary. One of the electrodes was grounded, the other one was driven by a 13.56 MHz frequency. The helix geometry assures for a homogeneous and stable plasma with high electric field strengths. The jet was operated at atmospheric pressure with helium as a carrier gas. The reactive gas silane (SiH_4) could be admixed to produce silicon nanoparticles. Typical flow rates in the jet range from 100 to 1000 standard cubic centimeters per minute (sccm). Nanoparticles exit the jet in a polydisperse stream and enter an annealing stage. The annealing stage consists of a stainless steel tube (No. 1.4571) which was formed into a two meter long coil inside a muffle furnace. The oven was heated to a temperature of 1000° C. For a flow of 500 sccm the 'time of flight' in the coil was estimated to be around 12 s. After passing this annealing stage, the full size distribution of particles could be either collected directly or a size selection could be done with the help of a differential mobility analyzer (DMA). The device used in this publication is the Long DMA (Model 3086, TSI company) which can be used to classify particles between 10 and 1000 nm. In basic principle, the DMA was cylindrical capacitor. The inner cylinder could be biased with a voltage U_{DMA}. For a set voltage, only particles with a corresponding electric mobility can pass the capacitor. Since the electric mobility of a particle and its electric mobility are proportional, setting a voltage only allows particles of a certain size to pass the device. For the collection of particles, a Nanometer Aerosol Sampler (Model 3089, TSI company) was used. Here, the TEM grid gets placed on an electrode that could be biased with up to 10 kV to attract the particles from the gas stream. The Nanometer Areosol Sampler could be placed at the output of the DMA, allowing a size selection on demand. Or it could be placed directly behind the oven to collect the full size distribution. Since only fraction of the size distribution was collected and the rest was discarded, collecting particles behind the DMA required longer collecting time (10 min instead of 2). For this publication, the particles were collected after the DMA with a voltage of $U_{DMA} = 450$ V resulting in the selection of a differential mobility corresponding to a particle diameter of $d = 30$ nm.

Structure Characterization by Transmission Electron Microscopy: The Janus-like nanoparticles were directly collected on C-lacey TEM grids from the generated particle flux during annealing at 1000 °C. Nanoscopic analyses were performed by transmission electron microscopy (TEM) on a Neoarm (ARM200F, JEOL) operated at 200 kV (cold field emission gun) equipped with an ASCOR (CEOS company) C_S-corrector for the probe forming system in scanning TEM mode (STEM). The local chemical composition of the nanoparticles' architecture was analyzed by energy-dispersive X-ray spectroscopy (EDS) using a dual silicon drift detector system and electron energy-loss spectroscopy (EELS, Gatan Enfinium ER spectrometer) in STEM mode. The dual-EELS acquisition mode was selected to record the zero-loss peak and the core-loss edges simultaneously, allowing for straight-forward post processing by deconvolution to reduce plural scattering contributions within the DigitalMicrograph (Gatan) software package. The EELS measurements were performed using an entrance aperture of 5 mm and a collection angle β of 100 mrad. The achieved energy-resolution was 0.63 eV for a selected dispersion of 50 meV/Channel. Spectrum imaging data sets of localized bulk plasmons were evaluated using the multiple linear least squares (MLLS) fitting routines in DM. Plotted EEL spectra were smoothed by a Savitzky-Golay filter using the Origin software. The particle size distribution was estimated by calculating the spherical particle diameter from an automatic assessment of the projected particle area using the ImageJ software.

Supporting Information

Supporting Information is available from the Wiley Online Library or from the author.

Acknowledgements

The authors gratefully acknowledge funding of this project by the German Research Foundation (DFG, project number 426208229).

Open access funding enabled and organized by Projekt DEAL.

Conflict of Interest

The authors declare no conflict of interest.

Data Availability Statement

The data that support the findings of this study are available from the corresponding author upon reasonable request.

Keywords

core-shell, Janus particle, nanoparticle, nanostructure, self-assembly

Received: June 21, 2023
Revised: September 1, 2023
Published online:

[1] T. Yang, L. Wei, L. Jing, J. Liang, X. Zhang, M. Tang, M. J. Monteiro, Y. I. Chen, Y. Wang, S. Gu, D. Zhao, H. Yang, J. Liu, G. Q. M. Lu, *Angew. Chem. Int. Ed.* **2017**, *56*, 8459.
[2] T. Tanaka, M. Okayama, Y. Kitayama, Y. Kagawa, M. Okubo, *Langmuir* **2010**, *26*, 7843.
[3] Y. Sun, F. Liang, X. Qu, Q. Wang, Z. Yang, *Macromolecules* **2015**, *48*, 2715.
[4] A. G. Butterfield, B. C. Steimle, R. E. Schaak, *ACS Mater. Lett.* **2020**, *2*, 1106.
[5] X. Li, L. Zhou, Y. Wei, A. M. El-Toni, F. Zhang, D. Zhao, *J. Am. Chem. Soc.* **2014**, *136*, 15086.
[6] G. Song, M. Chen, Y. Zhang, L. Cui, H. Qu, X. Zheng, M. Wintermark, Z. Liu, J. Rao, *Nano Letters* **2018**, *18*, 182.
[7] M. Vafaeezadeh, W. R. Thiel, *Angew. Chem. Int. Ed.* **2022**, *61*, e202206403.
[8] A. Kostopoulou, K. Brintakis, N. K. Nasikas, E. Stratakis, *Nanophotonics* **2019**, *8*, 1607.
[9] Y. Xia, X. Xia, H.-C. Peng, *J. Am. Chem. Soc.* **2015**, *137*, 7947.
[10] J. Qiu, Q. N. Nguyen, Z. Lyu, Q. Wang, Y. Xia, *Adv. Mater.* **2022**, *34*, 2102591.
[11] X. Li, c. Chen, D. Cui, W. Jiang, L. Han, N. Niu, *Coord. Chem. Rev.* **2022**, *454*, 214318.
[12] Y. Duan, X. Zhao, M. Sun, H. Hao, *Ind. Eng. Chem. Res.* **2021**, *60*, 1071.
[13] M. Dworschak, N. Kohlmann, F. Matějka, P. Galář, L. Kienle, J. Schäfer, J. Benedikt, *Plasma Processes Polym.* **2023**, *20*, 2200129.
[14] P.-C. Chen, M. Gao, S. Yu, J. Jin, C. Song, M. Salmeron, M. C. Scott, P. Yang, *Nano Lett.* **2021**, *21*, 6684.
[15] S. K. O'Boyle, A. M. Fagan, B. C. Steimle, R. E. Schaak, *ACS Materials Au* **2022**, *2*, 690.
[16] S.-Y. Tang, D. R. Mitchell, Q. Zhao, D. Yuan, G. Yun, Y. Zhang, R. Qiao, Y. Lin, M. D. Dickey, W. Li, *Matter* **2019**, *1*, 192.
[17] T. Sparrow, B. Williams, C. Rao, J. Thomas, *Chem. Phys. Lett.* **1984**, *108*, 547.
[18] P. D. Nguyen, D. M. Kepaptsoglou, Q. M. Ramasse, A. Olsen, *Phys. Rev. B* **2012**, *85*, 085315.
[19] A. Eljarrat, L.-C. L., S. Estradé, F. Peiró, *J. Microsc.* **2016**, *262*, 142.
[20] L. Mangolini, U. Kortshagen, *Nonthermal Plasma Synthesis of Silicon Nanocrystals*, chapter 13, John Wiley & Sons, Ltd, Hoboken, New Jersey **2010**, pp. 309–348.
[21] K. Sattler, *Handbook of nanophysics, Volume III: Nanoparticles and Quantum Dots*, CRC Press, Boca Raton, Florida **2010**.
[22] L. Mangolini, *J. Vac. Sci. Technol., B* **2013**, *31*, 020801.
[23] T. Lopez, L. Mangolini, *J. Vac. Sci. Technol., B* **2014**, *32*, 061802.
[24] S. Askari, I. Levchenko, K. Ostrikov, P. Maguire, D. Mariotti, *Appl. Phys. Lett.* **2014**, *104*, 163103.
[25] T. Lopez, L. Mangolini, *Nanoscale* **2014**, *6*, 1286.
[26] M. Hirasawa, T. Orii, T. Seto, *Appl. Phys. Lett.* **2006**, *88*, 093119.
[27] P. Roura, J. Farjas, A. Pinyol, E. Bertran, *Nanotechnology* **2007**, *18*, 175705.
[28] I. V. Talyzin, M. V. Samsonov, M. Y. Pushkar, V. V. Dronnikov, *Semiconductors* **2019**, *53*, 1090.
[29] R. Honig, R. C. of America. RCA Labratories Division, *Vapor Pressure Data for the More Common Elements*, David Sarnoff Research Center, Princeton, New Jersey **1957**.
[30] A. B. Gokhale, R. Abbaschian, *Bull. Alloy Phase Diagrams* **1990**, *11*, 468.
[31] K. D. Gilroy, A. Ruditskiy, H.-C. Peng, D. Qin, Y. Xia, *Chem. Rev.* **2016**, *116*, 10414.
[32] M. Hortamani, H. Wu, P. Kratzer, M. Scheffler, *Phys. Rev. B* **2006**, *74*, 205305.
[33] M. Hortamani, P. Kratzer, M. Scheffler, *Phys. Rev. B* **2007**, *76*, 235426.
[34] B. Geisler, P. Kratzer, T. Suzuki, T. Lutz, G. Costantini, K. Kern, *Phys. Rev. B* **2012**, *86*, 115428.
[35] D. Gilles, W. Bergholz, W. Schröter, *Br. J. Appl. Phys.* **1986**, *59*, 3590.
[36] E. R. Weber, *Appl. Phys. A* **1983**, *30*, 1.
[37] K. Adambaev, K. Yusupov, A. Yakubov, *Inorg. Mater.* **2003**, *39*, 942.
[38] S. J. Kim, K. N. Yoon, W.-S. Ko, E. S. Park, *APL Mater.* **2022**, *10*, 121105.

7 | Source material based synthesis of metal NPs and core-shell particles

Publication III: Tungsten NPs generated in an atmospheric pressure plasma jet

Authors	M. Dworschak, M. Müller, L. Kienle, J. Benedikt
Journal	Particle and Particle Systems Characterization [261]
Utilized Diagnostics	OES, Thermocouple Type K, SMPS, SEM, TEM
Own Contribution	Approx. 45%

Motivation:

Observations of the additional grounded electrode in the modified HelixJet showed that the electrode glows inside the plasma during jet operation. Using a smaller version of the jet could increase the temperature of a grounded electrode to a point where the electrode material could evaporate in the same way as the manganese from chapter 6.

Main results:

A downsized version of the HelixJet was used with a tungsten metal wire inserted as an additional grounded electrode on the middle axis of the jet. OES spectra contained the excitation wavelengths of tungsten, proving the evaporation (sublimation) of the metal. From black body radiation, the wire temperature could be estimated to be between 1700 °C and 2200 °C, depending on plasma power. TEM measurement revealed the formation of tungsten NPs. The nanoparticle size and shape could be tuned by the power densities.

RESEARCH ARTICLE

Particle & Particle Systems Characterization
www.particle-journal.com

Tungsten Nanoparticles Generated in an Atmospheric Pressure Plasma Jet

Martin Müller, Maren Dworschak, Jan Benedikt, and Lorenz Kienle*

The atmospheric pressure plasma source HelixJet has been used to generate tungsten nanocrystals with narrow size distributions, well defined size control and with a considerably good particle yield. Tungsten particles are produced as the result of an evaporation process of a tungsten wire inserted on the middle axis of the jet after the wire is heated by interaction with the plasma. Temperature measurements using a thermocouple and by optical emission spectroscopy showed that, while the overall temperature of the wire is very high, it is not in the range of the melting temperature of tungsten; however, it can reach values needed for sublimation. Additionally, the wire is heated selectively while the temperature of the jet components reaches only a few hundred degrees Celsius. The particles cluster into agglomerates and their formation has been analyzed in relation to the reliability of a commercial scanning mobility particle sizer spectrometer. The dependence of the particle morphology and crystal structure on the plasma parameters such as power and gas flow was studied via transmission electron microscopy and the average size of the tungsten nanocrystals could be tuned between 12 and 25 nm.

1. Introduction

Metal and especially tungsten nanoparticles have gained increasingly more interest over the last years due to their great application potential in a vast variety of scientific areas. Their large surface-to-volume ratio makes them a desirable material in catalysis, enhancing for example the activity of oxygen evolution reactions.[1] They are studied for their application in bio-medicine due to their antimicrobial and antibacterial effects.[2,3] Highly absorbing materials based on metal particles have great potential in the field of solar thermophotovoltaics, in which tungsten microstructures can help to overcome the Shockley-Queisser limit for photovoltaic cell.[4] Metal nanoparticles also open up ways to nanoscale optical devices such as metal nanoparticle waveguides.[5] Recently, highly sensitive sensors based on layers of metal nanoparticles on semiconductors have been tested.[6] Metals such as tungsten may offer a more cost-effective alternative to the most commonly studied materials to date, such as gold and silver. Nevertheless, the synthesis process of metal particles is still very complex and therefore challenging. State of the art methods mostly rely on chemical routes. These methods include solvothermal decomposition,[7] sonoelectrochemistry,[8] liquid-ammonia-based synthesis[9] and low temperature preparation from molten salt.[10] Those chemical synthesis approaches require careful selection and control of the reactants and reaction parameters. Sometimes even the handling of toxic substances is necessary. Plasma enhanced chemical methods can improve the preparation of nanoparticles in the direction of small-size particles and various alloys in one clean, gas-phase approach,[11] but they rely on the use of organometallic precursors. Nevertheless, microplasmas show some flexibility in fabrication of advanced nanomaterials.[12]

Physical methods often rely on methods consuming large amounts of energy such as gas aggregation techniques and laser ablation and they also often release toxic byproducts. The gas aggregation technique usually employs a source of the desired material that is evaporated and the supersaturated vapors subsequently condense in a temperature gradient region. Although various evaporation methods can be used allowing to prepare a wide range of materials, this technique lacks the versatility of chemical methods in terms of surface modification. Moreover, the physical synthesis of high melting point metal nanoparticles is challenging. One approach has been recently published by Acsente *et al.*, where tungsten particles could be synthesized using magnetron sputtering and gas aggregation.[13] Atmospheric plasma jets are a versatile option for the preparation of various nanostructures. The recently published HelixJet with a helical

M. Müller, L. Kienle
Group of Synthesis and Real Structure
Institute of Material Science
Kiel University
Kiel Germany
E-mail: mmu@tf.uni-kiel.de
M. Dworschak, J. Benedikt
Group of Experimental Plasma Physics
Institute of Experimental and Applied Physics
Kiel University
Kiel Germany
J. Benedikt, L. Kienle
Kiel Nano, Surface and Interface Science KiNSIS
Kiel University
Kiel Germany

The ORCID identification number(s) for the author(s) of this article can be found under https://doi.org/10.1002/ppsc.202400037

DOI: 10.1002/ppsc.202400037

ADVANCED SCIENCE NEWS
www.advancedsciencenews.com

Particle & Particle Systems Characterization
www.particle-journal.com

electrode geometry[14] enables the preparation of silicon and silicon and silicide nanoparticles[15] and offers stable operation by avoiding the chaotic nature of moving filamented discharge channels, that are common in conventional electrode geometries of atmospheric jets.[16,17]

In this publication we report on an approach for the generation of tungsten and other metal particles using an atmospheric plasma jet and a pure tungsten wire. A similar technique has been presented by Shimizu *et al.* , where a tungsten wire was etched using an oxygen microplasma for the localized deposition of tungsten oxide on a substrate.[18] In this report we use a noble argon plasma to synthesize pure tungsten particles covered with only a thin oxide-rich shell inside an atmospheric plasma jet. This method has the advantage of using a small, but scaleable and modular HelixJet setup that, unlike microplasma setups, has still a considerably large volume and thus allows for enhanced condensation of nanoparticle seeds, enabling the synthesis of much smaller particles than is the size of the constituents of tungsten containing nanostructured films deposited by such microplasmas. The use of an atmospheric pressure plasma is also a cost and space efficient alternative to low pressure magnetron sputtering setups. The use of an atmospheric plasma also enables to combine the presented method with chemical synthesis from a gas precursor and *in situ* plasma modification of the synthesized nanoparticles. The nanoparticles synthesized in this publication are classified using transmission electron microscopy (TEM) and parameter studies are carried out.

2. Experimental Setup and Diagnostics

2.1. Plasma Jet

The plasma source used in this publication is a smaller version of the HelixJet, which was first presented by Schäfer et al. in 2019. This atmospheric pressure plasma jet is a radio-frequency (RF) discharge with a dielectric barrier, which ensures for a stable and homogeneous plasma due to a novel electrode geometry.[14] The smaller version used in this publication consists of a quartz glass capillary with an inner diameter of $d = 3$ mm and a wall thickness of 1 mm. As it can be seen in **Figure 1**, a set of helix-shaped electrodes is placed around the capillary. One of the electrodes is grounded, while the other one is driven by a 13.56 MHz frequency. The length of capillary covered with electrodes is $l = 6$ cm making a plasma with volume of approximately 0.42 cm^3. Plasma generator and plasma source are connected via a matching network and the voltage signal is measured on the powered electrode using a voltage probe and an oscilloscope. This allows to read the root mean square (RMS) or peak-to-peak values of the RF voltage applied to the driven electrode. The jet can be fed with a mixture of noble and reactive gases through a gas inlet on the side roughly 2 cm upstream of the electrodes. For the production of metal nanoparticles, a wire connected to ground potential is placed on the middle axis of the jet reaching into the electrode space after the completion of a full helix turn. This ensures that the tip of the wire with a length of approx. 0.5 cm is always located in the plasma area and can thus be heated by the plasma. A tungsten wire with a purity of 99.99% and a diameter of 0.5 mm was used for the synthesis of tungsten nanoparticles. The outlet of the HelixJet can be connected directly to a scanning mobility particle sizer (SMPS) to measure size distribution functions of the synthesized nanoparticles as it has been described in ref. [15]. For all microscopy measurements, the out-stream of the jet can be led onto a substrate holder, which is positively biased at 1.9 kV. Particles can be collected here on, for example, transmission electron microscopy grids.

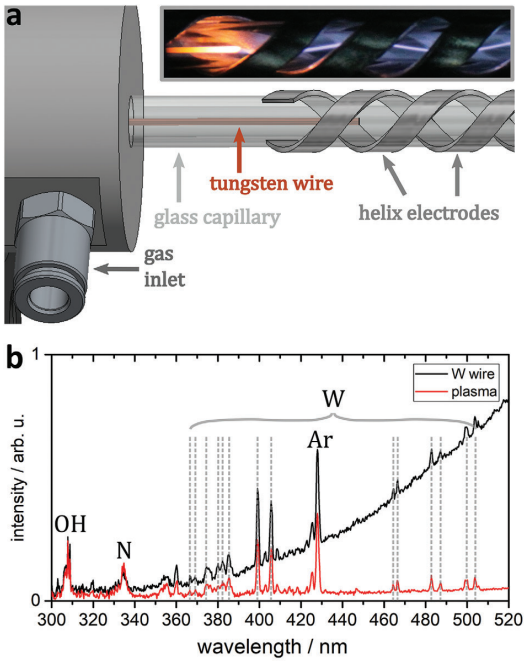

Figure 1. a) CAD sketch of the plasma source and the helix electrode geometry, as well as the inserted tungsten wire. A photograph of the glowing tungsten wire in an argon plasma with a formed filament is shown as an inset. b) Spectrum of the optical emission captured in the plasma around the tip of the tungsten wire, as well as in the wire-free plasma region.

2.1.1. Temperature Measurements

Temperature measurements were carried out to estimate the temperature which the tungsten wire experiences in the plasma environment. Two different approaches were chosen to validate the results of the temperature measurements. For the first approach, a type K thermocouple with a diameter of 1 mm was inserted into the plasma instead of the tungsten wire. The diameter of the thermocouple and the metal wire used for the nanoparticle synthesis were comparable, but not identical (1 mm and 0.5 mm, respectively). The temperature was then measured using an RS51 digital thermometer. The plasma conditions during the temperature measurement and during the nanoparticle synthesis process were identical. Temperatures were measured in argon as a carrier gas with 120 sccm flow and at RMS voltages of 680 V which corresponds to a plasma power of 120 W. The deposited power was measured by a V-I probe mounted after the matchbox directly in front of the powered electrode. A power of 120 W equals a power density of 280W/cm^3 which is slightly higher than what

ADVANCED SCIENCE NEWS
www.advancedsciencenews.com

Particle & Particle Systems Characterization
www.particle-journal.com

Table 1. Parameters of the samples created using a tungsten wire and the HelixJet at various plasma powers. Carrier gas was argon with a flow of 120 sccm.

Sample	Power	Temperature	Size
a	177 Wcm^{-3}	1700° C	12.1 ± 4.3 nm
b	203 Wcm^{-3}	1800° C	13.7 ± 2.8 nm
c	252 Wcm^{-3}	2200° C	16.6 ± 3.1 nm

proved to be needed for the tungsten nanoparticle synthesis, as the thinner tungsten wire can be heated more easily. The temperature measured on the thermocouple wire was 1350° C. This confirms that a macroscopic object suitably placed in a relatively low-power atmospheric plasma jet can be heated to high temperatures, although the quartz wall of the plasma jet heats up only to around 240° C as measured with an infrared thermometer. The main source of the wire heating appears to be an interaction with the plasma, e.g. due to the recombination of ions on the wire surface. An electrical current induced in the wire by the electromagnetic field around the electrodes connected to the RF generator may also have some influence.

To verify the effect of RF induced currents on the wire heating, the thermocouple was placed in the HelixJet again, but this time in air and without a noble gas flow. The generator power was set identical as for nanoparticle synthesis, i.e., the same RMS voltage measured by the voltage probe was used. No plasma was ignited due to the absence of a noble gas. The temperature at the thermocouple increased to around 130° C. This shows a slight influence of displacement currents on the heating of the wire, yet the interaction of the wire with the plasma is the most significant source of heating.

For the second approach, a near-infrared optical spectrometer (Ocean Optics HR4000CG-UV-NIR) was used to capture optical emission spectra (OES) of the plasma region including the glow of the tungsten wire. This spectrometer has been calibrated radiometrically using a tungsten calibration lamp. The temperature was then calculated from the background of the spectra, assuming black body radiation. For this, the 400–800 nm region was fitted using the Planck's law. The temperature of the tungsten wire calculated from the optical emission spectra (see Figure 1b) was increasing with the increase of the plasma power reaching up to 2200° C. A temperature of 2200° C is sufficient to achieve a perceptible evaporation (sublimation) of tungsten[19] even though the evaporation of tungsten is usually performed above 2500° C.[20,21] Still, it has to be noted that both approaches measure an average temperature value taken over an extended area/volume, while the temperature can be higher locally. Optical Emission spectra-based temperature values for different nanoparticle synthesis conditions are given in **Table 1**.

2.2. Characterization

The synthesized nanoparticles were directly deposited on copper TEM grids covered with a lacey carbon film (200 mesh) and observed in a transmission electron microscope (TEM). A field emission gun equipped FEI Tecnai F30 G^2 STwin operated at 300 kV was used to study nanoparticles in TEM mode and a Jeol NeoArm ARM200F operated at 200 kV and equipped with an ASCOR C_S corrector was used to observed the nanoparticles in scanning TEM (STEM) mode. The local elemental composition and distribution were examined by energy-dispersive X-ray (EDX) spectroscopy. Selected area electron diffraction (SAED) was performed to evaluate the crystallinity and crystal structure of the synthesized particles. The particle size distribution was calculated from particle diameters measured using the ImageJ software.

The effect of the plasma on the tungsten wire was observed *ex situ* by comparing scanning electron microscopy (SEM) images (Zeiss EVO 10) and the elemental composition (Oxford Instruments Xplore 15 EDS detector) before and after plasma treatment.

A Scanning Mobility Particle Sizer (SMPS) is a device used to access size distributions function of particles in a polydisperse aerosol stream. For this publication a Universal-SMPS (Model 3938) of the company TSI was used, which was equipped with a 1-nm-DMA (Model 3086). Particles are detected according to their differential electrical mobility under the assumption of spherical particles, therefore agglomerates of particles are detected as spherical particles with a bigger diameter. Additional TEM analysis is hence needed to validate the size distribution functions and differentiate individual particle size from agglomerate size.

3. Results and Discussion

Tungsten nanoparticles were synthesized in a non-thermal atmospheric-pressure plasma with argon as a carrier gas and a pure tungsten wire inserted inside the plasma as the source of material for the synthesis process. The plasma source has been operated at a flow of 120 sccm, the length of plasma was maintained at 6 cm. As visible in the inset of Figure 1a, the plasma consist of the plasma background with a diffuse appearance superimposed by a plasma filament starting at the tip of the tungsten wire. The formation of contracted filaments in argon gas RF discharges at atmospheric pressure is a usual phenomenon as reported for example by Siegeneger *et al.* and Schaefer *et al.*[16,17]

The tungsten wire reaches sufficiently high temperatures in the plasma at which sublimation is already possible. The wire has a smooth shape after the process, indicating that its surface reached a molten state. Therefore, tungsten atoms are released from the wire into the stream of noble gas that carries them through the plasma, where they act as precursors for the nucleation and subsequent growth of nanoparticles. The vaporized material is carried further away from the heated wire by the gas stream and then condensates spontaneously and forms nanoparticle nuclei. Optical emission of atomic tungsten can be observed in the OES spectra measured from any region of the plasma. All W-I lines in the 360 – 520 nm region are present as shown in Figure 1b. The growing nanoparticles are supplied with tungsten atoms, which are carried by the gas stream from the source wire, and further selectively heated by the plasma, which facilitates their crystallization.

A typical set of nanoparticles synthesized in the plasma source is shown in **Figure 2a**. The synthesized nanoparticles have circular cross sections with a narrow size distribution and an average diameter of 13.7 ± 2.8 nm. The nanoparticles were collected directly on a copper TEM grid from the gas flow as described above.

ADVANCED SCIENCE NEWS
www.advancedsciencenews.com

Particle & Particle Systems Characterization
www.particle-journal.com

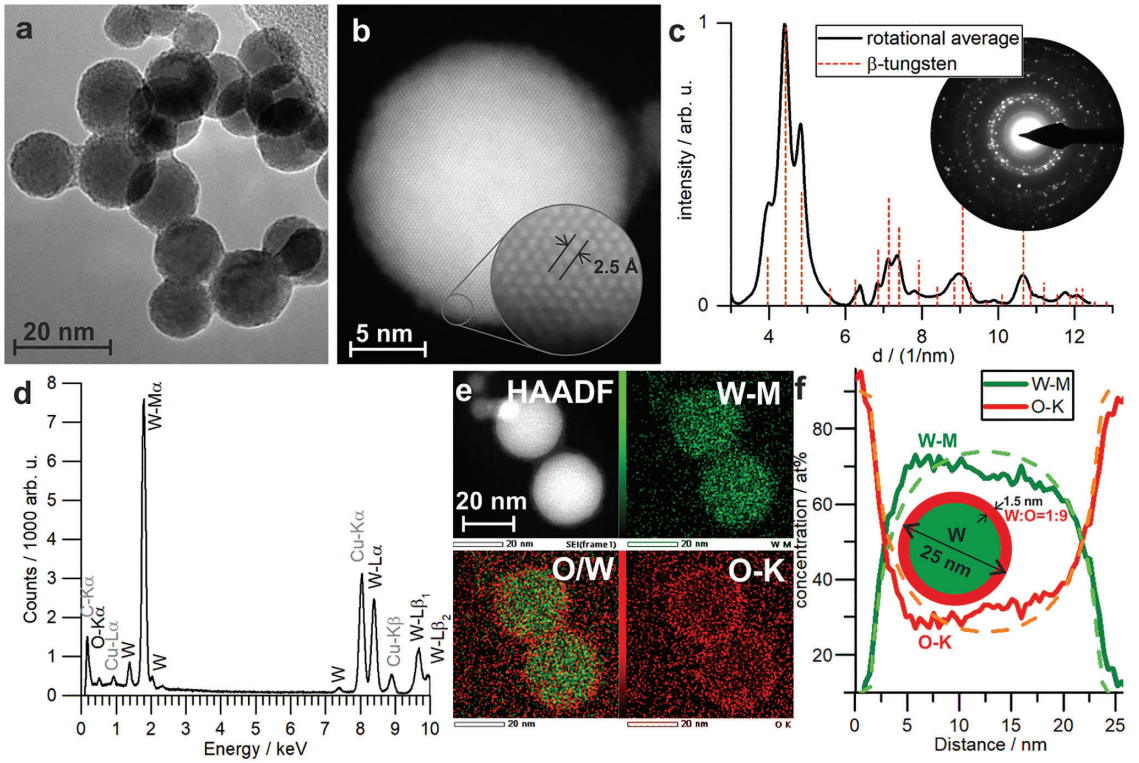

Figure 2. a) TEM micrograph of a typical set of tungsten nanoparticles synthesized in an atmospheric plasma source. b) HRSTEM micrograph of an 18 nm crystalline tungsten particle. c) Rotational average with the corresponding SAED pattern of the large number of particles shown in (a) shows the dominant presence of the β-tungsten phase. d) EDX spectra of a large assembly of tungsten nanoparticles. e) STEM-EDX measured on two ~25 nm tungsten nanoparticles. f) Extracted EDX line-scan profile across the tungsten nanoparticle with fitted profile (dashed lines) regarding to a subshell approach and model composition of the tungsten particle with an oxygen rich shell.

This allows to collect particles directly from the gas flow while avoiding a dispersion of them in liquid solutions. The average synthesis rate, which is in the order of units of $\mu g min^{-1}$, allows for the collection of a sufficient amount of particles in the timescale of seconds. However, the plasma jet can be operated safely on much larger timescales and is able to deposit thin layers of such nanoparticles on various substrates.

Lattice fringes can be seen within the particles, indicating the presence of a crystalline phase. Detailed observation of the nanocrystals using high-resolution TEM further reveals that the particles are monocrystalline (Figure 2b).

To assess the crystallinity of the nanoparticles and to determine the crystallographic phase, the selected area electron diffraction pattern is collected from which the rotational average is extracted and compared to possible tungsten phases. The diffraction pattern shown in (Figure 2c) reveals that the crystallographic phase of β-tungsten is dominantly present in the synthesized product.

The synthesized metal nanoparticles were further examined by STEM-EDX analysis, which reveals a homogeneous composition of tungsten nanocrystals with an increased oxygen content on their surface. The average tungsten to oxygen atomic ratio is above 3:1. The typical EDX spectrum of tungsten nanoparticles can be seen in Figure 2d. The assembly of nanoparticles on Figure 2a, from which the spectrum was collected, has an average composition calculated from the O–K and W–L peaks of ≈ 14 at% oxygen and 86 at% tungsten. Figure 2e shows elemental distribution maps of tungsten and oxygen measured over two ≈25 nm nanoparticles and the elemental line profile over one of them is then shown in Figure 2f. The nanoparticle selected for this line EDX profile measurement is about 25 nm in diameter. Approximately 1.5 nm on the surface are an oxygen-rich layer for which the EDX measurement shows a tungsten to oxygen ratio of ≈1:9. The EDX signal of such a shell can be subtracted from the overall signal applying the so called subshell approach[22] to calculate the composition of shell and core of the particle separately. With this arrangement of a core particle with an oxygen-rich shell, the simulated atomic composition profile is created and it corresponds to the measured profile as it can be seen in the Figure 2f. This shows that the core of the synthesized particle is made of pure tungsten.

The presence of incorporated oxygen in β-tungsten was also reported but the oxygen acts as an impurity and is not creating tungsten oxide.[23,24] However, in this case it appears that any oxygen present is separated at the particle surface.

ADVANCED SCIENCE NEWS
www.advancedsciencenews.com

Particle & Particle Systems Characterization
www.particle-journal.com

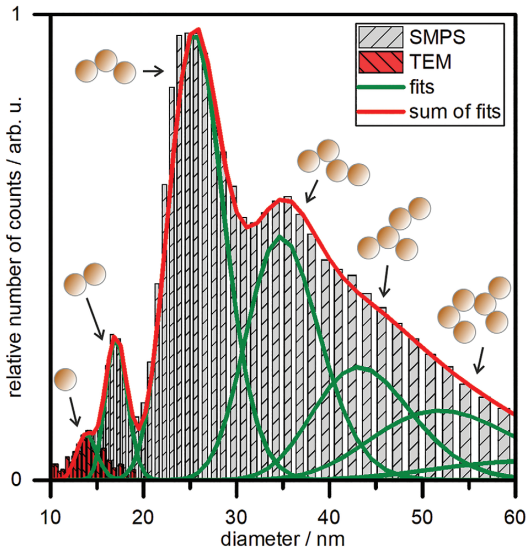

Figure 3. Size distribution of the tungsten particles from Figure 2 measured using an SMPS device and as measured from the TEM image. The peaks in the SMPS size distribution histogram are marked with the corresponding agglomerates of individual particles.

The production yield has been determined by measurements with a high precision scale and through SMPS measurements. Comparing the weight of the tungsten wire before and after the synthesis results in a wire weight loss rate of 2 mgh^{-1}. This allows for up to ≈ 30 µg of material per minute to be produced. Those values exceed silicon nanoparticles yields reported for reactive atmospheric plasmas in which the precursor for the material synthesis comes in a form of a reactive gas mixed with the carrier gas.[15] The SMPS measurement of produced particles is shown in the form of a histogram in **Figure 3**. A histogram of the individual particle sizes measured by TEM is also shown for comparison in red.

The size distribution of individual particles is quite narrow and can be explained by the same principle that applies to silicon particles synthesized in the HelixJet in a reactive plasma.[25] Particles in the plasma interact with electrons and ions. Due to the higher temperature and higher mobility of electrons in non-thermal plasmas, collisions with electrons prevail over collisions with ions and thus the particles acquire a negative charge, which then prevents them from agglomerating in the plasma. The selective plasma heating induced predominantly by ion (or radical) recombination on the particle surface increases the particle temperature above the temperature of the surrounding gas and enables their crystallization.

For the measurement of size distributions with SMPS, the plasma jet was connected directly to the device with a 10cm-long tubing to minimize the effect of particle agglomeration on the way to the device. Nevertheless, the SMPS measurements show, in addition to the small 10–20 nm particles, also a significant number of larger particles. This indicates that the particles, after leaving the plasma region, cluster into larger agglomerates and are evaluated by the SMPS as large spherical particles.

When taking a look at the results of the SMPS measurements in more detail, several peaks can be seen in the histogram. The first one overlaps with the histogram from TEM, corresponds to single particles and has a local maximum of around 14 nm. The other peaks then correspond to agglomerates of two, three and more small particles. The peak corresponding to an agglomerate of two small particles has a maximum ≈17 nm. This value fits exactly to a spherical particle of the same volume or mass as the sum of the volumes or masses of two small particles. Thus, it can be said that the mobility of an agglomerate of two particles corresponds to the mobility of an ideal spherical particle with the mass of two small particles and the SMPS is evaluating the volume and mass of such particles correctly. The next peak in the sequence has a maximum ≈25 nm and corresponds to an agglomerate of three small particles. Their combined mass would produce a particle of only 20 nm, showing that the mobility of such an agglomerate is already affected a lot by its shape and is further away from the ideal model that the SMPS works with. Thus, if we integrate the area under the mass distribution curve that the SMPS measures, we would get a final yield that is higher than the real yield.

By fitting those individual peaks in Figure 3 with a log-norm distribution, it can be estimated how many particles are really produced. This calculation provides a lower limit estimation of the real mass yield of the synthesized product since some particles are lost on the way to the SMPS. The yield based on this estimation provides a value of 1.3 µgmin^{-1}.

The changes of the used tungsten wire as induced by the plasma were studied using an SEM, as it can be seen in **Figure 4**. Before its first insertion into the plasma, the tungsten wire is covered by many parallel grooves along the wire length originating from its fabrication. Additionally, the tip of the wire formed by cutting it with pliers has many sharp protrusions. Native oxide is present on the surface of the wire, while the cut tip of the wire is only slightly oxidized, as visible in EDX measurements in the SEM (not shown here). After treatment with an argon plasma and subsequent nanoparticle synthesis, all the native oxide is reduced and all the sharp edges are obliterated. The tip of the wire, which was originally sharp, is rounded, as if it melted in the plasma. This indicates the local presence of a higher temperature on the very tip of the wire than what was measured from the optical emission spectra collected from a larger area around the tip.

The diameter of tungsten particles synthesized in an argon atmospheric pressure plasma is in the range of lower dozens of nanometers and can be affected with the plasma parameters such as power density or the flow of the carrier gas as it will be described below. Some parameters also affect the crystallographic phase and the shape of the nanoparticles.

3.1. Power Variation

The applied power has not only an indirect effect on the synthesis of the nanoparticles by influencing the plasma parameters, but also a direct effect on the heating of the tungsten wire and thus on the particle synthesis itself. **Figure 5**a–c shows a comparison of nanoparticles synthesized at different plasma power densities and at an argon gas flow of 120 sccm. While particles prepared in a plasma with a power density of 177 Wcm^{-3} have an average diameter as low as 12 nm (a), the diameter of particles prepared

ADVANCED SCIENCE NEWS
www.advancedsciencenews.com

Particle & Particle Systems Characterization
www.particle-journal.com

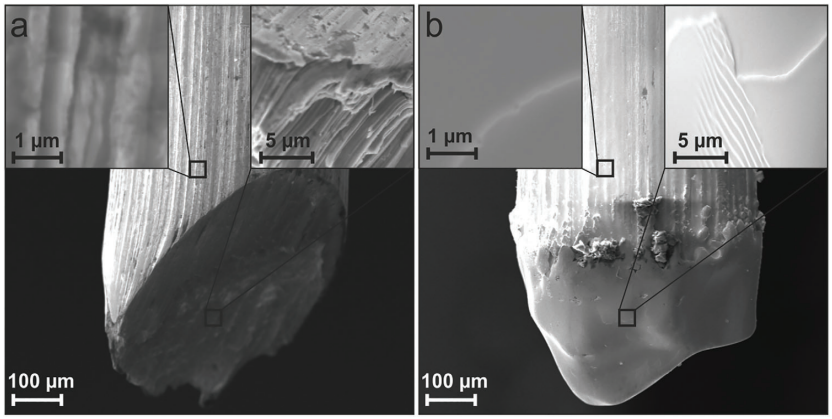

Figure 4. Fresh tungsten tip before (a) and after (b) being used in a plasma for the tungsten nanoparticles synthesis.

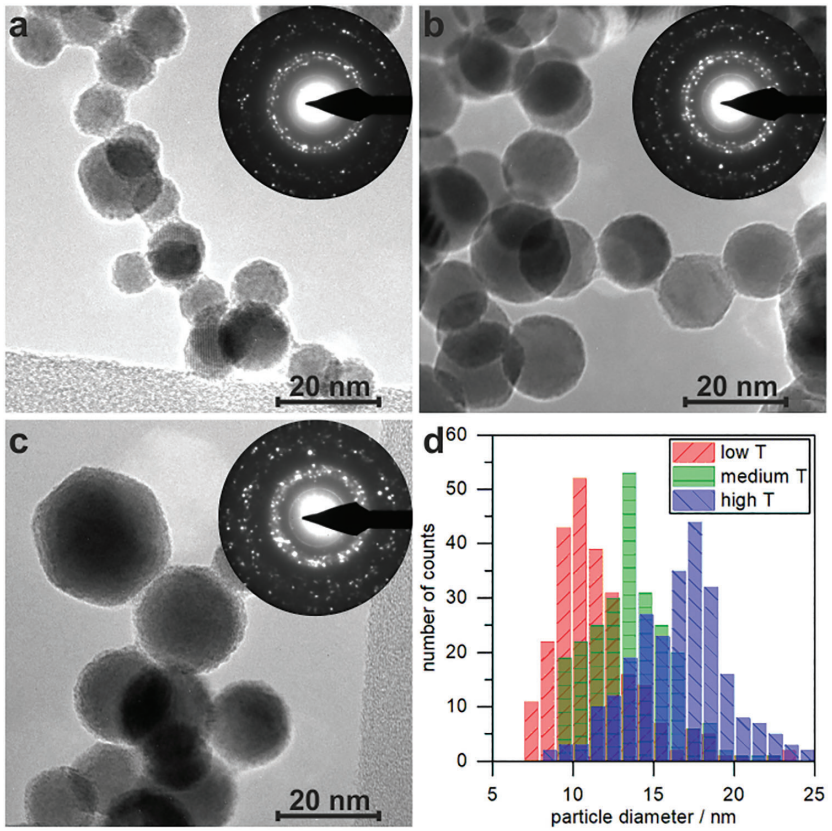

Figure 5. TEM micrographs of synthesized tungsten nanoparticles for increasing power densities (a–c). Size distributions for these particles (d).

ADVANCED SCIENCE NEWS
www.advancedsciencenews.com

Particle & Particle Systems Characterization
www.particle-journal.com

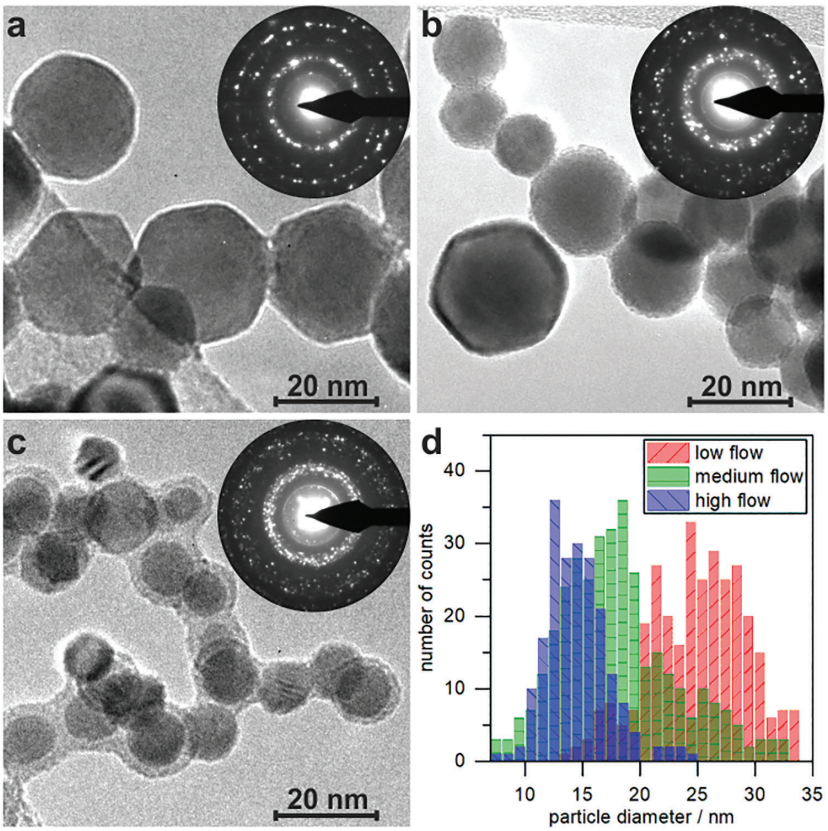

Figure 6. TEM micrographs of synthesized tungsten nanoparticles for increasing flow rates of argon as a carrier gas (a–c) and size distributions for these particles (d).

at 252 Wcm^{-3} increased up to 17 nm (c). All samples with the important synthesis parameters together with the average sizes and standard deviations for nanoparticles synthesized at various plasma power densities are summarized in Table 1. Figure 5d shows the size distributions of such particles.

As the power density of the plasma increases, the temperature of the tip of the tungsten wire inserted into the plasma also increases due to selective heating performed by the plasma. The higher temperature of the tungsten wire implies a faster evaporation of the metal into the plasma and a presence of more material allows to form larger nanoparticles as well as to synthesize more material. Regardless of the synthesis temperature, the synthesized material contains both spherical and faceted particles and the final product can be strongly affected with the gas flow.

3.2. Gas Flow Variation

The carrier gas flow rate, e.g. the velocity at which the gas flows, determines the residence time of the synthesizing particles in the plasma. The flow rate has a significant effect on the size and shape of the resulting tungsten nanoparticles as it is shown in **Figure 6**a–c in which the flow rate of the carrier gas was changed from 40 to 200 sccm. Figure 6d shows the size distributions of such particles. The plasma power was set in such a way to reach the highest temperature value of the tungsten wire used in the previous temperature variation series (2200 °C) and was the same for all tested gas flow rates.

A low flow rate provides enough time for the metal vapor to condensate and for the nanoparticles to form and grow and the resulting particles have an average diameter of 25 nm. On the other hand, the residence time is shortened at higher flow rates resulting in an average nanoparticle size as low as 15 nm. The results for various gas flows are summarized in **Table 2**.

Table 2. Parameters of the samples created using a tungsten wire and the HelixJet at various gas flows of argon as a carrier gas.

Sample	Gas Flow	Residence Time	Size
d	40 sccm	1.8 s	25.4 ± 4.7 nm
e	120 sccm	0.6 s	18.3 ± 5.5 nm
f	200 sccm	0.4 s	14.5 ± 2.9 nm

ADVANCED SCIENCE NEWS
www.advancedsciencenews.com

Particle & Particle Systems Characterization
www.particle-journal.com

The flow rate, and thus the time for which the nanoparticles stay in the plasma, has an influence on the crystallographic structure. Nanoparticles formed at low flow rates can be sufficiently heated by long interaction with the plasma and as a result they crystallize in the α-tungsten phase and form predominantly faceted nanocrystals. On the other hand, small, and mostly round nanoparticles can be formed using high gas flows. Such conditions give a short residence time and thus a shorter time for both growing and crystallization of particles in the plasma. As a result, such particles are mostly spherical in shape and are covered with a layer of ≈3 nm on their surface with a higher oxygen content. This layer is present on those small particles already from the beginning and very probably a result of the higher reactivity of smaller nanoparticles.

4. Conclusion

It has been shown that the atmospheric plasma source HelixJet can be successfully applied, in combination with a simple consumable metal wire, for the synthesis of metal nanoparticles. Since the source material for the nanoparticle synthesis is heated to a high temperature mainly by its interaction with the plasma, this method is also suitable for high melting point materials such as tungsten. Synthesis of mono-crystalline tungsten nanoparticles with an average size as low as 12 nm and with a fairly uniform distribution has been shown. SAED patterns show the presence of β-tungsten and, together with EDX measurements, the particles are seen to be composed of pure tungsten covered by a thin oxygen-rich layer on the surface. Moreover, a variation of parameters such as flow and power density, results in tuning the average size of nanocrystals, while the particles remain crystalline. The increase in residence time of particles in the plasma, which is achieved mostly by the reduction in the gas flow, allows for the particles to be sufficiently heated and prepared in the form of faceted α-tungsten. The here introduced approach for the generation of metal nanoparticles is cost-efficient and non-toxic compared to other state of the art methods and can reach a synthesis rate up to few milligrams per hour, which can be relatively easily scaled up by a parallelization of the HelixJet operation. Using an atmospheric plasma for the nanoparticle generation also opens up additional options to adapt the current set up. Reactive gases, such as silane, may be added to produce mixtures such as core-shell or alloy nanoparticles. The combination of this source with a second plasma source providing, for example, an oxygen plasma, can lead to the generation of metal oxides, which have their own interesting set of applications. Furthermore, the use of alloys or a combination of several wires instead of using a single pure metal wire, can also be tested.

Acknowledgements

We gratefully acknowledge funding of this project by the German Research Foundation (DFG, project number 426208229 and Major Research Instrumentation Program projects INST 257/595-1 and INST 257/704-1). The authors would like to thank Niklas Kohlmann for his help with the calculation of rotational averages and Luka Hansen for conducting the SEM measurements.

Open access funding enabled and organized by Projekt DEAL.

Conflict of Interest

The authors declare no conflict of interest.

Data Availability Statement

The data that support the findings of this study are available from the corresponding author upon reasonable request.

Keywords

atmospheric pressure plasma, metal, microscopy, nanoparticles, TEM, tungsten

Received: February 23, 2024
Revised: April 15, 2024
Published online:

[1] T. Kang, K. Kim, M. Kim, J. Kim, *Chem. Eng. J.* **2021**, *418*, 129403.
[2] R. K. Matharu, L. Ciric, G. Ren, M. Edirisinghe, *Nanomaterials* **2020**, *10*, 1017.
[3] M. A. Syed, U. Manzoor, I. Shah, S. H. A. Bukhari, *New microbiol.* **2010**, *33*, 329.
[4] C. Ungaro, S. K. Gray, M. C. Gupta, *Appl. Phys. Lett.* **2013**, *103*, 7.
[5] S. A. Maier, M. L. Brongersma, P. G. Kik, S. Meltzer, A. A. G. Requicha, H. A. Atwater, *Adv. Mater.* **2001**, *13*, 1501.
[6] K. Białas, D. Moschou, F. Marken, P. Estrela, *Microchim. Acta* **2022**, *189*, 4.
[7] P. K. Sahoo, S. K. Kamal, M. Premkumar, T. J. Kumar, B. Sreedhar, A. Singh, S. Srivastava, K. C. Sekhar, *Int. J. Refract. Hard Met.* **2009**, *27*, 784.
[8] H. Lei, Y.-J. Tang, J.-J. Wei, J. Li, X.-B. Li, H.-L. Shi, *Ultrason. Sonochem.* **2007**, *14*, 81.
[9] C. Schöttle, P. Bockstaller, D. Gerthsen, C. Feldmann, *Chem. Commun.* **2014**, *50*, 4547.
[10] S. Zhang, Y. Wen, H. Zhang, *Powder Technol.* **2014**, *253*, 464.
[11] W. Chiang, R. M. Sankaran, *Adv. Mater.* **2008**, *20*, 4857.
[12] W. Chiang, D. Mariotti, R. M. Sankaran, J. G. Eden, K. K. Ostrikov, *Adv. Mater.* **2019**, *32*, 18.
[13] T. Acsente, R. Negrea, L. Nistor, E. Matei, C. Grisolia, R. Birjega, G. Dinescu, *Mater. Lett.* **2017**, *200*, 121.
[14] J. Schäfer, A. Quade, K. J. Abrams, F. Sigeneger, M. M. Becker, C. Majewski, C. Rodenburg, *Plasma Processes Polym.* **2019**, *17*, 1900099.
[15] M. Dworschak, N. Kohlmann, F. Matějka, P. Galář, L. Kienle, J. Schäfer, J. Benedikt, *Plasma Processes Polym.* **2022**, *20*, 2.
[16] F. Sigeneger, J. Schäfer, R. Foest, D. Loffhagen, *Plasma Sources Sci. Technol.* **2019**, *28*, 055004.
[17] J. Schäfer, F. Sigeneger, J. Šperka, C. Rodenburg, R. Foest, *Plasma Phys. Contr. F.* **2017**, *60*, 014038.
[18] Y. Shimizu, A. C. Bose, D. Mariotti, T. Sasaki, K. Kirihara, T. Suzuki, K. Terashima, N. Koshizaki, *Jpn. J. Appl. Phys.* **2006**, *45*, 8228.
[19] H. A. Jones, I. L. r, G. M. J. Mackay, *Phys. Rev.* **1927**, *30*, 201.
[20] R. L. Axelbaum, J. I. Huertas, C. R. Lottes, S. Hariprasad, S. M. L. Sastry, *Mater. Manuf. Processes* **1996**, *11*, 1043.
[21] E. Plante, A. Sessoms, *J. Res. Natl. Bur. Stand. A Phys. Chem.* **1973**, *77A*, 237.
[22] M. Kamp, A. Tymoczko, R. Popescu, U. Schürmann, R. Nadarajah, B. Gökce, C. Rehbock, D. Gerthsen, S. Barcikowski, L. Kienle, *Nanoscale Adv.* **2020**, *2*, 3912.
[23] G. Mannella, J. O. Hougen, *J. Phys. Chem.* **1956**, *60*, 1148.
[24] Y. Shen, Y. Mai, *Mater. Sci. Eng., A* **2000**, *284*, 176.
[25] N. Wolff, M. Dworschak, J. Benedikt, L. Kienle, *Particle Systems and Characterization*, **2023**.

7.1 Combined gas phase and source material synthesis of metal silicon core-shell particles

The nanoparticle synthesis using atmospheric pressure plasmas in combination with a source material offers several ways for the generation of multielemental NPs such as metal alloys or core shell particles. For example, two metal wires consisting of different metals can be inserted on the middle axis of the jet together. A thorough analysis of the position of those wires inside the plasma and the careful selection of the plasma parameters could lead to the formation of alloy NPs, which are otherwise difficult to synthesize. When thinking of core-shell particles, one easy way for their generation can be the combination of a source material with the gas phase synthesis using gaseous precursors. As a first proof of principle to test the ability of atmospheric plasma jets to generate multielemental particles, a copper wire was inserted on the middle axis of the small HelixJet inside an argon plasma with a flow of 100 sccm and an admixture of 100 ppm silane. The used power was 100 W leading to a filamental discharge. Particles were collected on a lacey carbon Nickel TEM grid, to positively identify Copper, if it is integrated into the particles. The resulting particles are shown on their HRTEM image in Figure 7.1a and in the HAADF image in b. Those images show a dense crystalline core with a diameter of around 10 nm which is embedded in a shell of lighter amorphous material, that contains smaller crystalline NPs of the dense material. EDX spectra have been measured for these particles at their core in blue and at their shell in red (see Figure 7.1c). These results indicate that the combined synthesis worked to an extend. The source material synthesis in form of the copper metal wire generated copper nanocrystals of different sizes. All copper particles are covered by an amorphous silicon oxide shell. Small copper particles then attach to bigger copper particles, building agglomerates that look like a core-shell particle on the first glance. More thorough research is needed here to determine plasma parameters that result in a separation of both materials for a distinct copper core covered in an amorphous silicon-oxide layer.

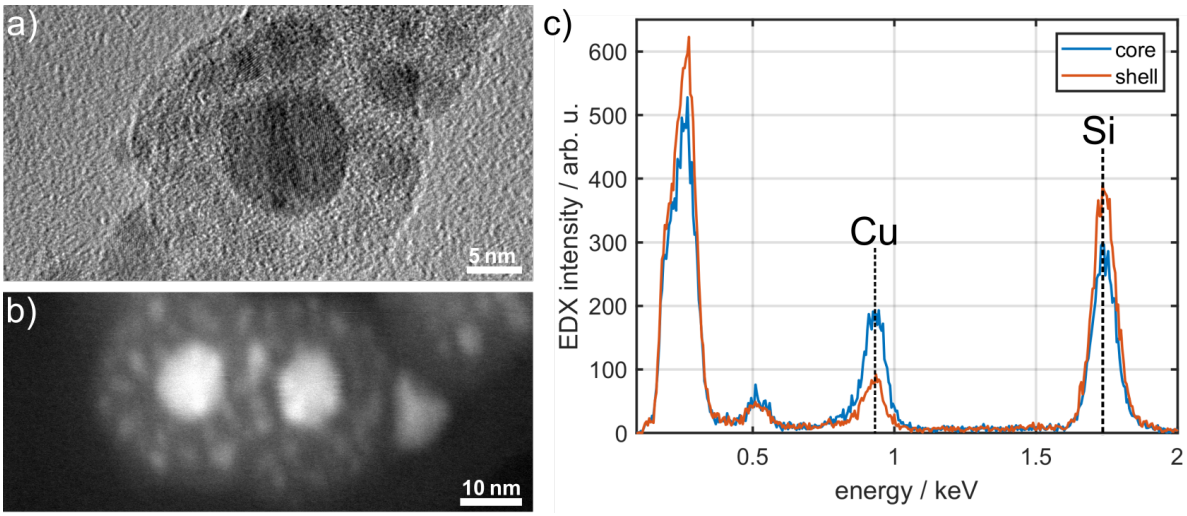

Figure 7.1: a) HRTEM image of a copper silicon core-shell particles. b) HAADF image of two core-shell particles. c) Corresponding EDX spectra that have been measured for the core in blue and for the shell of the particle in red.

8 | *In situ* monitoring of the particle passivation using a double jet setup

Publication IV: Surface passivation of silicon nanoparticles monitored by *in situ* FTIR

Authors	M. Dworschak, T. Tjardts, M. Müller, L. Kienle, J. Benedikt
Journal	Plasma Processes and Polymers [262]
Utilized Diagnostics	*in situ* FTIR, TEM, XPS, PL spectroscopy
Own Contribution	Approx. 80%

Motivation:

The surface modification is the key to tune the properties and therefore the applications of nanoparticles, as described in section 2.1.2. This is especially important for the photoluminescent properties of silicon nanocrystals. FTIR is an excellent tool to detect the surface passivation and bonds. Atmospheric pressure plasmas can be used in connection to an *in situ* FTIR setup, where the plasma output can be analyzed in a reflective setup in real time. Two HelixJets, one synthesizing the NPs and the second one subsequently modifying the surface, are connected to an FTIR setup to monitor the surface passivation.

Main results:

The experimental setup consisting of two combined HelixJet plasma sources and an *in situ* FTIR setup is explained in detail. A set of parameters for the first jet is found, that leads to the formation of photoluminescent silicon quantum dots. Using a pulsed operation for the second plasma jet and methane as the reactive gas, the formation of an Si-CH_3 peak could be observed in the *in situ* FTIR. XPS measurements confirm the presence of Si-C bonds on the nanoparticle surface. The photoluminescence shifted to blue and decreased in intensity.

Plasma Processes and Polymers

PLASMA PROCESSES AND POLYMERS

RESEARCH ARTICLE OPEN ACCESS

Surface Passivation of Silicon Nanoparticles Monitored by In Situ FTIR

Maren Dworschak[1] | Martin Müller[2] | Tim Tjardts[3] | Lorenz Kienle[2,4] | Jan Benedikt[1,4]

[1]Department of Experimental and Applied Physics, Group of Experimental Plasma Physics, Kiel University, Kiel, Germany | [2]Department of Material Science, Group of Synthesis and Real Structure, Kiel University, Kiel, Germany | [3]Department of Material Science, Chair of Multicomponent Materials, Kiel University, Kiel, Germany | [4]Kiel Nano, Surface and Interface Science KiNSIS, Kiel University, Kiel, Germany

Correspondence: Jan Benedikt (benedikt@physik.uni-kiel.de)

Received: 2 September 2024 | **Revised:** 29 October 2024 | **Accepted:** 21 November 2024

Funding: This study was supported by German Research Foundation (DFG, project number 426208229) and Major Research Instrumentation Program projects (INST 257/595-1 and INST 257/704-1).

Keywords: atmospheric pressure plasmas | FTIR | in situ | nanoparticles | silane | silicon | surface passivation | TEM | XPS

ABSTRACT

A setup consisting of two atmospheric plasma sources is used for the combined synthesis and passivation of nanoparticles. The silicon nanoparticles synthesized in the first source are analyzed for their chemical composition, morphology, and photoluminescence. The particles are then treated with a second plasma to induce surface passivation. The passivation process of the particles is monitored in real time using in situ infrared absorption spectroscopy. The results indicate that this treatment induces methylation of the silicon nanocrystals, which is further supported by XPS analysis. This surface passivation shifts the maximum of the photoluminescent signal to blue in the visible spectral region. Further optimization of the reported nanoparticle passivation process can provide a flexible tool for tuning nanoparticle properties.

1 | Introduction

Silicon nanoparticles (Si-NPs) and nanocrystals (Si-NCs) have gained significant attention in both scientific and industrial areas due to their unique properties and versatile applications. Si-NCs possess advantageous characteristics such as biocompatibility, biodegradability, and non-toxicity [1–3], making them promising candidates for various biomedical applications, including drug delivery and biomedical imaging [4, 5]. The tunable optical and electrical properties of Si-NCs, influenced by their size and surface termination [6], give them the prerequisites for the development of light-emitting devices [7], photovoltaics [8], and sensors [9, 10]. Surface passivation and functionalization resulting in the desired surface termination play a crucial role in modulating the photoluminescence (PL) intensity, quantum yield, as well as stability of Si-NPs. Non-thermal equilibrium plasmas operated at atmospheric pressure offer great flexibility in applications that are commonly carried out by low-pressure vacuum systems [11, 12]. This includes the synthesis of optical-quality Si-NPs or silicon quantum dots [13]. These nanoparticles typically possess highly sensitive surfaces and are susceptible to alterations in their properties over time due to aging. Moreover, surface modification of nanoparticles is often needed to improve the optical properties. The work of Kůsová et al. has shown that methyl groups bonded to the nanocrystal surface enhance the PL properties of Si-NPs significantly [14]. The electrochemically etched Si-NC powder dispersed in a solvent from a mixed aromatic hydrocarbon solution was irradiated with a UV laser. The original PL band at ~600–650 nm and a decay time of around 20 ms was replaced by a new rapidly decaying yellow band comparable to the PL of direct band gap materials. Organic residues attached to the Si-NC surface via both Si-C and Si-O-C bonds were found; however, the exact chemical mechanism remains unknown due to the complexity of the experiment. Further, it has been theoretically shown that passivation with methane can tune the

optical band gap of ultra-small (< 3 nm) nanoparticles [15]. The methyl groups attached to the surface of Si-NCs introduce a tensile strain in the particles, leading to an increase in the band gap and consequently blue-shifting the maximum of the PL signal. This passivation is supposedly also connected to an increase in the overall PL intensity. The analysis of the particle composition of both passivated and pristine particles can be carried out by various methods. Fourier Transformed Infrared Absorption spectroscopy (FTIR) is one of the preferred measurement techniques. To analyze the material generated in a plasma, the material is usually deposited on a substrate and then brought into the sample compartment of the FTIR spectrometer. In most cases, this will automatically expose the sample to ambient humid air and set off oxidation of the material. Oxidized functional groups could then be falsely identified to have their origin in the synthesis process.

In this paper, we report on a double atmospheric pressure plasma system with the combined synthesis of quantum dots in the first, and their modification in the second atmospheric pressure plasma source. A similar approach has been used already for low-pressure systems by other groups, such as Kortshagen et al., where one reactor was responsible for the particle generation and the second one for subsequent etching [16] or surface passivation [17]. A rather complicated double atmospheric process for the generation and treatment of nanoparticles has also been reported, for example, by Boies et al. [18]. In our work, the material properties and gas phase consumption of molecular precursors are monitored in situ using a reflective FTIR setup. The optical and other properties of the Si-NPs have been studied ex situ using transmission electron microscopy (TEM), and their photoluminescent properties related to surface passivation have been characterized.

2 | Experimental Setup and Diagnostics

2.1 | Plasma Sources

Synthesis and surface passivation of Si-NPs are performed separately in a two-step process in two similarly looking atmospheric pressure plasma jets that are connected in series. Both atmospheric plasma jets used in this publication are downsized versions of the HelixJet first published by Schäfer et al. in 2019 [19]. For the combined synthesis and passivation of the nanoparticles, two HelixJets are placed on top of each other. As seen in Figure 1 on the left, these jets consist of a quartz glass capillary with an outer diameter of 5 mm and a wall thickness of 1 mm. A set of helical electrodes is placed around each jet in a double helix structure. The electrodes cover the capillary in a length of 4 cm. One of each of the electrodes is grounded, while the other one is driven by a 13.56 MHz frequency. Both jets are connected to their respective generator by a matching network. The first jet is fed with varying amounts of argon as a carrier gas mixed with silane (SiH_4) as a reactive precursor gas for particle synthesis, while the second jet can be supplied with additional gases through a cylindrical connector with a symmetric gas feed placed between jets. The gas inlet is designed under an angle of 45° to support the laminar flow inside the jets and to avoid the formation of turbulent vortexes, which would lead to a loss of particles. The gas feed for

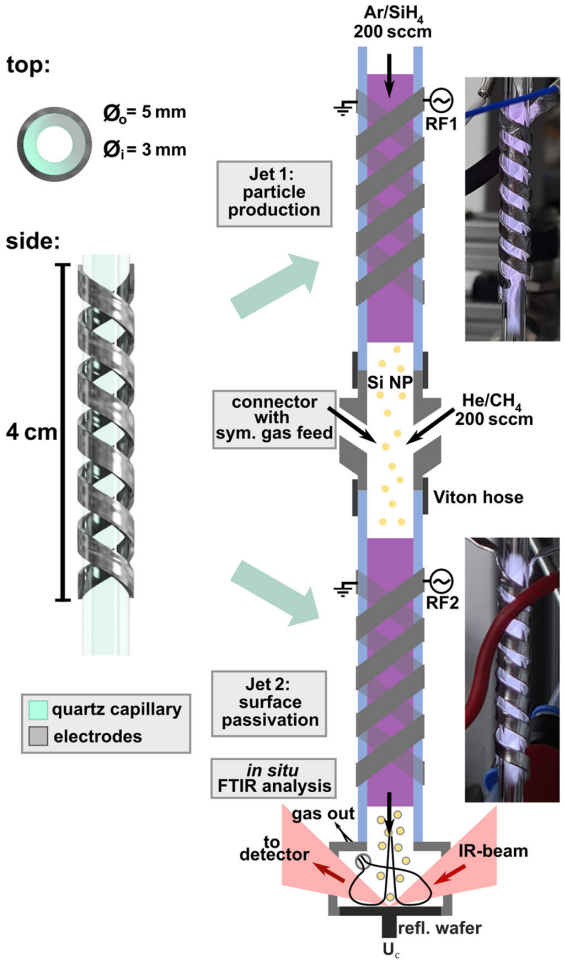

FIGURE 1 | Combined setup of two atmospheric pressure plasma sources connected via a symmetrical gas connector. The first jet is carrying out particle production, and the second one the surface passivation. The resulting particles and the consumption of precursors are monitored using in situ FTIR analysis.

the second jet uses helium as a carrier gas, with the possibility to mix a reactive gas to induce surface passivation.

Si-NCs were synthesized in the first jet using an RF power of 150 W and a gas flow of 200 sccm. The silane concentration was varied between 5 and 50 ppm by mixing pure argon with a fixed mixture of 100 ppm silane in argon. For the surface passivation of Si-NC synthesized in the first jet at a silane concentration of 5 ppm, the second jet has been fed with an additional 200 sccm of 0.05% CH_4 diluted in helium. Helium was chosen as a carrier gas to facilitate the plasma ignition [20] thus allowing for the second jet to be operated in a pulsed mode. To pulse the second generator, a TTL signal (0−5 V) has been utilized with different duty cycles. The pulse width of the signal has been chosen in agreement with the residence time of the particles in the second plasma. For an overall flow of 400 sccm, the average residence time of the particles in the second plasma volume is around 20 ms.

Using appropriate pulsing settings ensures that nanoparticles transitioning through the second plasma should pass through an ignited state at least once in their residence time. The pulse can be operated on different duty cycles to tune the dissociation degree of methane. A duty cycle of 0% corresponds to the second plasma being off (no treatment), while a continuous wave (cw) operation corresponds to a duty cycle of 100%. The generated and treated nanoparticles are carried downstream by the gas flow toward a polished substrate. Here, they are collected on a substrate using a positive bias voltage of U_c = 3 kV. Due to the negative charge of the particles, the positive bias results in a particle drift toward the substrate. This is important for the subsequent ex situ measurements as well as for the in situ FTIR analysis.

2.2 | In Situ Fourier Transform Infrared Spectroscopy

The FTIR in this study was carried out using a commercial Bruker VERTEX 80V spectrometer with a wavenumber resolution of 4 cm^{-1}. The IR beam can be coupled out of the spectrometer and then directed into the in situ setup as shown in Figure 2. The beam is focused and reflected by a mirror through a KBr window onto a biased substrate, where the nanoparticles are collected. A reflective substrate (e.g., a polished silicon wafer or stainless steel substrate) is chosen to reflect the IR beam through the second KBr window onto another mirror and then into a liquid-nitrogen-cooled MCT detector. The IR beam is then absorbed by the deposited particles and also in the gas phase inside the small chamber with the substrate, providing additional information about the presence and consumption of molecular precursors. The beam path outside the small chamber is flushed with dry nitrogen gas to ensure a dry environment and to minimize the absorption by CO_2 and H_2O coming from the ambient air. FTIR spectra are post-processed by the subtraction of polynomial background.

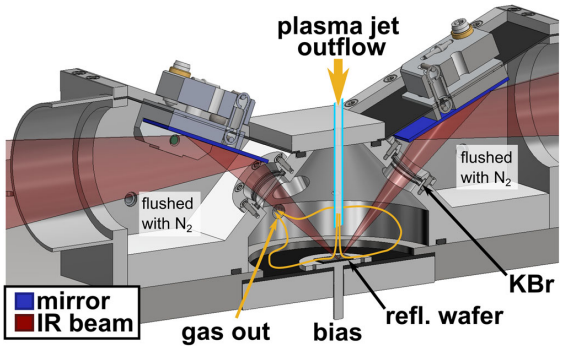

FIGURE 2 | CAD sketch of the in situ FTIR setup. The IR beam is exiting the device and is directed via a mirror onto a reflective wafer. The reflective wafer is placed directly under the outflow of the plasma jet. The beam path is flushed with nitrogen in the outer parts of the chamber; the core chamber is filled with gases exiting the jet.

2.3 | TEM

Direct investigation of particle sizes, morphology, crystal structure, and chemical composition was performed by TEM. In this case, a field emission gun equipped with FEI Tecnai F30 G^2 STwin operated at 300 kV was used to study nanoparticles in TEM bright field mode. TEM samples were obtained by placing TEM holey carbon copper grids below the output of the jet on a collection electrode that could be positively biased with 3 kV. The local elemental composition was examined by energy-dispersive X-ray (EDX) spectroscopy, providing estimated values of the oxygen concentration. A quantitative determination is beyond the scope of this study. The particle size distribution was calculated from particle diameters measured using the ImageJ software.

2.4 | X-Ray Photo-Electron Spectroscopy (XPS)

XPS was used to study the chemical composition and chemical bonds on the surface of the passivated Si-NPs. Corresponding samples were measured using an XPS UHV system from PREVAC Sp. z o. o., equipped with an Al-anode operating at 300 W. Widescans were performed by using three iterations and a pass energy of 200 eV. High-resolution scans were measured with 20 iterations and a pass energy of 50 eV. For the processing and analysis of the XPS spectra, the software CasaXPS (version 2.3.23) was used. The background correction was done by applying the Shirley algorithm [21]. For all recorded spectra, charge correction was applied by setting the C–C representing component in the fitted C 1s spectra of each sample to 284.8 eV.

2.5 | PL Measurements

The steady-state PL spectra were measured directly on the powdered sample using a Shamrock 300i imaging spectrograph (Andor; Oxford Instruments) coupled with a CCD camera. A HeCd laser (λ = 325 nm; P = 3.5 mW) was used to excite the Si-NPs. To minimize the influence of inhomogeneities and laser-induced modification of the sample, the measurement was repeated at different spots on the wafer surface and the collected spectra were compared. All spectra were corrected for the spectral sensitivity of the whole system.

3 | Results and Discussion

The aim of this study is to characterize the effect of plasma treatment on the optical properties of silicon quantum dots. Therefore, the operation parameters of the first jet have been optimized to generate small silicon nanocrystals that exhibit PL behavior. These reference particles can be then modified using the second jet. Particles in the first jet can be generated using argon as a carrier gas. Here, silane concentration, overall gas flow, and applied power are variables. These parameters have a significant influence on the composition and structure of the particles, where the Si-NP sizes usually scale with silane concentration. Residence time and plasma power have a strong effect on the crystallinity.

The TEM images of nanoparticles synthesized at various silane concentrations are shown in Figure 3. As can be expected, a larger concentration leads to larger nanoparticles because there is more material available in the plasma for them to grow. For a silane concentration of 5 ppm, quantum dots with average diameters of around 7.5 nm are formed. Regardless of size, the nanoparticles are crystalline, as indicated by the SAED insets, and have a spherical shape. A detailed study of electron diffraction patterns using rotational averages and their comparison with *d*-values of cubic silicon showed that the reflections in the SAED patterns correspond to FCC silicon. This shows that the applied power in combination with the selective heating of the nanoparticles [22] is sufficient to reach the crystallization temperature of larger nanoparticles up to 40 nm in diameter. Additionally, all nanoparticles have an amorphous oxygen-rich shell. For the samples from Figure 3, the average diameter as well as the maximum and minimum diameters observed in the TEM images were determined and are shown in Table 1. Using EDX, the atomic concentrations of silicon and oxygen were measured. Both the TEM images and EDX results show that as silane concentration decreases, both the average, and also maximum and minimum diameters of the nanoparticles also decrease. A closer analysis of the average atomic oxygen-to-silicon ratios shows an increase in oxygen content as particle size decreases. This is the consequence of the much larger surface-to-volume ratio of the smaller nanoparticles. Since every nanoparticle has a similar oxygen-rich amorphous shell, smaller particles will inherently exhibit a higher oxygen content, even though the quality of the crystal itself is good.

3.1 | FTIR Results/Particle Composition

Normalized FTIR spectra (measured during the deposition process after 10 min) of the largest and smallest deposited nanoparticles according to Table 1 are plotted in Figure 4. The FTIR band with the greatest peak intensity at around 1100 cm^{-1} corresponds to Si-O-Si bonds and its broad appearance can be explained by the simultaneous excitation of both longitudinal and transversal oscillation modes due to the incident angle of the reflective FTIR setup as explained in Ref [23]. This oxygen contamination results very probably from the residual water molecules in the system, impurities in the process gases, or leak of air into the setup. The wavenumbers in the range of 2100−2300 cm^{-1} contain the absorption peaks of the Si-H-bonds. Here, a much higher degree of non-oxidized Si-H-bonds is found in the 50 ppm sample of larger nanoparticles.

TABLE 1 | Average d_{avg} and maximum d_{max} diameters for silicon nanoparticles synthesized at different silane concentrations c_{SiH_4}, as well as the elemental compositions of these nanoparticles as determined by EDX.

	c_{SiH_4}	d_{avg} in nm	d_{max}	at% Si	at% O
a	50 ppm	16.3 ± 6.1	40.8 nm	94	6
b	25 ppm	14.5 ± 3.6	24.6 nm	85	15
c	10 ppm	9.3 ± 2.4	16.9 nm	72	28
d	5 ppm	7.4 ± 2.3	14.6 nm	48	52

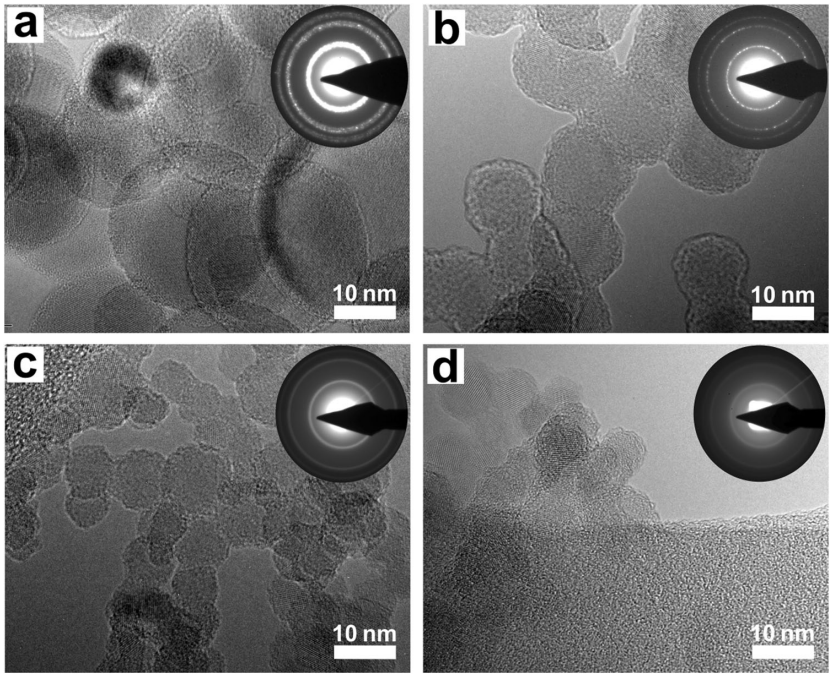

FIGURE 3 | TEM images of nanoparticles synthesized in the first jet at a power of 150 W with a fixed overall flow of 200 sccm at silane admixtures of (a) 50 ppm, (b) 25 ppm, (c) 10 ppm, and (d) 5 ppm.

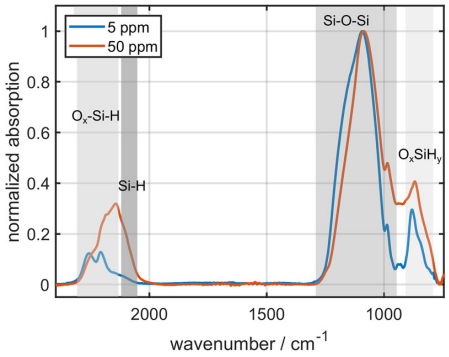

FIGURE 4 | In situ FTIR spectra of silicon nanoparticles generated at a silane admixture of 50 ppm in red and 5 ppm in blue. Applied plasma power was 150 W and the overall gas flow was 200 sccm.

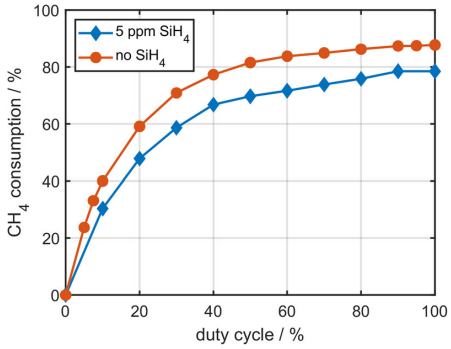

FIGURE 5 | Methane consumption for different duty cycles as measured for the case of particles being synthesized in the first jet (blue) and for the case of no particles produced (red).

Several factors can contribute to this effect. First, smaller Si-NPs are generated at smaller silane admixtures, where the ratio of silane to impurities is smaller and the oxidation larger. Second, the amount of the available hydrogen per surface site of Si-NPs is larger for larger Si-NPs. The silane molecule is a source of hydrogen in this process with a 4:1 H:Si ratio. Most of the silicon is located in the Si-NP volume for larger particles, leaving more hydrogen available per surface site in the plasma compared to the case of smaller Si-NPs, where much more Si is located at the surface. Moreover, hydrogen is likely located at the particle surface. Smaller particles are heated in the plasma more easily [22], allowing them to reach and stay at temperatures high enough for hydrogen desorption from the amorphous silicon to occur.

4 | Surface Passivation Using Methane

As discussed in the introduction, the passivation of the nanoparticle surface with methyl groups (and, in general, with hydrocarbon chains) can strongly influence the Si-NC optical properties. Therefore, plasma conditions have to be found that will enhance surface passivation with hydrocarbon functional groups, while preventing the fast deposition of a thick hydrocarbon layer. These conditions can be realized by a pulsed plasma operation, reducing the average specific energy per molecule. Mainly CH_3 fragments are generated as primary CH_4 dissociation products under these conditions [24]. The reactivity of CH_3 radicals is negligible in the gas phase [25], and it is rather slow at the surface. Additionally, atomic hydrogen is produced which can generate dangling bonds at the NP surface, to which the CH_3 radicals can attach with a higher probability (around 0.01) as has been observed in the case of their interaction with hydrocarbon films [26]. The low surface reactivity of CH_3 should make surface passivation more probable compared to thin film growth. The smallest crystalline particles synthesized at 5 ppm of silane in argon were selected for subsequent passivation experiments.

4.1 | Methane Consumption

As a first step, methane consumption is monitored by means of FTIR absorption in the gas phase measured at the methane band at a wavenumber of 3014 cm^{-1} in the exhaust gases coming out of the second plasma jet for its different duty cycles. This is later used as an indicator for the plasma chemistry processes. As can be seen in Figure 5, the consumption of methane in the second jet increases with the length of the duty cycle, as the CH_4 signal in the FTIR measurement becomes weaker, which is an expected result. This trend is consistent regardless of whether the first jet operates with argon alone or with the argon/silane mixture. However, methane consumption is slightly lower when silane is introduced into the first jet. When no silane is admixed (red curve), the maximum methane consumption is slightly higher and less CH_4 is leaving the second jet in the exhaust gases. When introducing silane in the first jet, there is more hydrogen in the system that can etch the amorphous carbon layers on the walls with CH_4 being one of the main etching products, as has been shown in Ref [27]. Additionally, nanoparticles will attract charges making the second plasma weaker. This can change the plasma chemistry. Higher methane dissociation in the second plasma indicates the presence of highly reactive methane fragments (CH_x radicals) that can lead to carbon film or dust formation. Since the aim is to passivate the Si-NC with methyl radicals, only a weak second plasma with lower CH_4 consumption is desirable. Therefore, a duty cycle below 10% should be used in this process as an optimal operation mode.

4.2 | FTIR Analysis of the Surface Passivation

Figure 6 shows the normalized and background-corrected FTIR spectra as measured by the in situ setup for untreated Si-NPs in blue, as well as for particles that were treated with a pulsed (50 Hz) plasma with a 0.05% methane admixture. A duty cycle of $D = 60\%$ is shown in yellow, and a duty cycle of $D = 7.5\%$ is shown in red. The peaks at 1100 and 800 cm^{-1} correspond to asymmetric stretching in Si-O-Si [28–30] and Si-O bending [31], respectively. They appear similar for both treated and untreated samples. In the wavenumber range from 2400 to 2000 cm^{-1}, Si-H_x [32, 33], R-Si-H_3 [34], and O-Si-H [32] bonds can be identified. Here, a treatment at high-duty cycles (yellow) seems to almost completely remove these bonds from the particle surface. Instead, several peaks in the region from 1800 to 1400 cm^{-1} appear, which indicate

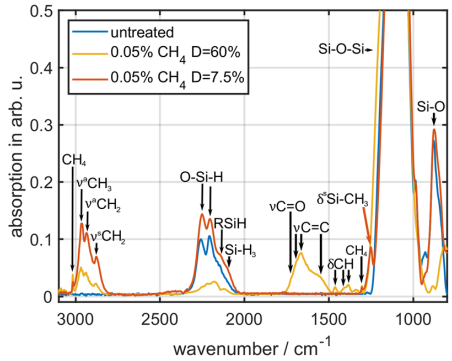

FIGURE 6 | FTIR spectra for nanoparticles synthesized at 5 ppm silane untreated (blue) and treated with 0.05% CH_4 admixture for duty cycles of 60% (yellow) and 7.5% (red). Spectra are shown normalized to the peak at 1100 cm^{-1}.

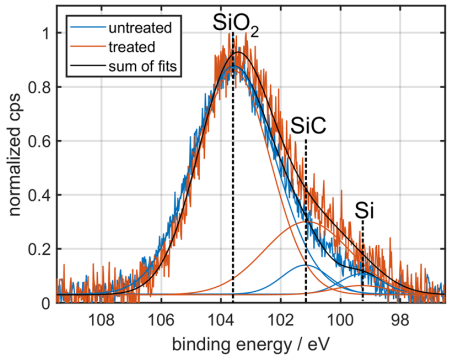

FIGURE 7 | Background-corrected and normalized XPS spectra for an untreated sample in blue and a sample treated with a duty cycle of 7.5% in red.

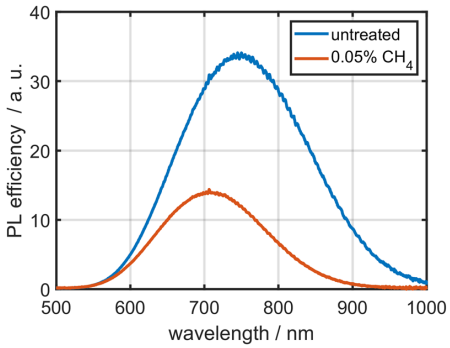

FIGURE 8 | Photoluminescence intensity spectra for nanoparticles synthesized at 5 ppm silane untreated (blue) and treated with 0.05% CH_4 admixture at a duty cycle of $D = 7.5\%$.

the formation of a thick hydrocarbon layer on top of the particles produced with duty cycle $D = 60\%$. The peak at 1720 cm^{-1} can be identified to be C = O stretching vibrations [35]. In the range from 1680 to 1550 cm^{-1}, the stretching vibrations of double-bonded carbon are found [36]. The region from 1450 to 1370 cm^{-1} includes the deformation vibrations of CH bonds [37].

The growth of a thin amorphous hydrocarbon carbon layer can be identified for all treated samples in the wavenumber region from 3000 to 2800 cm^{-1}, independent of the length of the duty cycle. Here, three peaks can be identified as the asymmetric stretching of CH_3 (2964 cm^{-1}) as well as the asymmetric (2934 cm^{-1}) and symmetric (2880 cm^{-1}) stretching of CH_2 according to Refs [38, 39]. This amorphous hydrocarbon layer is not present in the untreated sample (blue) and is also not observed when the first jet is switched off (not shown here). Therefore, a carbon thin film deposition on the substrate can be excluded and these new features in the spectra are present only due to a carbon film growing on top of the nanoparticles.

The last difference between the three spectra can be observed at a wavenumber of 1260 cm^{-1}. Here, only the sample treated at $D = 7.5\%$ exhibits a peak, which corresponds to the CH_3 deformation vibration in Si-CH_3. [29, 30]. This peak which is not present in the untreated sample can be an indicator for a successful surface passivation with CH_3. This will be further verified with XPS measurements.

Overall, the duration of the duty cycle strongly influences the passivation and termination of the Si-NPs. Untreated nanoparticles first exhibit Si-H bonds at the surface, which then quickly oxidize in ambient air, leaving the surface to be terminated by oxygen. For short duty cycles, a peak at 1260 cm^{-1} in the FTIR spectra indicates the successful attachment of methyl groups to silicon atoms at the nanoparticle surface, with the additional presence of C-bonded CH_3 and CH_2 groups. For increased duty cycles, a thick carbon layer is probably formed, completely covering the particle and preventing the formation of the other surface bonds as demonstrated by their reduced relative contribution to the absorption spectrum.

4.3 | XPS Results

XPS measurements have been carried out to further investigate the formation of Si-C bonds. Figure 7 shows the background-corrected and normalized spectra for the Si 2p core-level spectrum of an untreated sample (blue) and a sample treated at a duty cycle of $D = 7.5\%$ (red). Additionally, a sum of three Gaussian functions has been fitted to each spectrum. The starting parameters for the maxima of the fits were chosen corresponding to the binding energies for SiO_2 (103.6 eV), SiC (101.0 eV), and Si-Si in lattice silicon (99 eV) [40, 41]. When comparing the graphs and the fits, the treated sample exhibits a more pronounced Si-C peak. Despite the noise, a more prominent low-energy shoulder of the Si 2p peak is clearly visible, suggesting the presence of methyl groups or carbon bound to the surface of the Si-NPs. Together with the in situ FTIR data, this confirms the formation of silicon–carbon bonds and confirms the methylation of the Si NPs in the methane-containing plasma in the second jet.

4.4 | PL

The spectra of the PL measurements can be seen in Figure 8 for the untreated particles in blue, as well as the particles that

underwent treatment with CH_4 containing second plasma in red. All spectra were corrected for the spectral sensitivity of the whole system. Although the setup does not allow for the collection of absolute photoluminescent intensity, the spectra are expected to be comparable. Since nanoparticles of the same size were collected at similar conditions and with similar resulting thin films, the scattering of the excitation laser and the angular radiation of the PL from the sample will be comparable. Additionally, three independent measurements on three different spots of each sample yield similar photoluminescent intensity. Since the primary focus is on the wavelength shift, this shift can be quantitatively expressed. The untreated sample exhibits a strong PL signal with the maximum at a wavelength of 750 nm. In comparison, the sample treated with 0.05% CH_4 at a duty cycle of $D = 7.5\%$ shows a clear blue shift with a maximum at around 710 nm, but at only half the intensity. A similar behavior has already been observed by other research groups, where methylation was able to induce a blue shift in the PL signal, but at the same time reduced the overall PL intensity drastically [42]. Samples produced at duty cycles of 10% were not of optical quality and did not exhibit any PL. This is probably due to the thick CH layer on the particles.

5 | Conclusions

A set-up of two HelixJet plasma sources has been successfully used for the combined synthesis and treatment of Si-NPs with optical properties. TEM measurements revealed that monocrystalline particles of various sizes can be synthesized depending on the silane admixture. For small silane admixtures of around 5 ppm, the particles turned into quantum dots with average diameters of 7 nm exhibiting a PL response visible to the naked eye with a maximum at around 750 nm. When treating these particles with a second identical HelixJet plasma source with an admixture of helium-diluted CH_4 and operated in pulsed mode with variable duty cycle, the appearance of an $Si\text{-}CH_3$ absorption could be observed for a small duty cycle using a custom-built in situ FTIR setup, as well as the growth of an amorphous carbon layer on the silicon particles for duty cycles of 10% and above. For small duty cycles, the successful passivation of silicon with carbon groups could be verified by XPS analysis, where only the treated samples displayed the peak for silicon–carbon bonds. The methane plasma treatment with small duty cycles successfully led to a blue shift in the PL of silicon nanocrystals with the maximum shifted to 710 nm after the treatment.

Acknowledgments

We gratefully acknowledge funding of this project by the German Research Foundation (DFG, project number 426208229) and Major Research Instrumentation Program projects (INST 257/595-1 and INST 257/704-1). The authors would also like to thank Thomas Strunskus for his insights into the evaluation of the XPS data. Open Access funding enabled and organized by Projekt DEAL.

Conflicts of Interest

The authors declare no conflicts of interest.

Data Availability Statement

The data that support the findings of this study are available from the corresponding author upon reasonable request.

References

1. S. P. Low, N. H. Voelcker, L. T. Canham, and K. A. Williams, "The Biocompatibility of Porous Silicon in Tissues of the Eye," *Biomaterials* 30 (2009): 2873–2880, https://doi.org/10.1016/j.biomaterials.2009.02.008.

2. A. Fucikova, J. Valenta, I. Pelant, et al., "Silicon Nanocrystals and Nanodiamonds in Live Cells: Photoluminescence Characteristics, Cytotoxicity and Interaction With Cell Cytoskeleton," *RSC Advances* 4 (2014): 10334–10342, https://doi.org/10.1039/c3ra47574c.

3. K. Herynková, P. Šimáková, O. Cibulka, A. Fučíková, and M. Hubálek Kalbáčová, "Hydrophilic Luminescent Silicon Nanoparticles in Steric Colloidal Solutions: Their Size, Agglomeration, and Toxicity," *Physica Status Solidi C* 14 (2017): e1700195, https://doi.org/10.1002/pssc.201700195.

4. S. Chinnathambi, S. Chen, S. Ganesan, and N. Hanagata, "Silicon Quantum Dots for Biological Applications," *Advanced Healthcare Materials* 3 (2013): 10–29, https://doi.org/10.1002/adhm.201300157.

5. X. Ji, H. Wang, B. Song, B. Chu, and Y. He, "Silicon Nanomaterials for Biosensing and Bioimaging Analysis," *Frontiers in Chemistry* 6 (2018): 38, https://doi.org/10.3389/fchem.2018.00038.

6. M. Müller, P. Galář, J. Stuchlík, J. Kočka, J. Kupka, and K. Kůsová, "Synthesis and Surface Modification of Light Emitting Silicon Nanoparticles Using Non-Thermal Plasma Techniques," *European Physical Journal Applied Physics* 89 (2020): 20401, https://doi.org/10.1051/epjap/2020190263.

7. S. Morozova, M. Alikina, A. Vinogradov, and M. Pagliaro, "Silicon Quantum Dots: Synthesis, Encapsulation, and Application in Light-Emitting Diodes," *Frontiers in Chemistry* 8 (2020): 191, https://doi.org/10.3389/fchem.2020.00191.

8. M. Otsuka, Y. Kurokawa, Y. Ding, et al., "Silicon Nanocrystal Hybrid Photovoltaic Devices for Indoor Light Energy Harvesting," *RSC Advances* 10 (2020): 12611–12618, https://doi.org/10.1039/d0ra00804d.

9. H. Wang and Y. He, "Recent Advances in Silicon Nanomaterial-Based Fluorescent Sensors," *Sensors* 17 (2017): 268, https://doi.org/10.3390/s17020268.

10. B. Chu, H. Wang, B. Song, F. Peng, Y. Su, and Y. He, "Fluorescent and Photostable Silicon Nanoparticles Sensors for Real-Time and Long-Term Intracellular pH Measurement in Live Cells," *Analytical Chemistry* 88 (2016): 9235–9242, https://doi.org/10.1021/acs.analchem.6b02488.

11. W. Petasch, B. Kegel, H. Schmid, K. Lendenmann, and H. Keller, "Low-Pressure Plasma Cleaning: A Process for Precision Cleaning Applications," *Surface and Coatings Technology* 97 (1997): 176–181, https://doi.org/10.1016/S0257-8972(97)00143-6.

12. L. Holland, "Some Characteristics and Uses of Low-Pressure Plasmas in Materials Science," *Journal of Vacuum Science and Technology* 14 (1977): 5–15, https://doi.org/10.1116/1.569159.

13. T. Nozaki, K. Sasaki, T. Ogino, D. Asahi, and K. Okazaki, "Microplasma Synthesis of Tunable Photoluminescent Silicon Nanocrystals," *Nanotechnology* 18 (2007): 235603, https://doi.org/10.1088/0957-4484/18/23/235603.

14. K. Kůsová, O. Cibulka, K. Dohnalová, et al., "Brightly Luminescent Organically Capped Silicon Nanocrystals Fabricated at Room Temperature and Atmospheric Pressure," *ACS Nano* 4 (2010): 4495–4504, https://doi.org/10.1021/nn1005182.

15. P. Hapala, K. Kůsová, I. Pelant, and P. Jelínek, "Theoretical Analysis of Electronic Band Structure of 2- to 3-nm Si Nanocrystals," *Physical Review B* 87 (2013): 195420, https://doi.org/10.1103/physrevb.87.195420.

16. X. D. Pi, R. W. Liptak, S. A. Campbell, and U. Kortshagen, "In-Flight Dry Etching of Plasma-Synthesized Silicon Nanocrystals," *Applied Physics Letters* 91 (2007): e083112, https://doi.org/10.1063/1.2773931.

17. L. Mangolini and U. Kortshagen, "Plasma-Assisted Synthesis of Silicon Nanocrystal Inks," *Advanced Materials* 19 (2007): 2513–2519, https://doi.org/10.1002/adma.200700595.

18. A. M. Boies, J. T. Roberts, S. L. Girshick, B. Zhang, T. Nakamura, and A. Mochizuki, "SiO2 Coating of Silver Nanoparticles by Photo-induced Chemical Vapor Deposition," *Nanotechnology* 20 (2009): 295604, https://doi.org/10.1088/0957-4484/20/29/295604.

19. J. Schäfer, A. Quade, K. J. Abrams, et al., "HelixJet: An Innovative Plasma Source for Next-Generation Additive Manufacturing (3D Printing)," *Plasma Processes and Polymers* 17 (2020): 1900099, https://doi.org/10.1002/ppap.201900099.

20. S. P. Das, G. Dalei, and A. Barik, "A Dielectric Barrier Discharge (DBD) Plasma Reactor: An Efficient Tool to Measure the Sustainability of Non-Thermal Plasmas Through the Electrical Breakdown of Gases," *IOP Conference Series: Materials Science and Engineering* 410 (2018): 012004, https://doi.org/10.1088/1757-899x/410/1/012004.

21. D. A. Shirley, "High-Resolution X-Ray Photoemission Spectrum of the Valence Bands of Gold," *Physical Review B* 5 (1972): 4709–4714, https://doi.org/10.1103/physrevb.5.4709.

22. L. Mangolini and U. Kortshagen, "Selective Nanoparticle Heating: Another Form of Nonequilibrium in Dusty Plasmas," *Physical Review E* 79 (2009): 1–8, https://doi.org/10.1103/PhysRevE.79.026405.

23. T. de los Arcos, H. Müller, F. Wang, et al., "Review of Infrared Spectroscopy Techniques for the Determination of Internal Structure in Thin SiO2 Films," *Vibrational Spectroscopy* 114 (2021): 103256, https://doi.org/10.1016/j.vibspec.2021.103256.

24. S. Ravasio and C. Cavallotti, "Analysis of Reactivity and Energy Efficiency of Methane Conversion Through Non-Thermal Plasmas," *Chemical Engineering Science* 84 (2012): 580–590, https://doi.org/10.1016/j.ces.2012.09.012.

25. W. A. Pryor, D. L. Fuller, and J. P. Stanley, "Reactions of Radicals. 41. Reactivity Patterns of the Methyl Radical," *Journal of the American Chemical Society* 94 (1972): 1632–1638, https://doi.org/10.1021/ja00760a034.

26. A. von Keudell, "Formation of Polymer-Like Hydrocarbon Films From Radical Beams of Methyl and Atomic Hydrogen," *Thin Solid Films* 402 (2002): 1–37, https://doi.org/10.1016/s0040-6090(01)01670-4.

27. J. Benedikt, "Plasma-Chemical Reactions: Low Pressure Acetylene Plasmas," *Journal of Physics D: Applied Physics* 43 (2010): 043001, https://doi.org/10.1088/0022-3727/43/4/043001.

28. G. Socrates, Infrared and Raman Characteristic Group Frequencies: Tables and Charts, 3rd ed. (Chichester: John Wiley & Sons Inc., 2004).

29. L. M. Johnson, L. Gao, C. W. Shields, IV, et al., "Elastomeric Microparticles for Acoustic Mediated Bioseparations," *Journal of Nanobiotechnology* 11 (2013): 22, https://doi.org/10.1186/1477-3155-11-22.

30. V. Raballand, J. Benedikt, J. Wunderlich, and A. von Keudell, "Inactivation of *Bacillus atrophaeus* and of *Aspergillus niger* Using Beams of Argon Ions, of Oxygen Molecules and of Oxygen Atoms," *Journal of Physics D: Applied Physics* 41 (2008): 115207, https://doi.org/10.1088/0022-3727/41/11/115207.

31. J. Serra, P. González, S. Liste, et al., "FTIR and XPS Studies of Bioactive Silica Based Glasses," *Journal of Non-Crystalline Solids* 332 (2003): 20–27, https://doi.org/10.1016/j.jnoncrysol.2003.09.013.

32. P. Gupta, A. Dillon, A. Bracker, and S. George, "FTIR Studies of H2O and D2O Decomposition on Porous Silicon Surfaces," *Surface Science* 245 (1991): 360–372, https://doi.org/10.1016/0039-6028(91)90038-t.

33. Y. Ogata, H. Niki, T. Sakka, and M. Iwasaki, "Hydrogen in Porous Silicon: Vibrational Analysis of SiH x Species," *Journal of the Electrochemical Society* 142 (1995): 195–201, https://doi.org/10.1149/1.2043865.

34. D. A. Long, "Infrared and Raman Characteristic Group Frequencies. Tables and Charts George Socrates John Wiley and Sons, Ltd, Chichester, Third Edition, 2001. Price €135," *Journal of Raman Spectroscopy* 35 (2004): 905, https://doi.org/10.1002/jrs.1238.

35. M. Clin, O. Durand-Drouhin, A. Zeinert, and J. Picot, "A Correlation Between the Microstructure and Optical Properties of Hydrogenated Amorphous Carbon Films Prepared by RF Magnetron Sputtering," *Diamond and Related Materials* 8 (1999): 527–531, https://doi.org/10.1016/s0925-9635(98)00404-x.

36. V. Chhabra, K. Bambery, S. Bhattacharya, and Y. Shastri, "Thermal and in Situ Infrared Analysis to Characterise the Slow Pyrolysis of Mixed Municipal Solid Waste (MSW) and Its Components," *Renewable Energy* 148 (2020): 388–401, https://doi.org/10.1016/j.renene.2019.10.045.

37. P. K. Chu and L. Li, "Characterization of Amorphous and Nanocrystalline Carbon Films," *Materials Chemistry and Physics* 96 (2006): 253–277, https://doi.org/10.1016/j.matchemphys.2005.07.048.

38. P. Couderc and Y. Catherine, "Structure and Physical Properties of Plasma-Grown Amorphous Hydrogenated Carbon Films," *Thin Solid Films* 146 (1987): 93–107, https://doi.org/10.1016/0040-6090(87)90343-9.

39. B. Dischler, A. Bubenzer, and P. Koidl, "Hard Carbon Coatings With Low Optical Absorption," *Applied Physics Letters* 42 (1983): 636–638, https://doi.org/10.1063/1.94056.

40. D. S. Jensen, S. S. Kanyal, N. Madaan, et al., "Silicon (100)/SiO2 by XPS," *Surface Science Spectra* 20 (2013): 36–42, https://doi.org/10.1116/11.20121101.

41. G. Ervin, "Oxidation Behavior of Silicon Carbide," *Journal of the American Ceramic Society* 41 (1958): 347–352, https://doi.org/10.1111/j.1151-2916.1958.tb12932.x.

42. P. Galář, J. Stuchlík, M. Müller, J. Kočka, and K. Kůsová, "Highly Spherical SiC Nanoparticles Grown in Nonthermal Plasma," *Plasma Processes and Polymers* 19 (2021): e2100127, https://doi.org/10.1002/ppap.202100127.

9 | Summary and conclusions

This thesis has presented several options how atmospheric pressure plasmas can help facilitate the challenging synthesis of NPs with various elemental compositions. NPs and nanocrystals of silicon, tungsten and other materials were successfully synthesized. Pure particles, particles with a modified surface, core-shell particles and Janus-like particles could be prepared using atmospheric pressure plasmas.

The atmospheric plasma source HelixJet was chosen for the plasma-assisted NP synthesis. It consists of a quartz glass capillary surrounded by a set of helix-shaped electrodes. Such a jet design proved to be able to form silicon NPs from silane. However, when using higher admixtures of reactive gases such as silane or hydrogen, the jet became unstable and its simple design did not allow for long-term operation. As a first step, this jet was modified to ensure stable operation also at high admixtures of reactive gases. The previously mixed gas feed was separated into an inner and outer capillary, where the reactive gases were fed on the middle axis of the jet. Simulations in COMSOL Multiphysics® revealed the optimal flow values for the inner and outer capillary which resulted in a laminar flow. The simulation of the transport of concentrated species showed that the concentration of silane at the walls of the jet (and therefore the deposition rate) is neglectable when a laminar flow is established. This was also shown experimentally, since the operation time of the jet until the capillary needs to be replaced due to deposition increased, when the settings for a laminar flow were chosen. As a second modification, an additional grounded electrode was placed in close proximity to the RF helix electrode, which ignited a first plasma in the noble gas section. This plasma helped to generate radiation and additional secondary electrons which facilitate to ignite the reactive plasma at high mixtures of silane.

The modified version of the jet was used to synthesize silicon NPs. The plasma conditions were varied in terms of plasma power and hydrogen admixture. The size distributions of the synthesized particles were measured using a scanning mobility particle sizer. When setting the DMA voltage to a value corresponding to a particle diameter of 50 nm and measuring them using SEM, agglomerates could be found. This showed that agglomerates of smaller NPs can be falsely detected by the SMPS as one spherical NP of increased size, further stressing the necessity to always confirm size measurements with microscopy methods. For additional information on the crystallinity of the NPs, TEM was utilized. These measurements revealed that, for an optimal set of parameters, silicon nanocrystals could be produced. For small silane admixtures, these nanocrystals were turned into quantum dots that exhibited photoluminescent properties. These properties were analyzed in a collaboration with the Institute of Physics of the Czech Academy of Sciences in Prague using steady-state and time-resolved photoluminescence spectroscopy. Particles generated at higher powers and with hydrogen admixture showed an overall increased photoluminescence efficiency, while particles generated at lower powers and without hydrogen admixture were mostly amorphous. A closer look into the aging behavior of the photoluminescence signal revealed that the formation of an oxide layer on top of the nanocrystals in the first two weeks improved the intensity of the photoluminescence signal greatly. After this initial increase, the intensity remained unchanged or decreased only slightly, but an overall blue shift of the PL maximum was observed. This

process was self-limiting in nature. The blue shift could be attributed to a change of the size of the crystalline core.
For a next study, this HelixJet was connected with an in-flight annealing stage in the form of a stainless steel tube inside a muffle furnace. Evaporated manganese, iron and chromium from the stainless steel tube, in combination with the silicon NPs synthesized by the HelixJet, formed Janus particles with an interesting half-sphere structure. The complex shape and elemental composition of the particles were studied intensively in a collaboration with the group of Prof. Kienle at the Faculty of Engineering in Kiel. Choosing the right combination of annealing temperature and tubing material, this study builds the foundation for the possible synthesis of various silicon-based Janus particles.
Following the goal to synthesize silicon nanocrystals without additional hydrogen admixture, a smaller version of the jet was designed that exhibited an increased power density. Although this smaller jet was, in fact, able to generate photoluminescent nanocrystals without additional hydrogen admixture, it also opened the possibility for the synthesis of metal NPs in a top-down approach. For this, a metal wire was inserted into the middle axis of the jet in place of the inner capillary and the wire was heated by the interaction with the plasma. To test the ability of this setup to synthesize NPs even from high melting point materials, tungsten was chosen as the first source material. The temperature of the tungsten wire inside the jet could be measured using optical emission spectroscopy and the temperature was determined from the background black body radiation. The average temperature of the wire tip reached up to 2200 °C depending on the plasma power, though higher temperatures are expected to be reached locally. Different gas flows and plasma powers led to the formation of different tungsten NPs. With varying plasma power, the resulting temperature of the wire could be tuned and the amount of material evaporated into the plasma was controlled to produce NPs of different sizes. The mean particle diameter increased with plasma power. High flows helped to synthesize smaller particles, while lower flows led to larger particles. The flow also affected the residence time of NPs inside the plasma and with that the crystallographic phases of the tungsten nanocrystals. The parameters of the jet could be chosen to change the phase of the tungsten NPs between β- and faceted α-tungsten, further proving the ability of atmospheric plasmas to tailor NPs for a specific application by a simple variation of parameters.
In an unpublished study, the combination of both top-down and bottom-up approach was tested with a copper wire and the reactive gas silane. The combined synthesis of copper particles from a source material together with the gas phase synthesis of silane resulted in the formation of core-shell particles with a dense copper core and a silicon shell, as shown by TEM and EDX measurements. This study was a valuable first step for further research. In theory, different metal wires can be placed in the jet at different positions to explore the ability of the plasma jet to synthesize metal alloy or Janus particles.
Since the surface of NPs is the key to their characteristics and therefore to their possible applications, an optimal synthesis technique should also cover the possibility of surface passivation. In the last publication, two identical smaller versions of the HelixJet were combined in a double jet setup. The first jet was responsible for the silicon NP production and the second jet for the subsequent surface passivation. To achieve surface termination with methyl groups, the second jet was operated in a pulsed mode at different duty cycles with methane as the reactive gas. The double jet setup was connected to a reflective *in situ* FTIR setup, which allowed to monitor the consumption of reactive gases, as well as the chemical composition of the particles in real time. Analysis of the methane consumption showed that for

a duty cycle of 10 % already one third of the total methane was consumed. Since only the first dissociation of methane is desirable to achieve methylation, a higher duty cycle was not beneficial. The formation of Si-C bonds was observed for a duty cycle of 7.5 % in both FTIR and XPS measurements. Subsequent PL measurements of samples with and without surface passivation revealed that the methane treatment resulted in a blue shift but at the same time reduced the overall photoluminescent intensity. Here, further investigations could lead to full methylation of the NP surface and bring the increased PL intensity predicted by theoretical calculations.

Overall, it could be shown that atmospheric pressure plasmas offer great potential in the synthesis of various NPs from precursors both in the gas phase and in the form of solid source material. The properties of the particles can be tailored using different settings for plasma parameters such as flow, power or admixture of reactive gases.

Literature

[1] T. A. Egerton, I. R. Tooley, "UV absorption and scattering properties of inorganic-based sunscreens", *International Journal of Cosmetic Science* **2011**, *34*, 117–122.

[2] R. Gupta, H. Xie, "Nanoparticles in Daily Life: Applications, Toxicity and Regulations", *Journal of Environmental Pathology Toxicology and Oncology* **2018**, *37*, 209–230.

[3] W. J. Stark, P. R. Stoessel, W. Wohlleben, A. Hafner, "Industrial applications of nanoparticles", *Chemical Society Reviews* **2015**, *44*, 5793–5805.

[4] A. Sa'ar, M. Dovrat, J. Jedrzejewsky, I. Popov, I. Balberg, "The role of quantum confinement and surface chemistry in silicon nanocrystals at the strong confinement regime", *physica status solidi (a)* **2007**, *204*, 1491–1496.

[5] F. Hua, M. T. Swihart, E. Ruckenstein, "Efficient Surface Grafting of Luminescent Silicon Quantum Dots by Photoinitiated Hydrosilylation", *Langmuir* **2005**, *21*, 6054–6062.

[6] W. A. A. Mohamed, H. Abd El-Gawad, S. Mekkey, H. Galal, H. Handal, H. Mousa, A. Labib, "Quantum dots synthetization and future prospect applications", *Nanotechnology Reviews* **2021**, *10*, 1926–1940.

[7] S. Morozova, M. Alikina, A. Vinogradov, M. Pagliaro, "Silicon Quantum Dots: Synthesis, Encapsulation and Application in Light-Emitting Diodes", *Frontiers in Chemistry* **2020**, *8*.

[8] Y. Xia, H. Yang, C. T. Campbell, "Nanoparticles for Catalysis", *Accounts of Chemical Research* **2013**, *46*, 1671–1672.

[9] F. Tao, *Metal Nanoparticles for Catalysis*, 1st ed., (Eds.: J. Spivey, K. Philippot, T. Pal, M. Knecht, P. Liu, S. Suib, A. Roucoux, H. Yamashita, F. Alonso), Royal Society of Chemistry, Cambridge, **2014**, 1285 pp.

[10] S. Chen, R. Yuan, Y. Chai, F. Hu, "Electrochemical sensing of hydrogen peroxide using metal nanoparticles: a review", *Microchimica Acta* **2012**, *180*, 15–32.

[11] V. Mody, R. Siwale, A. Singh, H. Mody, "Introduction to metallic nanoparticles", *Journal of Pharmacy And Bioallied Sciences* **2010**, *2*, 282.

[12] C. Daruich De Souza, B. Ribeiro Nogueira, M. E. C. Rostelato, "Review of the methodologies used in the synthesis gold nanoparticles by chemical reduction", *Journal of Alloys and Compounds* **2019**, *798*, 714–740.

[13] H. Wang, X. Qiao, J. Chen, S. Ding, "Preparation of silver nanoparticles by chemical reduction method", *Colloids and Surfaces A: Physicochemical and Engineering Aspects* **2005**, *256*, 111–115.

[14] S. Navaladian, B. Viswanathan, R. P. Viswanath, T. K. Varadarajan, "Thermal decomposition as route for silver nanoparticles", *Nanoscale Research Letters* **2006**, *2*.

[15] E. Inshakova, O. Inshakov, "World market for nanomaterials: structure and trends", *MATEC Web of Conferences* **2017**, *129*, (Eds.: S. Bratan, S. Gorbatyuk, S. Leonov, S. Roshchupkin), 02013.

[16] M. J. Pitkethly, "Nanomaterials – the driving force", *Materials Today* **2004**, *7*, 20–29.

[17] N. Z. Janković, D. L. Plata, "Engineered nanomaterials in the context of global element cycles", *Environmental Science: Nano* **2019**, *6*, 2697–2711.

[18] J. Zheng, R. Yang, L. Xie, J. Qu, Y. Liu, X. Li, "Plasma-Assisted Approaches in Inorganic Nanostructure Fabrication", *Advanced Materials* **2010**, *22*, 1451–1473.

[19] D. Mariotti, R. M. Sankaran, "Perspectives on atmospheric-pressure plasmas for nanofabrication", *Journal of Physics D: Applied Physics* **2011**, *44*, 174023.

[20] G. S. Selwyn, J. Singh, R. S. Bennett, "In situ laser diagnostic studies of plasma-generated particulate contamination", *Journal of Vacuum Science and Technology A: Vacuum Surfaces and Films* **1989**, *7*, 2758–2765.

[21] L. Boufendi, A. Bouchoule, "Particle nucleation and growth in a low-pressure argon-silane discharge", *Plasma Sources Science and Technology* **1994**, *3*, 262–267.

[22] P. Ayyub, R. Chandra, P. Taneja, A. Sharma, R. Pinto, "Synthesis of nanocrystalline material by sputtering and laser ablation at low temperatures", *Applied Physics A Materials Science & Processing* **2001**, *73*, 67–73.

[23] U. Kortshagen, "Nonthermal plasma synthesis of semiconductor nanocrystals", *Journal of Physics D: Applied Physics* **2009**, *42*, 113001.

[24] L. Mangolini, U. Kortshagen, "Selective nanoparticle heating: Another form of nonequilibrium in dusty plasmas", *Physical Review E* **2009**, *79*, 026405.

[25] Z. Cao, Q. Nie, D. L. Bayliss, J. L. Walsh, C. S. Ren, D. Z. Wang, M. G. Kong, "Spatially extended atmospheric plasma arrays", *Plasma Sources Science and Technology* **2010**, *19*, 025003.

[26] A. Schutze, J. Jeong, S. Babayan, J. Park, G. Selwyn, R. Hicks, "The atmospheric-pressure plasma jet: a review and comparison to other plasma sources", *IEEE Transactions on Plasma Science* **1998**, *26*, 1685–1694.

[27] S. Moritz, A. Schmidt, J. Sann, M. H. Thoma, "Surface modifications caused by cold atmospheric plasma sterilization treatment", *Journal of Physics D: Applied Physics* **2020**, *53*, 325203.

[28] S. Bekeschus, T. von Woedtke, S. Emmert, A. Schmidt, "Medical gas plasma-stimulated wound healing: Evidence and mechanisms", *Redox Biology* **2021**, *46*, 102116.

[29] J. C. Harley, N. Suchowerska, D. R. McKenzie, "Cancer treatment with gas plasma and with gas plasma–activated liquid: positives, potentials and problems of clinical translation", *Biophysical Reviews* **2020**, *12*, 989–1006.

[30] T. Nozaki, K. Sasaki, T. Ogino, D. Asahi, K. Okazaki, "Microplasma synthesis of tunable photoluminescent silicon nanocrystals", *Nanotechnology* **2007**, *18*, 235603.

[31] B. Barwe, A. Stein, O. E. Cibulka, I. Pelant, J. Ghanbaja, T. Belmonte, J. Benedikt, "Generation of Silicon Nanostructures by Atmospheric Microplasma Jet: The Role of Hydrogen Admixture", *Plasma Processes and Polymers* **2014**, *12*, 132–140.

[32] B. Barwe, F. Riedel, O. E. Cibulka, I. Pelant, J. Benedikt, "Silicon nanoparticle formation depending on the discharge conditions of an atmospheric radio-frequency driven microplasma with argon/silane/hydrogen gases", *Journal of Physics D: Applied Physics* **2015**, *48*, 314001.

[33] R. M. Sankaran, D. Holunga, R. C. Flagan, K. P. Giapis, "Synthesis of Blue Luminescent Si Nanoparticles Using Atmospheric-Pressure Microdischarges", *Nano Letters* **2005**, *5*, 537–541.

[34] M. Vert, Y. Doi, K.-H. Hellwich, M. Hess, P. Hodge, P. Kubisa, M. Rinaudo, F. Schué, "Terminology for biorelated polymers and applications (IUPAC Recommendations 2012)", *Pure and Applied Chemistry* **2012**, *84*, 377–410.

[35] G. M. Whitesides, "Nanoscience, Nanotechnology and Chemistry", *Small* **2004**, *1*, 172–179.

[36] C. Kinnear, T. L. Moore, L. Rodriguez-Lorenzo, B. Rothen-Rutishauser, A. Petri-Fink, "Form Follows Function: Nanoparticle Shape and Its Implications for Nanomedicine", *Chemical Reviews* **2017**, *117*, 11476–11521.

[37] A. P. Alivisatos, "Semiconductor Clusters, Nanocrystals and Quantum Dots", *Science* **1996**, *271*, 933–937.

[38] Y. E. Panfil, M. Oded, U. Banin, "Colloidal Quantum Nanostructures: Emerging Materials for Display Applications", *Angewandte Chemie International Edition* **2018**, *57*, 4274–4295.

[39] R. Mazzaro, A. Gradone, S. Angeloni, G. Morselli, P. G. Cozzi, F. Romano, A. Vomiero, P. Ceroni, "Hybrid Silicon Nanocrystals for Color-Neutral and Transparent Luminescent Solar Concentrators", *ACS Photonics* **2019**, *6*, 2303–2311.

[40] F. Meinardi, S. Ehrenberg, L. Dhamo, F. Carulli, M. Mauri, F. Bruni, R. Simonutti, U. Kortshagen, S. Brovelli, "Highly efficient luminescent solar concentrators based on earth-abundant indirect-bandgap silicon quantum dots", *Nature Photonics* **2017**, *11*, 177–185.

[41] S. Chinnathambi, S. Chen, S. Ganesan, N. Hanagata, "Silicon Quantum Dots for Biological Applications", *Advanced Healthcare Materials* **2013**, *3*, 10–29.

[42] J. Jana, M. Ganguly, T. Pal, "Enlightening surface plasmon resonance effect of metal nanoparticles for practical spectroscopic application", *RSC Advances* **2016**, *6*, 86174–86211.

[43] J. R. Chelikowsky, M. L. Cohen, "Electronic structure of silicon", *Physical Review B* **1974**, *10*, 5095–5107.

[44] S. Adachi, *https://books.google.lu/books?id=HX6NtAEACAAJ&printsec=copyright&hl=deHandbook on physical properties of semiconductors*, *Vol. 3*, Kluwer, Boston, **2004**, 472 pp.

[45] A. Joullie, B. Girault, A. M. Joullie, A. Zien-Eddine, "Determination of the five first interband transitions above the lowest indirect band gap of the aluminum antimonide", *Physical Review B* **1982**, *25*, 7830–7833.

[46] H. Wiggers, A. Lorke in *Handbook of Nanophysics*, (Ed.: K. D. Sattler), CRC Press, **2010**, pp. 105–118.

[47] X. D. Pi, R. W. Liptak, J. Deneen Nowak, N. P. Wells, C. B. Carter, S. A. Campbell, U. Kortshagen, "Air-stable full-visible-spectrum emission from silicon nanocrystals synthesized by an all-gas-phase plasma approach", *Nanotechnology* **2008**, *19*, 245603.

[48] M. V. Wolkin, J. Jorne, P. M. Fauchet, G. Allan, C. Delerue, "Electronic States and Luminescence in Porous Silicon Quantum Dots: The Role of Oxygen", *Physical Review Letters* **1999**, *82*, 197–200.

[49] D. Kovalev, H. Heckler, G. Polisski, F. Koch, "Optical Properties of Si Nanocrystals", *physica status solidi (b)* **1999**, *215*, 871–932.

[50] M. Fujii, *Optical Properties of Intrinsic and Shallow Impurity-Doped Silicon Nanocrystals*, (Eds.: L. Pavesi, R. Turan), Wiley, **2010**, pp. 43–68.

[51] S. Enoch, *Plasmonics: From Basics to Advanced Topics, From Basics to Advanced Topics*, (Ed.: N. Bonod), Description based on publisher supplied metadata and other sources., Springer Berlin / Heidelberg, Berlin, Heidelberg, **2012**, 1330 pp.

[52] P. Bharadwaj, B. Deutsch, L. Novotny, "Optical Antennas", *Advances in Optics and Photonics* **2009**, *1*, 438.

[53] S. P. Gubin, *Magnetic Nanoparticles*, 1st ed., Description based on publisher supplied metadata and other sources., John Wiley & Sons, Incorporated, Newark, **2009**, 1482 pp.

[54] C. Casagrande, P. Fabre, E. Raphaël, M. Veyssié, ""Janus Beads": Realization and Behaviour at Water/Oil Interfaces", *Europhysics Letters (EPL)* **1989**, *9*, 251–255.

[55] S. Jiang, S. Granick, "Janus balance of amphiphilic colloidal particles", *The Journal of Chemical Physics* **2007**, *127*.

[56] T. Ouchi, R. Nakamura, T. Suzuki, H. Minami, "Preparation of Janus Particles Composed of Hydrophobic and Hydrophilic Polymers", *Industrial & Engineering Chemistry Research* **2019**, *58*, 20996–21002.

[57] Z. Nie, W. Li, M. Seo, S. Xu, E. Kumacheva, "Janus and Ternary Particles Generated by Microfluidic Synthesis: Design, Synthesis and Self-Assembly", *Journal of the American Chemical Society* **2006**, *128*, 9408–9412.

[58] Y. Yi, L. Sanchez, Y. Gao, Y. Yu, "Janus particles for biological imaging and sensing", *The Analyst* **2016**, *141*, 3526–3539.

[59] B. Ren, A. Ruditskiy, J. H. (Song, I. Kretzschmar, "Assembly Behavior of Iron Oxide-Capped Janus Particles in a Magnetic Field", *Langmuir* **2011**, *28*, 1149–1156.

[60] F. Liu, S. Goyal, M. Forrester, T. Ma, K. Miller, Y. Mansoorieh, J. Henjum, L. Zhou, E. Cochran, S. Jiang, "Self-assembly of Janus Dumbbell Nanocrystals and Their Enhanced Surface Plasmon Resonance", *Nano Letters* **2018**, *19*, 1587–1594.

[61] T. Yang, L. Wei, L. Jing, J. Liang, X. Zhang, M. Tang, M. J. Monteiro, Y. (Chen, Y. Wang, S. Gu, D. Zhao, H. Yang, J. Liu, G. Q. M. Lu, "Dumbbell-Shaped Bicomponent Mesoporous Janus Solid Nanoparticles for Biphasic Interface Catalysis", *Angewandte Chemie International Edition* **2017**, *56*, 8459–8463.

[62] C. Kang, A. Honciuc, "Influence of Geometries on the Assembly of Snowman-Shaped Janus Nanoparticles", *ACS Nano* **2018**, *12*, 3741–3750.

[63] B. Liu, J. Liu, F. Liang, Q. Wang, C. Zhang, X. Qu, J. Li, D. Qiu, Z. Yang, "Robust Anisotropic Composite Particles with Tunable Janus Balance", *Macromolecules* **2012**, *45*, 5176–5184.

[64] I. Schick, S. Lorenz, D. Gehrig, A.-M. Schilmann, H. Bauer, M. Panthöfer, K. Fischer, D. Strand, F. Laquai, W. Tremel, "Multifunctional Two-Photon Active Silica-Coated Au@MnO Janus Particles for Selective Dual Functionalization and Imaging", *Journal of the American Chemical Society* **2014**, *136*, 2473–2483.

[65] K. Chaudhary, Q. Chen, J. J. Juárez, S. Granick, J. A. Lewis, "Janus Colloidal Matchsticks", *Journal of the American Chemical Society* **2012**, *134*, 12901–12903.

[66] J. Yan, K. Chaudhary, S. Chul Bae, J. A. Lewis, S. Granick, "Colloidal ribbons and rings from Janus magnetic rods", *Nature Communications* **2013**, *4*.

[67] Y. Chen, F. Liang, H. Yang, C. Zhang, Q. Wang, X. Qu, J. Li, Y. Cai, D. Qiu, Z. Yang, "Janus Nanosheets of Polymer–Inorganic Layered Composites", *Macromolecules* **2012**, *45*, 1460–1467.

[68] R. Deng, F. Liang, P. Zhou, C. Zhang, X. Qu, Q. Wang, J. Li, J. Zhu, Z. Yang, "Janus Nanodisc of Diblock Copolymers", *Advanced Materials* **2014**, *26*, 4469–4472.

[69] A. V. Skobelkina, F. V. Kashaev, A. V. Kolchin, D. V. Shuleiko, T. P. Kaminskaya, D. E. Presnov, L. V. Golovan, P. K. Kashkarov, "Silicon Nanoparticles Formed via Pulsed Laser Ablation of Porous Silicon in Liquids", *Technical Physics Letters* **2020**, *46*, 687–690.

[70] A. Lazauskas, D. Gimžauskaitė, M. Ilickas, L. Marcinauskas, M. Aikas, B. Abakevičienė, D. Volyniuk, "Laser Ablation of Silicon Nanoparticles and Their Use in Charge-Coupled Devices for UV Light Sensing via Wavelength-Shifting Properties", *Nanomaterials* **2023**, *13*, 2915.

[71] R. Intartaglia, K. Bagga, F. Brandi, "Study on the productivity of silicon nanoparticles by picosecond laser ablation in water: towards gram per hour yield", *Optics Express* **2014**, *22*, 3117.

[72] M. Becker, J. Brock, H. Cai, D. Henneke, J. Keto, J. Lee, W. Nichols, H. Glicksman, "Metal nanoparticles generated by laser ablation", *Nanostructured Materials* **1998**, *10*, 853–863.

[73] V. Amendola, M. Meneghetti, "Laser ablation synthesis in solution and size manipulation of noble metal nanoparticles", *Physical Chemistry Chemical Physics* **2009**, *11*, 3805.

[74] J. E. Muñoz, J. Cervantes, R. Esparza, G. Rosas, "Iron nanoparticles produced by high-energy ball milling", *Journal of Nanoparticle Research* **2007**, *9*, 945–950.

[75] C. Lam, Y. Zhang, Y. Tang, C. Lee, I. Bello, S. Lee, "Large-scale synthesis of ultrafine Si nanoparticles by ball milling", *Journal of Crystal Growth* **2000**, *220*, 466–470.

[76] D. S. English, L. E. Pell, Z. Yu, P. F. Barbara, B. A. Korgel, "Size Tunable Visible Luminescence from Individual Organic Monolayer Stabilized Silicon Nanocrystal Quantum Dots", *Nano Letters* **2002**, *2*, 681–685.

[77] J. D. Holmes, K. J. Ziegler, R. C. Doty, L. E. Pell, K. P. Johnston, B. A. Korgel, "Highly Luminescent Silicon Nanocrystals with Discrete Optical Transitions", *Journal of the American Chemical Society* **2001**, *123*, 3743–3748.

[78] X. Ye, C. M. Wai, "Making Nanomaterials in Supercritical Fluids: A Review", *Journal of Chemical Education* **2003**, *80*, 198.

[79] J. D. Holmes, D. M. Lyons, K. J. Ziegler, "Supercritical Fluid Synthesis of Metal and Semiconductor Nanomaterials", *Chemistry – A European Journal* **2003**, *9*, 2144–2150.

[80] A. Shavel, L. Guerrini, R. A. Alvarez-Puebla, "Colloidal synthesis of silicon nanoparticles in molten salts", *Nanoscale* **2017**, *9*, 8157–8163.

[81] P. Yang, J. Zheng, Y. Xu, Q. Zhang, L. Jiang, "Colloidal Synthesis and Applications of Plasmonic Metal Nanoparticles", *Advanced Materials* **2016**, *28*, 10508–10517.

[82] J. Zhang, B. A. Grzybowski, S. Granick, "Janus Particle Synthesis, Assembly and Application", *Langmuir* **2017**, *33*, 6964–6977.

[83] T. Nisisako, T. Torii, T. Takahashi, Y. Takizawa, "Synthesis of Monodisperse Bicolored Janus Particles with Electrical Anisotropy Using a Microfluidic Co-Flow System", *Advanced Materials* **2006**, *18*, 1152–1156.

[84] B. Hamilton, "Porous silicon", *Semiconductor Science and Technology* **1995**, *10*, 1187–1207.

[85] J. Holm, J. T. Roberts, "Modifying the composition of hydrogen-terminated silicon nanoparticles synthesized in a nonthermal rf plasma", *Journal of Vacuum Science & Technology A: Vacuum Surfaces and Films* **2010**, *28*, 161–169.

[86] D. Mariotti, R. M. Sankaran, "Microplasmas for nanomaterials synthesis", *Journal of Physics D: Applied Physics* **2010**, *43*, 323001.

[87] R. Gresback, T. Nozaki, K. Okazaki, "Synthesis and oxidation of luminescent silicon nanocrystals from silicon tetrachloride by very high frequency nonthermal plasma", *Nanotechnology* **2011**, *22*, 305605.

[88] O. Yasar-Inceoglu, T. Lopez, E. Farshihagro, L. Mangolini, "Silicon nanocrystal production through non-thermal plasma synthesis: a comparative study between silicon tetrachloride and silane precursors", *Nanotechnology* **2012**, *23*, 255604.

[89] P. Chen, M. Colaianni, J. Yates, "Silicon backbond strain effects on NH3 surface chemistry: Si(111)-(7 × 7) compared to Si(100)-(2 × 1)", *Surface Science* **1992**, *274*, L605–L610.

[90] Y. H. Ogata, F. Kato, T. Tsuboi, T. Sakka, "Changes in the Environment of Hydrogen in Porous Silicon with Thermal Annealing", *Journal of The Electrochemical Society* **1998**, *145*, 2439–2444.

[91] L. Mangolini, D. Jurbergs, E. Rogojina, U. Kortshagen, "Plasma synthesis and liquid-phase surface passivation of brightly luminescent Si nanocrystals", *Journal of Luminescence* **2006**, *121*, 327–334.

[92] L. Mangolini, D. Jurbergs, E. Rogojina, U. Kortshagen, "High efficiency photoluminescence from silicon nanocrystals prepared by plasma synthesis and organic surface passivation", *physica status solidi c* **2006**, *3*, 3975–3978.

[93] G. Ledoux, O. Guillois, D. Porterat, C. Reynaud, F. Huisken, B. Kohn, V. Paillard, "Photoluminescence properties of silicon nanocrystals as a function of their size", *Physical Review B* **2000**, *62*, 15942–15951.

[94] G. Ledoux, J. Gong, F. Huisken, O. Guillois, C. Reynaud, "Photoluminescence of size-separated silicon nanocrystals: Confirmation of quantum confinement", *Applied Physics Letters* **2002**, *80*, 4834–4836.

[95] G. Li, Z. Tang, "Noble metal nanoparticle@metal oxide core/yolk–shell nanostructures as catalysts: recent progress and perspective", *Nanoscale* **2014**, *6*, 3995–4011.

[96] C. M. Wang, D. R. Baer, L. E. Thomas, J. E. Amonette, J. Antony, Y. Qiang, G. Duscher, "Void formation during early stages of passivation: Initial oxidation of iron nanoparticles at room temperature", *Journal of Applied Physics* **2005**, *98*, DOI 10.1063/1.2130890.

[97] L. Mangolini, U. Kortshagen, "Plasma-Assisted Synthesis of Silicon Nanocrystal Inks", *Advanced Materials* **2007**, *19*, 2513–2519.

[98] K. Y. Yoon, J. H. Byeon, C. W. Park, J. Hwang, "Antimicrobial Effect of Silver Particles on Bacterial Contamination of Activated Carbon Fibers", *Environmental Science & Technology* **2008**, *42*, 1251–1255.

[99] T. Hamouda, H. Kafafy, H. Mashaly, N. M. Aly, "Breathability performance of antiviral cloth masks treated with silver nanoparticles for protection against COVID-19", *Journal of Industrial Textiles* **2021**, *51*, 1494–1523.

[100] M. Manzano, M. Vallet-Regí, "Mesoporous Silica Nanoparticles for Drug Delivery", *Advanced Functional Materials* **2019**, *30*.

[101] V. Chandrakala, V. Aruna, G. Angajala, "Review on metal nanoparticles as nanocarriers: current challenges and perspectives in drug delivery systems", *Emergent Materials* **2022**, *5*, 1593–1615.

[102] T. A. Fedotcheva, A. Y. Olenin, K. M. Starostin, G. V. Lisichkin, V. V. Banin, N. L. Shimanovskii, "Prospects for Using Gold, Silver and Iron Oxide Nanoparticles for Increasing the Efficacy of Chemotherapy", *Pharmaceutical Chemistry Journal* **2015**, *49*, 220–230.

[103] M. M. Mahan, A. L. Doiron, "Gold Nanoparticles as X-Ray, CT and Multimodal Imaging Contrast Agents: Formulation, Targeting and Methodology", *Journal of Nanomaterials* **2018**, *2018*, 1–15.

[104] S. Laurent, S. Dutz, U. O. Häfeli, M. Mahmoudi, "Magnetic fluid hyperthermia: Focus on superparamagnetic iron oxide nanoparticles", *Advances in Colloid and Interface Science* **2011**, *166*, 8–23.

[105] S. Hwang, J. Lahann, "Differentially Degradable Janus Particles for Controlled Release Applications", *Macromolecular Rapid Communications* **2012**, *33*, 1178–1183.

[106] B. Hammer, J. K. Norskov, "Why gold is the noblest of all the metals", *Nature* **1995**, *376*, 238–240.

[107] M. Haruta, M. Daté, "Advances in the catalysis of Au nanoparticles", *Applied Catalysis A: General* **2001**, *222*, 427–437.

[108] R. Grisel, K.-J. Weststrate, A. Gluhoi, B. E. Nieuwenhuys, "Catalysis by Gold Nanoparticles", *Gold Bulletin* **2002**, *35*, 39–45.

[109] M. Haruta, "Gold catalysts prepared by coprecipitation for low-temperature oxidation of hydrogen and of carbon monoxide", *Journal of Catalysis* **1989**, *115*, 301–309.

[110] S. Veziroglu, A.-L. Obermann, M. Ullrich, M. Hussain, M. Kamp, L. Kienle, T. Leißner, H.-G. Rubahn, O. Polonskyi, T. Strunskus, J. Fiutowski, M. Es-Souni, J. Adam, F. Faupel, O. C. Aktas, "Photodeposition of Au Nanoclusters for Enhanced Photocatalytic Dye Degradation over TiO2 Thin Film", *ACS Applied Materials & Interfaces* **2020**, *12*, 14983–14992.

[111] S. Cheong, J. D. Watt, R. D. Tilley, "Shape control of platinum and palladium nanoparticles for catalysis", *Nanoscale* **2010**, *2*, 2045.

[112] A. Miyazaki, I. Balint, Y. Nakano, "Morphology Control of Platinum Nanoparticles and their Catalytic Properties", *Journal of Nanoparticle Research* **2003**, *5*, 69–80.

[113] S. M. Lloyd, L. B. Lave, H. S. Matthews, "Life Cycle Benefits of Using Nanotechnology To Stabilize Platinum-Group Metal Particles in Automotive Catalysts", *Environmental Science & Technology* **2005**, *39*, 1384–1392.

[114] Z. Liu, L. M. Gan, L. Hong, W. Chen, J. Y. Lee, "Carbon-supported Pt nanoparticles as catalysts for proton exchange membrane fuel cells", *Journal of Power Sources* **2005**, *139*, 73–78.

[115] B. Fang, N. K. Chaudhari, M.-S. Kim, J. H. Kim, J.-S. Yu, "Homogeneous Deposition of Platinum Nanoparticles on Carbon Black for Proton Exchange Membrane Fuel Cell", *Journal of the American Chemical Society* **2009**, *131*, 15330–15338.

[116] M. Ismael, "A review and recent advances in solar-to-hydrogen energy conversion based on photocatalytic water splitting over doped-TiO2 nanoparticles", *Solar Energy* **2020**, *211*, 522–546.

[117] C. Hariharan, "Photocatalytic degradation of organic contaminants in water by ZnO nanoparticles: Revisited", *Applied Catalysis A: General* **2006**, *304*, 55–61.

[118] M. A. Green, A. Ho-Baillie, H. J. Snaith, "The emergence of perovskite solar cells", *Nature Photonics* **2014**, *8*, 506–514.

[119] Y. Gao, Y. Wu, H. Lu, C. Chen, Y. Liu, X. Bai, L. Yang, W. W. Yu, Q. Dai, Y. Zhang, "CsPbBr3 perovskite nanoparticles as additive for environmentally stable perovskite solar cells with 20.46 % efficiency", *Nano Energy* **2019**, *59*, 517–526.

[120] F. Enrichi, A. Quandt, G. Righini, "Plasmonic enhanced solar cells: Summary of possible strategies and recent results", *Renewable and Sustainable Energy Reviews* **2018**, *82*, 2433–2439.

[121] S. Carretero-Palacios, A. Jiménez-Solano, H. Míguez, "Plasmonic Nanoparticles as Light-Harvesting Enhancers in Perovskite Solar Cells: A User's Guide", *ACS Energy Letters* **2016**, *1*, 323–331.

[122] M. Zebarjadi, K. Esfarjani, A. Shakouri, J.-H. Bahk, Z. Bian, G. Zeng, J. Bowers, H. Lu, J. Zide, A. Gossard, "Effect of nanoparticle scattering on thermoelectric power factor", *Applied Physics Letters* **2009**, *94*, 202105.

[123] W. Zhao, Z. Liu, Z. Sun, Q. Zhang, P. Wei, X. Mu, H. Zhou, C. Li, S. Ma, D. He, P. Ji, W. Zhu, X. Nie, X. Su, X. Tang, B. Shen, X. Dong, J. Yang, Y. Liu, J. Shi, "Superparamagnetic enhancement of thermoelectric performance", *Nature* **2017**, *549*, 247–251.

[124] H. Wu, G. Zheng, N. Liu, T. J. Carney, Y. Yang, Y. Cui, "Engineering Empty Space between Si Nanoparticles for Lithium-Ion Battery Anodes", *Nano Letters* **2012**, *12*, 904–909.

[125] C. He, S. Wu, N. Zhao, C. Shi, E. Liu, J. Li, "Carbon-Encapsulated Fe3O4 Nanoparticles as a High-Rate Lithium Ion Battery Anode Material", *ACS Nano* **2013**, *7*, 4459–4469.

[126] G. Cai, X. Wang, M. Cui, P. Darmawan, J. Wang, A. L.-S. Eh, P. S. Lee, "Electrochromo-supercapacitor based on direct growth of NiO nanoparticles", *Nano Energy* **2015**, *12*, 258–267.

[127] B. Wang, J. S. Chen, Z. Wang, S. Madhavi, X. W. (Lou, "Green Synthesis of NiO Nanobelts with Exceptional Pseudo-Capacitive Properties", *Advanced Energy Materials* **2012**, *2*, 1188–1192.

[128] J. Zhang, Y. Zhu, H. Lin, Y. Liu, Y. Zhang, S. Li, Z. Ma, L. Li, "Metal Hydride Nanoparticles with Ultrahigh Structural Stability and Hydrogen Storage Activity Derived from Microencapsulated Nanoconfinement", *Advanced Materials* **2017**, *29*, DOI 10.1002/adma.201700760.

[129] V. Bérubé, G. Radtke, M. Dresselhaus, G. Chen, "Size effects on the hydrogen storage properties of nanostructured metal hydrides: A review", *International Journal of Energy Research* **2007**, *31*, 637–663.

[130] P. Johansson, H. Xu, M. Käll, "Surface-enhanced Raman scattering and fluorescence near metal nanoparticles", *Physical Review B* **2005**, *72*, 035427.

[131] M. Moskovits, "Surface-enhanced spectroscopy", *Reviews of Modern Physics* **1985**, *57*, 783–826.

[132] Z.-Y. Li, Y. Xia, "Metal Nanoparticles with Gain toward Single-Molecule Detection by Surface-Enhanced Raman Scattering", *Nano Letters* **2009**, *10*, 243–249.

[133] F. Le, D. W. Brandl, Y. A. Urzhumov, H. Wang, J. Kundu, N. J. Halas, J. Aizpurua, P. Nordlander, "Metallic Nanoparticle Arrays: A Common Substrate for Both Surface-Enhanced Raman Scattering and Surface-Enhanced Infrared Absorption", *ACS Nano* **2008**, *2*, 707–718.

[134] S. A. Maier, P. G. Kik, H. A. Atwater, "Optical pulse propagation in metal nanoparticle chain waveguides", *Physical Review B* **2003**, *67*, 205402.

[135] S. A. Maier, P. G. Kik, H. A. Atwater, S. Meltzer, E. Harel, B. E. Koel, A. A. Requicha, "Local detection of electromagnetic energy transport below the diffraction limit in metal nanoparticle plasmon waveguides", *Nature Materials* **2003**, *2*, 229–232.

[136] Y. Fu, X. Zhou, "Plasmonic Lenses: A Review", *Plasmonics* **2010**, *5*, 287–310.

[137] Z. Chai, X. Hu, F. Wang, X. Niu, J. Xie, Q. Gong, "Ultrafast All-Optical Switching", *Advanced Optical Materials* **2016**, *5*.

[138] H. Inouye, K. Tanaka, I. Tanahashi, T. Hattori, H. Nakatsuka, "Ultrafast Optical Switching in a Silver Nanoparticle System", *Japanese Journal of Applied Physics* **2000**, *39*, 5132.

[139] Y. Zhu, H. I. Elim, Y.-L. Foo, T. Yu, Y. Liu, W. Ji, J.-Y. Lee, Z. Shen, A. T.-S. Wee, J. T.-L. Thong, et al., "Multiwalled carbon nanotubes beaded with ZnO nanoparticles for ultrafast nonlinear optical switching", *Advanced Materials* **2006**, *18*, 587–592.

[140] F. Maier-Flaig, J. Rinck, M. Stephan, T. Bocksrocker, M. Bruns, C. Kübel, A. K. Powell, G. A. Ozin, U. Lemmer, "Multicolor Silicon Light-Emitting Diodes (SiLEDs)", *Nano Letters* **2013**, *13*, 475–480.

[141] C. Wang, C. Yu, "Detection of chemical pollutants in water using gold nanoparticles as sensors: a review", *Reviews in Analytical Chemistry* **2012**, *32*, 1–14.

[142] K. J. Cash, H. A. Clark, "Nanosensors and nanomaterials for monitoring glucose in diabetes", *Trends in Molecular Medicine* **2010**, *16*, 584–593.

[143] P. Makaram, D. Owens, J. Aceros, "Trends in Nanomaterial-Based Non-Invasive Diabetes Sensing Technologies", *Diagnostics* **2014**, *4*, 27–46.

[144] Y. Sun, H. H. Wang, "High-Performance, Flexible Hydrogen Sensors That Use Carbon Nanotubes Decorated with Palladium Nanoparticles", *Advanced Materials* **2007**, *19*, 2818–2823.

[145] C. Ndaya, N. Javahiraly, A. Brioude, "Recent Advances in Palladium Nanoparticles-Based Hydrogen Sensors for Leak Detection", *Sensors* **2019**, *19*, 4478.

[146] I. Darmadi, F. A. A. Nugroho, C. Langhammer, "High-Performance Nanostructured Palladium-Based Hydrogen Sensors—Current Limitations and Strategies for Their Mitigation", *ACS Sensors* **2020**, *5*, 3306–3327.

[147] I. Langmuir, "Oscillations in Ionized Gases", *Proceedings of the National Academy of Sciences* **1928**, *14*, 627–637.

[148] P. K. Chu, X. Lu, *Low Temperature Plasma Technology: Methods and Applications*, 1st ed., CRC Press, **2013**.

[149] C. Bruce, R. Golde, "The lightning discharge", *Journal of the Institution of Electrical Engineers - Part II: Power Engineering* **1941**, *88*, 487–505.

[150] A. Angot, *The aurora borealis*, *Vol. 77*, D. Appleton & Company, **1897**.

[151] U. Stroth, *Plasmaphysik: Phänomene, Grundlagen und Anwendungen*, Springer Berlin Heidelberg, **2018**.

[152] A. Piel, *Plasma Physics*, Springer International Publishing, **2017**.

[153] M. A. Lieberman, A. J. Lichtenberg, *Principles of Plasma Discharges and Materials Processing*, Wiley, **2005**.

[154] H. Han, S. J. Park, C. e. a. Sung, "A sustained high-temperature fusion plasma regime facilitated by fast ions", *Nature* **2022**, *609*, 269–275.

[155] K. J. Kanarik, "Inside the mysterious world of plasma: A process engineer's perspective", *Journal of Vacuum Science & Technology A* **2020**, *38*.

[156] P. Debye, E. Hückel, "Zur Theorie der Elektrolyte. I. Gefrierpunktserniedrigung und verwandte Erscheinungen", *Physikalische Zeitschrift* **1923**, *24*, 305.

[157] P. J. Bruggeman, F. Iza, R. Brandenburg, "Foundations of atmospheric pressure non-equilibrium plasmas", *Plasma Sources Science and Technology* **2017**, *26*, 123002.

[158] L. R. Peterson, J. E. Allen, "Electron Impact Cross Sections for Argon", *The Journal of Chemical Physics* **1972**, *56*, 6068–6076.

[159] J. Townsend, *Electricity in Gases*, Clarendon Press, **1915**.

[160] F. Paschen, "Ueber die zum Funkenübergang in Luft, Wasserstoff und Kohlensäure bei verschiedenen Drucken erforderliche Potentialdifferenz", *Annalen der Physik* **1889**, *273*, 69–96.

[161] J. Park, I. Henins, H. W. Herrmann, G. S. Selwyn, "Gas breakdown in an atmospheric pressure radio-frequency capacitive plasma source", *Journal of Applied Physics* **2001**, *89*, 15–19.

[162] M. U. Lee, J. Lee, J. K. Lee, G. S. Yun, "Extended scaling and Paschen law for micro-sized radiofrequency plasma breakdown", *Plasma Sources Science and Technology* **2017**, *26*, 034003.

[163] M. Moravej, X. Yang, G. R. Nowling, J. P. Chang, R. F. Hicks, S. E. Babayan, "Physics of high-pressure helium and argon radio-frequency plasmas", *Journal of Applied Physics* **2004**, *96*, 7011–7017.

[164] L. Bárdos, H. Baránková, "Plasma processes at atmospheric and low pressures", *Vacuum* **2008**, *83*, 522–527.

[165] O. V. Penkov, M. Khadem, W.-S. Lim, D.-E. Kim, "A review of recent applications of atmospheric pressure plasma jets for materials processing", *Journal of Coatings Technology and Research* **2015**, *12*, 225–235.

[166] T. Bolgeo, A. Maconi, M. Gardalini, D. Gatti, R. Di Matteo, M. Lapidari, Y. Longhitano, G. Savioli, A. Piccioni, C. Zanza, "The Role of Cold Atmospheric Plasma in Wound Healing Processes in Critically Ill Patients", *Journal of Personalized Medicine* **2023**, *13*, 736.

[167] A. Maroofi, N. Navab Safa, H. Ghomi, "Atmospheric air plasma jet for improvement of paint adhesion to aluminium surface in industrial applications", *International Journal of Adhesion and Adhesives* **2020**, *98*, 102554.

[168] S. K. Alavi, O. Lotz, B. Akhavan, G. Yeo, R. Walia, D. R. McKenzie, M. M. Bilek, "Atmospheric Pressure Plasma Jet Treatment of Polymers Enables Reagent-Free Covalent Attachment of Biomolecules for Bioprinting", *ACS Applied Materials and Interfaces* **2020**, *12*, 38730–38743.

[169] M. Akter, A. Jangra, S. A. Choi, E. H. Choi, I. Han, "Non-Thermal Atmospheric Pressure Bio-Compatible Plasma Stimulates Apoptosis via p38/MAPK Mechanism in U87 Malignant Glioblastoma", *Cancers* **2020**, *12*, 245.

[170] M. Noeske, J. Degenhardt, S. Strudthoff, U. Lommatzsch, "Plasma jet treatment of five polymers at atmospheric pressure: surface modifications and the relevance for adhesion", *International Journal of Adhesion and Adhesives* **2004**, *24*, 171–177.

[171] Y.-w. Hsu, H.-C. Li, Y.-J. Yang, C.-c. Hsu, "Deposition of zinc oxide thin films by an atmospheric pressure plasma jet", *Thin Solid Films* **2011**, *519*, 3095–3099.

[172] J. Hnilica, J. Schäfer, R. Foest, L. Zajíčková, V. Kudrle, "PECVD of nanostructured SiO2in a modulated microwave plasma jet at atmospheric pressure", *Journal of Physics D: Applied Physics* **2013**, *46*, 335202.

[173] J. Choi, K. Matsuo, H. Yoshida, T. Namihira, S. Katsuki, H. Akiyama, "Characteristics of a DC-Driven Atmospheric Pressure Air Microplasma Jet", *Japanese Journal of Applied Physics* **2008**, *47*, 6459.

[174] D. P. Dowling, F. T. O'Neill, S. J. Langlais, V. J. Law, "Influence of dc Pulsed Atmospheric Pressure Plasma Jet Processing Conditions on Polymer Activation", *Plasma Processes and Polymers* **2011**, *8*, 718–727.

[175] Oh, Szili, Hatta, Ito, Shirafuji, "Tailoring the Chemistry of Plasma-Activated Water Using a DC-Pulse-Driven Non-Thermal Atmospheric-Pressure Helium Plasma Jet", *Plasma* **2019**, *2*, 127–137.

[176] R. B. Keller in *Design for Electromagnetic Compatibility–In a Nutshell*, Springer International Publishing, **2022**, pp. 135–143.

[177] A. Al-Shamma'a, S. Wylie, J. Lucas, J. D. Yan, "Atmospheric microwave plasma jet for material processing", *IEEE Transactions on Plasma Science* **2002**, *30*, 1863–1871.

[178] J. Kim, H. Sakakita, H. Ohsaki, M. Katsurai, "Microwave-excited atmospheric pressure plasma jet with wide aperture for the synthesis of carbon nanomaterials", *Japanese Journal of Applied Physics* **2014**, *54*, 01AA02.

[179] S. Wylie, A. Al-Shamma'a, J. Lucas, R. Stuart, "An atmospheric microwave plasma jet for ceramic material processing", *Journal of Materials Processing Technology* **2004**, *153–154*, 288–293.

[180] J. T. Hu, J. G. Wang, X. Y. Liu, D. W. Liu, X. P. Lu, J. J. Shi, K. Ostrikov, "Effect of a floating electrode on a plasma jet", *Physics of Plasmas* **2013**, *20*, DOI `10.1063/1.4817954`.

[181] G.-M. Xu, Y. Ma, G.-J. Zhang, "DBD Plasma Jet in Atmospheric Pressure Argon", *IEEE Transactions on Plasma Science* **2008**, *36*, 1352–1353.

[182] A. M. Lietz, M. J. Kushner, "Electrode configurations in atmospheric pressure plasma jets: production of reactive species", *Plasma Sources Science and Technology* **2018**, *27*, 105020.

[183] J. Schäfer, A. Quade, K. J. Abrams, F. Sigeneger, M. M. Becker, C. Majewski, C. Rodenburg, "HelixJet: An innovative plasma source for next-generation additive manufacturing (3D printing)", *Plasma Processes and Polymers* **2019**, *17*, 1900099.

[184] A. H. Pfund, "Bismuth black and its applications", *Review of Scientific Instruments* **1930**, *1*, 397–399.

[185] W. Becker, R. Fettig, W. Ruppel, "Optical and electrical properties of black gold layers in the far infrared", *Infrared Physics & Technology* **1999**, *40*, 431–445.

[186] H. Haberland, M. Karrais, M. Mall, Y. Thurner, "Thin films from energetic cluster impact: A feasibility study", *Journal of Vacuum Science & Technology A: Vacuum Surfaces and Films* **1992**, *10*, 3266–3271.

[187] A. Shelemin, O. Kylián, J. Hanuš, A. Choukourov, I. Melnichuk, A. Serov, D. Slavínská, H. Biederman, "Preparation of metal oxide nanoparticles by gas aggregation cluster source", *Vacuum* **2015**, *120*, 162–169.

[188] O. Polonskyi, A. M. Ahadi, T. Peter, K. Fujioka, J. W. Abraham, E. Vasiliauskaite, A. Hinz, T. Strunskus, S. Wolf, M. Bonitz, H. Kersten, F. Faupel, "Plasma based formation and deposition of metal and metal oxide nanoparticles using a gas aggregation source", *The European Physical Journal D* **2018**, *72*.

[189] A. Vahl, J. Strobel, W. Reichstein, O. Polonskyi, T. Strunskus, L. Kienle, F. Faupel, "Single target sputter deposition of alloy nanoparticles with adjustable composition via a gas aggregation cluster source", *Nanotechnology* **2017**, *28*, 175703.

[190] Y. Shimizu, A. C. Bose, D. Mariotti, T. Sasaki, K. Kirihara, T. Suzuki, K. Terashima, N. Koshizaki, "Reactive Evaporation of Metal Wire and Microdeposition of Metal Oxide Using Atmospheric Pressure Reactive Microplasma Jet", *Japanese Journal of Applied Physics* **2006**, *45*, 8228.

[191] R. M. Roth, K. G. Spears, G. D. Stein, G. Wong, "Spatial dependence of particle light scattering in an rf silane discharge", *Applied Physics Letters* **1985**, *46*, 253–255.

[192] A. Bouchoule, A. Plain, L. Boufendi, J. P. Blondeau, C. Laure, "Particle generation and behavior in a silane-argon low-pressure discharge under continuous or pulsed radio-frequency excitation", *Journal of Applied Physics* **1991**, *70*, 1991–2000.

[193] C. Courteille, J.-L. Dorier, J. Dutta, C. Hollenstein, A. A. Howling, T. Stoto, "Visible photoluminescence from hydrogenated silicon particles suspended in a silane plasma", *Journal of Applied Physics* **1995**, *78*, 61–66.

[194] A. A. Howling, J.-L. Dorier, C. Hollenstein, "Negative ion mass spectra and particulate formation in radio frequency silane plasma deposition experiments", *Applied Physics Letters* **1993**, *62*, 1341–1343.

[195] C. A. Dejoseph, P. D. Haaland, A. Garscadden, "On the Decomposition of Silane in Plasma Deposition Reactors", *IEEE Transactions on Plasma Science* **1986**, *14*, 165–172.

[196] Y. Watanabe, "Dust phenomena in processing plasmas", *Plasma Physics and Controlled Fusion* **1997**, *39*, A59–A72.

[197] U. V. Bhandarkar, M. T. Swihart, S. L. Girshick, U. R. Kortshagen, "Modelling of silicon hydride clustering in a low-pressure silane plasma", *Journal of Physics D: Applied Physics* **2000**, *33*, 2731–2746.

[198] K. De Bleecker, A. Bogaerts, R. Gijbels, W. Goedheer, "Numerical investigation of particle formation mechanisms in silane discharges", *Physical Review E* **2004**, *69*, 056409.

[199] A. A. Fridman, L. Boufendi, T. Hbid, B. V. Potapkin, A. Bouchoule, "Dusty plasma formation: Physics and critical phenomena. Theoretical approach", *Journal of Applied Physics* **1996**, *79*, 1303–1314.

[200] L. Mangolini, E. Thimsen, U. Kortshagen, "High-Yield Plasma Synthesis of Luminescent Silicon Nanocrystals", *Nano Letters* **2005**, *5*, 655–659.

[201] L. Canham, "Introductory lecture: origins and applications of efficient visible photoluminescence from silicon-based nanostructures", *Faraday Discussions* **2020**, *222*, 10–81.

[202] B. Li, J. Zhou, Y. Han, Q. Wang, H. Liu, "Impact of heat treatment on NBOHC luminescence of OH-containing and H2-impregnated fused silica for deep-ultraviolet applications", *Journal of Luminescence* **2019**, *209*, 31–38.

[203] A. J. Kontkiewicz, A. M. Kontkiewicz, J. Siejka, S. Sen, G. Nowak, A. M. Hoff, P. Sakthivel, K. Ahmed, P. Mukherjee, S. Witanachchi, J. Lagowski, "Evidence that blue luminescence of oxidized porous silicon originates from SiO2", *Applied Physics Letters* **1994**, *65*, 1436–1438.

[204] S. Askari, I. Levchenko, K. Ostrikov, P. Maguire, D. Mariotti, "Crystalline Si nanoparticles below crystallization threshold: Effects of collisional heating in non-thermal atmospheric-pressure microplasmas", *Applied Physics Letters* **2014**, *104*.

[205] A. N. Goldstein, "The melting of silicon nanocrystals: Submicron thin-film structures derived from nanocrystal precursors", *Applied Physics A Materials Science & Processing* **1996**, *62*, 33–37.

[206] M. Hirasawa, T. Orii, T. Seto, "Size-dependent crystallization of Si nanoparticles", *Applied Physics Letters* **2006**, *88*.

[207] N. J. Kramer, R. J. Anthony, M. Mamunuru, E. S. Aydil, U. R. Kortshagen, "Plasma-induced crystallization of silicon nanoparticles", *Journal of Physics D: Applied Physics* **2014**, *47*, 075202.

[208] C. K. Goertz, W.-H. Ip, "Limitation of electrostatic charging of dust particles in a plasma", *Geophysical Research Letters* **1984**, *11*, 349–352.

[209] U. Kortshagen, U. Bhandarkar, "Modeling of particulate coagulation in low pressure plasmas", *Physical Review E* **1999**, *60*, 887–898.

[210] D. D. Koleske, S. M. Gates, B. Jackson, "Atomic H abstraction of surface H on Si: An Eley–Rideal mechanism?", *The Journal of Chemical Physics* **1994**, *101*, 3301–3309.

[211] M. S. Valipa, D. Maroudas, "Atomistic analysis of the mechanism of hydrogen diffusion in plasma-deposited amorphous silicon thin films", *Applied Physics Letters* **2005**, *87*, DOI 10.1063/1.2158033.

[212] K. Sinniah, M. G. Sherman, L. B. Lewis, W. H. Weinberg, J. T. Yates, K. C. Janda, "Hydrogen desorption from the monohydride phase on Si(100)", *The Journal of Chemical Physics* **1990**, *92*, 5700–5711.

[213] S. Amaral, J. de Carvalho, M. Costa, C. Pinheiro, "An Overview of Particulate Matter Measurement Instruments", *Atmosphere* **2015**, *6*, 1327–1345.

[214] T. Ajtai, N. Utry, M. Pintér, A. Rahman, B. Kurilla, G. Sárossy, L. Deák, J. Baladincz, P. Raffai, G. Szabó, Z. Bozóki, "The investigation of diesel soot emission using instrument combination of multi-wavelength photoacoustic spectroscopy and scanning mobility particle sizer", *Scientific Reports* **2024**, *14*.

[215] W. D. van Dijk, S. Gopal, P. T. J. Scheepers, "Nanoparticles in cigarette smoke; real-time undiluted measurements by a scanning mobility particle sizer", *Analytical and Bioanalytical Chemistry* **2011**, *399*, 3573–3578.

[216] K. M. Yun, S. Y. Lee, F. Iskandar, K. Okuyama, N. Tajima, "Effect of X-ray energy and ionization time on the charging performance and nanoparticle formation of a soft X-ray photoionization charger", *Advanced Powder Technology* **2009**, *20*, 529–536.

[217] N. A. Fuchs, "On the stationary charge distribution on aerosol particles in a bipolar ionic atmosphere", *Geofisica Pura e Applicata* **1963**, *56*, 185–193.

[218] M. Adachi, Y. Kousaka, K. Okuyama, "Unipolar and bipolar diffusion charging of ultrafine aerosol particles", *Journal of Aerosol Science* **1985**, *16*, 109–123.

[219] H. M. Lee, C. Soo Kim, M. Shimada, K. Okuyama, "Bipolar diffusion charging for aerosol nanoparticle measurement using a soft X-ray charger", *Journal of Aerosol Science* **2005**, *36*, 813–829.

[220] B. Han, M. Shimada, M. Choi, K. Okuyama, "Unipolar Charging of Nanosized Aerosol Particles Using Soft X-ray Photoionization", *Aerosol Science and Technology* **2003**, *37*, 330–341.

[221] A. Wiedensohler, H. Fissan, "Aerosol charging in high purity gases", *Journal of Aerosol Science* **1988**, *19*, Sixteenth Annual Conference of the Gesellschaft fur Aerosolforschung, 867–870.

[222] J. Kim, G. Mulholland, S. Kukuck, D. Pui, "Slip correction measurements of certified PSL nanoparticles using a nanometer differential mobility analyzer (nano-DMA) for Knudsen number from 0.5 to 83", *Journal of Research of the National Institute of Standards and Technology* **2005**, *110*, 31.

[223] D.-R. Chen, D. Pui, D. Hummes, H. Fissan, F. Quant, G. Sem, "Design and evaluation of a nanometer aerosol differential mobility analyzer (Nano-DMA)", *Journal of Aerosol Science* **1998**, *29*, 497–509.

[224] P. Kulkarni, P. Baron, K. Willeke, *Aerosol Measurement: Principles, Techniques and Applications*, Wiley, **2011**.

[225] S. Heidenreich, H. Büttner, "Investigations about the influence of the Kelvin effect on droplet growth rates", *Journal of Aerosol Science* **1995**, *26*, 335–339.

[226] D. R. Warren, K. Okuyama, Y. Kousaka, J. H. Seinfeld, R. C. Flagan, "Homogeneous nucleation in supersaturated vapor containing foreign seed aerosol", *Journal of Colloid and Interface Science* **1987**, *116*, 563–581.

[227] S. L. Girshick, "The dependence of homogeneous nucleation rate on supersaturation", *The Journal of Chemical Physics* **2014**, *141*.

[228] W. Hinds, *Aerosol Technology: Properties, Behavior and Measurement of Airborne Particles*, Wiley, **1999**.

[229] W. C. Hinds, Y. Zhu, *Aerosol Technology: Properties, Behavior and Measurement of Airborne Particles, 3rd Edition*, 3rd ed., John Wiley & Sons, **2022**.

[230] T. Kodas, T. T. Kodas, M. J. Hampden-Smith, *Aerosol processing of materials*, Wiley, New York, **1999**, 680 pp.

[231] W. Stöber, "A note on the aerodynamic diameter and the mobility of non-spherical aerosol particles", *Journal of Aerosol Science* **1971**, *2*, 453–456.

[232] D. B. Williams, C. B. Carter, *Transmission Electron Microscopy*, Springer US, **1996**.

[233] M. Knoll, E. Ruska, "Das Elektronenmikroskop", *Zeitschrift für Physik* **1932**, *78*, 318–339.

[234] D. B. Williams, C. B. Carter, *Transmission Electron Microscopy*, Springer US, **2009**.

[235] G. Cliff, G. W. Lorimer, "The quantitative analysis of thin specimens", *Journal of Microscopy* **1975**, *103*, 203–207.

[236] P. W. Atkins, *Atkins' physical chemistry*, Eleventh edition, (Eds.: J. de Paula, J. J. Keeler), Oxford University Press, Oxford, **2018**, 908 pp.

[237] N. B. Colthup, L. H. Daly, S. E. Wiberly, *Introduction to infrared and Raman spectroscopy*, 3. ed., 6. reprint, Academic Press, **1998**, 547 pp.

[238] D. A. Long, "Infrared and Raman characteristic group frequencies. Tables and charts George Socrates John Wiley and Sons, Ltd, Chichester, Third Edition", *Journal of Raman Spectroscopy* **2004**, *35*, 905–905.

[239] A. A. Michalson, E. W. Morely, "On the Relative Motion of the Earth and the Luminiferous Ether", *The American Journal of Science* **1880**, 120–129.

[240] P. Galář, J. Khun, A. Fučíková, K. Dohnalová, T. Popelář, I. Matulková, J. Valenta, V. Scholtz, K. Kůsová, "Non-thermal pulsed plasma activated water: environmentally friendly way for efficient surface modification of semiconductor nanoparticles", *Green Chemistry* **2021**, *23*, 898–911.

[241] H. Lemmetyinen, N. V. Tkachenko, B. Valeur, J.-i. Hotta, M. Ameloot, N. P. Ernsting, T. Gustavsson, N. Boens, "Time-resolved fluorescence methods (IUPAC Technical Report)", *Pure and Applied Chemistry* **2014**, *86*, 1969–1998.

[242] K. Kůsová, T. Popelář, "On the importance of onset times and multiple-wavelength analysis of photoluminescence decays", *Journal of Applied Physics* **2019**, *125*.

[243] Y. B. Golubovskii, V. Nekuchaev, S. Gorchakov, D. Uhrlandt, "Contraction of the positive column of discharges in noble gases", *Plasma Sources Science and Technology* **2011**, *20*, 053002.

[244] J. Schafer, J. Sperka, G. Gott, L. Zajickova, R. Foest, "High-Speed Visualization of Filament Instabilities and Self-Organization Effect in RF Argon Plasma Jet at Atmospheric Pressure", *IEEE Transactions on Plasma Science* **2014**, *42*, 2454–2455.

[245] F. Sigeneger, J. Schäfer, R. Foest, D. Loffhagen, "Phase-resolved modeling of a filamentary argon plasma in an RF plasma jet", *Plasma Sources Science and Technology* **2019**, *28*, 055004.

[246] L. L. Alves, L. Marques, "Fluid modelling of capacitively coupled radio-frequency discharges: a review", *Plasma Physics and Controlled Fusion* **2012**, *54*, 124012.

[247] J. Schäfer, R. Foest, A. Quade, A. Ohl, K.-D. Weltmann, "Local deposition of SiOx-plasma polymer films by a miniaturized atmospheric pressure plasma jet (APPJ)", *Journal of Physics D: Applied Physics* **2008**, *41*, 194010.

[248] J. Schäfer, R. Foest, A. Ohl, K.-D. Weltmann, "Miniaturized non-thermal atmospheric pressure plasma jet - Characterization of self-organized regimes", *Plasma Physics and Controlled Fusion* **2009**, *51*, 124045.

[249] J. Schäfer, F. Sigeneger, J. Šperka, C. Rodenburg, R. Foest, "Searching for order in atmospheric pressure plasma jets", *Plasma Physics and Controlled Fusion* **2017**, *60*, 014038.

[250] P. Potzinger, F. W. Lampe, "Electron impact study of ionization and dissociation of monosilane and disilane", *The Journal of Physical Chemistry* **1969**, *73*, 3912–3917.

[251] I. Choquet, S. Björklund, J. Johansson, J. Wigren, "Clogging and Lump Formation During Atmospheric Plasma Spraying with Powder Injection Downstream the Plasma Gun", *Journal of Thermal Spray Technology* **2007**, *16*, 512–523.

[252] F. Miranda, F. Caliari, A. Essiptchouk, G. Pertraconi, *Atmospheric Plasma Spray Processes: From Micro to Nanostructures*, IntechOpen, **2019**, Chapter 5, pp. 4–5.

[253] COMSOL, Comsol Multiphysics Reference Manual: Version 6.0, access date: 23.04.25, COMSOL, Stockholm, Sweden, **2021**.

[254] O. Reynolds, "An Experimental Investigation of the Circumstances Which Determine Whether the Motionof Water Shall Be Direct or Sinuous and of the Law of Resistance in Parallel Channels", *Philiosophical Transactions of the Royal Society of London* **1883**, *174*, 935–982.

[255] J. Lin, Y. Lin, P. Liu, M. J. Meziani, L. F. Allard, Y.-P. Sun, "Hot-Fluid Annealing for Crystalline Titanium Dioxide Nanoparticles in Stable Suspension", *Journal of the American Chemical Society* **2002**, *124*, 11514–11518.

[256] R. Suresh, V. Ponnuswamy, R. Mariappan, "Effect of annealing temperature on the microstructural, optical and electrical properties of CeO2 nanoparticles by chemical precipitation method", *Applied Surface Science* **2013**, *273*, 457–464.

[257] L. Soriano, M. Abbate, A. Fernández, A. González-Elipe, F. Sirotti, G. Rossi, J. Sanz, "Thermal annealing of defects in highly defective NiO nanoparticles studied by X-ray and electron spectroscopies", *Chemical Physics Letters* **1997**, *266*, 184–188.

[258] S. Niesar, A. R. Stegner, R. N. Pereira, M. Hoeb, H. Wiggers, M. S. Brandt, M. Stutzmann, "Defect reduction in silicon nanoparticles by low-temperature vacuum annealing", *Applied Physics Letters* **2010**, *96*.

[259] M. Dworschak, N. Kohlmann, F. Matějka, P. Galář, L. Kienle, J. Schäfer, J. Benedikt, "Silicon nanocrystal synthesis with the atmospheric plasma source HelixJet", *Plasma Processes and Polymers* **2023**, *20*.

[260] N. Wolff, M. Dworschak, J. Benedikt, L. Kienle, "Transmission Electron Microscopy Investigation of Self-assembled "Si/Mn4Si7-Alloy" Janus Nanosphere Architectures Produced by a HelixJet Atmospheric Plasma Source", *Particle and Particle Systems Characterization* **2024**, *41*.

[261] M. Müller, M. Dworschak, J. Benedikt, L. Kienle, "Tungsten Nanoparticles Generated in an Atmospheric Pressure Plasma Jet", *Particle & Particle Systems Characterization* **2024**, *41*.

[262] M. Dworschak, M. Müller, T. Tjardts, L. Kienle, J. Benedikt, "Surface Passivation of Silicon Nanoparticles Monitored by In Situ FTIR", *Plasma Processes and Polymers* **2025**, *22*, 2400206.

List of own publications

Parts of this thesis published in peer-reviewed journals

1. **Maren Dworschak**, Niklas Kohlmann, Filip Matějka, Pavel Galář, Lorenz Kienle, Jan Schäfer and Jan Benedikt, *"Silicon nanocrystal synthesis with the atmospheric plasma source HelixJet",* Plasma Processes and Polymers, 2022, 20, 2, 20:e2200129
   https://doi.org/10.1002/ppap.202200129

2. Niklas Wolff, **Maren Dworschak**, Jan Benedikt and Lorenz Kienle, *"Transmission Electron Microscopy Investigation of Self-assembled 'Si/Mn_4Si_7-Alloy' Janus Nanosphere Architectures Produced by a HelixJet Atmospheric Plasma Source"*, Particle & Particle Systems Characterization, 2023, 42, 3, 2300094
   https://doi.org/10.1002/ppsc.202300094

3. Martin Müller, **Maren Dworschak**, Jan Benedikt and Lorenz Kienle, *"Tungsten Nanoparticles Generated in an Atmospheric Pressure Plasma Jet"*, Particle & Particle Systems Characterization, 2024, 41, 2400037
   https://doi.org/10.1002/ppsc.202400037

4. **Maren Dworschak**, Martin Müller, Tim Tjards, Lorenz Kienle and Jan Benedikt, *"Surface passivation of silicon nanoparticles monitored by in situ FTIR"*, Plasma Processes and Polymers, 2025, 22, 4, 2400206
   https://doi.org/10.1002/ppap.202400206

Further publications in peer-reviewed journals

5. **Maren Dworschak**, Oguz Han Asnaz and Franko Greiner, *A minimally invasive electrostatic particle extractor for nanodusty plasmas and its application for the verification of in situ Mie polarimetry*, Plasma Sources Science and Technology, 2021, 30, 3, 035011
   https://doi.org/10.1088/1361-6595/abe4c0

Acknowledgments

Zunächst möchte ich mich bei Prof. Dr. Jan Benedikt dafür bedanken, dass er mir dieses spannende Projekt anvertraut hat und mir die Möglichkeit gegeben hat, so viele wertvolle Erfahrungen im Rahmen dieser Doktorarbeit zu sammeln. Das Thema des Projektes hat mich von Anfang an begeistert und ich habe mich besonders über die internationalen Kooperationen gefreut, die durch ihn möglich geworden sind. Ich bin ihm sehr dankbar, dass er nach dem Abschied von Sadegh Askari aus unserer Arbeitsgruppe ohne zu zögern die Betreuung meiner Arbeit übernommen hat. Vielen Dank für die zahlreichen Gespräche und Brainstorming-Sitzungen, die mir immer neue Ideen gegeben haben, welche Messungen als nächstes durchgeführt werden können. Es war schön, einen Doktorvater zu haben, der selbst gerne ab und zu im Labor vorbeischaut und der sich genau so gefreut hat, wie ich, als die Partikel endlich das erste Mal Photolumineszenz gezeigt haben.

Außerdem möchte ich mich bei Volker Rohwer, Michael Poser und Frank Brach bedanken. Ohne sie wäre diese Arbeit kaum möglich gewesen. Wenn im Labor mal dringend eine neue Gasleitung benötigt wurde, konnte ich mir sicher sein, dass Volker sie in 15 Minuten fertigstellt, obwohl seine Liste an Aufgaben jeden Tag unendlich lang ist. Danke dafür, und danke auch für die tollen und ehrlichen Gespräche, die ich mit dir führen konnte. Michael Poser danke ich insbesondere für die tatkräftige Unterstützung bei der Umsetzung einer Interlock-Funktion, die meine eigene Sicherheit beim Umgang mit der 10kV-Sammelspannung jeden Tag gewährleistet hat. Außerdem möchte ich mich bei ihm für die Planung der AG-Ausflüge und die damit verbundene private Kajak-Stunde bedanken, die mir sehr viel Spaß gebracht hat.
Frank Brach danke ich für die Unterstützung mit dem Design und der Fertigung der *in-situ*-Kammer, die wirklich wunderbar funktioniert und zu tollen Messergebnissen geführt hat.

Des Weiteren möchte ich mich bei meinen Kollegen Tristan Winzer und Christian Schulze bedanken, die zu echten Freunden geworden sind. Die Abende mit euch, an denen wir Kinderserien geguckt haben, waren eine super Abwechslung vom Doktoranden-Alltag.

Außerdem möchte ich mich bei meiner Büropartnerin Kerstin Sgonina bedanken. Vielen Dank, dass ich mit dir wirklich über alles reden und dir alles anvertrauen konnte. Danke auch für deine fachliche Hilfe, insbesondere in Bezug auf Comsol.
Mein Dank gilt natürlich auch allen anderen Doktoranden und Mitgliedern der Arbeitsgruppe für die schöne Zeit, die leckeren Kuchen und die ausschweifenden Gespräche in den Kaffeerunden. Das werde ich vermissen.

Bedanken möchte ich mich auch bei meinen Kooperationspartnern an der technischen Fakultät für die gute Zusammenarbeit. Ich weiß, dass es sehr lange dauert, ein Grid ins TEM zu bringen und ich weiß auch, dass amorphes Silizium auf amorphem Kohlenstoff keine schöne

Probe ist. Deswegen möchte ich mich für eure Geduld bedanken, denn es waren in den ersten Jahren sehr viele amorphe Proben, die ihr für mich analysieren musstet, bis endlich die Partikel kristallin waren. Aber dann haben wir auch zwei schöne Paper gemeinsam veröffentlicht.

Ebenso gilt mein Dank meinen internationalen Kooperationspartnern in Prag für die gute Zusammenarbeit und die neuen geschlossenen Freundschaften: Děkuju za spolupráci!

Zuletzt möchte ich mich bei meiner Familie bedanken. Meine Eltern, die mich zu jedem Zeitpunkt meines Studiums unterstützt haben und mir das Vertrauen gegeben haben, dass ich alles schaffen kann, was ich mir vornehme. Das selbe gilt für meine Schwester Maike, die immer für mich da war. Danke auch, dass ihr euch alle die Zeit genommen habt, diese Arbeit zu lesen und zu korrigieren.

Meinem Freund Martin gebührt das letzte Dankeschön. Ich hatte das große Glück, dich über unsere gemeinsame Forschungsarbeit kennenzulernen. Seitdem haben wir zusammen schon viele Hürden gemeistert. Ohne dich wäre diese Arbeit niemals möglich gewesen. Und das liegt nicht nur daran, dass wir gemeinsam Paper für diese Arbeit veröffentlicht haben. Du bist mein Rückhalt und meine unerschöpfliche Quelle der Motivation. Ich weiß, dass ich mich immer auf dich verlassen kann und ich bin dir unendlich dankbar für deine Unterstützung. Ich freue mich auf die gemeinsame Zukunft mit dir.

Declaration of Authorship

Hiermit versichere ich, dass die vorliegende Dissertation, abgesehen von der Beratung durch den Betreuer und der Verwendung der angegebenen Hilfsmittel, nach Inhalt und Form meine eigene Arbeit ist. Die Arbeit ist unter Einhaltung der Regeln guter wissenschaftlicher Praxis der Deutschen Forschungsgemeinschaft entstanden.
Ich erkläre weiterhin, dass die vorliegende Arbeit in gleicher oder ähnlicher Form noch nicht im Rahmen eines anderen Prüfungsverfahrens vorgelegen hat, veröffentlicht, oder zur Veröffentlichung eingereicht wurde. Außerhalb eines Prüfungsverfahrens veröffentlichte Teile sind als solche gekennzeichnet. Mir wurde kein akademischer Grad entzogen.

Kiel, den